Exploring the role of primary cilia in growth plate function and mechanoadaptation by combining high resolution tissue imaging and complex *in vitro* models



Théana Johnson

St Edmund Hall
University of Oxford

Supervised by:

Associate Professor Angus Wann

Professor Eleanor Stride

Professor Tonia Vincent

A thesis submitted for the degree of

Doctor of Philosophy

August 2025

Abstract

Primary cilia are essential organelles in skeletogenesis, with key roles in chondrogenesis, osteogenesis and limb patterning. The micrometre-scale size and delicate structure of primary cilia poses a significant challenges to their *in vivo* analysis, particularly, for example, within the matrix rich, dense but also dynamic environment of the growth plate. In this project, I developed and applied a high-resolution 3D imaging and analysis pipeline to characterise primary cilia organisation in the postnatal murine growth plate. Using endogenous fluorescent reporters and semi-automated image analysis, I quantitatively mapped cilia prevalence, orientation, length and basal body positioning across thousands of chondrocytes from multiple anatomical regions. These data revealed spatial patterns in cilia organisation, particularly in the resting zone of the middle of the growth plate, implying local micro-environmental influences.

To investigate the functional relevance of these patterns, I examined how genetic deletion of *Ift88* and mechanical unloading affect ciliary structure and growth plate architecture. Both *Ift88* deletion and limb offloading resulted in tibial growth plate shortening accompanied by subtle reductions in percentage ciliation in the hypertrophic zone. These did not arise with changes in cilia length or orientation, raising questions about the relationship between ciliary morphology and function. My findings, combined with other studies in the literature, suggest that primary cilia may integrate spatial and mechanical cues in a context-dependent manner and highlight the need for further research into the molecular mechanisms linking cilia structure to tissue-level outcomes.

I then described the further development of an *in vitro* osteochondral model, incorporating a BMP-2 gradient and mechanical loading to assess cilia-mediated responses in a controlled bioengineered context. Adipose-derived murine mesenchymal stem cells and costal chondrocytes were used as a chondroprogenitor source in order to exploit the genetic tools available in mouse lines, such as conditional *Ift88* deletion. Although differentiation of mouse MSCs proved difficult, the system demonstrated the feasibility of generating a spatially patterned growth factor gradient *in vitro* and applying mechanical loading, offering a promising framework for further refinement.

Together, this work combines *in vivo* and *in vitro* approaches to advance our understanding of primary cilia in skeletal development and provides methodological platforms for future research in cartilage biology mechanotransduction and ciliopathies.

Acknowledgements

Firstly, I would like to thank my supervisor Angus. Before I applied to DPhil positions, people I had met in my experiences in research had always emphasised how important one's supervisor is to a DPhil experience. And I couldn't have hoped for a better supervisor than Angus. You have provided me with an environment so supportive to my research and wellbeing, always being enthusiastic and encouraging. Experimental failures did not seem so demoralising after showing them to Angus, as he always helped me think through them and come out of a meeting with fresh energy. This has allowed me to develop both professionally and personally. So thank you Angus!

Thank you to my co-supervisors Eleanor and Tonia for providing me with valuable guidance and feedback. Your fresh perspectives were always useful in guiding my research.

One person who has been so central in my DPhil experience is Swati - I could not imagine having started my DPhil without Swati. She not only taught me so much in the lab and helped me kick off the project, but was also so fun to spend time with. We have laughed so much together, and have formed a friendship. Thank you for being there in the more challenging times, to talk through things over coffee (always), gossip, party, eat ramen!

Thank you to everyone in the Kennedy Institute who has helped with experiments in this project. In particular, thank you to Tino and Jadwiga for all the help with the mouse work. Thank you to Ida, Oyindamola and Rhiannon for the always beautiful histology work. Thank you to Jacky for the help setting up the image analysis pipeline.

It isn't often that you get to publicly celebrate your friends for the incredible human beings that they are, so, yes, I am going to use my DPhil acknowledgements to do just that.

Ula - meeting you has most likely been the highlight of my DPhil. I can't thank you enough for everything you have done for me during this time - from all of

our catch-up chats, being a minute away (literally) when in need, supporting me through all the lows and toughest moments both personally and in the lab, always being up for an adventure! I have so many incredible memories with you and I can't wait to make more.

Thank you Vicky for all the lab lunches, fun times outside the lab, laughs at our silly adventures.

Dan and Omer, I have loved the little crew we have formed with Ula and Vicky. Our activities and trips have been my favourite moments in Oxford. Thank you and here's to climbing many more summits!

Momo, thank you for all our knit and chat evenings, and all the laughs. Thank you Boris for always eating my cakes and introducing me to so many board games.

Thank you to all my fellow Teddies - Steph, Kat, Natalie, Camille, Ed, Radwa, Sally - for sharing this Oxford and DPhil experience and all the incredible memories.

Thank you to all my friends in the Kennedy - Julia, Thea, Kaitlyn, Isolde, Dafni, Cecilia, Val, Tom, Jane - for making days in the lab so fun.

Very importantly, I would like to thank the women in my life who I have known for years and sometimes decades. We may live in different cities, countries and continents, but their friendship is so central to my life - Laure, Zoé, Kathryn, Marine and Stella. Having all of you come to visit me in Oxford has been so special, and you enduring friendship means the world to me.

Laure - thank you always being there, knowing me so well, sharing lots of fous rires, indulging my silliness, and just being you!

Zoé - 19 years later (!), thank you for being such a loyal friend, always checking up on me and coming to see me so often.

Kathryn - I will always remember first meeting you 10 years ago in our first year halls, and I instantly knew we would be friends. Thank you for being a rock for so many years. And thank you for always letting me stay with you in London.

Marine - thank you for, by going in before me, guiding me in this DPhil experience and always being up for a little adventure.

Stella - thank you for this special bond we have, for making me discover so many new places and always being such a strong supportive presence.

Thank you to my brothers - Laumer and Emmeran - for bringing so much laughter and silliness to my life. Life is more fun with you in it!

Last but certainly not least, thank you to my parents - my biggest cheerleaders in life. You have always supported me in everything I do, and brought an enthusiasm that I sometimes didn't even have. I am sure you will attempt to read this thesis, so good luck! Thank you for coming to visit Oxford so often. Thank you for always being proud of me, and for always being so supportive.

This DPhil has run alongside some of the most difficult times in my life but also some of the most joyous, and I am forever grateful to all of these people for being there for it all. They say it takes a village, so thank you to my village.

Declaration

I hereby declare that I am the sole author of this thesis. No part of this thesis has been submitted for a degree at this or any other university. The work presented herein is entirely my own, except where explicitly stated in the text and as detailed below:

- **Animal work**: Mouse breeding, care and tamoxifen administration were carried out by technicians at the Biology Service Unit, Kennedy Institute of Rheumatology, in particular Mr Albertino Bonifacio. Mouse surgeries were performed by Dr Jadwiga Miotla-Zarebska.
- **Histology**: Tissue processing for histological analysis was performed by Dr Ida Parisi, Ms Rhiannon Cook and Ms Oyindamola Ajisegiri. Tissue sectioning was conducted by Dr Parisi, Ms Cook, Ms Ajisegiri and myself.
- **FACS**: FACS analysis of specific cell surface proteins on adipose-derived mesenchymal stem cells was performed by Dr Swati Midha.

Supervision was provided by Associate Professor Angus Wann, Professor Eleanor Stride and Professor Tonia Vincent. This research was funded by a Kennedy Trust Prize Studentship and received financial support from the BBSRC.

Contents

List of Figures **xiv**

List of Tables **xx**

List of Abbreviations **xxi**

1 Introduction **1**

1.1 Skeletal development 2

1.1.1 Endochondral ossification 2

1.1.2 The growth plate 4

1.2 The primary cilium 9

1.2.1 Structure and function 9

1.2.2 Assembly 12

1.2.3 IFT88 14

1.2.4 The role of the primary cilium in skeletal development 15

1.3 *In vitro* bioengineered models 23

1.3.1 Cell sources &materials 24

1.3.2 Growth plate *in vitro* models 28

1.4 Project aims 34

2 Development of a high resolution imaging and analysis method to study primary cilia in the murine growth plate **36**

2.1 Introduction . . . 37

2.2 Materials & Methods . . . 39

2.2.1 Animals . . . 39

2.2.2 Tissue collection & processing . . . 39

2.2.3 Confocal imaging . . . 40

2.2.4 Image analysis pipeline . . . 40

2.2.5 3D spherical coordinates . . . 42

2.2.6 Data analysis . . . 42

2.3 Results . . . 46

2.3.1 High resolution imaging . . . 46

2.3.2 Image analysis pipeline . . . 46

2.4 Discussion . . . 50

3 Ciliation in the mouse post-natal growth plate **55**

3.1 Introduction . . . 56

3.2 Materials & Methods . . . 60

3.2.1 Animals, tissue collection, imaging &analysis . . . 60

3.2.2 Micro-computed tomography (MicroCT) . . . 60

3.2.3 Histology . . . 61

3.2.4 Statistical analysis . . . 61

3.3 Results . . . 62

3.3.1 Murine growth plate characterisation by microCT, histology and fluorescence microscopy . . . 62

3.3.2 Cell volume in the growth plate . . . 64
3.3.3 Cell orientation in the growth plate . . . 67
3.3.4 Percentage ciliation in the growth plate . . . 69
3.3.5 Primary cilia length in the growth plate . . . 70
3.3.6 Primary cilia orientation in the growth plate . . . 72
3.3.7 Centriole position in the growth plate . . . 73
3.4 Discussion . . . 77
3.4.1 Cell volume in the growth plate . . . 77
3.4.2 Cell orientation in the growth plate . . . 78
3.4.3 Percentage ciliation in the growth plate . . . 79
3.4.4 Primary cilia length in the growth plate . . . 80
3.4.5 Primary cilia orientation in the growth plate . . . 82
3.4.6 Centriole position in the growth plate . . . 87

4 Ciliation in the Ift88 cKO and immobilised mouse post-natal growth plate 91

4.1 Introduction . . . 92
4.2 Materials & Methods . . . 95
4.2.1 Animals, tissue collection, imaging &analysis . . . 95
4.2.2 Tamoxifen treatment . . . 95
4.2.3 Double neurectomy . . . 95
4.2.4 Ki67 staining . . . 96
4.2.5 Statistical analysis . . . 97
4.3 Results . . . 98
4.3.1 Growth plate phenotype of the *Ift88* cKO . . . 98

4.3.2 Growth plate phenotype of the offloaded and contralateral *Ift88*$^{fl/fl}$ growth plates . . . 108

4.4 Discussion . . . 118

4.4.1 Effect of *Ift88* knockout on growth plate cell and primary cilia organisation . . . 118

4.4.2 Effect of mechanical loading on growth plate cell and primary cilia organisation . . . 128

5 *In vitro* osteochondral model generation using murine cells 134

5.1 Introduction . . . 135

5.1.1 *In vitro* models . . . 135

5.1.2 BMP-2 . . . 137

5.1.3 GelMA . . . 138

5.1.4 Buoyancy-driven BMP-2 gradient . . . 140

5.2 Materials & Methods . . . 144

5.2.1 Murine cell isolations &characterisation . . . 144

5.2.2 RNA extraction . . . 146

5.2.3 qPCR . . . 146

5.2.4 Immunophenotypic characterisation by fluorescence-activated cell sorting (FACS) . . . 147

5.2.5 GelMA & HepMA synthesis & characterisation . . . 148

5.2.6 Mechanical testing . . . 149

5.2.7 Buoyancy-based gradient generation . . . 150

5.2.8 Histology . . . 152

5.2.9 Statistical analysis . . . 152

5.3 Results . . . 153

5.3.1 MSC characterisation . . . 153
5.3.2 Costal chondrocyte characterisation . . . 158
5.3.3 Material synthesis and mechanical characterisation . . . 158
5.3.4 3D cell cultures inside gels . . . 159
5.3.5 Gradient generation . . . 165
5.4 Discussion . . . 167
5.4.1 Murine MSC and costal chondrocyte characterisation . . . 167
5.4.2 Material synthesis and characterisation . . . 170
5.4.3 3D cell cultures inside gels . . . 171

6 Application of the gradient osteochondral model to study the role of primary cilia organisation in osteochondral differentiation 173

6.1 Introduction . . . 174
6.2 Materials & Methods . . . 177
6.2.1 Gradient *in vitro* model . . . 177
6.2.2 In vitro IFT88 deletion . . . 178
6.2.3 Western blotting . . . 179
6.3 Results . . . 181
6.3.1 AD MSCs inside the BMP-2 gradient . . . 181
6.3.2 Costal chondrocytes inside the BMP-2 gradient . . . 182
6.3.3 In vitro *Ift88* deletion . . . 186
6.3.4 *Ift88* and loading regulation of differentiation in vitro . . . 190
6.4 Discussion . . . 194
6.4.1 AD MSCs inside the BMP-2 gradient . . . 194
6.4.2 Mechanical loading of AD MSCs inside the BMP-2 gradient . . . 195

6.4.3 Costal chondrocytes inside the BMP-2 gradient 196

6.4.4 Mechanical loading of costal chondrocytes inside the BMP-2 gradient 198

6.4.5 *Ift88 in vitro* deletion 199

7 Discussion **205**

7.1 Overall discussion 205

7.2 Limitations 214

7.3 Future work 218

7.4 Conclusion 220

Appendices

Bibliography **243**

List of Figures

1.1 **Stages of endochondral ossification during long bone development** . . . 3

1.2 **Organisation and molecular regulation of the growth plate during endochondral ossification** . . . 5

1.3 **Primary cilium structure and intraflagellar transport (IFT) mechanisms** . . . 11

1.4 **Two main pathways of primary cilium assembly** . . . 13

1.5 **Ihh signalling regulation via the primary cilium** . . . 18

1.6 **Disruption in cell and tissue architecture by *Ift88* genetic mutations affects growth plate organisation at different ages** 20

1.7 **Schematic illustration of various fabrication techniques for creating gradient hydrogels used in tissue engineering applications** . . . 31

2.1 **Spherical coordinates** . . . 43

2.2 **Flowchart describing the steps of the analysis pipeline run in R to calculate cell, primary cilia and centriole characteristics** 44

2.3 **Primary cilia in the growth plate of a 6-week old ARL13B-Centrin-2 mouse imaged with the 40x objective** . . . 47

2.4 **Primary cilia in the subchondral bone (A), trabecular bone (B), kidney (C) and articular cartilage (D) of 6-week old ARL13B-Centrin-2 mouse** . . . 48

2.5 Cell, primary cilia and centriole detection on an image of a 6-week old growth plate in arivis Vision4D 49

3.1 Histological staining of the tibial growth plate of a 4-week old mouse 63

3.2 MicroCT of mouse tibial growth plates 64

3.3 Safranin-O staining (A-D) and primary cilia imaging (E-H) of murine growth plates at different ages 65

3.4 (A) Primary cilia in the growth plate a of a 6-week old *Ift88*$^{fl/fl}$ mouse 66

3.5 6-week old *Ift88*$^{fl/fl}$ murine growth plate stained with DAPI and phalloidin 67

3.6 Cell organisation differs by zone and region in the 6-week old *Ift88*$^{fl/fl}$ growth plate 68

3.7 Varying percentage ciliation in the different regions and zones of the 6-week old *Ift88*$^{fl/fl}$ growth plate 69

3.8 Primary cilia length is longer in the hypertrophic zone of the 6-week old *Ift88*$^{fl/fl}$ growth plate 70

3.9 Primary cilia orientation is consistent throughout the 6-week old *Ift88*$^{fl/fl}$ mouse growth plate 71

3.10 Average resultant per cilium in the resting, proliferating and hypertrophic zones of the middle and lateral regions of the 6 week-old *Ift88*$^{fl/fl}$ growth plate 73

3.11 Disperse centriole position in the 6-week old *Ift88*$^{fl/fl}$ growth plate 74

3.12 (A) Primary cilia and (B) centriole organisation in the resting zone of a 6-week old *Ift88*$^{fl/fl}$ growth plate 76

4.1 Age and timing of tamoxifen administration, surgeries and tibia collection for *Ift88* cKO experiment (A) and *Ift88*$^{fl/fl}$ offloading experiment (B) 96

4.2 Changes in length measured from thresholded microCT images of *Ift88*$^{fl/fl}$ (A) and *Ift88* cKO (B) growth plates. (C) Thresholded growth plate lengths of *Ift88*$^{fl/fl}$ and *Ift88* cKO limbs 99

4.3 Safranin-O staining and primary cilia imaging of the *Ift88*$^{fl/fl}$ (A) and *Ift88* cKO (B) growth plates across ages 100

4.4 Differences in cell organisation between the *Ift88*$^{fl/fl}$ and *Ift88* cKO growth plates 101

4.5 Differences in percentage ciliation between the *Ift88*$^{fl/fl}$ and *Ift88* cKO growth plates 104

4.6 Differences in primary cilia length between the *Ift88*$^{fl/fl}$ and *Ift88* cKO growth plates 105

4.7 Differences in primary cilia orientation between the 6-week old *Ift88*$^{fl/fl}$ and *Ift88* cKO growth plates 106

4.8 Average resultant per cilium in the resting, proliferating and hypertrophic zones of the middle and lateral regions of the *Ift88*$^{fl/fl}$ (A) and *Ift88* cKO (B) growth plates 107

4.9 Differences in centriole position between the 6-week old *Ift88*$^{fl/fl}$ and *Ift88* cKO growth plates 108

4.10 Change in percentage of Ki-67 positive cells in the growth plates of 2, 4 and 10 week old mice 109

4.11 (A)Ki-67 staining in the growth plate of a 6 week-old *Ift88*$^{fl/fl}$ mouse. (B) Percentage of Ki-67 positive cells in the *Ift88*$^{fl/fl}$ and *Ift88* cKO growth plates 109

4.12 Differences in length measured from thresholded microCT images of the *Ift88*$^{fl/fl}$ (A), *Ift88*$^{fl/fl}$ offloaded (B) and *Ift88*$^{fl/fl}$ contralateral (C) growth plates. (D) Thresholded growth plate lengths of *Ift88*$^{fl/fl}$, *Ift88* cKO, *Ift88*$^{fl/fl}$ offloaded and *Ift88*$^{fl/fl}$ contralateral limbs 110

4.13 Primary cilia imaging in the middle of the growth plates of *Ift88*$^{fl/fl}$ offloaded (A) and contralateral (B) limbs 111

4.14 Cell organisation in *Ift88*$^{fl/fl}$, *Ift88*$^{fl/fl}$ offloaded and *Ift88*$^{fl/fl}$ contralateral growth plates . . . 112

4.15 Percentage ciliation in the *Ift88*$^{fl/fl}$, *Ift88* cKO, *Ift88*$^{fl/fl}$ offloaded and contralateral growth plates . . . 114

4.16 Differences in primary cilia length between the *Ift88*$^{fl/fl}$, Ift88 cKO, *Ift88*$^{fl/fl}$ offloaded and *Ift88*$^{fl/fl}$ contralateral growth plates . . . 115

4.17 Differences in primary cilia orientation between the 6-week old *Ift88*$^{fl/fl}$, Ift88 cKO, *Ift88*$^{fl/fl}$ offloaded and *Ift88*$^{fl/fl}$ contralateral growth plates . . . 116

4.18 Differences in centriole position between the 6-week old *Ift88*$^{fl/fl}$, Ift88 cKO, *Ift88*$^{fl/fl}$ offloaded and *Ift88*$^{fl/fl}$ contralateral growth plates . . . 117

5.1 (A) GelMA synthesis with methacryloyl substitution. (B) GelMA photocrosslinking with UV light in the presence of a photoinitiator . . . 139

5.2 Schematic overview of the fabrication and application of a BMP-2 gradient hydrogel system for osteochondral tissue engineering . . . 141

5.3 (A) Moulds used for the gradient gels - a 3 mm thick silicone sheet fit between two glass slides. (B) Polymerised GelMA gradient gels inside the moulds . . . 151

5.4 Morphology of AD (A) and BM (B) MSCs. Crystal violet staining of AD (C) and BM (D) MSC CFUs after 14 days of culture . . . 154

5.5 Adipogenic differentiation of MSCs . . . 155

5.6 Osteogenic differentiation of MSCs . . . 156

5.7 Chondrogenic differentiation of MSCs . . . 157

5.8 Percentage cells stained positive for MSC markers Sca-1 and CD105 and negative control hematopoietic stem cell markers CD45 and CD34. (Performed by Dr Swati Midha) . . . 158

5.9 Comparative gene expression profiles of chondrogenic markers in costal chondrocytes cultured in flasks after isolation . 159

5.10 GelMA and HepMA synthesis 160

5.11 Live-dead assay of AD MSCs and costal chondrocytes cultured inside 10% GelMA 161

5.12 3D GelMA culture conditions (no BMP-2 gradient) 162

5.13 Electropherogram of the RNA extracted from AD MSCs cultured inside GelMA 163

5.14 Gene expression profiles of AD MSCs cultured inside gels (no gradients) (A) without BMP-2, (B) with 100 ng/mL BMP-2 added to the culture medium on day 10, (C) with BMP-2 bound to HepMA inside the gel, and (D) gene expression profile of mouse tibial bone and costal cartilage for comparison 164

5.15 Buoyancy-driven gradient formation 165

6.1 (A) Mechanical loading setup for GelMA gradients (8 x 4 x 3 mm) seeded with AD MSCs and costal chondrocytes using the ElectroForce 5500 system. (B) Gel setup in the 24-well plate. (C) Side view of a single gel in a well held in place by the piston at its top surface. (D) Gradient gel loading timeline 178

6.2 Gene expression profiles of AD MSCs cultured inside BMP-2 gradients across 42 days 183

6.3 Safranin-O (A,C) and toluidine blue staining (B,D) of BMP-2 gradients gels seeded with AD MSCs and costal chondrocytes on day 28 184

6.4 Gel loading under displacement control 185

6.5 Gene expression profiles on day 18 of AD MSCs cultured inside BMP-2 gradients and loaded from day 14 to 18 at 10% strain for 1 hour at 1 Hz for 5 days compared to static culture 186

6.6 Gene expression profiles of costal chondrocytes cultured inside BMP-2 gradients across 42 days 187

6.7 **Gene expression profiles on day 11 of costal chondrocytes cultured inside BMP-2 gradients and loaded from day 7 to 11 at 10% strain for 1 hour at 1 Hz for 5 days compared to static culture** 188

6.8 **Ift88 stability study** 189

6.9 ***In vitro Ift88* 2D deletion** 190

6.10 **Gene expression profiles on day 11 of costal chondrocytes cultured inside BMP-2 gradients treated 5 µM 4-OH-T for 96 hours from day 7** 191

6.11 **Gene expression profiles on day 14 of costal chondrocytes cultured inside BMP-2 gradients treated 5 µM 4-OH-T for 96 hours from day 7 to 11 and loaded from day 11 to 14 at 10% strain for 1 hour at 1 Hz compared to static culture** . . 192

6.12 **Costal chondrocytes inside the BMP-2 gradient on day 28** . . 193

1 R code used for measuring the cell, primary cilia and centriole features from the Excel spreadsheet exported out of arivis for the analysis pipeline. 223

2 **Spherical coordinates of the position of centrioles in (A) non-ciliated and (B) ciliated cells** 240

3 **Ct values of housekeeping genes tested in MSCs differentiated in 2D (A) and costal chondrocytes cultured in GelMA (B)** . 240

4 **Stress–strain curve of a GelMA hydrogel** 241

5 **Western blot testing the IFT88 antibody** 241

List of Tables

4.1 **Ratio of the number of resting to proliferating to hypertrophic cells in the growth plate.** 110

5.1 **qPCR reaction mix.** 147

5.2 **qPCR target genes and corresponding TaqMan Gene Expression Assay IDs (ThermoFisher).** 148

7.1 **Evaluation of the achievement of project aims set out in Chapter 1** 215

2 **Transcripts per million (TPM) from bulk RNA sequencing of the growth plate of a 6 week-old C57BL/6 wild-type mouse.** 242

List of Abbreviations

2D, 3D	Two or three-dimensional, referring in this thesis to spatial dimensions.
4-OH-T	4-hydroxytamoxifen
ACAN	Aggrecan
AD MSCs	Adipose-derived mesenchymal stem cell
ATP	Adenosine triphosphate
Alpl	Alkaline phosphatase
BGLAP	Osteocalcin
BM MSCs	Bone marrow-derived mesenchymal stem cell
BMP	Bone morphogenetic protein
Ca^{2+}	Calcium ion
cAMP	Cyclic adenosine monophosphate
CFU	Colony forming unit
CGM	Complete growth media
cKO	Conditional knockout
Col1,2,9,10,11	Collagen type I, II, IX, X, XI
DAPI	4',6-diamidino-2-phenylindole
diH_20	Deionised water
DoF	Degree of functionalisation
DMEM	Dulbecco's Modified Eagle Medium
DMSO	Dimethyl sulfoxide
ECM	Extracellular matrix
FACS	Fluorescence-activated cell sorting

FBS . . . . . Fetal bovine serum

FGF . . . . . Fibroblast growth factor

FITC . . . . . Fluorescein isothiocyanate

GAGs . . . . . Glycosaminoglycans

GAPDH . . . . . Glyceraldehyde-3-phosphate dehydrogenase

GelMA . . . . . Gelatin methacryloyl

GFP . . . . . Green fluorescent protein

H&E . . . . . Haematoxylin and eosin

HepMA . . . . . Heparin methacryloyl

Hh . . . . . Hedgehog

IFT . . . . . Intraflagellar transport

IHC . . . . . Immunohistochemistry

Ihh . . . . . Indian hedgehog

IGF . . . . . Insulin growth factor

iPSC . . . . . Induced pluripotent stem cell

ITS+1 . . . . . Insulin–transferrin–selenium supplement

MAA . . . . . Methacrylic anhydride

MEF2C . . . . . Myocyte enhancer factor 2C

MicroCT . . . . . Micro-computed tomography

MMP . . . . . Matrix metalloproteinase

MSC . . . . . Mesenchymal stem cell

NMR . . . . . Nuclear magnetic resonance

orpk . . . . . Oak ridge polycystic kidney

PBS . . . . . Phosphate buffered saline

PBS-X . . . . . PBS with 0.05% Triton X-100

PCP . . . . . Planar cell polarity

Penstrep . . . . . Penicillin-streptomycin

PFA . . . . . Paraformaldehyde

PC1,2 . . . . . Polycystin-1,2

PRG4 . . . . . Lubricin

Ptch . . . . . Patched

PTHrP . . . . . Parathyroid hormone-related protein

qPCR . . . . . Quantitative polymerase chain reaction

RANKL . . . . . Receptor activator of nuclear factor kappa-B ligand

RIN . . . . . RNA integrity number

RNA . . . . . Ribonucleic acid

Runx2 . . . . . Runt-related transcription factor 2

Smo . . . . . Smoothened

SOX9 . . . . . Sex determining region Y-related high mobility group-box gene 9

SP7 . . . . . Osterix

SPP1 . . . . . Osteopontin

TBP . . . . . TATA-binding protein

TBST . . . . . Tris-buffered saline with 0.1% Tween-20

TGF-β . . . . . Transforming growth factor β

TPM . . . . . Transcripts per million

UV . . . . . Ultraviolet

VEGFA . . . . . Vascular endothelial growth factor

YAP . . . . . Yes-Associated protein

1

Introduction

Contents

1.1 Skeletal development 2

1.1.1 Endochondral ossification 2

1.1.2 The growth plate 4

1.2 The primary cilium 9

1.2.1 Structure and function 9

1.2.2 Assembly 12

1.2.3 IFT88 14

1.2.4 The role of the primary cilium in skeletal development . . 15

1.3 *In vitro* bioengineered models 23

1.3.1 Cell sources &materials 24

1.3.2 Growth plate *in vitro* models 28

1.4 Project aims 34

1.1 Skeletal development

1.1.1 Endochondral ossification

In mammals, bone development starts during late embryogenesis, with limb buds first visible at around 4 weeks of gestation in humans, and extends into early adulthood, typically concluding between the ages of 20 and 25 [1]. The human skeleton arises from three distinct embryonic lineages: neural crest cells, which contribute to the craniofacial skeleton; the paraxial mesoderm, which gives rise to the axial skeleton (skull, spine, ribs, sternum); and the lateral plate mesoderm, which forms the appendicular skeleton (hips, shoulders, arms, legs) [2, 3].

The formation and maturation of bone occurs through two principal mechanisms: intramembranous ossification, responsible for generating flat bones such as those of the skull directly from mesenchymal stem cells (MSCs) differentiating into osteoblasts, and endochondral ossification, where MSCs differentiate into chondrocytes before becoming bone (Fig. 1.1) [4].

At the onset of skeletogenesis, in endochondral ossification, mesenchymal precursor cells condense into aggregates at the sites of the future bones, under the effect of transforming growth factor β (TGF-β), which promotes the expression of molecules involved in the condensation process such as N-cadherin, neural cell adhesion molecule, fibronectin and tenascin-C (Fig. 1.1) [5]. The cells proliferate and start expressing Sex determining region Y-related high mobility group-box gene 9 (*SOX9*), considered a master transcription factor in chondrogenesis [6]. *SOX9* is turned on prior to and required for the condensation of MSCs during foetal development, and for

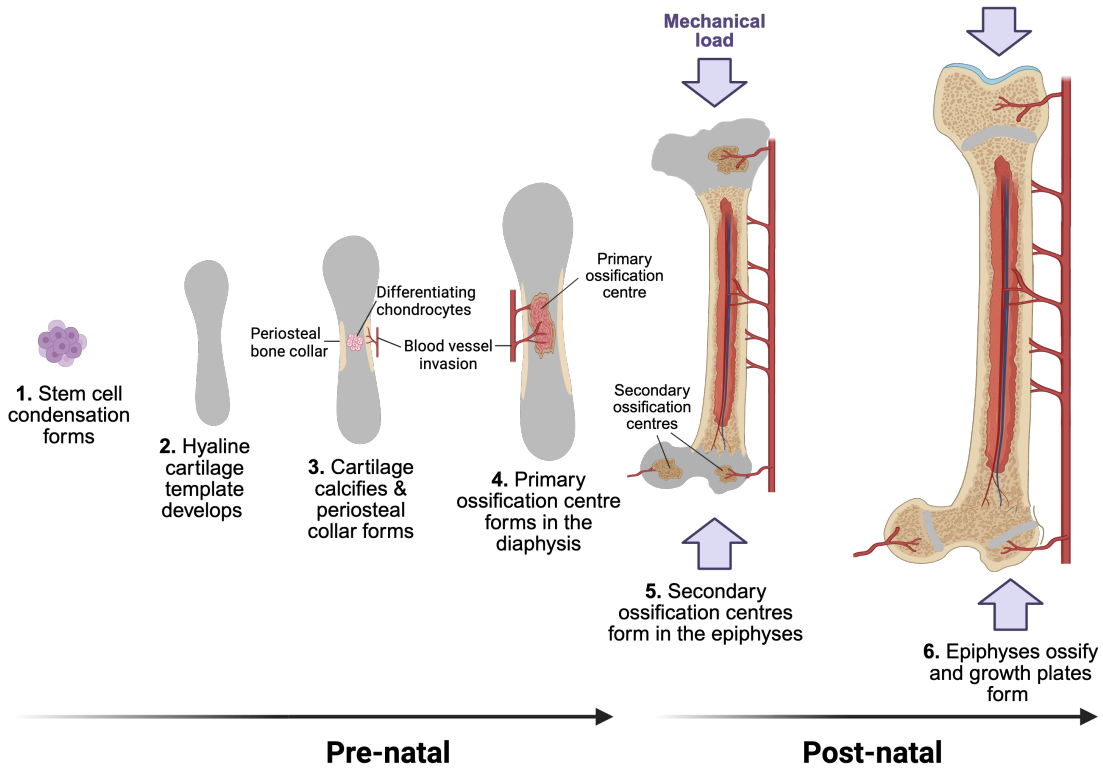


Figure 1.1: Stages of endochondral ossification during long bone development. Endochondral ossification begins prenatally with a mesenchymal condensation, from which a cartilage template forms. Chondrocyte proliferate and differentiate, accompanied by vascular invasion. As the matrix mineralises, the primary ossification centre is established in the diaphysis. Subsequent formation of secondary ossification centres in the epiphyses gives rise to growth plates at the epiphyses. Mechanical load contributes to bone maturation, growth plate organisation and remodelling.

their differentiation into chondrocytes [7]. Then, under the effect of growth factors, including insulin growth factor 1 (IGF-1), fibroblast growth factor 2 (FGF-2) and bone morphogenic proteins (BMPs) 2, 4, 7 and 14, the aggregated MSCs differentiate into chondrocytes and start producing aggrecan and collagens type II, IX and XI. These chondrocytes form a cartilage template for the future bone [2, 4, 6, 8–10].

As skeletal development continues, the chondrocytes at the centre of the cartilage deposit matrix proteins and enlarge to become hypertrophic (Fig. 1.1). *SOX9* is downregulated and Runt-related transcription factor 2 (*RUNX2*) is upregulated, to promote expression of hypertrophic markers, such as collagen type X. Hypertrophic chondrocytes direct adjacent perichondrial cells to become osteoblasts and form

a collar of compact bone around the diaphysis of developing bone, which later becomes the periosteum. The matrix around the hypertrophic chondrocytes calcifies and vascularisation follows, with invasion of osteoblasts, osteoclasts, endothelial and haematopoietic cells from the perichondrium. The marrow cavity and trabecular bone begins to replace the cartilage template [1, 2]. This first region of bone formation is the primary ossification centre (Fig. 1.1). The hypertrophic chondrocytes ultimately undergo apoptosis or transdifferentiate into osteoblasts. Whilst chondrocytes go through these transitions, the cartilaginous scaffold continues to expand through the proliferation of chondrocytes, to enable bone elongation [6].

1.1.2 The growth plate

As the primary ossification centre expands, the differentiating chondrocytes organise in clusters and start to adopt a columnar organisation that directs the lengthening of the bone [11]. Secondary ossification centres are formed at both ends of the bone, called epiphyses, during early postnatal development (Fig. 1.1). Chondrocytes organise into growth plates between the epiphysis and diaphysis. These are responsible for the continued endochondral ossification of long bones after birth [2]. The secondary ossification centre protects the underlying growth plate from mechanical stresses and increases the stiffness of the entire epiphyseal structure, which prevents severe distortion and consequent instability during locomotion [12]. At the end of growth, the plates completely ossify and disappear in humans.

Mammalian growth plates are organised into three zones: the resting, proliferating and hypertrophic zones (Fig. 1.2). In the resting zone at the epiphyseal end of the growth plate, chondrocytes are small and rounded, are irregularly scattered in cartilage matrix and have stem-like properties – they are not terminally differentiated and can produce daughter cells that can remain 'stem' cells or differentiate into proliferating chondrocytes [13–15]. They provide a supply of chondrocyte progenitors and produce the parathyroid hormone-related protein (PTHrP) to send a forwards signal for

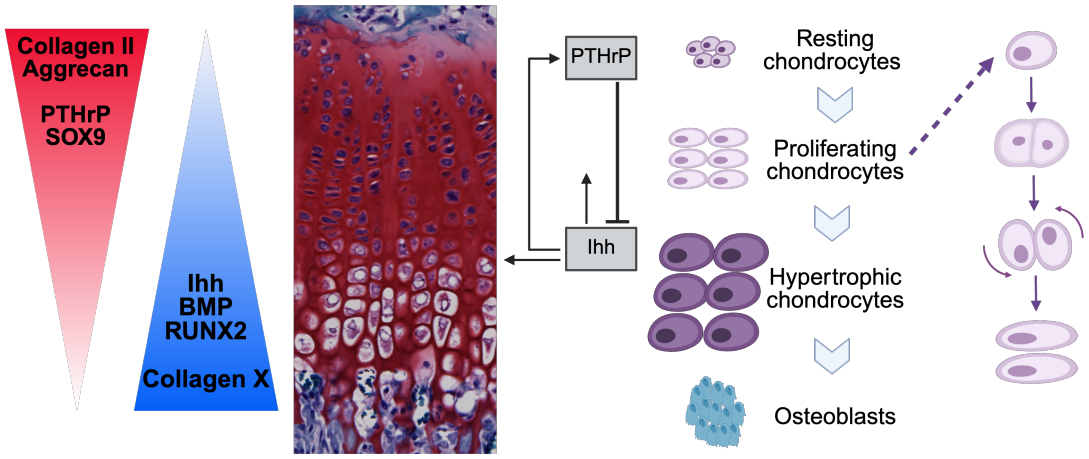


Figure 1.2: Organisation and molecular regulation of the growth plate during endochondral ossification. The growth plate is structured into distinct zones of chondrocyte differentiation: resting, proliferating and hypertrophic. The Indian Hedgehog (Ihh)-PTHrP feedback loop coordinates the transition between proliferative and hypertrophic states. PTHrP is produced by resting zone chondrocytes and prevents the hypertrophic differentiation of proliferating chondrocytes. Pre-hypertrophic chondrocytes produce Ihh, which promotes the proliferation of surrounding chondrocytes and acts back on resting zone chondrocytes to promote PTHrP production. Transitions between zones is driven by gradients in growth factor expression and characterised by gradients in extracellular matrix (ECM) properties. Proliferating chondrocytes organise into columns by a process of cell division followed by cell rotation.

proliferating chondrocytes to maintain their proliferation and delay hypertrophy [6, 14, 16, 17]. This proliferative capacity decreases with age until the growth plate ultimately closes at the end of adolescence in humans [13].

As they enter the proliferating zone, chondrocytes become flattened and organise vertically in columns (Fig. 1.2). The highest proliferation rate occurs at the top of the columns. Collagen type II production is increased in this zone [18]. Columns are formed as cells divide at an axis parallel to growth, which is followed by daughter cells becoming flattened and undergoing a 90° rotation around each other to form stacks of cells (Fig. 1.2) [19, 20]. The arrangement into columns is functionally significant: it restricts lateral cell spreading and maximises the directional bone growth [11, 20]. Chondrocyte post-mitotic rotation and stacking is regulated by proteins like adhesion molecule α-parvin, β1 integrins, and Wnt-planar cell polarity (PCP) signalling [21–23].

Pre-hypertrophic chondrocytes differentiate into hypertrophic chondrocytes. Hypertrophic chondrocytes increase 20-fold in volume, due to increased organelle synthesis and rapid intracellular water uptake [24]. This expansion is the primary engine of bone elongation. Hypertrophic chondrocytes downregulate expression of early cartilage extracellular matrix (ECM) genes such as collagen type II and express collagen type X – a hallmark of hypertrophic chondrocytes. The switch from pre-hypertrophic to hypertrophic is induced by RUNX2, RUNX3 and myocyte enhancer factor 2C (MEF2C) [7, 18, 25].

Late hypertrophic chondrocytes begin to mineralise their surrounding ECM and produce vascular endothelial growth factor A (VEGFA), which triggers angiogenesis and vascularisation of the region [26]. They also express pre-osteoblast markers such as the receptor activator of nuclear factor kappa-B ligand (RANKL) and matrix metalloproteinases 9 and 13 (MMP-9/13). RANKL plays a role in the resorption of calcified cartilage, induces osteoclastogenesis and the formation of the marrow space during endochondral ossification [27]. MMP-9/13 promote vascular invasion and the replacement of cartilage by bone [28]. As the MMPs resorb the ECM, more MMPs and VEGFA are available in the ossification centre. This results in the recruitment of chondroclasts to the vascular front. Chondroclasts are a subtype of osteoclasts that express MMP-9 and are responsible for the resorption of cartilaginous ECM in the hypertrophic zone [26, 29]. In parallel, cells in the perichondrium flanking the hypertrophic zone differentiate into osteoblasts, thus extending the periosteum with the growth of the bone. Osteoblast lineage cells from the periosteum invade the calcified cartilage, and cartilage is replaced by bone and bone marrow [6].

Historically, hypertrophy has been considered the terminal state of chondrocytes, following which they undergo degenerative maturation, characterised by cell cycle exit, nuclear condensation and apoptosis, leaving their calcified ECM as a scaffold on which invading blood vessels and osteoblasts form new bone tissue [18]. Increasing evidence, lineage tracing experiments in particular, suggests that hypertrophic chondrocytes undergo transdifferentiation and become osteoblasts and osteocytes

[30, 31]. Studies also suggest that hypertrophic chondrocytes de-differentiate into a newly identified 'chondrocyte-derived osteoprogenitor'-like cell, before differentiating into osteoblasts [32].

The morphological and biochemical features of chondrocyte apoptosis differ from that of classical apoptotic cells, which has led the term 'chondroptosis' to be coined to refer to the apoptotic mechanisms of most chondrocytes. Briefly, in chondroptosis, the chromatin is not marginalised into large solid masses, but small patches of condensed chromatin are spread throughout the nucleus. There is an expansion in the endoplasmic reticulum and Golgi apparatus before the cell is degraded from within, leaving remnants and vesicular debris and ultimately an empty lacuna [33]. In traditional apoptosis, vesicles containing cell fragments called apoptotic bodies appear which are phagocytosed or undergo necrosis. Chondrocyte death is suggested to be linked to calcification and/or deprivation of nutrients and oxygen [31]. In addition to the precise mechanisms yet to be elucidated, there remains debate and unanswered questions surrounding the morphology and frequency of chondroptosis and transdifferentiation events [34].

The growth plate is complexly regulated by multiple signalling pathways including TGF-βs, Hedgehog (Hh), BMPs, Wnt, growth hormone, IGF-1 and FGFs, hypoxia inducible factor-1-a, thyroid hormone, oestrogen, androgen, glucocorticoids and vitamin D [35, 36]. Of the members of the Hh protein family, Indian Hedgehog (Ihh) plays a key role in bone development and cartilage formation. Crucially, an Ihh-PTHrP loop tightly regulates the rate of chondrocyte hypertrophic transition and thus of bone formation in the growth plate (Fig. 1.2) [17, 28, 37]. Ihh is expressed by pre-hypertrophic and hypertrophic chondrocytes. Ihh acts on nearby cells (resting and proliferative chondrocytes, and the perichondrium) to stimulate the production of PTHrP, mainly in the resting zone. PTHrP, in turn, acts on proliferating chondrocytes to maintain their proliferative state and prevent premature hypertrophic differentiation. As proliferating chondrocytes move away from the source of PTHrP (toward the hypertrophic zone), PTHrP concentration decreases, allowing these

cells to exit the proliferative phase and become pre-hypertrophic and express Ihh, perpetuating the feedback loop. This loop ensures balanced bone growth by tightly controlling the timing of chondrocyte differentiation [17, 28, 37].

SOX9, with SOX5 and SOX6, activates cartilage-specific ECM genes in early chondrocytes, such as collagens type II, IX and XI, and aggrecan. It then remains highly expressed postnatally by resting, proliferating and pre-hypertrophic chondrocytes [38]. SOX9 maintains chondrocyte identity and prevents chondrocyte progression from proliferation to hypertrophic stage by keeping chondrocyte maturation regulators RUNX2 and MEF2C in check. Downregulation of *SOX9* in hypertrophic chondrocytes is required for vascular invasion and degradation of calcified hypertrophic cartilage in the growth plate.

Pre-hypertrophic and hypertrophic chondrocytes express *RUNX2*, an early marker of osteogenesis, which continues to be expressed in osteoblasts. It regulates genes for vascular invasion, such as *VEGFA* and drives *COL10* transcription in hypertrophic chondrocytes [39–42]. It is required for the survival and transdifferentiation of hypertrophic chondrocytes during foetal development and regulates osteoblast differentiation in the early stages of endochondral bone formation. Hypertrophic chondrocytes also express genes typical of bone cells, such as alkaline phosphatase (*ALPL*), osteopontin (*SPP1*), bone sialoprotein, osterix (*SP7*) and osteocalcin (*BGLAP*) [7]. Transdifferentiation and osteoblastogenesis seems to require RUNX2, whilst SOX9 prevents it [32, 43].

The growth plate presents overlapping patterns of different *BMP* expression. *BMP-2*, *BMP-4* and *BMP-6* are expressed in pre-hypertrophic and hypertrophic chondrocytes. *BMP-7* is expressed by proliferating chondrocytes, particularly in regions adjacent to the perichondrium. *BMP-2*, *BMP-3*, *BMP-4* and *BMP-5* are expressed in the perichondrium. BMPs are also essential to maintain *SOX9* expression in early condensations and *BMP* signalling increases expression of Ihh in pre-hypertrophic

chondrocytes, and so can increase the proliferation of chondrocytes and the length of proliferating columns [9, 39].

Mechanical modulation of growth was first elucidated by the Hueter-Volkman law, where increased pressure on the growth plate retards growth and reduced pressure accelerates it [44–46]. It is however qualitative and does not take into account factors such as the type and rate of load, growth plate dimensions and stage of growth that might influence the sensitivity to mechanical loading. Studies since the inception of this law have revealed the complexity with which load regulates growth plate activity. Absence of mechanical loading on the growth plate during active growth results in shortened limbs, reduced proliferation and hypertrophic differentiation, and disorganised columns and cytoskeleton in several studies [47–50].

Primary cilia play a role in both regulating the response of cells within the growth plate to many of the complex biological signals regulating growth, not least Hh signalling, but also to mechanical forces within the growth plate, as will be discussed further later on [47, 51].

1.2 The primary cilium

1.2.1 Structure and function

The primary cilium is non-motile solitary organelle present in most mammalian cell types during growth arrest in developing and mature tissues [52]. As opposed to motile cilia, primary cilia lack dynein arms conveying the ability to generate beating. They coordinate cell signalling pathways during development and in tissue homeostasis and play a role in regulating cell migration, differentiation, re-entry into the cell cycle, specification of the plane of cell division and apoptosis [53, 54].

Primary cilia are made up of an axoneme of nine doublet microtubules that extend from a basal body, which comprises a modified version of the mother centriole of the centrosome. The axoneme is surrounded by a ciliary membrane (Fig. 1.3 A, B). Primary cilia have nine peripheral microtubule doublets (9+0 architecture), as opposed to motile cilia which have nine peripheral microtubule doublets and a central pair (9+2 architecture). Cilia are 200 to 300 nm in diameter and up to 15 µm long depending on the cell type [55, 56]. The basal body dictates the position of the cilium and acts as a template for the formation of the axoneme. It is made up of cylindrical centrioles composed of nine triplet microtubule 'blades' arranged in a barrel shape.

In certain cell types, such as neurons, pancreatic cells, retinal pigment epithelial cells and chondrocytes, the primary cilium is rooted inside a ciliary pocket, an invagination of the plasma membrane [57–61] (Fig. 1.3 C, D). In the absence of a ciliary pocket, the cilium protrudes out of the cell, with the basal body in the same plane as the plasma membrane.

The primary cilium is an evolutionarily conserved organelle that has persisted throughout the eukaryotic lineage, from unicellular protists to complex vertebrates, reflecting its fundamental role in sensing and coordinating environmental and intracellular signals. Motile cilia and flagella first evolved in unicellular eukaryotes for locomotion and fluid movement. These structures shared the canonical 9+2 axoneme, differentiating later as sensory and non-motile cilia (primary cilia) in multicellular organisms. In metazoans, the primary cilium shifted towards non-motile, sensory and signalling functions, integrating diverse extracellular cues [62]. It acts as a mechanochemical transducer, essential in interpreting fluid flow, mechanical loading, and morphogen gradients. The retention of the cilium across such a wide phylogenetic range underscores its adaptive significance and provides insight into the mechanisms by which it mediates signal transduction, spatial organisation, and tissue-level patterning in vertebrate systems [62, 63].

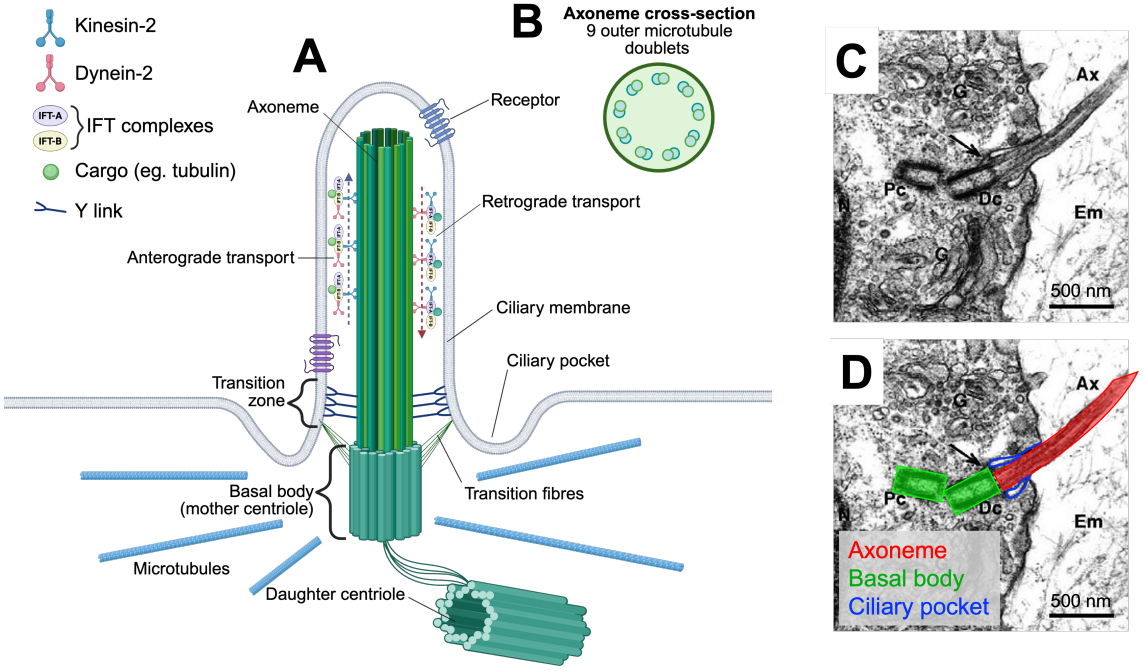


Figure 1.3: Primary cilium structure and intraflagellar transport (IFT) mechanisms. (A) The primary cilium projects from the surface of the cell and consists of a microtubule-based axoneme enclosed by a ciliary membrane. The axoneme is anchored to the cell via the basal body, derived from the mother centriole, and is surrounded at its base by the transition zone. IFT particles (IFT-A and IFT-B complexes) mediate bidirectional trafficking along the axoneme: IFT-B (in complex with kinesin-II) facilitates anterograde transport towards the ciliary tip, while IFT-A (in complex with dynein-2) supports retrograde transport back to the base. Associated cargo includes signalling proteins, axoneme and membrane components. Transition fibres anchor the basal body to the ciliary membrane. The transition zone acts as a selective barrier regulating entry and exit of proteins. **(B)** Cross-section of the axoneme highlights its characteristic 9+0 microtubule arrangement. **(C)** Transmission electron microscopy image of a chick embryo chondrocyte, **(D)** with the different ciliary compartments highlighted. Em = extracellular matrix, Ax = axoneme, Dc = distal centriole, Pc = proximal centriole, G = Golgi apparatus. Modified from [57].

One function of the primary cilium is to sequester the centriole, in order to inhibit cell division at the appropriate time in the cell cycle. As such, most cells that have a primary cilium are non-cycling differentiated cells or stem cells in G_0. The primary cilium is resorbed in cells that re-enter the cell cycle and divide, then grow again on daughter cells as they become quiescent again.

Receptors, ion channels and transporter proteins are located on the cilium membrane and its basal body, which allows primary cilia to facilitate cells' response to chemical

and mechanical cues they receive from their surrounding environment. These include mechanical forces such as fluid flow, tension and compression, signalling molecules such as Hh, TGF-β and Wnt ligands, chemical compounds such as olfactory molecules and physical cues such as light on the retina [64, 65]. Some proteins are found widely on primary cilia across different cell types and others are cell type dependent to allow for specialised signalling [63]. Existing evidence indicates that the composition of these ciliary proteins can dynamically shift over time in response to specific developmental and homeostatic signals, enabling cellular adaptation to specific cues [66]. Primary cilia are also essential for Hh and Wnt signalling and developmental processes such as left-right axis specification, limb and neural patterning [67].

1.2.2 Assembly

There are two pathways for cilia assembly - intracellular and extracellular (Fig. 1.4). The intracellular pathway assembles a cilium within a ciliary pocket. When the cell enters G_0, the mother centriole attaches to a Golgi-derived vesicle (Fig. 1.4 A). The axoneme of the primary cilium then grows above the centriole, projecting into the vesicle lumen [69]. The microtubules polymerise at the growing tip of the projection, and nearby vesicles fuse with the membrane surrounding the growing axoneme [70]. The vesicle eventually reaches the cell membrane and the ciliary membrane fuses with the plasma membrane, to expose the primary cilium at the cell surface, where ciliary growth continues for up to several micrometres to form the mature cilium [59]. This pathway is predominantly employed by non-polarised or less specialised cells such as fibroblasts, mesenchymal cells, and certain sensory cells. The presence of a ciliary pocket in chondrocytes suggest they assemble cilia via the intracellular pathway.

In the extracellular pathway, the mother centriole migrates towards the cell surface and docks to the plasma membrane (Fig. 1.4 B). The docking is thought to be mediated in part by distal appendages of the centriole also known as transition fibres. Once docked, the axoneme extends directly into the extracellular space [59],

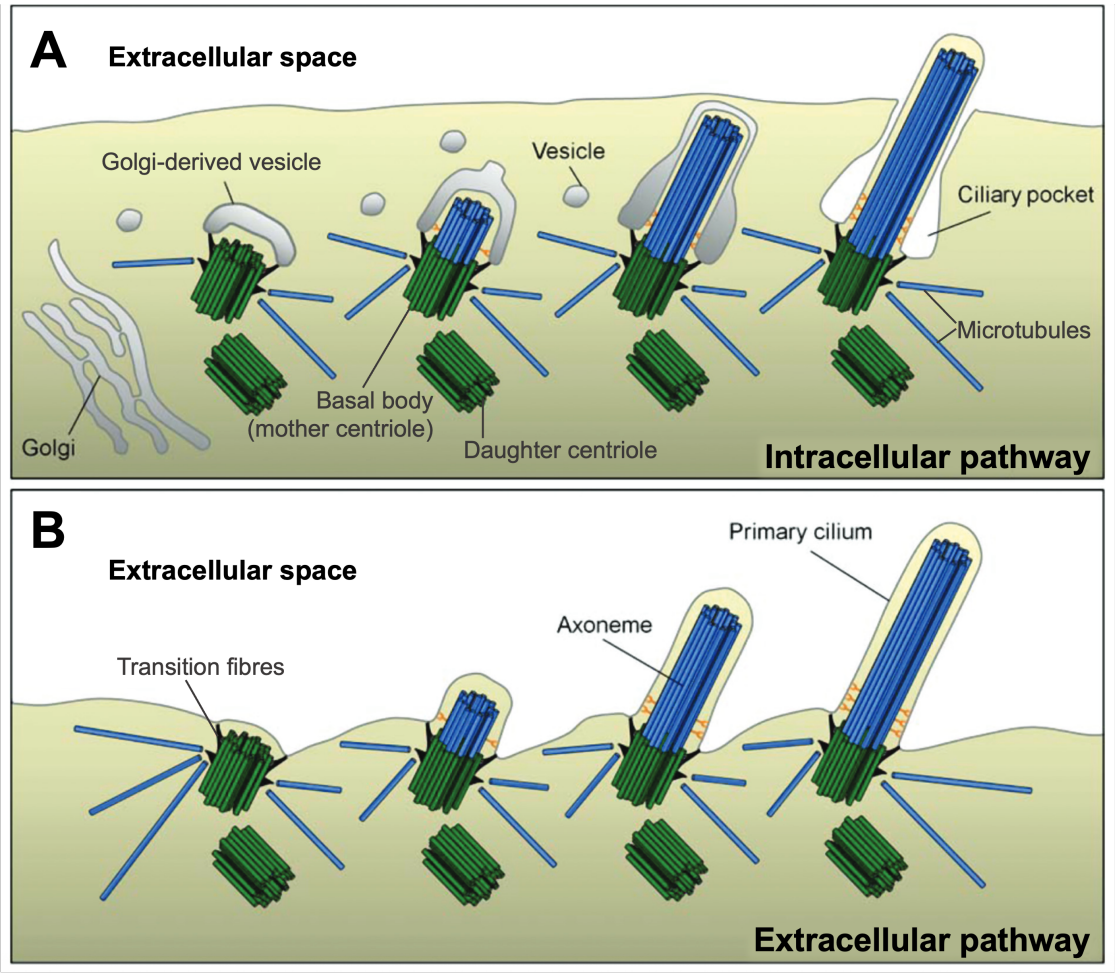


Figure 1.4: Two main pathways of primary cilium assembly. (A) Intracellular pathway: Initiation begins with the docking of a Golgi-derived vesicle to the basal body (mother centriole), forming a ciliary vesicle that encapsulates the growing axoneme within the cell. The axoneme elongates within this vesicle, with nearby vesicles joining. The sheath subsequently fuses with the cell membrane to expose the ciliary membrane to the extracellular space. **(B)** Extracellular pathway: The basal body migrates directly to and docks at the plasma membrane. Axoneme extension occurs extracellularly, directly from the membrane surface. Modified from [68].

[69]. This pathway is used by polarised epithelial and specialised multiciliated cells, allowing direct cilium emergence on the cell surface.

The microtubules grow at the 'plus' end of the axoneme which is oriented towards the distal tip, whereas their 'minus end' are continuous with the microtubules of the basal body at the proximal end [71]. The attachment point of the membrane corresponds to the ciliary necklace – the transition region where the ciliary membrane joins the general cell membrane [72]. At the base of the cilium is a ciliary pore

complex, made up of transition fibres, which attach the basal body to the plasma membrane, and the ciliary necklace (Fig. 1.3). The ciliary pore complex ensures only select proteins and particles pass into the ciliary compartment and be passed on to intraflagellar transport (IFT) proteins for transport up the cilium [71]. During mitosis, the cilium resorbs and the mother centriole moves back to the mitotic spindle pole. During cilia assembly and resorption, microtubules are dynamically built in cycles of polymerisation and de-polymerisation of αβ-tubulin heterodimers [73].

1.2.3 IFT88

Intraflagellar transport (IFT) is a conserved mechanism that is essential to ciliogenesis and cilia function [74]. Ciliary proteins are synthesised in the cytoplasm and transported into the cilium along axonemal microtubules by IFT proteins. Transport from the base of the cilium to the tip is called anterograde transport and transport from the tip to the base is called retrograde transport. Heterotrimeric kinesin-2 motor proteins drive anterograde transport and cytoplasmic dynein-2 drives retrograde transport [75–77] (Fig. 1.3 A).

IFT proteins play distinct roles in mediating ciliary function. They are organised into complexes A and B (IFT-A & IFT-B). The complexes mediate the contact between cargo proteins and motors [77]. IFT proteins are named according to their size in kDa. IFT-A regulates retrograde transport, whereas IFT-B regulates anterograde transport.

IFT88 is a key component of the IFT-B complex, bridging the IFT-B1 and IFT-B2 subcomplexes at the cilium's tip [78, 79]. It is essential for sustaining the bidirectional transport of tubulin heterodimers along the axoneme, a process vital for the assembly and proper function of primary cilia.

Mutations in IFT88 disrupt the formation of ciliary structures in embryonic nodes, kidneys and limbs, preventing ciliation or reducing cilia length [80–82]. Loss of the gene also disrupts the establishment of planar cell polarity [83]. This leads to a

wide array of cellular and physiological consequences including left-right asymmetry defects, disordered Hh signalling and polycystic kidney disease. Beyond its conserved ciliary functions, IFT88 also has reported non-ciliary roles, such as regulating the cell cycle and migration in some contexts [84, 85].

In endochondral ossification, IFT88 is indispensable for coordinating chondrocyte maturation, endochondral bone formation, integration of mechanical cues, vascular invasion, and overall bone growth and healing, via its essential role in primary cilium assembly and signalling in cartilage and bone cells. IFT88 supports the activity of key signalling pathways, such as Ihh, to ensure proper limb bone development [86].

1.2.4 The role of the primary cilium in skeletal development

The primary cilium in chondrocytes

The position, projection and orientation of the primary cilium in chondrocytes is suggested to be dependent on the structural organisation and mechanical properties of the surrounding ECM. Macromolecules inside the ECM, such as collagen fibres and proteoglycans, make direct contact with primary cilia which express ECM receptors integrins and transmembrane protein chondroitin sulfate proteoglycan 4 [57, 87].

ECM deposition in chondrocytes is also closely associated with primary cilia, which appear to play a regulatory role in the synthesis and organisation of key ECM components. Studies have shown that disruption of ciliary function can alter the expression of matrix proteins such as collagen type II and aggrecan in both articular and growth plate cartilage, leading to defects in ECM composition and structure. This suggests that primary cilia contribute to spatial and temporal control of ECM deposition during cartilage development and maintenance [81, 88, 89].

Mechanotransduction

The microtubules of the primary cilium contain acetylated and detyrosinated α-tubulins, which makes them very stable and provides the flexural rigidity necessary to respond mechanical cues by bending [90]. One of the main signalling cascades suggested to be activated by cilium bending is calcium (Ca^{2+}) signalling. The mechanism of this process is surrounded by debate. Praetorius & Spring (2001) showed that primary cilia-localised Ca^{2+} concentration in kidney cells increased with exposure to fluid flow, mediated through the opening of mechanically sensitive Ca^{2+} channels located on the cilium or at its base [91]. No flow-induced Ca^{2+} influx appears in kidney cells lacking polycystin-1 (PC1) or blocked polycystin-2 (PC2), two membrane proteins mutated in polycystic kidney disease and located to the primary cilium, suggesting a role for them in mediating this mechanosensing of the primary cilium [92]. Delling et al. (2016), however, suggest the Ca^{2+} concentration increase observed in primary cilia after bending from fluid flow originates in the cytoplasm and propagates into the cilium in mice [90, 93]. The same group also showed that the primary cilium is a separate Ca^{2+} compartment to the cytoplasm, regulated by a specific Ca^{2+} channel [94]. These different theories may have arisen due to differences in techniques used. Praetorius & Spring (2001,2003) use the calcium-sensitive fluorescent probe Fluo-4-AM and measured fluorescence intensity as a proxy for Ca^{2+} concentration, whereas Delling et al. (2013, 2016) used a mouse line with a calcium indicator confined to the cilium, thus imaging specifically at the cilium rather than overall fluorescent intensity as an indicator of ciliary Ca^{2+} concentration [91, 93–95].

Cilia's putative sensing of Ca^{2+} upon mechanical activation has also been shown to drive the breaking of left-right body symmetry, with asymmetric fluid sensing by PC2 at the ventral node of mouse embryos [96, 97]. Both Djenoune et al. (2023) and Katoh et al.(2023) observe an increase in the frequency of intracellular and intraciliary Ca^{2+} oscillations after bending caused by mechanical stimulation with optical tweezers of immotile nodal cilia in zebrafish and mouse embryos, respectively, which disappears in embryos lacking the PC2 channel [96, 98]. Katoh et al. (2023) describe the

asymmetric localisation of the channel on the cilium which may explain the response to force as the cilium bends. These studies suggest PC2-dependent intraciliary Ca^{2+} transient signals are mechanically generated due to the flow during left-right organisation and ciliary mechanosensation is determinative for left-right development.

As such, there remains uncertainty as to how exactly primary cilia are mediating mechanical forces into cell responses, in different contexts during development and tissue homeostasis. Resnick & Hopfer (2008) hypothesise that "fluid flow bends the cilium, converting kinetic energy of the fluid into elastic energy, which drives strain-sensitive proteins to initiate or participate in flow-dependant signalling and regulator processes" in their mathematical model of the mechanical environment of the cilium [99].

The studies that have focused on the chondrocyte mechanosensory function of primary cilia have suggested that compressive mechanical loading of chondrocytes triggers release of adenosine triphosphate (ATP) into the pericellular micro-environment through mechanosensitive hemichannels expressed on the primary cilium [100]. Once released from the cell, ATP activates purine receptors and triggers intracellular Ca^{2+} signalling cascades, which ultimately modulates cell function in response to mechanical load through activation of transcription regulators in a process that requires primary cilia [101, 102].

The role of the primary cilium in endochondral ossification and the growth plate

Primary cilia play a key role in regulating endochondral ossification but also other bone forming mechanisms including intramembranous ossification, fracture repair and osteoblast differentiation [103]. There is *in vitro* and *in vivo* evidence that primary cilia regulate osteogenic, chondrogenic differentiation as well as bone responses to mechanical loading, and thus, and are critical in skeletal development and maintaining bone homeostasis [86]. The primary cilium is essential for proper function of the

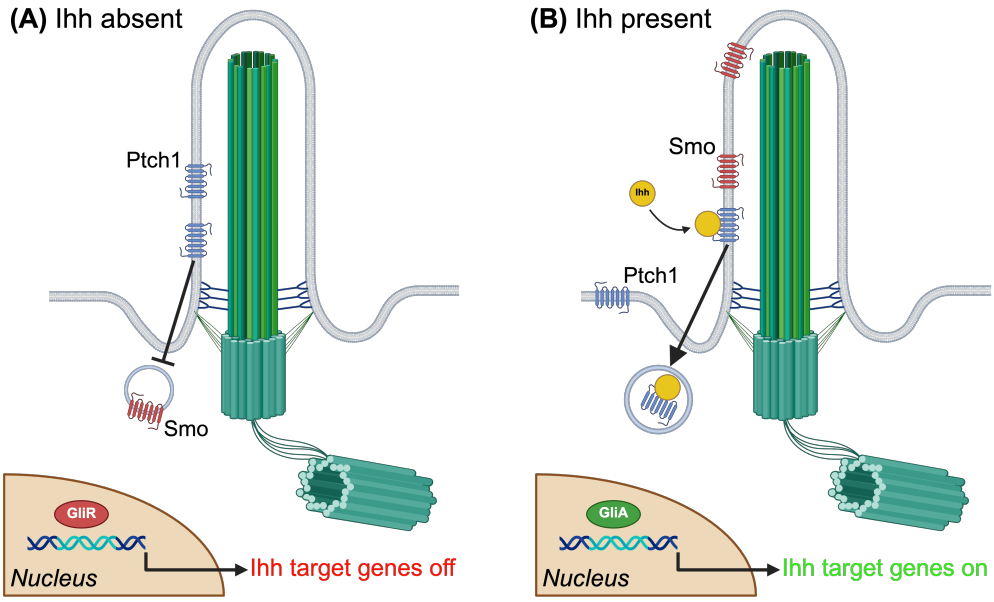


Figure 1.5: Ihh signalling regulation via the primary cilium. (A) In the absence of Ihh, the Ptch1 receptor localises to the primary cilium and inhibits Smo entry into the cilium. As a result, the Gli transcription factors are processed into their repressor form (GliR), which inhibits transcription of Ihh target genes. **(B)** Upon binding of Ihh to Ptch, the receptor is internalised and removed from the cilium, allowing Smo to enter and accumulate in the primary cilium. This triggers the activation of Gli proteins into their activator form (GliA), which promotes transcription of Ihh target genes.

Ihh–PTHrP feedback loop in the growth plate by acting as a critical signalling hub for the Ihh pathway.

Key components of the Ihh signalling pathway are localised to the primary cilium (Fig. 1.5). Ihh binds to the membrane receptor Patched (Ptch1) localised to the cilium, through which it controls the activity of the Gli transcription factors, of which there are three: Gli1, Gli2 and Gli3. Gli2 and Gli3 can act both as activators and repressors, depending on their processing. Gli1 is a transcriptional target of the Ihh pathway [104]. In the absence of Ihh, Ptch1 keeps the pathway off by preventing the accumulation of the transmembrane protein Smoothened (Smo) in the cilium (Fig. 1.5 A) [105, 106]. When Smo is inactive, Gli transcription factors are proteolytically processed to make a transcriptional repressor that binds to Ihh target genes and blocks their transcription. When Ihh binds to Ptch1, it inactivates the receptor which then moves out of the cilium (Fig. 1.5 B). This relieves the repression of

Smo and leads to its accumulation in primary cilia. This promotes conversion of full-length Gli into a transcriptional activator [105, 106].

The concentration of these critical Ihh signalling components at the tip of the cilium allows efficient response to low levels of ligands [107]. Certain IFT proteins and motors are required for Ihh signalling, after activation of Smo and prior to the transcription of Ihh targets by Gli [107, 108]. Mutations in cilia or IFT proteins and motors disrupt Ihh signalling, which results in erroneous processing of Gli transcription factors.

In MSCs cultured *in vitro*, primary cilia are required for adipogenic, osteogenic and chondrogenic differentiation of MSCs and for maintaining the phenotype of differentiated cells [54]. They also promote osteoblastic differentiation and bone formation by sensing fluid flow [109]. In chondoprogenitor cells, primary cilia deletion reduces their chondrogenic potential and regulates the mechanical stimulation of chondrogenesis as their removal reduces the increase in chondrogenic gene expression under load [110, 111]. These responses are transmitted through signalling pathways localised to the primary cilium such as Ihh and Wnt-β-catenin.

In vivo, primary cilia act as mechanosensors for load-induced bone formation, as the absence of cilia dampens the formation of new bone in response to mechanical stimuli [112, 113]. When primary cilia are mutated in chondrocytes and osteochondroprogenitors, the organisation, proliferation and differentiation of chondrocytes in the growth plate is disrupted suggesting a role of primary cilia in regulating skeletal growth in the growth plate. This can result in limb shortening, shortened and disorganised growth plates, craniofacial abnormalities, hypomineralisation and dwarfism, suggesting altered signalling pathways, often Hh and Wnt, that impact skeletal differentiation (Fig. 1.6) [47, 81, 88, 89, 111, 114–118].

The interaction between cells and the ECM is essential for proper chondrocyte proliferation within the growth plate. Disruption of this interaction, either through genetic deletion of ciliary components or altered ECM composition, has been shown to

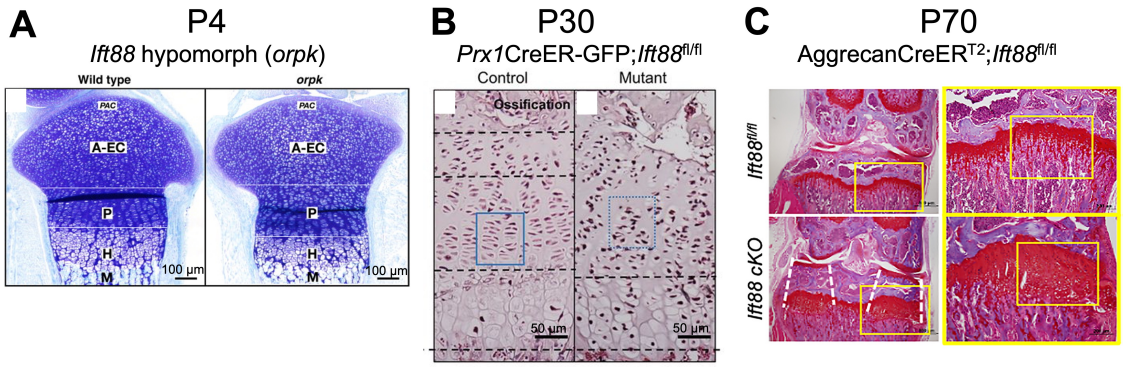


Figure 1.6: Disruption in cell and tissue architecture by *Ift88* genetic mutations affects growth plate organisation at different ages. (A) Toluidine blue staining of the tibial growth plates of P4 wild-type and *orpk* mice. orpk growth plates were shorter with disrupted cell morphology, density and organisation. PAC = presumptive articular cartilage, A-EC = articular-epiphyseal cartilage, P = proliferating, H = hypertrophic [81]. **(B)** Hematoxylin & eosin (H&E) staining of the tibial growth plates of P30 (4.5 weeks) control *Ift88*$^{fl/fl}$ and *Prx1*CreER-GFP;*Ift88*$^{fl/fl}$ mice. *Ift88* deletion was induced with tamoxifen at P17. Mutant growth plates had disrupted columnar and flattened cell organisation, with cell cluster (Dashed blue box) [114]. **(C)** Safranin O staining of the tibial growth plates of P70 (10 weeks) *Ift88*$^{fl/fl}$ and AggrecanCreER^{T2};*Ift88*$^{fl/fl}$ mice. Ift88 deletion was induced at P56. *Ift88* cKO growth plates were expanded in the periphery, with swollen and disorganised hypertrophic chondrocytes Yellow boxed regions are shown at higher magnification on the right [47].

impair proliferative signalling pathways, leading to reduced chondrocyte proliferation and subsequent growth plate disorganisation [119, 120].

As such, primary cilia play a key role during skeletal development, by maintaing the organisation and function of the growth plate.

Ciliopathies

Genetic mutations which lead to dysfunction of cilia (motile and non-motile) and result in disrupted organogenesis during embryonic and postnatal development cause a wide range of human diseases and developmental disorders, known as ciliopathies. These can be described as first-order, where a ciliary gene presents a mutation, and second-order ciliopathy, where genes encoding for non-ciliary proteins required to maintain cilia function are mutated. There are a number of known mutations in humans, which cause more than 30 diseases identified as ciliopathies [121] .

Many ciliopathies present skeletal manifestations, including polydactyly, constricted ribcages, scoliosis and stunted growth often associated with apparently disrupted endochondral ossification and growth plate disorganisation [122–125]. The growth plate disorganisation phenotypes include loss of cellular shape, disrupted zone ratios, shortened growth plate, loss of column arrangement. Some ciliopathies are also associated with alterations in cilia length [126–128].

IFT88 has also been implicated in several ciliopathies [82, 129]. IFT88 null mutations are embryonically lethal [130]. A hypomorphic IFT88 mouse line, called oak ridge polycystic kidney (*orpk*), lead to cilia that are stunted and malformed, and causes polycystic kidney disease, severe growth retardation, limb polydactyly, retinal degeneration, and cerebellar hypoplasia [131, 132]. It is often used as a model to study ciliopathy disease development.

The Cre-lox system has allowed conditional deletion of *Ift88* in targeted cells and tissues in mice [47, 80, 89, 114]. Deletion of IFT88 or related genes in the growth plate leads to premature growth plate closure [35, 88]. The *orpk* mouse also displays shortened and disorganised growth plates, with proliferating chondrocytes that were less flattened and columnar (Fig. 1.6 A) [81]. Deletion of *Ift88* in the mesenchyme in embryos and in the first four weeks postnatally led to disorganised and/or shortened growth plates leading to stunted limb growth (Fig. 1.6 B) [86, 114]. In contrast, deletion of *Ift88* in the adolescent growth plate (after four weeks) disrupts chondrocyte differentiation and ossification, leading to expanded growth plates, failed bone formation and disorganised hypertrophic chondrocytes (Fig. 1.6 C) [47]. These phenotypes don't model a specific ciliopathy but provide information on the function of primary cilia in skeletal development.

As such, disorganised growth plates have been observed in patients and mouse models [116–118, 133, 134]. In these phenotypes the cellular organisation is lost, but there is very little characterisation of the organisation of primary cilia, which

may be affected and would be important in determining their role in determining cell polarity and function.

The role of the primary cilium's organisation in cell organisation

In several tissues, primary cilia have been shown to adopt a distinct orientation. In polarised epithelial tissues of tubular organs, such as the nephron of the kidney, the pancreatic ducts and the hepatobiliary tree of the liver, primary cilia point towards the lumen [92]. High levels of shear stress in the vasculature causes cilia of endothelial cells to be shorter and fewer [135, 136]. These are thought to detect blood flow and convert these mechanical signals into chemical cues within the cells, regulating their response to shear stress. In vascular smooth muscle cells, primary cilia preferentially orient their axonemes at around 60° to the cross-sectional plane of the artery, projecting into the ECM [137]. In the brain, primary cilia exhibit region-specific orientation patterns, with consistent alignment observed among structures that are anatomically or functionally connected [138]. In tendons, primary cilia align parallel to the collagen fibres and the long axis of the tendon [139, 140]. This aligns with the primary tensile loading direction of the tendon. In weight-bearing articular cartilage, superficial zone primary cilia point away from the articular surface. In the deep zone, primary cilia point both towards and away the articular surface. In non-weight bearing cartilage, this axonemal orientation is lost [141]. Cilia associated with specialised sensory functions such as in the olfactory epithelium, retina, and inner ear, rely not just on their molecular composition, but also on their precise orientation for optimal function [142–144].

There is a strong relationship between cellular architecture (primary cilia, cytoskeleton) and tissue-level organisation, including cell polarity. Cilium formation is linked to the direction of cellular division, with mitotic spindle misorientation observed with loss of IFT20 in kidneys [145]. The planar cell polarity (PCP) pathway governs apical actin assembly, which is necessary for orienting ciliary microtubules, and is also key for cilia formation and function [53, 146]. The Wnt-PCP pathway is also

crucial for chondrocyte orientation in the growth plate, therefore there might be a close interplay governing cilia and cell organisation.

The primary cilium is thought to play a role in guiding post-mitotic cell movements necessary for re-establishing the columnar organisation of growth plate chondrocytes following cell division [147]. The cilium coordinates Wnt, Ihh and β1 integrin signalling, all of which are crucial for establishing planar cell polarity, cell migration, and orientation in chondrocytes [21, 22]. This clear link has been observed through phenotypic studies, however a detailed characterisation of primary cilium organisation in the growth plate is missing. Cilia orientation studies have often been performed in 2D, which omits crucial dimensional information, and on limited cell numbers. A comprehensive characterisation of cilia organisation in the growth plate could establish clear links with cellular organisation and shed light into their functional relationship.

1.3 *In vitro* bioengineered models

To better understand the mechanisms regulating growth plate activity, a range of investigative approaches is required. Ideally, these processes would be studied in human growth plate samples across various developmental stages. However, such samples are challenging to acquire. Mouse models are useful in studying growth plate biology, particularly the effects of genetic disruptions. In parallel, bioengineered models offer an opportunity to model tissue regions and sometimes overall architecture and perform targeted experiments to uncover molecular mechanisms. These also have potential for implantation, particularly as the cartilage has limited regenerative and healing capacity.

Bioengineering models are *in vitro* models that combine cellular, mechanical, material and electrical engineering components to recapitulate biological processes. They offer the ability to tune both cell intrinsic and extrinsic biochemical and biophysical components including cell type, material and matrix composition, mechanical load,

size and design, culture regimen, making it possible to create models that range from simple to complex [148]. With the complexity of *in vivo* pathways and mechanisms, simple 3D *in vitro* models present the opportunity to unpick elements individually and understand their contribution to a wider biological phenomenon. Compared to 2D cell culture, these models offer the ability to culture cells in a micro-environment closer to that of the native tissue. This is particularly important for cells like chondrocytes, which dedifferentiate when cultured in 2D and whose surrounding 3D ECM is key to their cellular function [149, 150].

The same methodologies and analyses performed on *in vivo* models and cell cultures can be performed on bioengineered models, includes cell and nuclei sequencing, quantitative polymerase chain reaction (qPCR), histological staining, Western blotting, microscopy imaging. Combined, these analytical approaches offer a comprehensive view of the biological and structural characteristics of bioengineered models, supporting their validation and use in studying physiological or pathological processes. The *in vitro* nature of these models make all of these techniques very accessible. The focus here will be on osteochondral and growth plate models that exist and their potential for the study of skeletal development.

1.3.1 Cell sources & materials

Cell sources

Bioengineered osteochondral models rely on the careful selection and manipulation of multiple factors to replicate the complex structure and function of native tissue. Among these, the choice of cell source is fundamental. Typically differentiated cells, progenitor cells and/or multipotent stem cells are used. Each cell type brings distinct advantages and limitations depending on the model's purpose and the tissue zone being mimicked.

Growth plate chondrocytes differ in their function and tissue architecture to articular cartilage chondrocytes. Ideally, stem cells giving rise to the resting chondrocytes of the growth plate should be used, however these remain elusive and difficult to harvest [14, 15, 151]. Recent advances have enabled the derivation of both articular and growth plate chondrocyte-like populations from embryonic stem cells. Through stage-specific modulation of key signalling pathways, these cells can be guided toward distinct chondrogenic lineages and have demonstrated the ability to maintain their specialised phenotype when implanted subcutaneously *in vivo* [152–154].

Given that both chondrocytes and osteoblasts originate from the bone marrow, bone marrow-derived MSCs (BM MSCs) have garnered considerable interest for tissue engineering applications. BM MSCs can be directed toward either chondrogenic or osteogenic fates, making them especially suitable for biphasic or zonal osteochondral constructs. While BM MSCs are widely studied, alternative sources such as adipose-derived MSCs (AD MSCs), synovial fluid-derived MSCs, and periosteal-derived progenitors have also been explored [155]. Synovial MSCs in particular show enhanced chondrogenic differentiation potential, whereas AD MSCs are more accessible but may require stronger induction protocols [156]. Each MSC source presents trade-offs in terms of availability, expansion capacity and differentiation bias.

Moreover, co-culturing MSCs with primary chondrocytes has been shown to enhance chondrogenic differentiation [157]. In more advanced models, tri-cultures involving endothelial cells have been explored to simulate vascular invasion during endochondral ossification [158]. These multi-lineage systems better capture the cellular crosstalk observed during skeletal development. Using induced pluripotent stem cells (iPSCs) offer the benefit of patient-specific modelling and can be directed toward osteochondral lineages through defined differentiation protocols [153].

When differentiated cells are used directly, chondrocytes and osteoblasts are commonly combined to recapitulate the zonal composition of osteochondral tissue. However,

their *in vitro* expansion is limited by dedifferentiation, particularly in chondrocytes, which rapidly shift toward a fibroblastic phenotype characterised by reduced expression of collagen type II and aggrecan [149, 150]. Maintaining the native phenotype typically requires three-dimensional culture systems or supplementation with pro-chondrogenic factors like TGF-β3.

Scaffold materials

Scaffold fabrication for osteochondral tissue engineering typically employs either natural or synthetic polymers, each offering distinct advantages. A rational approach to selecting natural polymers is to mimic the ECM composition of native cartilage and bone, thereby providing biologically relevant cues to support cell adhesion, proliferation and lineage-specific differentiation.

For the bone compartment, collagen type I, an abundant component of native bone ECM, in combination with hydroxyapatite is frequently used [159]. Other natural polymers such as gelatin (a denatured form of collagen), chitosan (derived from chitin in crustacean shells), alginate (extracted from brown seaweed), and silk fibroin (from silkworm cocoons) have also been explored due to their biocompatibility, biodegradability and ability to support osteogenic differentiation. These polymers can be used alone or blended with bioactive ceramics like hydroxyapatite or tricalcium phosphate to enhance mechanical strength and bioactivity in bone tissue engineering applications [160].

In the cartilage region, scaffolds aim to replicate the unique proteoglycan-rich microenvironment of hyaline cartilage. Materials such as collagen type II, glycosaminoglycans (GAGs), gelatin, alginate and hyaluronic acid are commonly employed due to their ability to maintain chondrocyte phenotype and promote cartilaginous matrix deposition [160, 161].

Alongside natural materials, synthetic polymers are widely used because of their reproducibility, tunable mechanical properties and ease of processing. For both the

bone and cartilage phases, the most frequently used synthetic polymers are polylactic acid, polyglyocolic acid and polycaprolactone. To enhance functionality, these polymers are often functionalised with ECM-derived or integrin-binding peptides to improve cell integration and response, or loaded with growth factors such as TGF-β and BMP-2. Composite scaffolds combining natural and synthetic elements are increasingly being developed to leverage the stability of synthetic polymers with the biological activity of natural ECM components [28, 159].

Recent advances in osteochondral scaffold techniques have focused on developing biomimetic structures capable of supporting both cartilage and subchondral bone regeneration, aiming to restore the complex, zonal architecture of osteochondral tissue. A number of osteochondral scaffold systems have been developed to recreate the functional and structural complexity of the cartilage–bone interface. Biphasic and triphasic constructs remain the most widely studied, each designed to recapitulate the distinct yet continuous architecture of cartilage, calcified cartilage, and subchondral bone. Biphasic scaffolds use two distinct phases for cartilage and bone, such as softer agarose or fibrin-based hydrogels for chondral zones paired with stiffer poly(lactic-co-glycolic acid), polycaprolactone, or bioactive glass layers for bone support [162]. Trilayered models further refine this by including an intermediate calcified cartilage layer, promoting seamless integration and improved interface stability *in vivo* [163]. Gradient scaffolds, fabricated to provide smooth transitions in mechanical properties and biochemical cues, further improve osteochondral integration. These often employ techniques like 3D bioprinting to build continuous supports from synthetic polymers to ECM-derived hydrogels, incorporating signalling molecules to guide cell differentiation across zones as will be discussed further in later sections.

Modular approaches enable precise control over scaffold architecture, combining bioprintable matrices with nano-hydroxyapatite, decellularised ECM, or liposomes to boost osteogenic and chondrogenic function. Bioactive enhancements via embedded growth factors and responsive materials facilitate integration and cell recruitment, improving healing outcomes [160, 163].

Collectively, these advances illustrate the move toward gradient and multiphasic scaffold architectures capable of recapitulating the native biochemical and biomechanical environment of the osteochondral junction. Such systems not only hold translational potential for cartilage repair but also provide a versatile experimental framework for studying the coupled chondrogenic–osteogenic processes that underpin endochondral ossification, as explored in the present study.

1.3.2 Growth plate *in vitro* models

The growth plate is an osteochondral interface. This interface features a gradual transition from soft, avascular cartilage to rigid, highly vascularised subchondral bone. This gradient includes variations in cell types, ECM composition, mechanical properties and mineral content that allow for effective load transmission and functional integrity of both cartilage and bone. The interface forms through tightly regulated biological processes involving spatiotemporal gradients of morphogens, cellular differentiation, matrix remodelling and mineralisation (Fig. 1.2). Growth factors and signalling pathways (BMPs, Wnt, Hh) guide the differentiation of progenitor cells into chondrocytes and osteoblasts, establishing the zonal architecture. Modelling, repairing or regenerating the osteochondral interface is difficult because of its complex gradient composition and the distinct biological requirements of cartilage and bone. Traditional single-tissue scaffolds fail to replicate this gradient, resulting in poor modelling and therefore reduced applicability in research. An effective engineered growth plate should ideally: (i) contain resting, proliferating and hypertrophic chondrocytes that interact to maintain tissue homeostasis; (ii) preserve key signalling pathways, such as Ihh/PTHrP, BMPs, Wnt, and remain responsive to both molecular and mechanical environmental cues, and (iii) support chondrocyte proliferation and matrix synthesis, thereby contributing to regulated bone elongation through endochondral ossification.

In vitro gradient generation

To replicate the native osteochondral interface, scaffolds are often designed with distinct layers or gradients in composition and mechanical properties. These zonal strategies aim to support tissue-specific cell behaviours and promote seamless integration between cartilage and bone compartments.

Multiphasic scaffolds can be fabricated by juxtaposing different scaffold materials to create distinct regions with different ECMs, as well as different mechanical properties [164]. As the growth plate is positioned between two layers of bone, multiphasic scaffolds provide a potential avenue for growth plate *in vitro* models. Continuous gradient scaffolds are, however, preferred to monophasic and biphasic designs as they provide seamless transitions and reducing mechanical instability between juxtaposed materials.

Gradients embedded within scaffolds can be of different forms:

- Material gradients: varying composition and stiffness along the scaffold length [165–169].
- Structural gradients: zonal pore sizes, architectures and fibre alignments to mimic native tissue microstructure [170–173].
- Biochemical gradients: controlled delivery or immobilisation of growth factor and signalling molecules along a gradient to induce spatially defined cell differentiation [169, 174–178].

Advanced methods in the bioengineering field enable precise control over scaffold gradients in mechanical stiffness, biochemical composition and structural architecture (Fig. 1.7). These techniques allow for the creation of both discrete (multiphasic) and continuous gradient scaffolds:

- Sequential layering allows for precise layer-by-layer deposition of different materials (Fig. 1.7 A) [166, 179]
- 3D bioprinting incorporates living cells and biomaterials directly into the printing process. By adjusting the bioink composition in real-time during printing, gradients in biochemical signals, cell density or ECM components can be introduced (Fig. 1.7 A) [170, 173].
- Microfluidic systems offer fine spatial and temporal control over fluid mixing and flow, enabling the generation of continuous biochemical gradients in scaffolds (Fig. 1.7 A) [177]
- Electrospinning produces fibrous scaffolds that mimic the native ECM. By varying solution parameters or switching source materials during fabrication, spatial gradients in fibre alignment, density or composition can be created (Fig. 1.7 A) [165].
- Component redistribution - starting with a homogeneous system and using an applied force, such as centrifugation, buoyancy, magnetic or electric fields, to redistribute components into a gradient (Fig. 1.7 B) [171, 174, 176, 178]
- Controlled phase changes - spatially controlled exposure to heat or light for crosslinking, enabling certain scaffold regions to become stiffer or more cross-linked than others (Fig. 1.7 C) [167, 168].
- Postmodification - gradients can be imposed onto preformed scaffolds via techniques like diffusion of signalling molecules or photo-patterning. This enables the overlay of biochemical gradients without altering the scaffold's bulk properties (Fig. 1.7 D) [169, 175].

Of interest in this project are biochemical gradients of growth factors that promote patterned differentiation of cells. TGF-βs and BMPs are relevant growth factors to pattern in gradients, as they are expressed in gradients across the growth plate, and are strong promoters of chondrogenesis and osteogenesis, respectively. In addition,

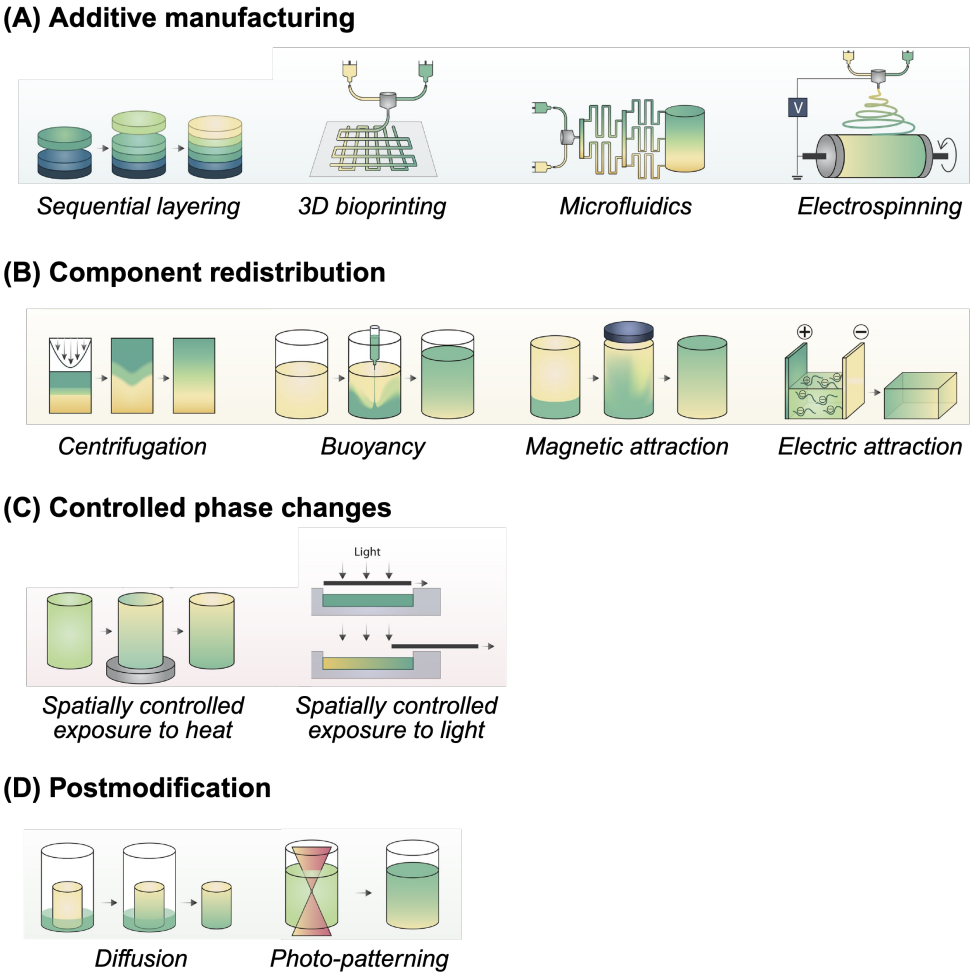


Figure 1.7: Schematic illustration of various fabrication techniques for creating gradient hydrogels used in tissue engineering applications.

the two proteins can also have mutually inductive effects on differentiation [180, 181]. RUNX2 is another option as it plays an essential role in the commitment of MSCs to the osteoblastic lineage [182].

Modelling of growth plate signalling & architecture

Some studies have achieved growth plate-like differentiation *in vitro*. Human foetal bone marrow MSCs were differentiated into chondrocytes in pellets with a gene expression profile resembling growth plate cartilage [183]. These models, however, lack any zonal organisation. Randall et al. (2012) showed that activation of the Wnt-PCP signalling pathway promotes the formation of columns inside pellets of

growth plate chondrocytes [184].

In one study, rat-derived calvarial osteoblasts and bovine articular chondrocytes were mixed with alginate modified with an arginine-glycine-aspartic acid-containing peptide sequence to promote cell proliferation, then injected into the subcutaneous into 4-week old mice. After 26 weeks, the implants displayed a cell organisation reminiscent of the growth plate [185]. A similar phenomenon was observed when iPSCs-derived hypertrophic cartilage was implanted in mice and organised into a growth-plate structure [186, 187]. These methods exploit the self-organisation capacity of cells when in the right environment.

Zonal architecture of chondrocytes was also achieved by encapsulating primary mouse growth plate chondrocytes inside alginate beads and treating with Ihh. Hypertrophic chondrocytes expressing collagen type X appeared on the peripheral ring of the beads and collagen type II-expressing cells in the centre [188]. This recapitulated the types of cells found in the growth plate and is a step towards emulating the zonal architecture of the growth plate.

In *in vivo*/*in vitro* hybrid approaches, growth plate explants have been dissected from growth plates of mice, swines or rabbits and cultured *in vitro* and/or loaded to study matrix protein biosynthesis and the effect of mechanical load on chondrocytes [189–194]. Explant cultures, however, are short lived and involve maintaining cells in the context of origin, thus rendering it difficult to extrinsically control cell biology *in vitro*. As with many bioengineered models, they contribute to developing knowledge specific aspects of cell and tissue biology, which help improve new biomaterial models of the growth plate.

Organ-on-chip technologies employ microfluidic channels to create adjacent compartments where different cell types can be cultured. The culture conditions can be optimised to those *in vivo* in terms of pH, mechanical properties and nutrients. This technology is starting to be used to model different forms of osteochondral interfaces,

especially focusing on creating heterogeneous culture conditions or biochemical gradients [195, 196].

Bioengineering technologies are further being developed to improve and add complexity to current models. Acoustic patterning using ultrasounds, for instance, can be used to achieve columnar organisations of cells inside gel constructs [197, 198]. Advances in 3D bioprinting technology, in particular, allows great precision in directing cellular organisation. Vasculature can be included by using sacrificial ink [199–201]. The complexity that can be added to models by incorporating different cells, materials, growth factors is particularly amenable to modelling the heterogeneity of the different zones of the growth plate. These developments hold promise for building more physiologically relevant models.

Clinical applications

Bioengineered models can also be humanised, which offers clinical potential, especially when genetic diseases such as ciliopathies are caused by many different mutations that continue to be discovered to this day. There is, therefore, a need for patient-specific models, which can be achieved by using a patient's own cells or iPSCs inside *in vitro* models. Due to its avascular nature, the growth plate has a limited capacity to self-regeneration and injuries to it need to be treated immediately due to its role in development. This presents opportunities in the field of regenerative medicine which can exploit tissue engineering strategies for disease management and injury repair in children.

Bioengineered models are useful to understand biological mechanisms in tissues and organs, and further to study disease mechanisms and develop therapies. The ability to manipulate genetic background of the cells within an *in vitro* environment offers a rare opportunity to evaluate cellular mechanisms at a molecular level. In the case of ciliopathies, the management of many ciliopathy patients is often limited to

corrective therapy, therefore needing a deeper understanding of disease mechanisms in order to design targeted therapies and improve clinical outcomes.

In vitro models are being used to study primary cilia function. 3D *in vitro* systems, such as rosettes and mouse gastruloids, have allowed the study of ciliogenesis and cilia function during early development [202]. These provide valuable platforms for studying centriole and cilium development within a controlled and closely monitored experimental framework, offering more physiologically relevant insights than traditional 2D cultures by better recapitulating the 3D cellular context.

Bioengineered models are already being used to study disease mechanisms. Pretemer et al. (2021) developed a protocol to differentiate iPSCs into hypertrophic chondrocytes inside pellet. iPSCs with chondrodysplasia mutations displayed cell disorganisation when pellets were inserted subcutaneously into mice, as well as changes in cell-matrix interactions, metabolism, matrix composition and bone homeostasis as studied through transcriptomic changes. They used their model for drug testing [203].

A combination of *in vivo*, *in vitro* and *in silico* models and tools are currently being used to study primary cilia, each with their own advantages and limitations [47, 51, 204–206]. Their complementary use can be exploited to understand the mechanistic biology of this micrometre-scale organelle.

1.4 Project aims

Given the structural and functional complexity of the growth plate, this project adopts an interdisciplinary approach to investigate the role of the primary cilium in regulating growth plate organisation and function. Specifically, the study has the following aims and associated hypotheses:

1. Characterise the spatial organisation and morphological features of primary cilia across distinct zones of the postnatal mouse growth plate, providing insights into their potential role in growth plate architecture and zonal function. I hypothesise that primary cilia prevalence is different between the centre and the periphery of the growth plate and that primary cilia have distinct lengths and orientations in the different zones of the growth plate.

2. Assess how this organisation is changed in an *Ift88* conditional knockout model and in the absence of load. I hypothesise that primary cilia prevalence, length and orientation are altered by *Ift88* conditional knockout and limb offloading.

3. Establish an *in vitro* model of osteochondral differentiation that recapitulates key aspects of growth plate development and organisation.

4. Interrogate the role of primary cilia in orchestrating osteochondral differentiation under defined mechanical loading conditions using the *in vitro* model, to better understand how ciliary structure and function contribute to mechanotransduction during skeletal development. I hypothesise that mechanical loading and deletion of *Ift88 in vitro* will alter cell differentiation within the osteochondral model.

2

Development of a high resolution imaging and analysis method to study primary cilia in the murine growth plate

Contents

2.1 Introduction **37**

2.2 Materials & Methods **39**

2.2.1 Animals 39

2.2.2 Tissue collection & processing 39

2.2.3 Confocal imaging 40

2.2.4 Image analysis pipeline 40

2.2.5 3D spherical coordinates 42
2.2.6 Data analysis 42
2.3 Results 46
2.3.1 High resolution imaging 46
2.3.2 Image analysis pipeline 46
2.4 Discussion 50

This chapter is based on the published paper: Johnson, T., Midha, S. & Wann, A. Volumetric Imaging and Analysis of Primary Cilia in Musculoskeletal Tissue using the ARL13B-Centrin-2 Mouse Model. *Journal of Visualized Experiments*, 217 (2025) [207].

2.1 Introduction

Due to its micrometer-scale size and the non-specificity of immunohistochemistry (IHC) antibodies, the primary cilium is challenging to image *in situ*, in a high throughput manner and without optical biases. An understanding of the organisation of primary cilia inside tissues is important to begin to understand how they regulate cellular behaviour at the organ level and how this may be disrupted in disease contexts. Incidence, length, and orientation of primary cilia have been shown to vary within and between tissues, suggestive of a role for tissue organisation to their function [139, 141, 208]. Previous studies that have imaged primary cilia in the growth plate have been limited to 2D, which loses information related to cilia organisation in tissue or are limited to a small number of cells in 3D, which reduces the scale and power of the analysis [209, 210].

Using a native fluorescent signal ensures strong localisation and specificity. Native fluorescent signals can, however, be challenging to image in mineralised tissues, as the long decalcification process to embed tissues in paraffin can result in loss

of signal. Cryosectioning samples frozen in the native state prevents this loss by speeding up the embedding and sectioning process.

To image primary cilia *in situ*, a double transgenic mouse line was generated by Bangs et al. (2015), which expresses ADP-ribosylation factor-like protein (ARL13B) fused to mCherry and Centrin-2 fused to a green fluorescent protein (GFP) [211]. ARL13B is a small guanosine triphosphatase localised to the primary cilium membrane, and Centrin-2 is a protein localised to the two centrioles at the base of the cilium [212, 213]. This mouse line, therefore, allows fluorescently labelled primary cilia to be imaged without the need for IHC. The protocol described here makes use of this transgenic line to image primary cilia in 3D in murine postnatal growth plates with confocal microscopy, only requiring additional 4',6-diamidino-2-phenylindole (DAPI) staining. Hundreds of primary cilia in hundreds of cells can be imaged and analysed collectively in a tissue context. An image analysis pipeline subsequently measures cell orientation and volume, primary cilia incidence, length, and orientation in the different regions of the growth plate, and centriolar position.

2.2 Materials & Methods

Unless stated otherwise, all chemicals used were from Sigma Aldrich.

2.2.1 Animals

All mice were housed in the biomedical services unit at the Kennedy Institute, University of Oxford. Mice were housed no more than 6 single-sex mice per cage, in individually ventilated cages and maintained under 12-hour light/dark conditions at an ambient temperature of 21°C. Two mouse lines were used for this project: *AggrecanCreER^{T2};Ift88$^{fl/fl}$;Centrin-2-GFP.ARL13b-mCherry* (*Ift88* conditional knockout (cKO)) and *Ift88$^{fl/fl}$;Centrin 2-GFP.ARL13b-mCherry* (*Ift88$^{fl/fl}$*) [47, 211]. For all experiments, apart from double neurectomy where only male mice were used, both sexes were used. The mice were fed a certified mouse diet (Special Diets Services: Rat and Mouse No. 3, pelleted), and water *ad libitum*. Animal husbandry and experiments were conducted in accordance with the University of Oxford ethical frameworks and under a Project license as granted by the UK Home Office. Mice were euthanised by filling a box containing the mice with CO_2 up to 80% by volume and maintaining its concentration for 5 minutes. Death was confirmed by performing cervical dislocation.

2.2.2 Tissue collection & processing

The hind leg knees were dissected out, and trimmed of excess fat and muscle tissue. The tissue was fixed in a neutral buffered formalin solution of 1.3 M formaldehyde at room temperature for 4 hours, then in 0.325 M formaldehyde at 4°C overnight. The tissue was then transferred to 0.30 g/mL sucrose in deionised water (diH_2O), and gently rotated at room temperature overnight or at 4°C for 72 hours. The

tissue was subsequently cryoembedded in super cryoembedding medium, with the kneecap facing down, and stored at -20°C.

50 µm-thick tissue sections were cut with a cryostat, using Kawamoto cryofilm tape. Throughout, care was taken to keep the tissue in the dark to avoid fluorescent signal loss. Sections were thawed, washed with three 5-minute washes in phosphate buffered saline (PBS) and nuclei stained with 10 µM 4',6-diamidino-2-phenylindole (DAPI) for 1 minute. After three 5-minute washes in PBS, the sections were mounted with SlowFade Glass Antifade Mountant (Invitrogen) and left at room temperature overnight. Imaging was performed the following day. The same protocol was applied to kidney tissues also imaged.

2.2.3 Confocal imaging

Images were acquired using a Zeiss 980 Airyscan 2 confocal microscope with an immersion oil 40x/1.4 objective. Images were taken in the middle and lateral regions of the growth plate. Images were one tile across, and three to five tiles down. 40 µm-thick Z-stacks of 0.15 µm intervals were acquired in the DAPI, mCherry and GFP channels. The superresolution SR-8Y Airyscan mode was used. The resolution in x/y of this mode was 120/160 nm and 450 nm in z. The images were airyscan processed and stitched using the ZEN software (Zeiss).

2.2.4 Image analysis pipeline

The arivis Vision4D software (Zeiss) was used for analysis. A custom pipeline was created which consisted of the following steps:

- **Cell detection step**: Using the Cellpose Python Segmenter, cells were detected based on background GFP and DAPI signal [214]. Detected cells outside the

volume range of 200 to 30,000 µm^3 were excluded based on true volume of cells [215]. Detected cells were stored as objects.

- **Primary cilia and centriole detection step**: Primary cilia were detected based on mCherry signal and only included if they were between 0.3 and 12 µm^3 in volume. Centrioles were detected based on GFP signal and included if between 0.02 and 2 µm^3 in volume. These thresholds were determined based on the volume of these organelles and optimisation based on observed detection. Pairs of centrioles that were detected together were split in two. Cilia and centrioles were matched to their corresponding stored cells based on overlapping signal.

- **Results export**: Features of the cells, primary cilia and centrioles were exported in an Excel spreadsheet. Included features were:

  - Number of Children (children of cells are primary cilia and centrioles)
  - Name
  - Parent Names (growth plate zone for cells and parent cell for primary cilia and centrioles)
  - 3D Oriented Bounds (minimum outer box of the object)
    - Short side, Middle side and Long side
    - Angle XY, Angle XZ and Angle YZ
  - Bounding Box
    - Coordinates X1, X2, Y1, Y2, Z1, Z2
    - SizeX, SizeY, SizeZ (distance between the coordinates)
  - Centre of Geometry X, Y, Z,
  - Object's First & Last Plane and Count (number of planes the object occupies)
  - Sphericity
  - Volume

– Surface Area

2.2.5 3D spherical coordinates

Spherical coordinates are a three-dimensional (3D) coordinate system used to define the position of a point in space by its distance from a fixed origin and two angles (Fig. 2.1 A-C). A point is described using three values:

- r - the radial distance from the origin
- ϕ - the polar angle measured as the inclination from the positive z-axis ($0° \leq \phi \leq 180°$)
- θ - the azimuthal angle measured as the projection on the xy-plane from the positive x-axis ($0° \leq \theta \leq 360°$)

When analysing 3D orientation of primary cilia, r is the length of the primary cilium and its 3D orientation is described by ϕ_{cilium} and θ_{cilium} (Fig. 2.1 D). These angles have previously been used to describe ciliary axonemal orientation [139, 141, 210, 216]. For the centrioles, the origin of the system is the centre of the cell and $\phi_{\text{centriole}}$ and $\theta_{\text{centriole}}$ describe the position of the centriole near the cell surface (Fig. 2.1 E). To measure cell orientation, the θ_{cell} was described as the angle between the major axis of the cell and the y-axis (medial-lateral axis) in the yz plane (Fig. 2.1 F).

2.2.6 Data analysis

An R code pipeline was developed to calculate relevant measures from the Excel spreadsheet exported out of arivis from the image analysis pipeline (Fig. 2.2, Appendix Fig. 1). Features calculated were:

- Cell volume

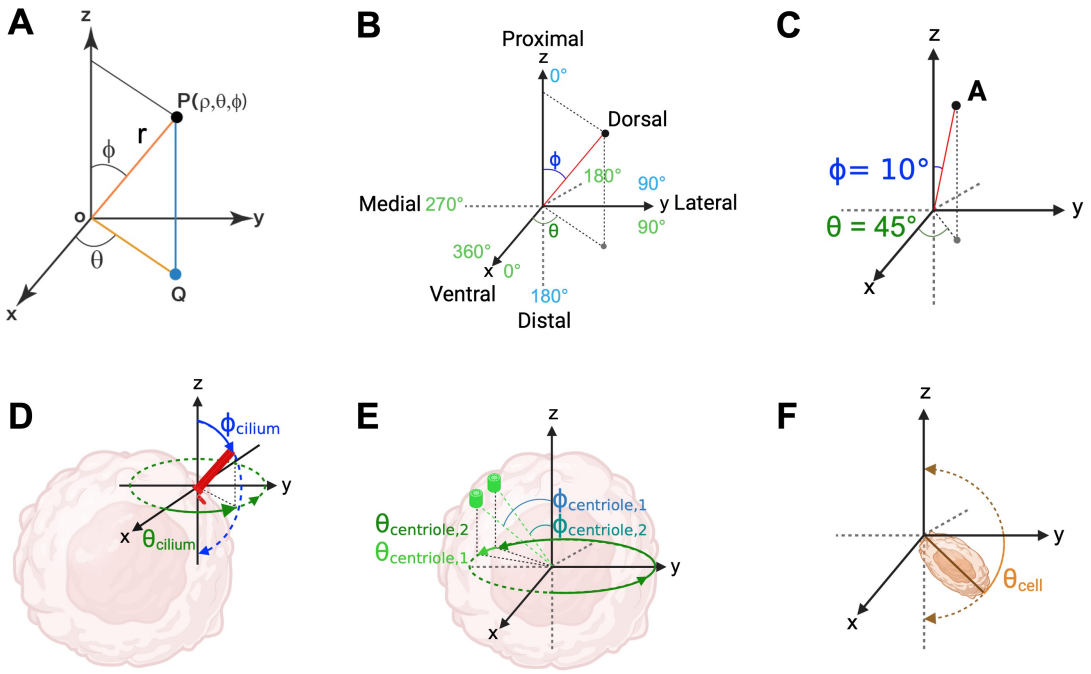


Figure 2.1: Spherical coordinates. **(A)** Spherical coordinate system, **(B)** with anatomical directions and angle values. **(C)** Example point A has spherical coordinates $\phi = 10°$ & $\theta = 45°$. Spherical coordinate system position to measure primary cilium axoneme orientation **(D)** and centriole position **(E)** spherical coordinates, and cell angle θ_{cell} **(F)**.

- Cell θ angle to medial-lateral plane (θ_{cell})
- Primary cilium length
- Primary cilium 3D orientation
  - Primary cilium ϕ angle (ϕ_{cilium})
  - Primary cilium θ angle (θ_{cilium})
- Primary cilium resultant

  The resultant is calculated as:

$$R = \sqrt{\left(\sum x_i\right)^2 + \left(\sum y_i\right)^2 + \left(\sum z_i\right)^2} \tag{2.1}$$

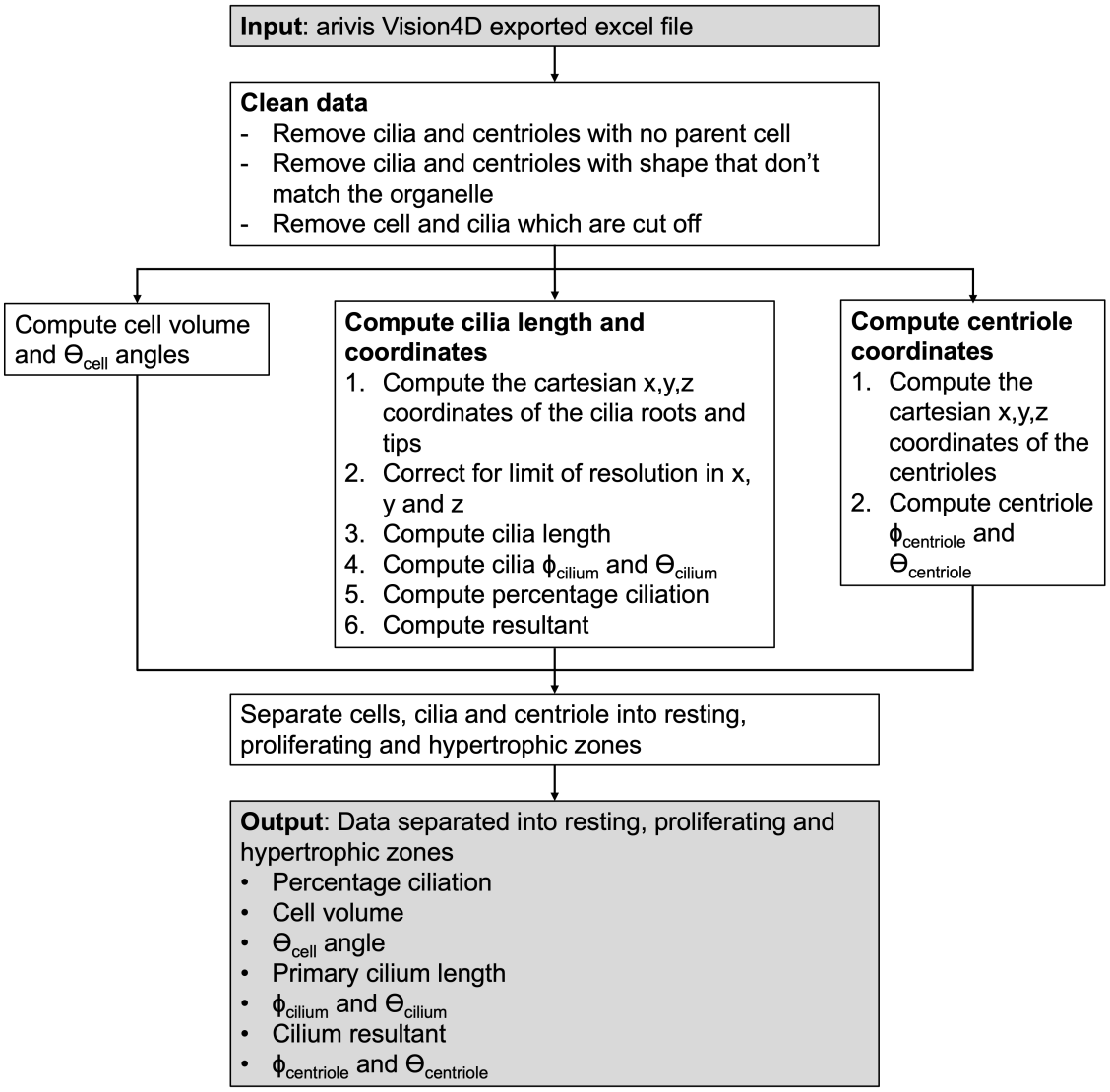


Figure 2.2: Flowchart describing the steps of the analysis pipeline run in R to calculate cell, primary cilia and centriole characteristics.

where

x_i : unit vector component of cilium i along the x-axis,

y_i : unit vector component of cilium i along the y-axis,

z_i : unit vector component of cilium i along the z-axis.

The resultant is a numerical expression to quantify how aligned vectors (cilia) are. When vectors are perfectly aligned (i.e. all point in the same direction),

the magnitudes of their components add up constructively. This results in a large resultant magnitude relative to the number of vectors being summed. Therefore the larger the resultant, the more aligned the cilia are.

To compare across groups of different sizes, the resultant is normalised to the number of vectors (n):

$$R_{\text{normalised}} = \frac{\sqrt{\left(\sum x_i\right)^2 + \left(\sum y_i\right)^2 + \left(\sum z_i\right)^2}}{n} \tag{2.2}$$

- Centriole 3D position in the cell
  - Centriole ϕ angle ($\phi_{\text{centriole}}$)
  - Centriole θ angle ($\theta_{\text{centriole}}$)

2.3 Results

2.3.1 High resolution imaging

The growth plate of 6-week-old mouse was imaged using the described protocol to give representative results of the method. An image of all three regions of the growth plate - resting, proliferative, and hypertrophic - was captured and run through the analysis pipeline (Fig. 2.3 A). Individual cells can be identified with the DAPI staining (gray), with their ciliary axoneme in magenta and their centrioles in green. The resolution using this method is high enough to discriminate individual centrioles. At this resolution, the cilia can be visualised in their 3D environment, pointing in different directions (Fig. 2.3 B, C).

This method also works for imaging primary cilia and their centrioles in other mouse tissues. Primary cilia were successfully imaged in the subchondral and trabecular bone, kidneys and articular cartilage (Fig. 2.4). The axonemes have different morphologies in these tissues - short in the subchondral and trabecular bone, long in the kidney and with high punctate intracellular ARL13B signal in the articular cartilage.

2.3.2 Image analysis pipeline

After acquisition, the growth plate images were opened in arivis Vision4D for analysis. The pipeline involved multiple detection steps to detect cells, primary cilia axonemes and pairs of centrioles (Fig. 2.5 A-D). The cells are detected based on the DAPI and background GFP signal, the cilia based on the mCherry signal and centrioles based on the GFP signal. The high 3D resolution can be seen from the side views of the detection (Fig. 2.5 E, G). The resolution is high enough to discriminate

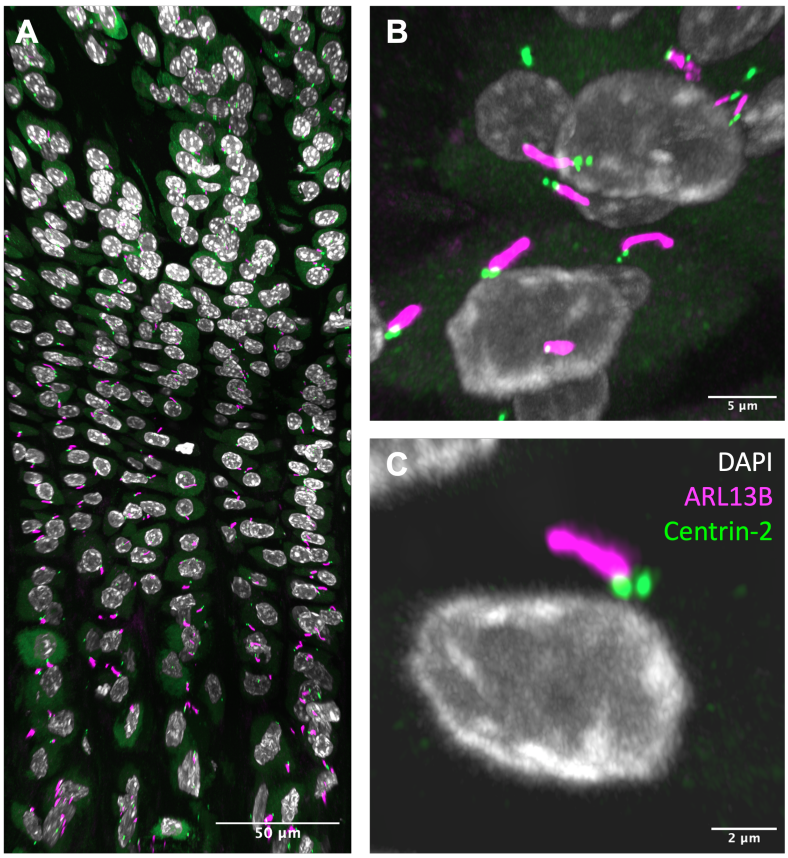


Figure 2.3: Primary cilia in the growth plate of a 6-week old ARL13B-Centrin-2 mouse imaged with the 40x objective. **(A)** All three regions of the growth plate - resting, proliferating, hypertrophic - are visible. **(B)** Zoom in on a proliferating cells, showing cilia pointing in different directions. **(C)** Zoom in on an individual primary cilium and its two centrioles.

between primary cilia pointing to the side and those pointing backwards. In addition, individual centrioles can be detected (Fig. 2.5 F).

The results of the detection were subsequently run through a customised R code to quantify cell, primary cilia and centriole features (Fig. 2.2). The results of this analysis for a 6-week old mouse growth plate will be presented in chapters 3 & 4.

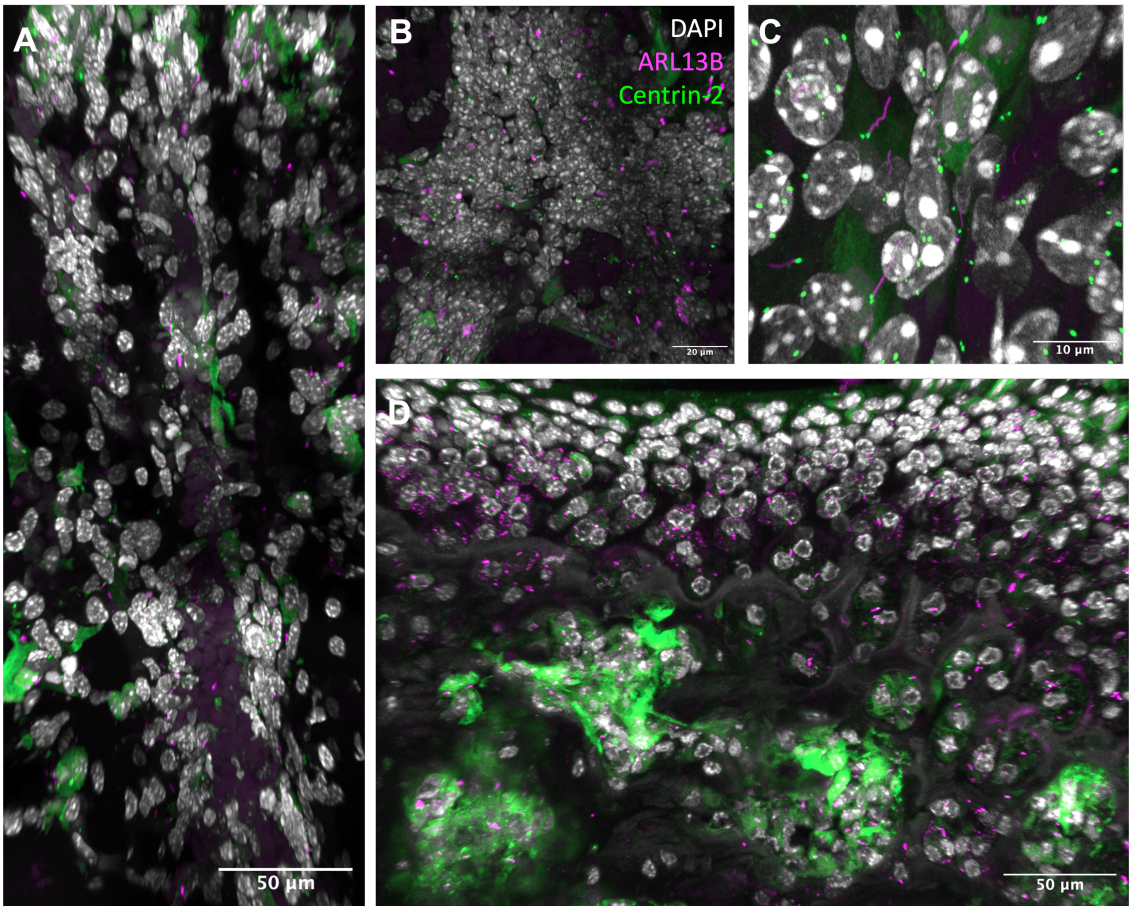


Figure 2.4: Primary cilia in the subchondral bone (A), trabecular bone (B), kidney (C) and articular cartilage (D) of 6-week old ARL13B-Centrin-2 mouse.

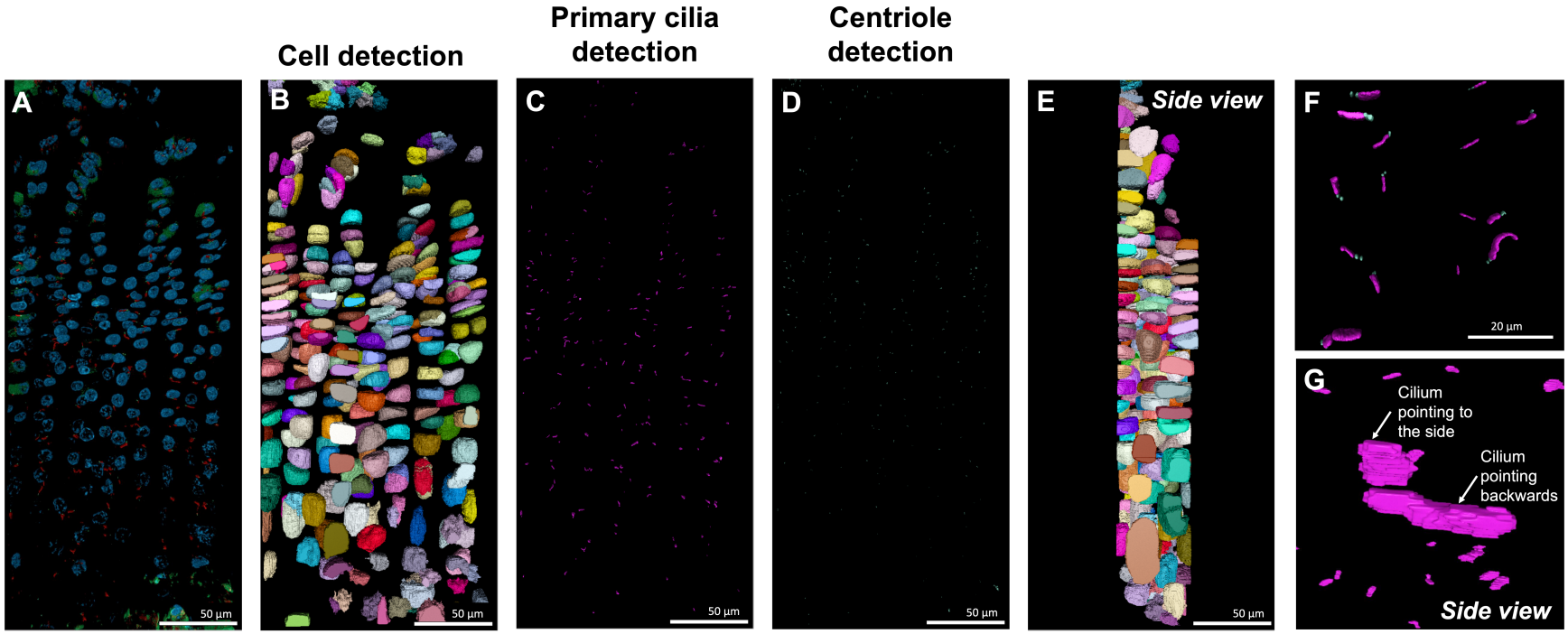


Figure 2.5: Cell, primary cilia and centriole detection on an image of a 6-week old growth plate in arivis Vision4D. (A) Image appearance in the software. Cell **(B)**, primary cilia **(C)** and centriole **(D)** detection. **(E)** Side view of the cell detection. **(F)** Primary cilia and centriole detection together. **(G)** Zoomed in side view of primary cilia detection.

2.4 Discussion

This protocol has allowed successful imaging of primary cilia in tissues. It has been optimised to work with this mouse line and for the purposes of studying primary cilia organisation in the growth plate. There are a few key considerations to take into account when performing it. It is essential to proceed with the tissue processing and embedding steps immediately after collection. The blocks and slides of tissue, however, can be kept for at least 3 months at -20°C. Several steps in this protocol can be modified to suit different applications, in particular, section thickness, magnification, and z-stack parameters. This will impact the depth of imaging and the resolution obtained. Changes in numerical aperture and resolution mode could be used to obtain an even higher resolution and the z-stacks interval size decreased. However, this would increase imaging time or reduce the size of the field of view that can be imaged. The imaging parameters described here are the minimum requirements identified for 3D analysis of primary cilia orientation. Lower resolution images, with lower magnification objectives, can also be captured to visualise primary cilia across a larger region of tissue; however, these are not suitable for analysis of cilia orientation in 3D as centrioles are not clearly distinguishable and the z-resolution is not high enough to determine 3D orientation.

The choice of mounting medium is important to obtain high resolution. The refractive index of the mounting medium must be similar to that of the immersion medium to minimise image degradation in the z-stack. The refractive index of the mountant and the immersion oil used here had refractive indexes of 1.52 and 1.518, respectively. The Airyscan function on the confocal microscope used here offered super-resolution images. Other super-resolution microscopes could be used; however, it was found that using the confocal mode only was not sufficient to obtain the resolution required for the size of the areas imaged without creating files that were too large to analyse. The maximum resolution of the Multiplex SR-8Y Airyscan mode is 120/160 nm in x/y and 450 nm in z, and a maximum number of frames per second of 47.5. The

Multiplex SR-4Y Airyscan mode, which presents a maximum resolution of 140 nm in x/y and 450 nm in z but images at half the speed with a maximum number of frames per second of 25, does not to present a significant difference for imaging primary cilia in 3D. Similarly, the Airyscan SR mode, which offers the highest resolution on the microscope used - 120 nm in x/y and 350 nm in z - would take longer to image, as its maximum number of frames per second is 4.7 [217]. To account for the lower z resolution relative to the x,y dimensions, a correction is applied within the R-based analysis pipeline to adjust ciliary vector coordinates accordingly.

This mouse line has previously been used to image primary cilia in the embryo, primary cell cultures, muscle fibres and the retinal pigment epithelium [211, 218, 219]. Here, the primary cilia in kidney, cartilage, and bone tissue were successfully imaged (Fig. 2.4). Some optimisation of imaging settings will likely be required for different tissues; however, this cryosectioning protocol should ensure preservation of the signal. For example, background GFP signal can be observed in muscle tissue. To minimise this, the wavelength range of the lasers can be narrowed to reduce overlap with the wavelength of other lasers.

Two-cell thick sections (40-60 µm) sections are sufficient to obtain 3D orientation information in the growth plate, as this allows imaging of whole cells and their primary cilia. For other tissues where cells are larger than chondrocytes, such as adipocytes, thicker sections may be required to collect cell population data. Depending on the depth resolution of the microscope used, it may not be possible to image deep into thicker sections. Tissue clearing techniques would likely lead to loss of the endogenous mCherry and GFP signal due to the time it requires. This was explored, as clearing methods were used for other imaging in the limb but it was not found necessary in this context. Previous experience with endogenous CD31-RFP suggested clearing techniques would need careful, bespoke to sample, optimisation. This method can also be combined with IHC to image primary cilia in combination with other proteins, for example, a cell membrane protein.

The transgene on ARL13B may have an effect on ARL13B expression and primary cilia length. Previous studies have measured different primary cilia lengths with the ARL13B-Centrin-2 line (increased in the order of 0.5 µm) compared to non-transgene ARL13B in certain regions of the mouse brain, with no difference in others [220]. Another study observed differences in primary cilia length in a GFP-tagged ARL13B mouse line compared to untagged ARL13B in mouse embryonic fibroblasts [212]. This represents a limitation of the methodology. However, since cilia lengths were compared across different zones and regions of the growth plate in subsequent analyses, any effect of the ARL13B transgene on absolute cilia length would not compromise the validity of these comparisons.

In addition, manual validation of the detection thresholds for cells, primary cilia and centrioles was performed to ensure that automated segmentation and classification outputs corresponded to biological structures. While this step provided an essential level of quality control, it also introduced an element of subjectivity inherent to manual adjustments, which may vary between datasets or observers. Consequently, despite efforts to apply consistent criteria, this process introduces a degree of arbitrariness that could influence the comparability of results when reproduced by different users or under varying imaging conditions.

Imaging very small subcellular structures, such as cilia, centrioles, mitochondria and synaptic nanodomains, requires methods that surpass the diffraction limit of conventional light microscopy. A number of high resolution imaging methodologies and automated detection pipelines have been developed both for primary cilia and other organelles. The most widely used high-resolution imaging approaches include Airyscan microscopy, expansion microscopy, lattice light sheet, single-molecule localisation microscopy, structured illumination microscopy, cryo-electron microscopy [221–223]. Each method offers unique combinations of resolution, temporal capacity and cell compatibility. The optimal technique depends on whether the priority is sub-nanometre details, dynamic live imaging, maximal labelling flexibility or ease of workflow.

Advanced imaging and segmentation workflows can yield quantitative insights into subcellular structures, but also underline the challenges of defining biologically meaningful thresholds and parameters for feature extraction [224, 225]. As with cilia and centrioles, the accuracy of such analyses often depends on precise calibration of imaging parameters and robust validation against manually annotated datasets to ensure reproducibility across experimental systems.

Another limitation is the potential impact of the fixation method on primary cilia axonemal length and shape. Most considerations of fixation methods primarily try to improve antibody penetration for IHC [226]. For example, cold methanol fixation is rapid and allows better antibody penetration but can deform tissue, including possibly the shape of the ciliary axoneme [216]. The degree of such deformation, however, has not been definitively measured in these studies. Formalin, used here, fixes tissue primarily by cross-linking proteins, preserving the cell and tissue structures and preventing decomposition. In these conditions, it is likely that primary cilia will be cross-linked to the extracellular matrix (ECM) through β1 integrins, The preservation of general morphology, including the overall structure of the growth plate and ciliary positioning is suitable for the light microscopy performed here. For electron microscopy applications, delicate and fine ultrastructural features of primary cilia may be affected.

The image analysis pipeline in this protocol was designed to subsequently measure the ciliation percentage, length, and 3D orientation of primary cilia, as well as centriole position in the growth plate. The image analysis software allows for custom pipelines to be made by changing the steps involved. The output of this pipeline is an Excel spreadsheet with the measures of the chosen features for the cells, cilia and centrioles detected. Post analysis was then performed in R according to the purposes of the study. As with the imaging settings, the pipeline steps and specific settings can be changed to work on different images and according to the aims of the study. Software and methods have been released to automatically detect cilia in images however these

are limited to 2D images, to measuring single parameters such as length, require manual input, or when they measure orientation is a 2D angle [224, 225, 227].

By leveraging endogenous fluorescent signals, the method circumvents key limitations of IHC, notably the time-consuming protocol, poor signal-to-noise ratio, non-specific staining and reduced antibody penetration at greater tissue depths. The ability to analyse large numbers of cilia across defined zones enables more robust and reproducible measurements and offers a valuable platform for functional studies, including comparisons of ciliary organisation in genetic knockout models. This pipeline facilitates investigation of hypotheses across complex tissues such as how mechanical loading influence cilia orientation, whether ciliary structure correlates with zone-specific cell fate decisions, or how centriolar positioning shifts in zones undergoing hypertrophy versus proliferation. The number of cells that can be captured allows us to investigate primary cilia and centriole orientation at a specific zone and regional level, enabling direct comparisons across different growth plate compartments. This enables detailed exploration of spatial heterogeneity in cilia-mediated signalling during both development and disease.

3

Ciliation in the mouse post-natal growth plate

Contents

3.1 Introduction **56**

3.2 Materials & Methods **60**

3.2.1 Animals, tissue collection, imaging &analysis 60

3.2.2 Micro-computed tomography (MicroCT) 60

3.2.3 Histology 61

3.2.4 Statistical analysis 61

3.3 Results **62**

3.3.1 Murine growth plate characterisation by microCT, histology and fluorescence microscopy 62
3.3.2 Cell volume in the growth plate 64
3.3.3 Cell orientation in the growth plate 67
3.3.4 Percentage ciliation in the growth plate 69
3.3.5 Primary cilia length in the growth plate 70
3.3.6 Primary cilia orientation in the growth plate 72
3.3.7 Centriole position in the growth plate 73
3.4 Discussion 77
3.4.1 Cell volume in the growth plate 77
3.4.2 Cell orientation in the growth plate 78
3.4.3 Percentage ciliation in the growth plate 79
3.4.4 Primary cilia length in the growth plate 80
3.4.5 Primary cilia orientation in the growth plate 82
3.4.6 Centriole position in the growth plate 87

3.1 Introduction

In the growth plate, chondrocytes are spatially organised into columns aligned along the axis of bone elongation. These cells progress through defined stages of differentiation - resting, proliferating, and hypertrophic - each associated with distinct morphological, molecular and extracellular matrix (ECM) features. This highly ordered arrangement is critical for directional growth and structural integrity of developing long bones. Disruption of this columnar organisation is observed in several ciliopathies, implicating the primary cilium in the regulation of cellular polarity and tissue architecture [116, 133, 134]. This raises the broader question of whether the primary cilium actively contributes to establishing or maintaining tissue organisation in highly anisotropic structures like the growth plate.

While the importance of primary cilia in normal skeletal development is well established, detailed characterisation of their spatial organisation, particularly their 3D orientation within the tissue, remains limited. Most studies to date have focused on ciliary presence or length, with few addressing their orientation relative to cell and tissue axes, a parameter potentially crucial for directional signalling and morphogenesis.

Cell polarity in the growth plate is governed by an interplay of intrinsic and extrinsic cues. Signalling pathways such as planar cell polarity (PCP), Wnt and TGF-β have been implicated in establishing planar cell polarity and directing polarised behaviours in many tissues, including cartilage [228, 229]. These pathways may act upstream or in parallel with ciliogenesis that follows cell division, with the cilium serving as a key signalling hub to coordinate responses to environmental cues.

Primary cilia may play a key role in establishing matrix organisation and tissue anisotropy by linking mechanical cues to polarised cellular behaviours. To fulfil this role, the cilium must be able to sense the directionality of mechanical forces and transduce these signals to coordinate spatially appropriate responses. Its close physical association with the Golgi apparatus suggests it could influence the orientation of ECM secretion and the organisation of the cytoskeleton [60]. This positioning may guide the polarised secretion of ECM components and matrix-remodelling proteins, thereby directing the local micro-environment and contributing to anisotropic tissue structure [147, 230].

Primary cilia length varies significantly between tissues and developmental stages. In chondrocytes, cilia are typically short - ranging from 2 to 3 µm, compared with those in kidney epithelial cells (5 to 6 µm) or neurons (up to 9 µm) [127, 210, 231–233]. This variation is thought to reflect cell type-specific functional demands and differences in local biomechanical or biochemical environments. However, further studies integrating detailed phenotypic characterisation with quantitative ciliary analysis are needed to elucidate these relationships.

Cilia length is dynamically regulated by a range of intracellular factors including calcium levels, cyclic adenosine monophosphate (cAMP), cAMP-dependent protein kinase activity, and the actin and microtubule cytoskeleton [127, 234–236]. Moreover, inflammatory cytokines and ECM cues have been shown to influence axonemal assembly, suggesting that ciliary morphology is not static but adjusts in response to mechanical and chemical stimuli [231, 236]. Such regulation may be particularly important in cartilage, where the ECM is dense and mechanically dynamic, exposing chondrocytes to fluctuating compressive forces and biochemical gradients. In this context, the ability of cilia to modulate their length may enable fine-tuned control of mechanosensitive signalling pathways, such as Hedgehog (Hh) and Wnt, thereby influencing chondrocyte behaviour, matrix homeostasis and tissue integrity.

The positioning of the centriole pair, from which the primary cilium extends, is closely linked to both ciliogenesis and cell polarity. In epithelial and neuronal tissues, centrosome positioning is essential for orienting the mitotic spindle, establishing cell polarity and coordinating directional cell migration [237]. In the growth plate, similar mechanisms may underlie the transition from a rounded resting chondrocytes to a polarised, columnar proliferating cell. Disruption of centrosome or cilium positioning could thus have an impact on growth plate organisation and function.

I hypothesise that primary cilia organisation - specifically their prevalence, length, orientation - contributes to the establishment and maintenance of columnar architecture in the adolescent growth plate, potentially by influencing chondrocyte polarity and responsiveness to mechanical and biochemical cues. Previous studies have demonstrated regional differences in ciliation patterns, mechanical loading and tissue disruption across the growth plate, suggesting that ciliary function may be spatially regulated [47, 238, 239]. Moreover, gradients of key morphogens, such as those involved in the Hh-PTHrP feedback loop, are known to orchestrate chondrocyte proliferation and differentiation along the longitudinal axis of the growth plate, raising the possibility that primary cilia mediate zone-specific differences

in signal transduction. These zonal and regional differences may be reflected in ciliary structure.

In this chapter, I characterise the 3D organisation of cells, primary cilia and centrioles in the tibial growth plate of 6-week-old mice using high-resolution 3D imaging and quantitative analysis. By assessing variation across differentiation zones (resting, proliferative, hypertrophic) and spatial regions (middle vs lateral), I aim to uncover how ciliary architecture and cell polarity are coordinated, and how their spatial heterogeneity may contribute to the establishment and maintenance of the growth plate's highly ordered structure.

3.2 Materials & Methods

Unless stated otherwise, all chemicals used were from Sigma Aldrich.

3.2.1 Animals, tissue collection, imaging & analysis

Animal husbandry, mouse limb collection, confocal imaging and analysis was performed as per Chapter 2. For phalloidin staining, prior to DAPI staining, sections were stained with Alexa Fluor 568 phalloidin (Invitrogen) for 45 minutes, in the dark, at room temperature.

Due to the nature of experiments in Chapter 4, where it is being used to induce the activity of the Cre recombinase to excise the *Ift88* gene, tamoxifen was administered to the mice imaged in this Chapter (except in Fig. 3.2 D). Tamoxifen was dissolved in 90% sunflower oil and 10% ethanol at a concentration of 20 mg/mL by sonication. 50 µL tamoxifen was administered via intraperitoneal injection to mice at 4 weeks of age on 3 consecutive days an tibia collected 2 weeks later at 6 weeks.

3.2.2 Micro-computed tomography (MicroCT)

Knee joints were imaged using a Quantum FX Microcomputed Tomograph scanner (Perkin Elmer). Knees were placed kneecap down and imaged using the following acquisition parameters: 90 kV voltage, 160 µA current, 5 mm field of view, 3 minutes of acquisition time (fine scanning). Scans were exported as DICOM files.

DICOM files were loaded into ImageJ/Fiji as image sequences. The femoral growth plates were chosen as an anatomical reference to orient the knee joints. The images were then re-sliced to produce coronal sections through the whole joint. The disappearance of the lateral meniscus from view at the distal end of the joint

in the image sequence was chosen as an anatomical reference to select the section to measure. The image was converted from greyscale to thresholded by applying a threshold function with the Ostu method with parameters 125 to 255 intensity values. 9 measurements were made across the growth plate in both the greyscale and thresholded images - 3 in each of the medial, middle and lateral regions (Fig. 3.2 A, B). The measurements were averaged to calculate growth plate length.

3.2.3 Histology

Knee joints were fixed in 10% formalin for 24 hours at room temperature. Joints were decalcified in 0.5 M ethylenediaminetetraacetic acid, paraffin embedded, and coronally sectioned at a thickness of 4 µm. Sections were collected from the middle of the joint. Sections were cleared in xylene, rehydrated in graded alcohols and stained.

Sections were imaged with a Zeiss Axioscan 7 under brightfield with a 10x objective. Picosirius red stained sections were imaged under polarised light with a Olympus BX51 light microscope with a U-AN reflected light analyser.

3.2.4 Statistical analysis

Paired student t tests were performed to compare the greyscale and thresholded microCT measurements of growth plate lengths of the same mice and percentages ciliation between the regions of the growth plate. Kolmogorov-Smirnov tests adjusted for multiple comparisons were performed to compare distributions of cell volumes, θ_{cell}, ϕ_{cilium}, θ_{cilium}, $\phi_{\text{centriole}}$ and $\theta_{\text{centriole}}$. One and two-way ANOVA tests were performed to compare the percentages ciliation, primary cilia lengths and resultants in the different zones and regions of the growth plate.

3.3 Results

3.3.1 Murine growth plate characterisation by microCT, histology and fluorescence microscopy

The growth plate of a 4-week old was stained with cartilage and bone specific histological stains in order to visualise their proteoglycan and mineral content (Fig. 3.1). Safranin-O/fast green stains areas rich in proteoglycans in red and bone in green/blue (Fig. 3.1 A, F). Alcian blue stains glycosaminoglycans (GAGs) in blue (Fig. 3.1 B). Toluidine blue stains polyanionic molecules such a sulfated GAGs and nucleic acids in blue (Fig. 3.1 C). Alizarin red stains calcium deposits in red - this staining is performed on cryosections that aren't subject to decalcification as paraffin embedded joints have been (Fig. 3.1 D). Finally, picosirius red stains collagen fibres in red under polarised light (Fig. 3.1 E). Growth plate cartilage, rich in proteoglycans and GAGs, stains positively for cartilage stains safranin-O, alcian and toluidine blue (Fig. 3.1 A-C). Alizarin and picosirius red stain the subchondral, cortical and trabecular bone regions and not the growth plate region (Fig. 3.1 D, E). In a 4-week old mouse, the growth plate is active and chondrocytes are arranged in columns in the proliferating and hypertrophic zones (Fig. 3.1 F). These stains of the growth plate can serve as reference to compare to *in vitro* model staining in Chapters 5 & 6, to assess successful proteoglycan deposition and mineralisation.

The length of the growth plate from above the resting zone to the bottom of the hypertrophic zone was measured by microCT. Nine measurements across the width of the growth plate were taken in greyscale and thresholded images (Fig. 3.2 A, B). Greyscale length measurements are shorter than thresholded as they exclude the calcified cartilage at the bottom of the growth plate (Fig. 3.2 C). The threshold value used is above the detection value of calcified cartilage therefore appears black in the thresholded images and is included in the growth plate length. Thresholded

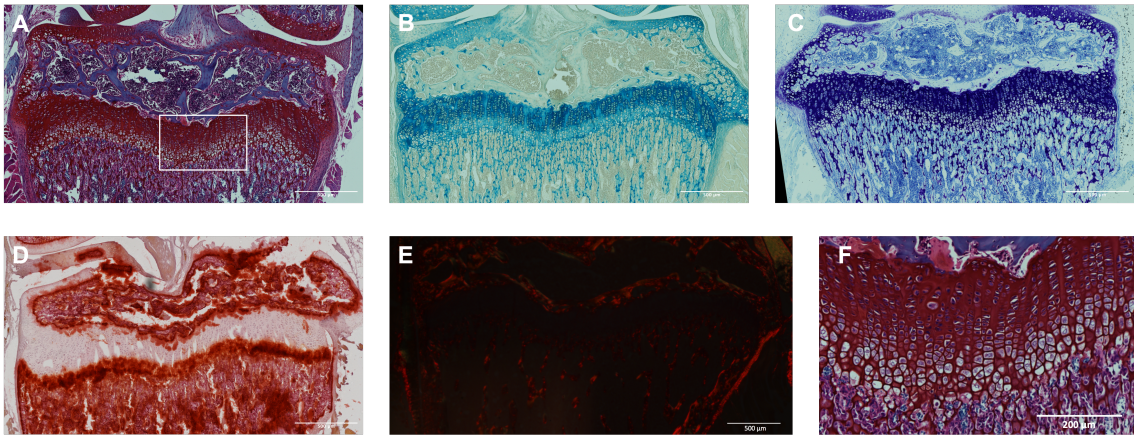


Figure 3.1: Histological staining of the tibial growth plate of a 4-week old mouse. Safranin O/fast green **(A)**, alcian blue **(B)**, toluidine blue **(C)**, alizarin red **(D)** and picosirius red **(E)** staining. **(F)** Enlarged view of the white box in (A). Scale bars for A-E = 500 µm.

values were used for subsequent analysis as the black and white contrast makes measurements more accurate. Growth plate measurements confirm that as mice get older and the growth plates less active, they become shorter (Fig. 3.2 D).

To assess ciliation in the growth plate at these different levels of activity, the primary cilia of growth plates from different ages were imaged (Fig. 3.3). Growth plates of all the ages were ciliated. The youngest growth plates (2 weeks) had the longest growth plates with the most cells and cells in the longest and most defined columns (Fig. 3.3 A, E). Old, inactive growth plates (10 weeks) were short, with a reduced hypertrophic zone (Fig. 3.3 D, H).

Cilia analysis was performed on both male and female mice, with no difference observed between the sexes. 6-week *Ift88*$^{fl/fl}$ growth plates were imaged at high resolution for subsequent analysis (Fig. 3.4). Individual axonemes pointing into the ECM and their centrioles can be visualised in 3D in each of the growth plates zones - resting, proliferating and hypertrophic (Fig. 3.4 B, C, D). Bends and undulations were sometimes seen along the axoneme length, as previously described in chondrocytes [240]. As an example of the importance of using 3D imaging for studying primary cilia in tissues, a primary cilium looked to be pointing down from the front view

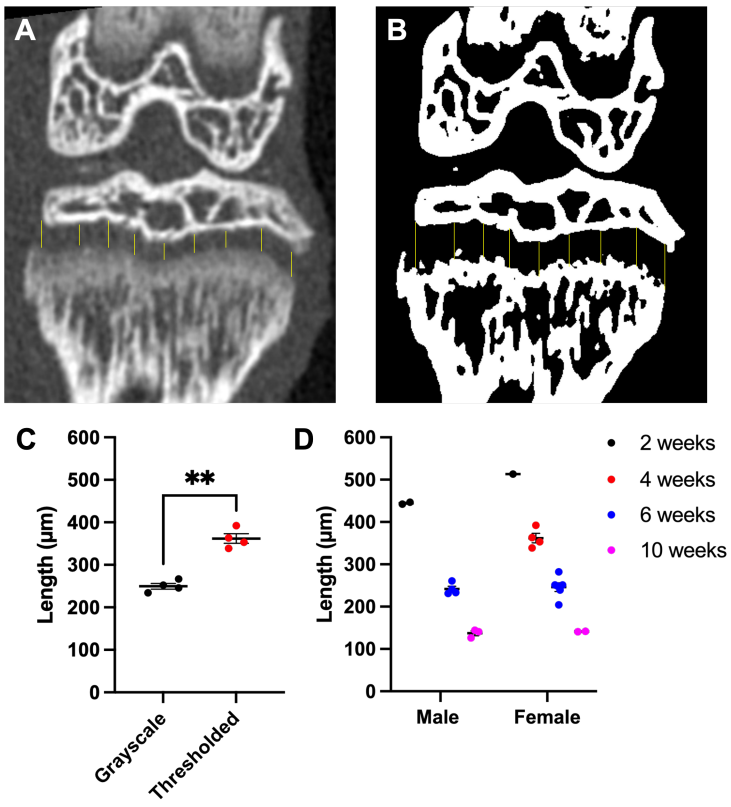


Figure 3.2: MicroCT of mouse tibial growth plates. Greyscale **(A)** and thresholded **(B)** images of a 4-week old growth plate. **(C)** Greyscale growth plate length measurements compared with thresholded measurements for female 4-week old mice. p** = 0.0021 (paired t test). **(D)** Thresholded growth plate lengths at different ages. Mean ± SEM. n = 2-5 mice.

(Fig. 3.4 E). When this same cilium was viewed from the side, its true orientation was revealed to be pointing forwards (Fig. 3.4 F).

6-week *Ift88*$^{fl/fl}$ growth plates were also stained with phalloidin, which binds to F-actin filaments (Fig. 3.5). This allows visualisation of the cell shapes of chondrocyte in the growth plate, in particular the expansion in volume of hypertrophic chondrocytes.

3.3.2 Cell volume in the growth plate

For analysis of cell and cilia organisation in the growth plate, 3 to 5 tile-long images covering the resting, proliferating and hypertrophic zones and 1 tile-wide images were acquired - one in the middle region and one in the lateral region for

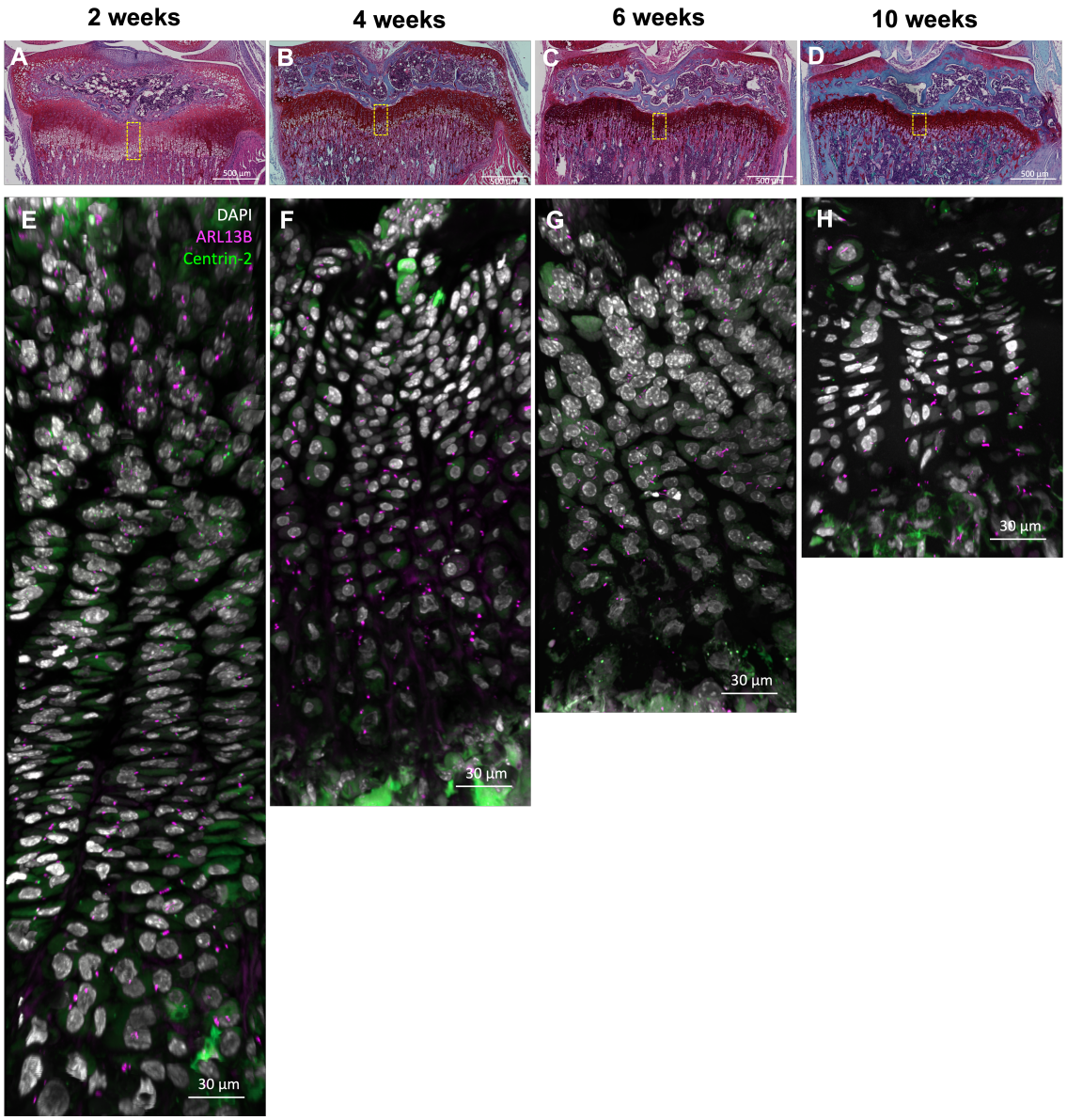


Figure 3.3: Safranin-O staining (A-D) and primary cilia imaging (E-H) of murine growth plates at different ages. E, G and H were acquired with the SR8Y Airyscan mode and F with the Co8Y mode (lower resolution, faster). Yellow boxes are representative of the regions of the growth plate imaged for fluorescence, they were not directly imaged on the histology section.

each mouse (Fig. 3.6 A). These regions were selected in order to determine any differences between the central and peripheral regions of the growth plate, as previous studies have reported region-specific variations in response to ciliary deletion [47]. Investigating these regions separately may therefore reveal whether primary cilia play distinct roles in maintaining tissue architecture and signalling responsivity

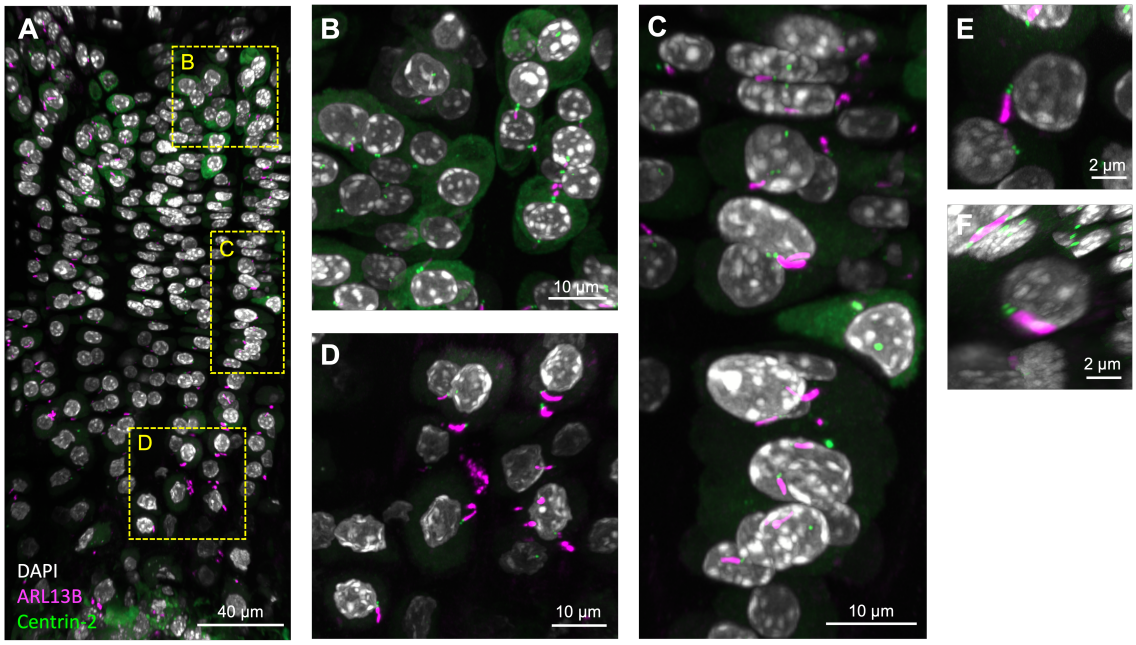


Figure 3.4: (A) Primary cilia in the growth plate a of a 6-week old *Ift88*$^{fl/fl}$ mouse. Yellow boxes indicate regions that are enlarged in the resting **(B)**, proliferating **(C)** and hypertrophic **(D)** zones. **(E)** Single cilium viewed from the front. **(F)** The same cilium viewed from the side.

in different parts of the growth plate.

The images were run through the image analysis and data analysis pipelines (Fig. 2.5, 2.2). The cell volume was measured in order to ensure the correct cell detection, which is crucial for subsequent cell orientation measurement. Cell volume was measured based on the cell detection in the analysis pipeline (Fig. 2.5 B). This detection was performed based on the DAPI and background GFP signal. The volumetric representation is of the whole cell, corresponding to the background GFP, therefore the volume measured was of the cell, not just the nuclei. Resting and proliferating cells' volumes ranged between approximately 500 and 1200 µm^3, with medians of 521.6 and 622.8 µm^3 respectively (Fig. 3.6 B). All the distributions/medians were statistically different from each other. The hypertrophic cells had a distribution that skewed higher than resting and proliferating cells, ranging from approximately 500 to 2500 µm^3 with a median of 924.7 µm^3. This is in line with the fact that hypertrophic chondrocytes expand in volume. The chondrocyte volumes were in the range of previous studies [215].

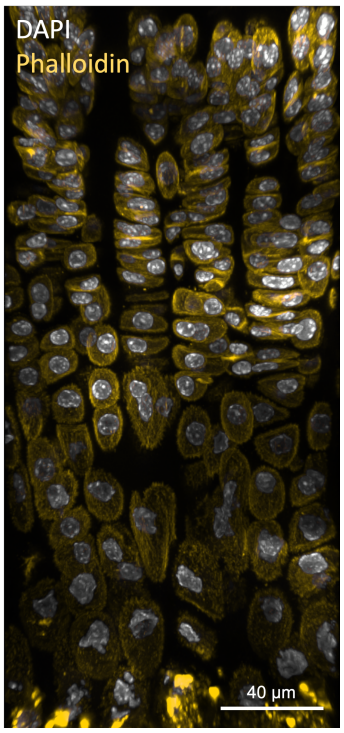


Figure 3.5: 6-week old *Ift88*$^{fl/fl}$ murine growth plate stained with DAPI and phalloidin.

The DAPI and GFP signal in the hypertrophic zone appear shrunk, as the cell detection does not fill up the whole cell (Fig. 2.5). The phalloidin staining of the growth plate shows the true size of the hypertrophic chondrocytes (Fig. 3.5). Therefore this data is probably underestimating the hypertrophic cells' volume.

3.3.3 Cell orientation in the growth plate

The orientation of the main axis of cells with respect to the medial-lateral axis in the growth plate was measured by the angle of the longitudinal axis of the cell with respect to the medial-lateral direction (θ_{cell}) (Fig. 3.6 C, D). A cell which is perfectly horizontal and in line with the medial-lateral plane would have a θ_{cell} equal to 0°. θ_{cell} ranges from -90°(vertically down) to 90° (vertically up).

In the proliferating zone, across both regions, θ_{cell} had a mode around 0° (Fig. 3.6 E). These cells were therefore horizontally aligned. In the proliferating zone, cells

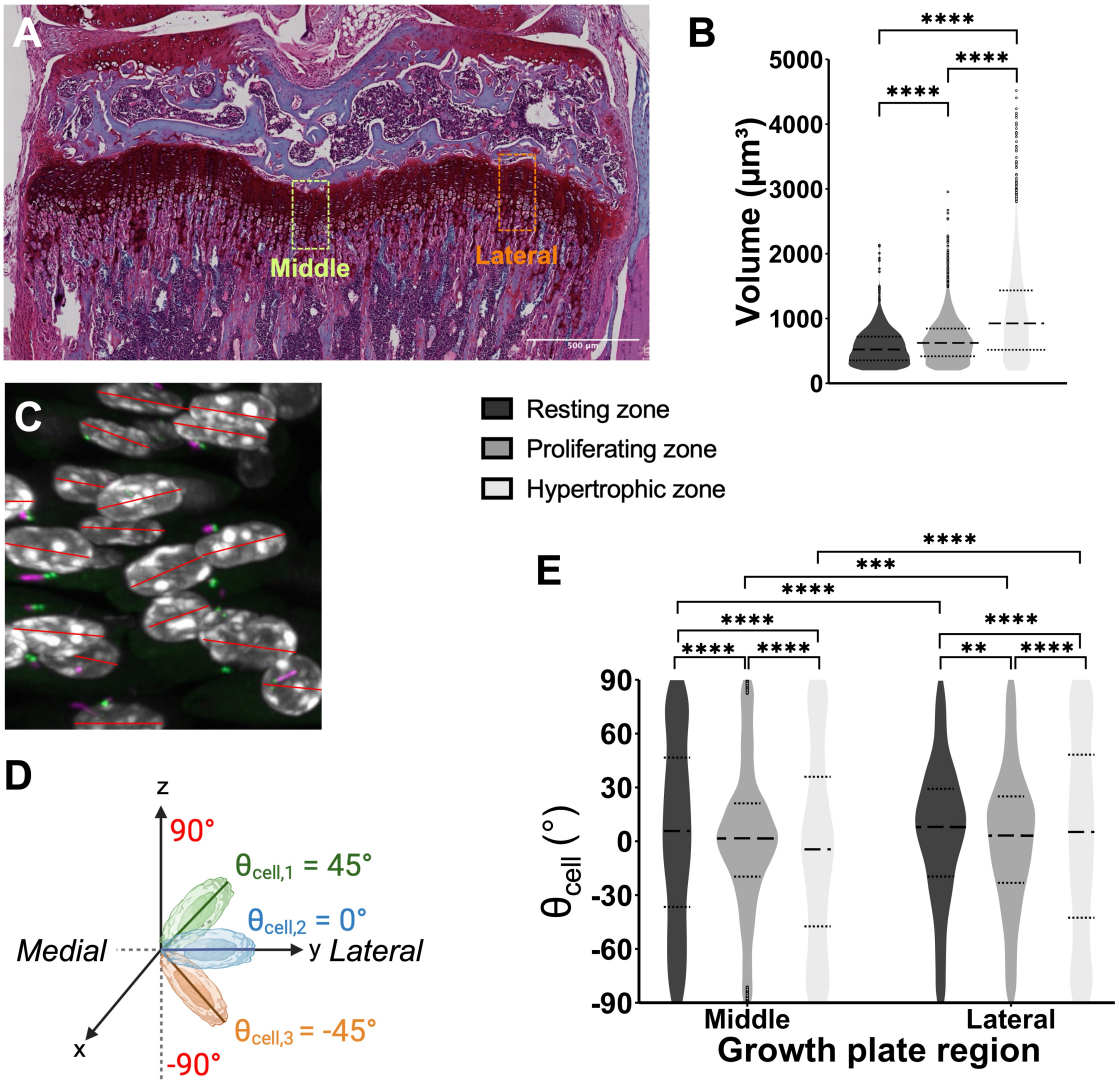


Figure 3.6: Cell organisation differs by zone and region in the 6-week old *Ift88*$^{fl/fl}$ growth plate. **(A)** Safranin-O stain of the growth plate of a 6-week old *Ift88*$^{fl/fl}$ mouse. Boxes indicate regions that were imaged with fluorescence microscopy. **(B)** Cell volume in the resting, proliferating and hypertrophic zones of the growth plate. Dashed lines represent median (longer dashes) and first and third quartiles (shorter dashes). p**** < 0.0001 (Kolmogorov–Smirnov test adjusted for multiple comparisons). n = 18 mice (2074 to 6359 cells per zone) **(C)** Major/longitudinal axis (red line) of cells in the proliferating zone of the growth plate. **(D)** Cell orientation angle with respect to the medial-lateral plane θ_{cell}. **(E)** Distribution of θ_{cell} in the resting, proliferating and hypertrophic zones of the middle and lateral regions of the growth plate. Dashed lines represent median (longer dashes) and first and third quartiles (shorter dashes). p** = 0.0024, p*** = 0.00016, p**** < 0.0001 (Kolmogorov–Smirnov test adjusted for multiple comparisons) n = 18 mice (947 to 2737 cells per zone/region).

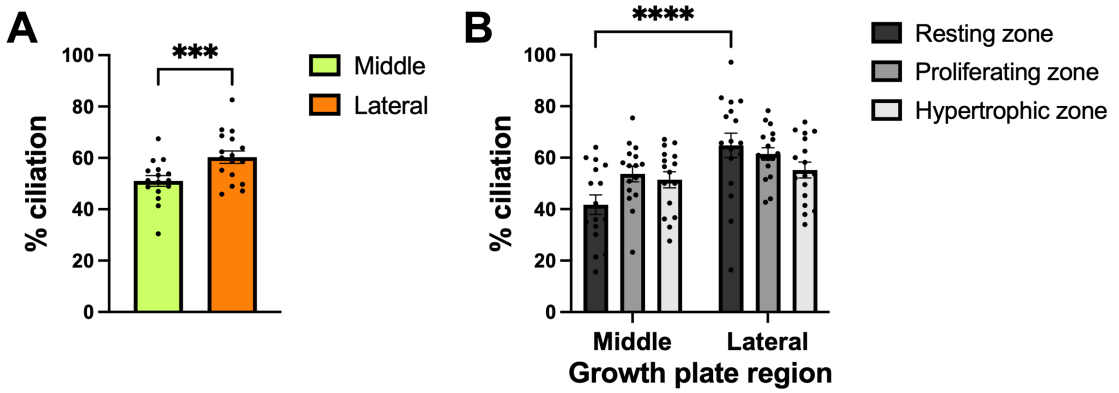


Figure 3.7: Varying percentage ciliation in the different regions and zones of the 6-week old *Ift88*$^{fl/fl}$ growth plate. **(A)** Percentage ciliation by growth plate region. Mean ± SEM. p*** = 0.0007 (paired t test). **(B)** Percentage ciliation in the different zones and regions of the growth plate. Mean ± SEM. p**** < 0.0001. All other comparisons are not statistically significant (two-way ANOVA). n = 18 mice (947 to 3622 cells per zone/region).

are arranged in columns, therefore are more likely to be in the same orientation (Fig. 3.4 C). In the resting zone of the middle region of the growth plate, the θ_{cell} distribution is spread across all values. This is also true in the hypertrophic zone of the middle and lateral region (Fig. 3.6 E). This suggests the chondrocytes in these zones are randomly orientated. The resting zone cells of the lateral region, however, had a mode around 0°, suggesting a horizontal alignment. In the resting zone, chondrocytes aren't highly aligned in columns, but they can still be in a horizontal orientation, just dispersed randomly around the ECM.

3.3.4 Percentage ciliation in the growth plate

Next, the percentage of cell with a primary cilium in the growth plate was measured. Irrespective of zone, the percentage ciliation in the lateral region was higher than that of the middle region, ~60% vs ~51% (Fig. 3.7 A). Looking into the origin of this difference in the different zones, the percentage of cells that had a cilium in the resting, proliferating and hypertrophic zone by region was measured. Ciliation is statistically significantly higher in the resting zone of the lateral region, with a

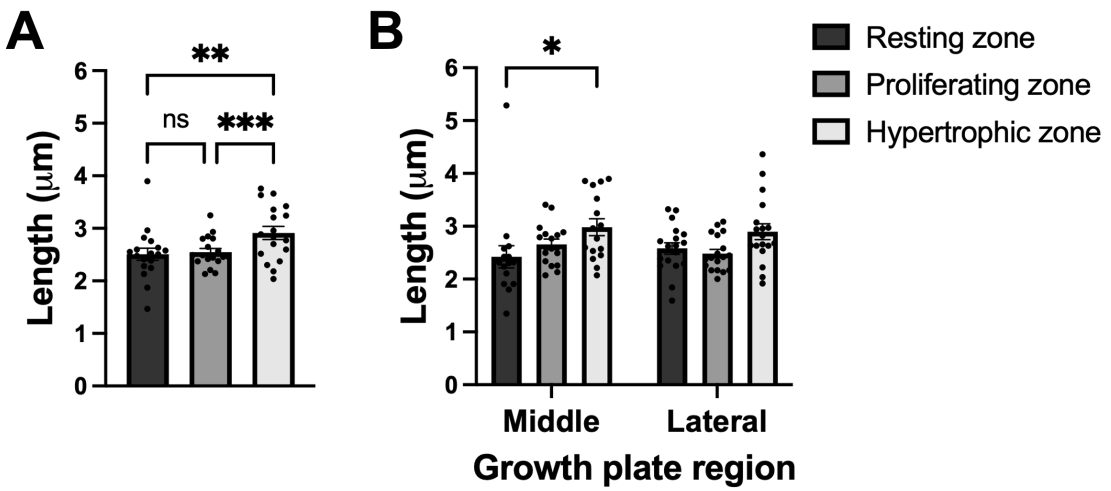


Figure 3.8: Primary cilia length is longer in the hypertrophic zone of the 6-week old *Ift88*$^{fl/fl}$ growth plate. (B) Primary cilia length in the different zones across the width of the growth plate. Mean ± SEM. p** = 0.0031, p*** = 0.0004 (one-way ANOVA) n = 18 mice (1028 to 3391 cilia per zone). Each data point is the average cilium length in the growth plate zone of one mouse. **(B)** Primary cilia length in the resting, proliferating and hypertrophic zones of the middle and lateral regions of the growth plate of a 6-week old *Ift88*$^{fl/fl}$ mouse. Mean ± SEM. p* = 0.0198. All other comparisons are not statistically significant (two-way ANOVA). n = 18 mice (466 to 1922 cilia per zone/region). Each data point is the average cilium length in the growth plate zone and region of one mouse.

mean of 65%, compared with the resting zone in the middle region, which has a mean of 42% (Fig. 3.7 B). This difference contributes to the difference observed in the middle region compared to the lateral region. The percentage ciliation in the other zones and regions was comparatively similar.

3.3.5 Primary cilia length in the growth plate

Next, the length of the axoneme of the primary cilium in the growth plate was measured. The length was measured in the resting, proliferative and hypertrophic zones of the growth plate. The primary cilia in the hypertrophic zone were longer compared with both the resting and proliferating zones (Fig. 3.8 A). To investigate where this difference came from, the primary cilia lengths in the different zones between middle and lateral regions of the growth plate were compared (Fig. 3.8 B). In the middle region, the primary cilia were statistically significantly longer in the

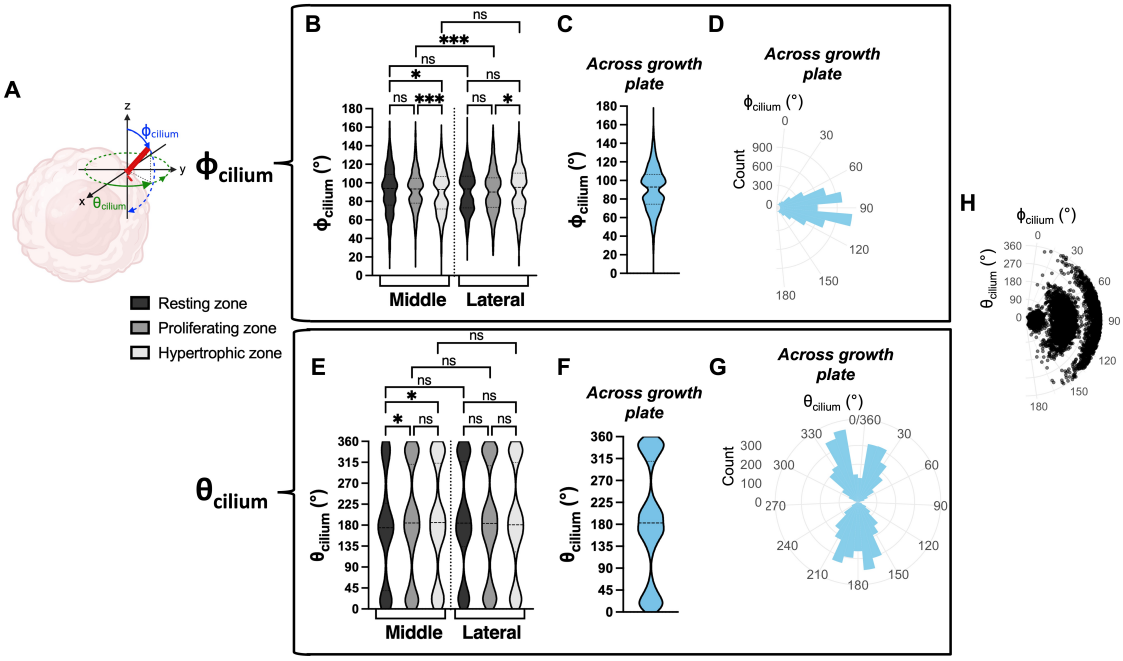


Figure 3.9: Primary cilia orientation is consistent throughout the 6-week old *Ift88*$^{fl/fl}$ mouse growth plate. (A) Spherical coordinates of primary cilia. **(B)** Distribution of primary cilia ϕ_{cilium} angles in the resting, proliferating and hypertrophic zones of the middle and lateral regions of the growth plate. Dashed lines represent median (longer dashes) and first and third quartiles (shorter dashes). p* = 0.022 (resting middle vs hypertrophic middle), p* = 0.016 (proliferating lateral vs hypertrophic lateral), p*** = 0.00082 (proliferating middle vs hypertrophic middle), p*** = 0.00082 (proliferating middle vs proliferating lateral) (Kolmogorov–Smirnov test adjusted for multiple comparisons). n = 18 mice (466 to 1922 cilia per zone/region) **(C)** Distribution and **(D)** rose plots and circular scatter plot of ϕ_{cilium} angles across the whole growth plate. n = 18 mice (5802 cilia). **(E)** Distribution of primary cilia θ_{cilium} angles in the resting, proliferating and hypertrophic zones of the middle and lateral regions of the growth plate. Dashed lines represent median (longer dashes) and first and third quartiles (shorter dashes). p* = 0.047 (resting middle vs proliferating middle), p* = 0.047 (resting middle vs hypertrophic middle) (Kolmogorov–Smirnov test adjusted for multiple comparisons). n = 18 mice (466 to 1922 cilia per zone/region). **(F)** Distribution and **(G)** rose plots and circular scatter plot of θ_{cilium} angles across the whole growth plate. n = 18 mice (5802 cilia). **(H)** Circular scatter plot of ϕ_{cilium} and θ_{cilium} angles across the whole growth plate. n = 18 mice (5802 cilia).

hypertrophic zone (median = 2.9 µm) compared with the resting zone (median = 2.3 µm). In the lateral region, the hypertrophic chondrocyte cilia were also longer than the resting and proliferating cilia, though not statistically significant.

3.3.6 Primary cilia orientation in the growth plate

To measure 3D orientation of primary cilia, the spherical coordinates ϕ_{cilium} and θ_{cilium} were measured across the different zones and regions of the growth plate. The two angles represent the direction the axoneme of the cilium is pointing in (Fig. 3.9 A). The ϕ_{cilium} distribution was between 40° and 140° for all zones and regions of the growth plate, exhibiting a symmetric pattern centred around 0° (horizontal orientation) (Fig. 3.9 B). All areas had fewer cilia with ϕ_{cilium} around 90° except the resting zone of the middle region. The other distributions had modes around 70° and 100°. This distribution suggests an inclination of primary cilia that is horizontal, but not perfectly horizontal ($\phi_{\text{cilium}} = 90°$). The proliferating zone cilia consistently had a different distribution of orientations compared with the hypertrophic zone in both regions. The proliferating cilia distributions were different between the two regions. Figure 3.9 D and G represents the same data as Figure 3.9 C and F in rose plots, which provides a visual perspective of all the angles across the whole growth plate.

The θ_{cilium} angles were clustered around ~30°, ~180° and ~350° (Fig. 3.9 E). Visually, this corresponds to the cilia pointing forwards and back or anatomically dorsal and ventral (Fig. 3.9 F, G). The only difference in distribution was observed in the resting zone of the middle region compared all the other regions and zones, where there were fewer cilia clustered around ~350°.

This analysis shows that primary cilia are non-randomly oriented in both elevation and planar direction, across thousands of cilia from multiple regions across 18 mice (Fig. 3.9 H). There are few statistically significant differences between the zones and regions of the growth plate, with the exception of the resting zone of the middle region which presents slight difference in terms of ϕ_{cilium} and θ_{cilium} distribution. Figure 3.12 A gives a visual perspective of what this spherical coordinate distribution looks like in 3D, with cilia pointing primarily horizontally slightly up and down, and to the front and back.

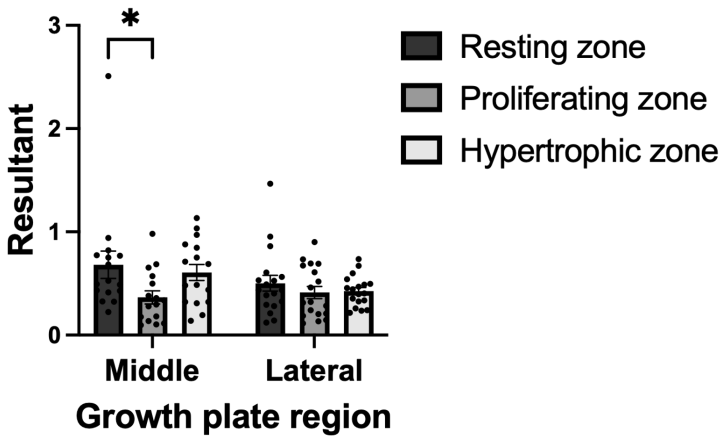


Figure 3.10: Average resultant per cilium in the resting, proliferating and hypertrophic zones of the middle and lateral regions of the 6 week-old *Ift88*$^{fl/fl}$ growth plate. Mean ± SEM. p* = 0.019. All other comparisons are not statistically significant (two-way ANOVA) n = 18 mice (466 to 1922 cilia per zone/region).

The resultant is a quantitative measure of how uniformly aligned a set of vectors, in this case cilia, are. A higher resultant value indicates greater alignment across the population, while lower values suggest a more dispersed or random orientation (Equation 2.1, 2.2). The resultant for primary cilia in the growth plate was measured to determine whether certain zones or spatial regions exhibit more consistent ciliary orientation, which could imply region-specific coordination. The highest resultant values were in the resting and hypertrophic zones of the middle region (Fig. 3.10). However, the overall differences in resultant magnitude between zones and regions were modest, indicating that primary cilia are similarly aligned across the growth plate, with no sharply defined domains of greater coherence.

3.3.7 Centriole position in the growth plate

Given that primary cilia orientation was found to be non-random, the subcellular positioning of centrioles was examined. As centrioles anchor the base of the cilium, they dictate the site from which the axoneme projects. In addition, centrioles play a key role in establishing the polarity of cell division, suggesting that their positioning during ciliogenesis may also be subject to spatial bias.

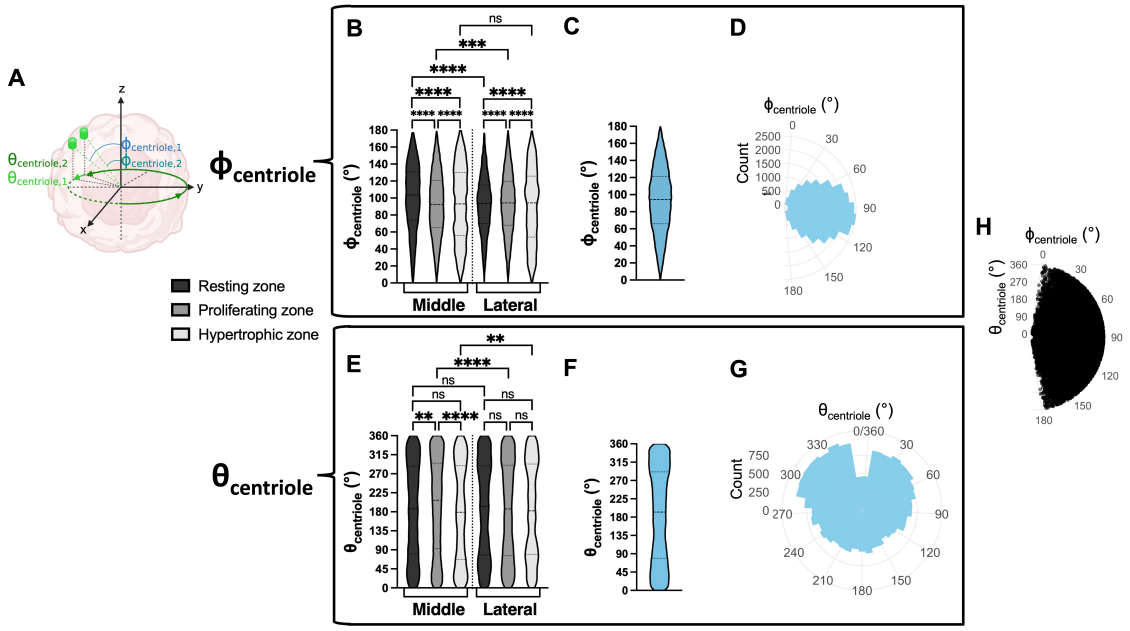


Figure 3.11: Disperse centriole position in the 6-week old *Ift88*$^{fl/fl}$ growth plate. **(A)** Spherical coordinates of centrioles. **(B)** Distribution of centriole $\phi_{centriole}$ angles in the resting, proliferating and hypertrophic zones of the middle and growth plate. Dashed lines represent median (longer dashes) and first and third quartiles (shorter dashes). p*** = 0.00024, p**** < 0.0001 (Kolmogorov–Smirnov test adjusted for multiple comparisons). n = 18 mice (1885 to 8204 centrioles per zone/region). **(C)** Distribution and **(D)** rose plot of $\phi_{centriole}$ angles across the whole growth plate. n = 18 mice (25,740 centrioles). **(E)** Distribution of centriole $\theta_{centriole}$ angles in the resting, proliferating and hypertrophic zones of the middle and growth plate. Dashed lines represent median (longer dashes) and first and third quartiles (shorter dashes). p** = 0.0016 (resting middle vs proliferating middle), p** = 0.0023 (hypertrophic middle vs hypertrophic lateral), p**** < 0.0001. (Kolmogorov–Smirnov test adjusted for multiple comparisons). n = 18 mice (1885 to 8204 centrioles per zone/region). **(F)** Distribution and **(G)** rose plot of $\theta_{centriole}$ angles across the whole growth plate. n = 18 mice (25,740 centrioles). **(H)** Circular scatter plot of $\phi_{centriole}$ and $\theta_{centriole}$ angles across the whole growth plate. n = 18 mice (25,740 centrioles).

For the centrioles, the two spherical coordinates $\phi_{centriole}$ and $\theta_{centriole}$ represent the position of the centre of each centriole relative to the centre of the cell (Fig. 3.11 A). $\phi_{centriole}$ in the resting and proliferating zones show broad distributions centred between 40° and 120°, suggesting centrioles are positioned mainly away from the proximal-distal positions (Fig. 3.11 B, C, D). The resting zone of the middle region had a higher median than the two other zones. Hypertrophic centrioles present a more spread out distribution across all angle values. Many of the distributions are statistically different from each other, however the positions of centrioles they span are generally similar.

The $\theta_{\text{centriole}}$ distribution is broad across all angles between 0 and 360° (Fig. 3.11 E, F, G). There are slightly more centrioles at two modes around 50 and 300°. The median in the proliferating zone of the middle region is also higher than others. Though differences in distributions were statistically significant between certain zones and regions, the positioning of centrioles remained similar across the whole angle spectrum.

As with the primary cilia, Figures 3.11 C, D, F and G show the same data of all centrioles across the growth plate. Figures 3.11 D, G and H are rose and circular plot visuals demonstrating the general distribution of centriole positions across all spherical coordinates. On the cell surface, this translates as the centrioles being positioned at any point around the cell (Fig. 3.12 B). Appreciating that not all cells are ciliated, I considered whether there was a difference in the position of centrioles between cells that formed a cilium and those that did not. The position of the centrioles of ciliated cells and non-ciliated cells did not show differences (Appendix Fig. 2).

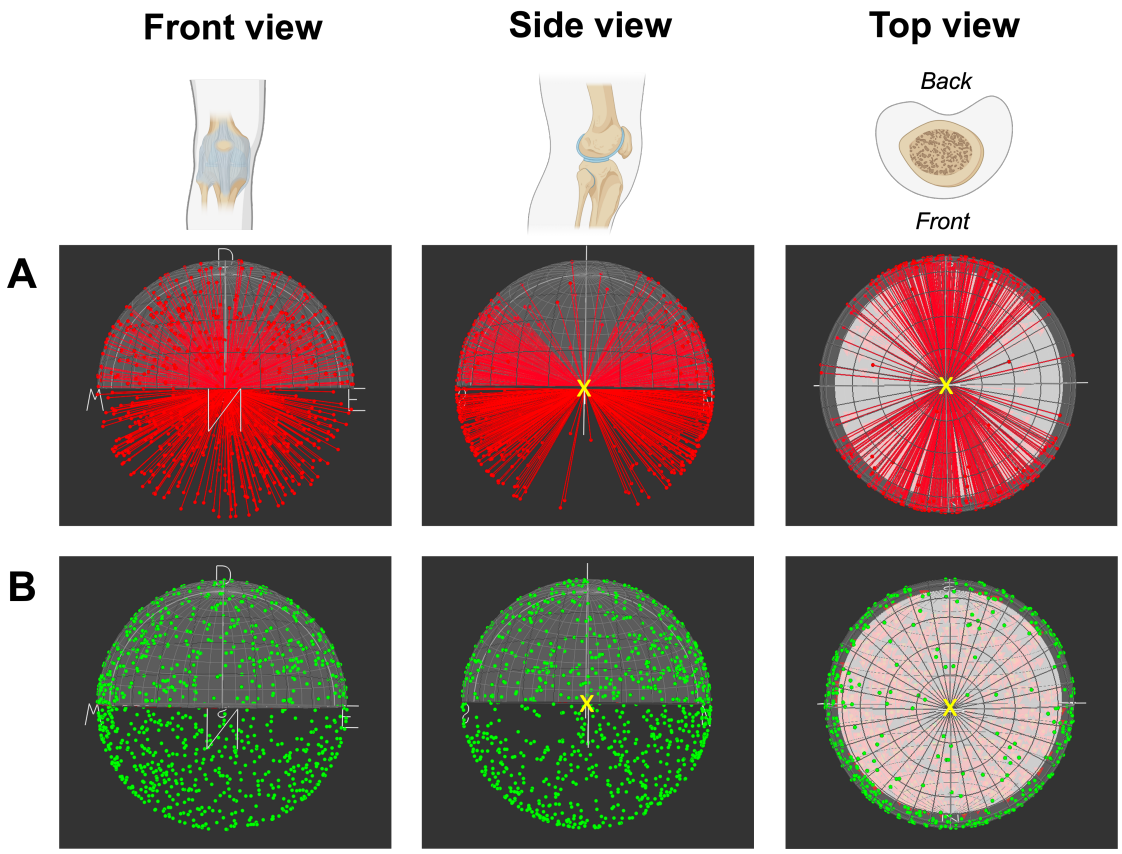


Figure 3.12: (A) Primary cilia and (B) centriole organisation in the resting zone of a 6-week old *Ift88*$^{fl/fl}$ growth plate. For primary cilia, the yellow cross denotes where the cell would be with cilia pointing out. For centrioles, the yellow cross denotes the centre of the cell with centriole position relative to this centre. The geological software Stereonet was used for visualisation.

3.4 Discussion

In this chapter, I applied the high-resolution 3D imaging and analysis methodology developed in Chapter 2 to characterise primary cilia architecture in the growth plate of 6-week-old control mice. This developmental time point represents a stage of active but postnatal endochondral ossification, where growth plate organisation is well established and chondrocytes are arranged into distinct functional zones. By leveraging endogenous fluorescent markers and automated image processing, I quantitatively mapped the organisation of the growth plate and extracted detailed information on primary cilia characteristics, including axoneme orientation, basal body positioning, ciliation prevalence, and axonemal length, across thousands of cells from 18 animals.

This analysis establishes a robust baseline for understanding how primary cilia are organised in healthy tissue, which is essential before evaluating the impact of genetic or mechanical perturbations. In doing so, I provide a comprehensive mapping of primary cilia organisation that can serve as a reference for comparison in later chapters. The next Chapter will assess how disruptions, such as conditional deletion of *Ift88* or altered mechanical loading, affect growth plate structure and whether these changes are associated with alterations in primary cilia prevalence or orientation. By beginning with the unperturbed system, I aim to disentangle the contributions of ciliary organisation to growth plate dynamics and provide a foundation for understanding their role in skeletal development.

3.4.1 Cell volume in the growth plate

Due to the data heavy nature of the images, the medial region was not imaged for this study, and the lateral region considered representative of peripheral regions of the growth plate. To quantify key features of the highly structured growth plate, cell

volume and orientation were measured. The volume of chondrocytes increased from the resting and proliferating zone to the hypertrophic zone (Fig. 3.6 B). Volume of growth plate cells from a P5 mouse measured by diffraction phase microscopy were 600 μm^3 for resting and proliferating chondrocytes and between 2000 and 14,000 μm^3 for hypertrophic chondrocytes [215]. The measurement of resting and proliferating cell volumes made here are in line with this. However, the volume of hypertrophic cells was likely underestimated due to the GFP signal not filling the whole cell, therefore the true volume expansion is probably higher.

3.4.2 Cell orientation in the growth plate

The growth plate has a very defined chondrocyte organisation. This is often described qualitatively. With my imaging methodology, I was able to quantify some of these organisational features of the growth plate, in particular to understand whether there are any differences between zones and regions.

There is a difference between the orientation of the resting zone cells in the middle and lateral region - middle cells are more randomly orientated than lateral cells (Fig. 3.6 E). There may be several explanations for this. Modelling has shown that the peripheral regions of the growth plate experience higher mechanical stresses compared with the middle [238, 239]. Therefore, perhaps differential mechanical stress influences the alignment of cells. However the proliferating and hypertrophic zones are not organised differentially between the middle and lateral regions. Another explanation maybe that the growth plate is slightly domed in the lateral region. This curvature could alter the local orientation cues for chondrocytes, including ECM micro-environment and collagen fibre organisation, especially at the top-most resting zone. The lateral region may be subject to edge effects not present in the centre. This difference in the resting zone of the middle region is also found in the percentage ciliation values, where it is lower compared with the lateral region (Fig. 3.7 A).

The proliferating cells are expected to be in the same orientation, aligned horizontally into vertical stacks. The orientation of proliferating cells measured provides validation for the accuracy of the method in measuring cell orientation. Proliferating cells have been previously quantitively described as being the most organised in the growth plate, with the major axis of the cell paralleling the medial-lateral plane [210, 216, 241]. Hypertrophic cells lose the flattened structure and aligned orientation, as they expand in volume and prepare for transdifferentiation or apoptosis.

The cellular column organisation in the growth plate is achieved through a coordinated mechanism of cell division and rotation. Following division in a plane parallel to the longitudinal axis of bone growth, newly produced daughter cells pivot around each other, stacking to form a column along the tissue's elongation axis. Cell adhesion molecules like N-cadherin contribute to the stable stacking and linkage of these cells after division. The planar cell polarity pathway is essential for this coordinated behaviour [20]. ECM stiffness, mechanical cues and compressive forces are all implicated in promoting the alignment of columns along the longitudinal bone axis, thus reinforcing bone growth [48, 242, 243].

Notably, recent studies reveal variation during development. In embryos, column formation via full rotation of the division plane is less frequent, resulting in more clusters or irregular stacks, whereas in post-natal growth plates, complex columns - both ordered and somewhat disordered - are predominant [11]. This suggests the process is dynamic and regulated differently over time and across anatomical locations.

3.4.3 Percentage ciliation in the growth plate

Quantifying cilia prevalence offers valuable information about the physiological relevance of primary cilia in a given tissue and reflects the cell cycle state of the cells. The ciliation percentages measured here are in the same range as previous reports though measured at different ages and with slight differences in ratios of

zones (Fig. 3.7) [47, 111, 244]. The method used here provides a more accurate counting method based on detection of cilia axoneme compared with manual counting or immunohistochemistry (IHC) staining detection, and its high throughput allows for more regional detail.

The differences in mechanical strains and micro-environments between the middle and lateral region highlighted above may explain the higher ciliation in the lateral region. The higher mechanical stresses experienced by the lateral region may justify its requirements for more cilia to integrate mechanical signals [238]. Modelling indicates that at the edges of the growth plate, chondrocytes are subject to higher transverse and shear strains [239]. These strains can trigger adaptive cellular responses, potentially upregulating ciliation as part of the tissue's mechanosensory response. Experiments in Chapter 4 will test whether differential mechanical load triggers such changes in ciliation in the growth plate

It could be expected that the proliferating region have the lowest ciliation, as cilia form when cells exit the cell cycle. However, in tissue sections the cell division event in the proliferation zone where cells are side by side before rotating into columns is very rarely captured. It probably occurs very fast, and the cell state observed in sections is that of cells between cell divisions, thus able to ciliate.

3.4.4 Primary cilia length in the growth plate

Due to the high resolution imaging I performed, I was able to measure primary cilia length in 3D. Primary cilia length is often associated with activity, therefore by measuring in the different zones and regions of the growth plate, I could gain insight into this relationship in this tissue.

The primary cilia lengths measured here are consistent with the range measured in previous studies (Fig. 3.8) [210, 231, 232, 245]. The hypertrophic cells have the largest volume in the growth plate and also have the longest cilia. This is in contrast with

the shortest cilia measured in the hypertrophic zone of the humerus elbow in embryos [244]. This detection was based on acetylated α-tubulin, whereas here ARL13B signal is detected. As ARL13B is localised to the ciliary membrane, it can indicate the full length of the ciliary projection, including any membrane extensions beyond the axonemal core. Acetylated α-tubulin marks the microtubule-based structural core within the cilium, which may not reach the absolute tip of the ciliary membrane in every instance. Cilia length measurements based on acetylated α-tubulin have been shown to be different to measurements based on ARL13B [225, 246, 247]. Acetylated α-tubulin can also label non-ciliary microtubules, potentially leading to false positives, whereas ARL13B is more specific for primary cilia [248]. In addition, the function of primary cilia may differ between embryonic and postnatal stages, reflecting the distinct tissue architecture and extracellular matrix cues present at each stage.

The stiffness of surrounding substrate or ECM has been shown to regulate cilia length. Mouse articular chondrocyte cultured on softer substrate (5 kPa) had shorter cilia than stiffer substrates (50 kPa) [232]. Primary cilia may activate different signalling pathways in different stiffness. The differences in percentage ciliation and cilia length between the zones may be explained by differences in mechanical strain experienced in the different zones of the growth plate. Chondrocytes in different zones of the growth plate experience varying compressive strains, with hypertrophic chondrocytes showing higher strain and compression [239, 242, 249].

The length of the cilia was measured from one end to the other. Some cilia are bent, therefore length may have been underestimated. A limitation of this method is that it does not currently measure the amount of bending in cilia which are sometimes curved [225].

Cilia length is thought to influence function in various ways. Chondrogenic differentiation in pre-chondrocyte cells and osteogenic differentiation of MSCs and pre-osteoblast cells is associated with elongation of primary cilia [250]. Osteocytes with longer cilia were more mechanosensitive as measured by increased expression of

osteogenic markers [251]. Longer cilia may be subjected to greater membrane tension, potentially activating stretch-sensitive ion channels within the ciliary membrane or generating increased bending forces at the base, thereby initiating mechanotransduction signalling. An increased ciliary length may also expand the surface available for receptor localisation, potentially amplifying the cell's responsiveness to extracellular signals. The receptor and signalling composition within primary cilia is dynamic, enabling context-dependent adaptation to external cues through regulated cycles of assembly and disassembly that vary across cell types and tissues [252].

3.4.5 Primary cilia orientation in the growth plate

Given the highly organised cellular architecture of the growth plate, I investigated whether primary cilia also exhibit a defined spatial orientation, and whether this orientation is related to underlying tissue structure. Previous assumptions about cilia orientation in the growth plate have largely been based on limited or two-dimensional datasets, often without quantitative analysis at scale. In this chapter, I aim to address this gap by providing a more detailed and comprehensive characterisation of primary cilia orientation within the native three-dimensional context of the growth plate.

Primary cilia in the growth plate are not randomly orientated. They primarily have an orientation that is horizontally up and down up to 45°, and forwards and back (Fig. 3.9, 3.12 A). This varies minimally between zones and regions of the growth plate. From cell to cell, however, axonemal orientation is highly variable within a zone or region. It is not possible to predict the exact orientation a neighbouring and daughter cell will adopt, only a range of possible orientations. This range of possible orientations is exemplified by the low resultant values. There is therefore a defined orientation with both random and non-random components.

Alignment of cilia in particular orientations may serve for coordinated sensory input and integration. In addition, this raises the question whether the orientation of the

ciliary axoneme is significant only for signal transduction within an individual cell or does orientation play a role in intercellular signalling via the ECM in order to provide an integrated response from the tissue to extracellular cues.

Previous studies have described primary cilia organisation in the growth plate, however these suffer from several limitations. Andrea et al. (2010) used IHC staining for acetylated α-tubulin to image primary cilia in the growth plate [209]. They suggest that primary cilia are organised randomly in the resting zone and become polarised in the proliferating and hypertrophic zones, aligning with the chondrocyte columns. These results are only qualitative and not quantitative. In addition, it is stated in the methods that "only cilia that appeared on at least three consecutive images and approximately 90° to the incident light were analysed". This removes from the analysis all the cilia which are not perpendicular to the incident light and could appear as dots in the 2D image, but are actually cilia pointing in the z-direction. There is therefore selection bias in the data. This study also found the shortest cilia lengths in the proliferating zone and the highest percentage ciliation in the resting zone. By choosing only select cilia for analysis and measuring them in 2D, the primary cilia lengths are also likely not representative of true length.

Another group developed an algorithm for analysing primary cilia 3D orientation in growth plate chondrocytes, applied to images of IHC staining of acetylated α-tubulin [210, 216]. This study took into account the 3D nature of ciliary orientation and described spherical coordinates ϕ and θ. They compared wild-type and $Smad1/5^{cKO}$ cell and ciliary organisation in E16.5 growth plates. They observed that the ϕ angle of the cilium with respect to the major axis of the cell clustered around 10 and 80° in the wild-type. The θ angle was randomly distributed. They observed a loss of the 10° cluster in $Smad1/5^{cKO}$, a misorientation which they suggest disrupted chondrocyte positioning following cell division in the proliferating zone. This could explain the $Smad1/5^{cKO}$ growth plate phenotype, which is characterised by loss of columnar organisation of chondrocytes.

This analysis was only applied to the proliferation zone of the growth plate and up to 149 cells were analysed, compared to the thousands of cells analysed here. The method also required manual data collection from images, including cell outlining and cilium length measurement, prior to input into the algorithm to calculate angles. With time, this type of semi-automatic mathematical algorithm has been replaced by imaging analysis software. In this project, arivis Vision4D is able to perform the cell, cilia and centriole detection automatically.

In another study, the cilia orientation in different zones of the humerus of E14.5 mice was studied, again based on IHC staining of acetylated α-tubulin [244]. The detection was more automatic - based on volumetric detection of staining. However, only one 2D angle was measured to define orientation. In the elbow resting zone, the cilia were pointing away and towards the joint. In the proliferation zone, cilia were pointing in all directions. The method used in this study also require manual following of individual axonemes through z-stacks, which is labour intensive and thus limits n numbers.

The tissue that most resembles growth plate cartilage is articular cartilage, with a zonal organisation of chondrocytes and deep zone chondrocytes arranged in columns. In articular cartilage, the orientation of the ciliary axoneme changes in superficial zone and deep zone chondrocytes. In load-bearing regions, the axonemes of superficial chondrocytes point away from the articular surface, whereas deep zone cells point their cilia towards and away the articular surface [81, 141]. This defined orientation is lost in non-load-bearing tissue. The polarisation of cilia observed only in load-bearing articular cartilage related links cilia organisation to the direction of biophysical stimuli, as is seen in tendons [139]. This orientation may shield cilia from the high compressive and tensile forces. The absence of cilia in line with the bone longitudinal axis ($\phi_{\text{cilium}} = 0°$ or $180°$) observed in this project may also be a mechanism to shield them from the high mechanical forces experienced on the limb. There may also be physical constraints that prevent cilia from orienting directly upwards or downwards, due to the close proximity of neighbouring cells above and below, particularly within the organised columns of the growth plate.

As described in the introduction, chondrocyte primary cilia are embedded in a ciliary pocket. The extent of invagination of the primary cilium in this ciliary pocket is varied. With this imaging methodology, the ciliary pocket is not visible. It can be visualised with electron microscopy or with assays which differentiate between intracellular and extracellular cilia [59, 253]. The ciliary pocket is a dynamic structure that controls the micro-environment around the base of the cilium. It is important for vesicular trafficking, sensory function and controlling exposure to signalling factors, in addition to providing a stable actin-cilium interface for the basal body and axonemal positioning [59, 61, 254]. At present, it remains unclear how the extent of pocket enclosure changes over time within an individual cell or across a cell population, or why some cells exhibit a pocket while neighbouring cells do not. Research is needed into whether the pocket's depth or configuration changes dynamically to regulate the sensitivity and orientation of the cilium. By partially or wholly surrounding the axoneme, the pocket can spatially regulate exposure of the axoneme to signalling factors, which may affect orientation decisions during development or cellular responses. The ciliary pocket may provide a micro-environment that physically stabilises the axoneme or its basal body, influencing both the initial site of axoneme emergence and the axis of its growth. In addition, the ciliary pocket is implicated in basal body positioning, which may indirectly affect the spatial orientation of the axoneme.

In the images presented here, primary cilia axonemes sometimes appear bent or curved. Bending of the axoneme in these cells occurs passively, as it is displaced along with the ECM during compressive movement [57]. The level of bending is however limited compared with the freedom of movement observed in epithelial-based primary cilia in tubular organs with a fluid environment [255]. Compressive loading of cartilage initiates a complex cascade of mechanotransduction events essential for skeletal patterning and growth. This includes deformation of chondrocytes, generation of hydrostatic pressure gradients, interstitial fluid flow, and distortion of the charged extracellular matrix, contributing to local shifts in osmolarity and pH [256]. These mechanical and biochemical changes can modulate cell metabolism by triggering

intracellular responses such as nuclear deformation, cytoskeletal reorganisation, and altered levels of signalling molecules like nitric oxide and calcium ions (Ca^{2+}) [257–259]. Notably, compression-induced elevations in intracellular Ca^{2+} may depend on bending of the primary cilium's axoneme, suggesting that structural deformation of the cilium may be a key requirement for its function as a mechanosensor [96, 98].

It also has been suggested the ciliary tip may have a pressure sensing mechanism to receive signals from the external environment, which are then transmitted along the axoneme to the cell body to initiate signal transduction pathways [260]. This would be particularly the case if primary cilia do not bend easily dynamically and adopt a permanent orientation due to confinement by the ECM.

In scratch wound experiments, most vascular smooth muscle cells' cilia reoriented toward the wound edge - a response that was largely prevented by blocking β1-integrin [137]. In addition to implicating primary cilia in cell migration and wound healing, these findings suggest that post-wounding ciliary repositioning is at least partly driven by interactions between ciliary integrins and the ECM.

Since the chondrocyte axoneme has been shown to form direct attachments with the extracellular matrix, its 3D orientation is likely to be relatively fixed, though still subject to variation due to mechanical loading [57, 87, 102]. There is, however, some evidence that ciliation may be dynamic - not in terms of the site of emergence once established, but in its ability to rapidly alter orientation in response to external cues. After a growth plate fracture, the proportion of ciliated chondrocytes increased in the resting and proliferating zones of the growth plate during repair. Ciliation rose shortly after injury and returned to baseline as healing concludes [111]. In the brain, primary cilia are shown to dynamically oscillate in length and orientation within a 24-hour period [138].

The position from which the primary cilium emerges from the cell can also be interesting to study. With this method the position of the base of the cilium is not directly measured, however can be inferred from centriole position. The site at

which the cilium emerges may be linked to the plane of cell division or the direction of cellular migration. In the humerus of E14.5 mice, cilia of resting chondrocytes preferentially position their cilia in the region of the cell that is away from the joint line. In the proliferating and hypertrophic zones, cilia emerge mainly from the medial region of the cell [244]. Another group described the axonemes as projecting from a position near the cell's centre and that this position was independent of its axonemal orientation [140]. Axonemes in superficial zone cells of load bearing regions of articular cartilage emerge from the side of the cell facing the subchondral bone, away from the articular surface. In deep zone cells, axonemes emerge from the cell in equal proportions facing toward or away from the articular surface. In non-load bearing regions, this positioning is lost [141].

In actively dividing chondrocytes of the proliferating zone, the position of the axoneme may be determined shortly after cell division, potentially constrained by the plane of division and the internal organisation of the cell. This suggests that in proliferating cells of the growth plate, the positioning of the axoneme would be inherited through successive divisions. In contrast, in hypertrophic chondrocytes, which divide less, the axoneme's position would remain fixed following their final division.

The imaging methodology presented here could be used to study changes in ciliation and cilia organisation in the growth plate with age, answering questions relating growth plate activity to cilia organisation. Ciliation has been shown to change with age, therefore it would be interesting to know whether cilia length and orientation changes as well [111]. The mechanical properties of the growth plate change with age, which is likely to contribute to changes in ciliation.

3.4.6 Centriole position in the growth plate

In the same way that primary cilia axoneme orientation may be important to function, the position of the base of the axoneme may also be crucial. As such, I mapped

the positioning of centrioles, which make up the basal body of the cilium, across the cell, using spherical coordinates of the centre of the centrioles.

In this study, centrioles do not have a preferred position in the cell, compared with the oriented cilia axonemes. The differences between the growth plate zones were small. The centrioles determine the position from the cilia emerge, therefore suggesting that primary cilia can emerge from any point in the chondrocytes in the growth plate.

Centriole position is determined by cell shape and confluence, translated through extracellular geometric cues and intracellular cytoskeletal motors [261]. They are sometimes found at the centre of the cell, which is especially characteristic of non-motile and non-polarised cultured cells. In polarised adherent cells, the nucleus-centrosome axis forms a polarised internal organisation aligned to the directional cues provided by the adhesive micro-environment. The centrosomes and Golgi apparatus position close to the cell centroid, while the nucleus shifts towards non-adhesive edges, to direct the polarisation [262]. Centrioles shift to the edge of the cell in different contexts, for example to polarise, to organise microtubules for cell division and to form primary cilia [261]. The primary cilium and centrioles are intimately connected to the Golgi apparatus which contributes to positioning of the cilium with reference to the cell [60].

Chondrocytes in the proliferating zone initially divide parallel to the bone's growth direction and then undergo a 90° rotation, resulting in a final division plane perpendicular to growth, which is essential for proper columnar organisation. Centrioles determine the plane of cell division by organising the mitotic spindle and orienting it relative to the cell cortex, thereby guiding where the cleavage furrow forms during cytokinesis [237]. This process is fundamental for symmetric division and tissue architecture, especially in structured tissues like the growth plate. Since a polarised positioning of centrioles is not observed in the growth plate, it can be suggested that though centriole positioning is important for cell division orientation, post-mitosis

position is not crucial. Following division and rotation, chondrocytes may then place their centrioles randomly around the cell.

When chondrocytes were cultured on glass coverslips, the centrioles positioned toward the basal membrane (the side of the substrate surface) compared with being more evenly distributed on the surfaces of the cells when cultured on gels [232]. This points to a link between centriolar position and ECM stiffness. As no difference was observed in centriole position between zones of the growth plate, mechanical impact of the surrounding ECM on this position may not be significant *in situ*. The potential impact of load on the limb will be tested in Chapter 4.

It is important to note that the resting zone of the middle region of the growth plate was consistently the group that displayed the most marked differences across multiple parameters, including cell orientation, ciliation percentage, cilia length and orientation, centriole positioning, and the magnitude of the resultant vector. This repeated divergence suggests that the resting zone, particularly in the centre of the growth plate, may possess a distinct micro-environment compared to its peripheral counterparts. These differences could reflect variations in local mechanical load, ECM composition, nutrient or oxygen gradients, or signalling activity. As the resting zone contains slowly dividing, stem-like chondrocytes that give rise to proliferative columns, even subtle changes in their organisation or ciliary function could have disproportionate effects on downstream growth plate behaviour. Therefore, the contrast between the middle and peripheral regions in this zone may represent a critical spatial boundary within the tissue, where environmental cues are most sharply delineated and primary cilia-mediated sensing plays a particularly important role in regulating growth plate dynamics.

In conclusion, whilst the concept, proposed from previously more limited imaging of cilia in the growth plate, that cilia orientate parallel to chondrocyte columns perhaps guiding their formation is attractive, it is not borne out in these data. However, with the results from this project suggesting a different orientation, a less

direct mechanism of cilia directing cellular movements needs to be deciphered. The robustness of this study is emphasised by the high mouse numbers, unseen in primary cilia orientation studies in the growth plate before. In motile cilia, 3D orientation is key to function, as evidenced by many ciliopathies presenting defects in ciliary organisation. Therefore the same could be true of primary cilia. The effects of ciliary disruption on cell and cilia organisation will be discussed in the next Chapter.

4

Ciliation in the Ift88 cKO and immobilised mouse post-natal growth plate

Contents

4.1 Introduction **92**

4.2 Materials & Methods **95**

4.2.1 Animals, tissue collection, imaging &analysis 95

4.2.2 Tamoxifen treatment 95

4.2.3 Double neurectomy 95

4.2.4 Ki67 staining 96

4.2.5 Statistical analysis 97

4.3 Results **98**

4.3.1 Growth plate phenotype of the *Ift88* cKO 98
4.3.2 Growth plate phenotype of the offloaded and contralateral *Ift88*$^{fl/fl}$ growth plates 108
4.4 Discussion 118
4.4.1 Effect of *Ift88* knockout on growth plate cell and primary cilia organisation 118
4.4.2 Effect of mechanical loading on growth plate cell and primary cilia organisation 128

4.1 Introduction

Having mapped the organisation of cell, primary cilia and centrioles in a naive 6-week old growth plate, I was next interested in how this may be disrupted with genetic manipulation of ciliary genes and modulation of mechanical loading experienced by the limb.

There is existing evidence that primary cilia experience structural changes in disease and genetic deletions. In articular cartilage, primary cilia length is increased in osteoarthritis. Loss of *Ift80* embryonically and postnatally in chondrocytes disrupted cilia formation [89]. Loss of ciliary genes in other cell types have also caused reduction in primary cilia percentage and length [88, 263, 264]. In these studies, the disruption of normal axonemal positioning appears to compromise ciliary function, highlighting an interdependent relationship in which spatial misalignment of the axoneme interferes with the cilium's ability to mediate key signalling and mechanosensory processes.

Ift88 null mutations are embryonically lethal due to failed hedgehog (Hh) signalling during embryonic patterning and organogenesis [132]. *Ift88* hypomorphic mice exhibit multiple skeletal patterning defects and reduced postnatal growth, pointing

to disruptions in the process of endochondral ossification [81]. This is associated with a reduction in cilia length and numbers.

Being interested in the growth plate cartilage, an aggrecan-Cre was used to conditionally delete *Ift88* in aggrecan expressing cells. Aggrecan being one of the most abundant proteoglycan in cartilage, this deletion particularly targeted chondrocytes. Deletion was performed at 4 weeks to study the effect of ciliary disruption on the growth plate during adolescence. This has been the subject of previous work in our group [47, 80].

Deletions of *Ift88* in the adolescent growth plate lead to an expanded growth plate and loss of organised columnar structure particularly in the peripheral regions [47]. The disruptions in the primary cilia structures themselves were not studied. They would provide an understanding in the mechanisms leading to the phenotype and shed light on the cilia's structure-function relationship.

In addition, primary cilia orientation play a key role in the mechanosensory function of cells. In the growth plate, mechanical unloading has been shown to reverse the abnormalities induced by *Ift88* disruption [47]. This highlights the tightly coupled relationship between primary cilia and mechanical load. Differences in primary cilia organisation between load-bearing and non-load-bearing regions were observed in articular cartilage, suggesting that cilia orientation is a critical factor in the cellular response to mechanical stimuli [141].

I therefore hypothesise that deletion of *Ift88* in the growth plate disrupts primary cilia prevalence and organisation, thereby altering cellular and tissue architecture. Given the known role of primary cilia in sensing mechanical cues, I further hypothesise that modifying the mechanical load experienced by the limb, through offloading, would also lead to a change in primary cilia and growth plate architectures, which would either mimic or diverge from the phenotype observed in the *Ift88* conditional knockout (cKO). By comparing the effects of genetic disruption and altered mechanical loading,

I aim to disentangle the relative contributions of cilia-dependent signalling and mechanical forces to the organisation of the growth plate. In this chapter, I characterise the skeletal phenotype, cellular arrangement and ciliary and centriole organisation in both *Ift88* mutant and mechanically offloaded limbs to test these hypotheses.

4.2 Materials & Methods

Unless stated otherwise, all chemicals used were from Sigma Aldrich.

4.2.1 Animals, tissue collection, imaging & analysis

Animal husbandry, mouse limb collection, confocal imaging and analysis was performed as per Chapter 2. MicroCT, histology and data analysis was performed as per Chapter 3.

4.2.2 Tamoxifen treatment

Tamoxifen was dissolved in 90% sunflower oil and 10% ethanol at a concentration of 20 mg/mL by sonication. 50 µL tamoxifen was administered via intraperitoneal injection to mice at 4 weeks of age on 3 consecutive days an tibia collected 2 weeks later at 6 weeks (Fig. 4.1 A).

4.2.3 Double neurectomy

The double neurectomy surgeries were performed by Dr Jadwiga Zarebska. Tamoxifen was administered in the 3 days before surgery (Fig. 4.1 B). One or two days before surgery, mice were transferred to cages containing soft bedding. Surgery was performed as previously described [47]. Briefly, animals were prepared anaesthetised, the right limb shaved and a longitudinal incision was made from the right knee joint up and inward toward the groin. The femoral nerve was transected using micro-dissecting scissors and a 0.5 cm section was removed. The wound was sutured. The mouse was turned onto its front and the right hindlimb was stretched out. An incision was made from the spine outward and 2 to 4 mm region of the sciatic nerve

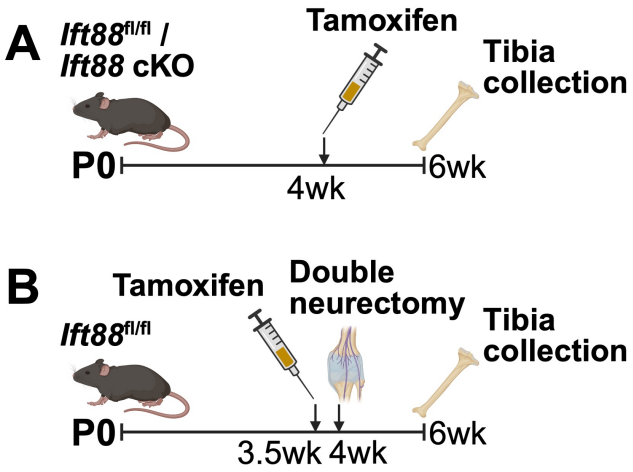


Figure 4.1: Age and timing of tamoxifen administration, surgeries and tibia collection for *Ift88* cKO experiment (A) and *Ift88*$^{fl/fl}$ offloading experiment (B).

was removed. This wound was also sutured. Mice were subsequently housed in soft bedding without environment-enhancing balconies or tubes to prevent aggravation of exposed skin. Animals were disturbed as little as possible. Sudocrem was applied to the skin of the foot if aggravated.

4.2.4 Ki67 staining

Fixed, unstained coronal knee sections were deparaffinised, rehydrated in graded alcohols, and washed with milliQ water. Antigen retrieval was performed by incubating in 0.01 M Na citrate buffer (pH 6.0) at 95°C for 20 minutes. Sections were washed once with PBS with 0.05% Triton X-100 (PBS-X) then blocked with blocking buffer made up of 5% goat serum in PBS-X for 1 hour at room temperature. Sections were subsequently incubated with Ki67 antibody (Abcam AB15580) in blocking buffer overnight at 4°C. An immunoglobulin G control was performed by replacing the Ki67 antibody with a mouse immunoglobulin G (ThermoFisher) antibody. A no primary antibody control was also performed. The next day, sections were washed in two changes of PBS-X for 5 minutes each, then incubated with goat anti-rabbit Alexa Fluor 555 secondary antibody in blocking buffer for 2 hours at room temperature in

the dark. Samples were washed twice with PBS-X for 5 minutes each and mounted with ProLong Gold Antifade Mountant with DAPI (Invitrogen) overnight at room temperature in the dark. Slide were stored at -20°C in the dark.

Sections were imaged with a Zeiss Axioscan 7 under fluorescent light with a 10x objective and the DAPI and Cy3 channels.

In order to measure the percentage of Ki-67 positive, the software QuPath was used. Cells were detected based on the DAPI signal using the 'Cell detection' function. Then, Ki-67 positive cells were detected using the 'Object Classifier' function. The percentage of Ki-67 positive cells was calculated from proportion of Ki-67 positive cells out of the total number of cells.

4.2.5 Statistical analysis

Unpaired student t tests were performed to compare the microCT measurements of growth plate lengths, percentages ciliation and percentages of Ki67-positive cells between mouse phenotypes. Kolmogorov-Smirnov tests adjusted for multiple comparisons were performed to compare distributions of cell volumes, θ_{cell}, ϕ_{cilium}, θ_{cilium}, $\phi_{\text{centriole}}$ and $\theta_{\text{centriole}}$. Two-way ANOVA tests were performed to compare the cell volume, percentages ciliation, primary cilia lengths and resultants in the different zones and regions of the growth plate between mouse phenotypes.

4.3 Results

The *Ift88*$^{fl/fl}$ data presented here is the same as measured in Chapter 3.

4.3.1 Growth plate phenotype of the *Ift88* cKO

In order to study the effect of ciliary disruption on endochondral ossification and ciliation in the growth plate, *Ift88* was conditionally deleted in aggrecan expressing cells using the *Ift88* cKO (*AggrecanCreER*^{T2}*;Ift88*$^{fl/fl}$*;Centrin-2-GFP.ARL13b-mCherry*) line. Tamoxifen was administered at 4 weeks and tibias collected at 6 weeks. The *Ift88*$^{fl/fl}$ line (*Ift88*$^{fl/fl}$*;Centrin 2-GFP.ARL13b-mCherry*) was used as control and also administered tamoxifen in order to control for its effects.

Ift88 cKO growth plate length

Growth plate lengths were measured using the same methodology as in Chapter 3, whereby nine measurements were made across the width of the growth plate (Fig. 3.2). *Ift88* cKO mice have shorter growth plates than *Ift88*$^{fl/fl}$ mice in males and females (Fig. 4.2). The peripheral regions of the *Ift88* cKO growth plate were narrowed compared with the *Ift88*$^{fl/fl}$ growth plate (Fig. 4.2 A, B).

Safranin-O staining showed that both *Ift88*$^{fl/fl}$ and *Ift88* cKO growth plates had chondrocytes arranged in columns (Fig. 4.3). The longer peripheral regions of the *Ift88*$^{fl/fl}$ growth plates are also visible with this staining.

As in Chapter 3, cilia analysis was performed on both male and female mice, with no difference observed between the sexes. Primary cilia were imaged in *Ift88*$^{fl/fl}$ and *Ift88* cKO growth plates in the lateral and medial regions (Fig. 4.3). Both growth plates were ciliated throughout the chondrocyte zones.

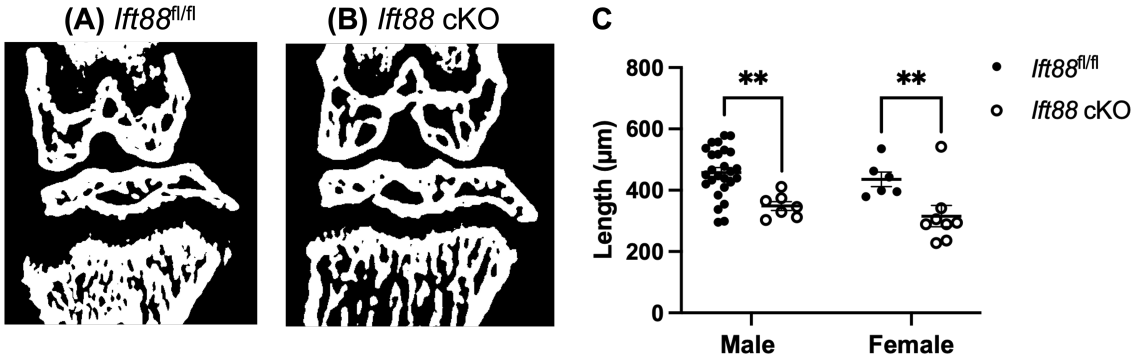


Figure 4.2: Changes in length measured from thresholded microCT images of *Ift88*$^{fl/fl}$ (A) and *Ift88* cKO (B) growth plates. (C) Thresholded growth plate lengths of *Ift88*$^{fl/fl}$ and *Ift88* cKO limbs. Mean ± SEM. p** = 0.0035 (male) p** = 0.0060 (female) (multiple unpaired t test corrected for multiplicity) n = 6-26 mice.

Cell volume and organisation in the *Ift88* cKO growth plate

As the growth plate were different lengths, I investigated whether this difference was also translated in a different in cell morphology and organisation. The ratio of the number of resting to proliferating to hypertrophic cells was the same between *Ift88*$^{fl/fl}$ and *Ift88* cKO - 1 to 3.1 to 1.5. The cell organisation of these growth plates were characterised in order to determine if the phenotype was associated with disrupted cell architecture.

For the cell volume distributions, both Kolmogorov–Smirnov (black asterisks) and two-way ANOVA (red asterisks) statistical tests were performed in order to compare differences betweens distributions and means, respectively (Fig. 4.4 A). The resting chondrocytes of the *Ift88* cKO growth plate had a similar mean to the *Ift88*$^{fl/fl}$ chondrocytes but a small, but statistically significant, difference in distribution. The proliferating chondrocytes of the *Ift88* cKO had a statistically significant difference in distribution and mean compared with the *Ift88*$^{fl/fl}$ proliferating chondrocytes. The greatest difference was observed in the hypertrophic chondrocytes in both distribution and mean. The median hypertrophic chondrocyte volume in the *Ift88* cKO was 741.5 µm^3 compared with 924.7 µm^3 in the *Ift88*$^{fl/fl}$ growth plate (Fig. 4.4 B). As discussed in the Chapter 3, in the hypertrophic cells, the volume detected is of shrunk cells compared with the true volume. This decrease volume may still be

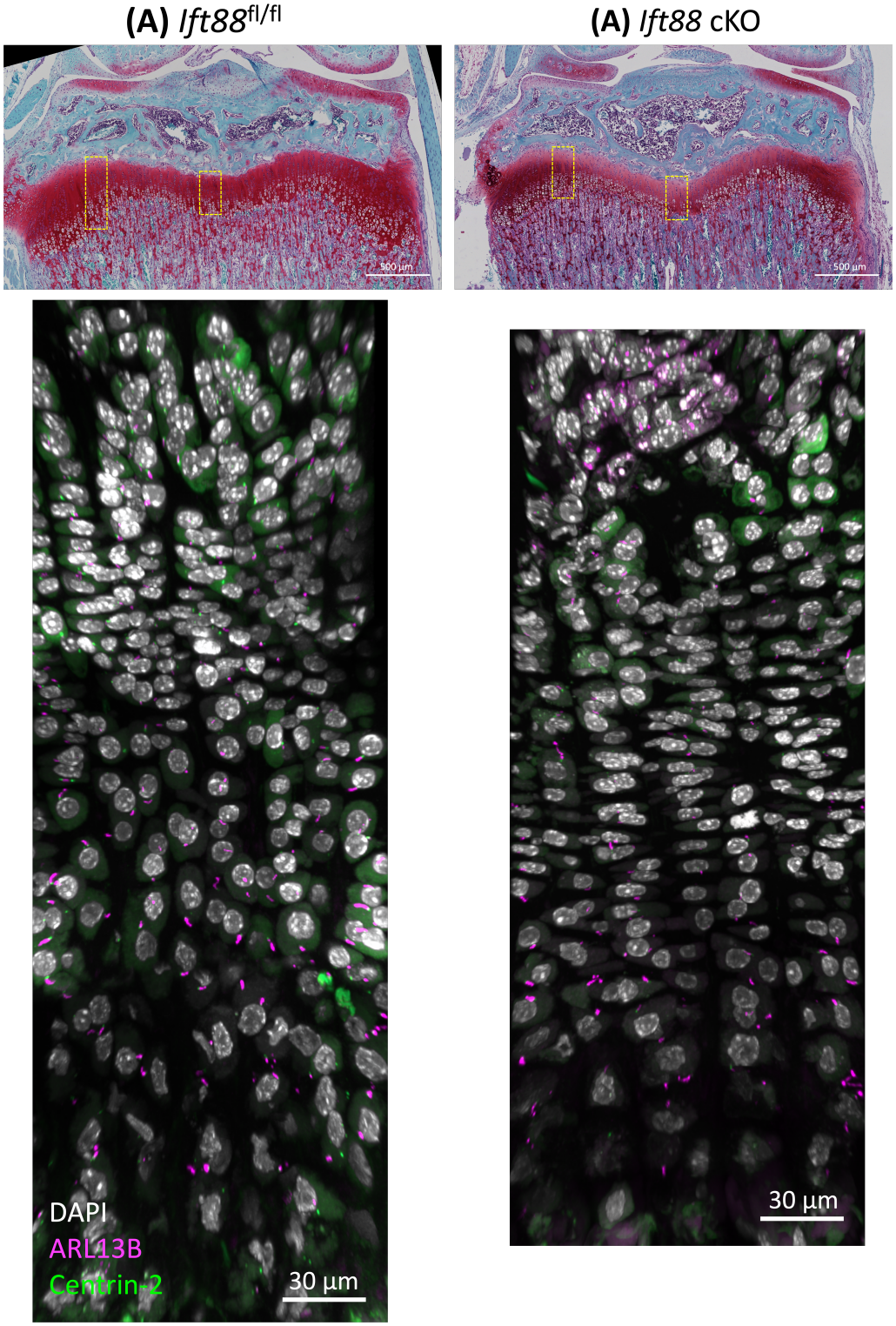
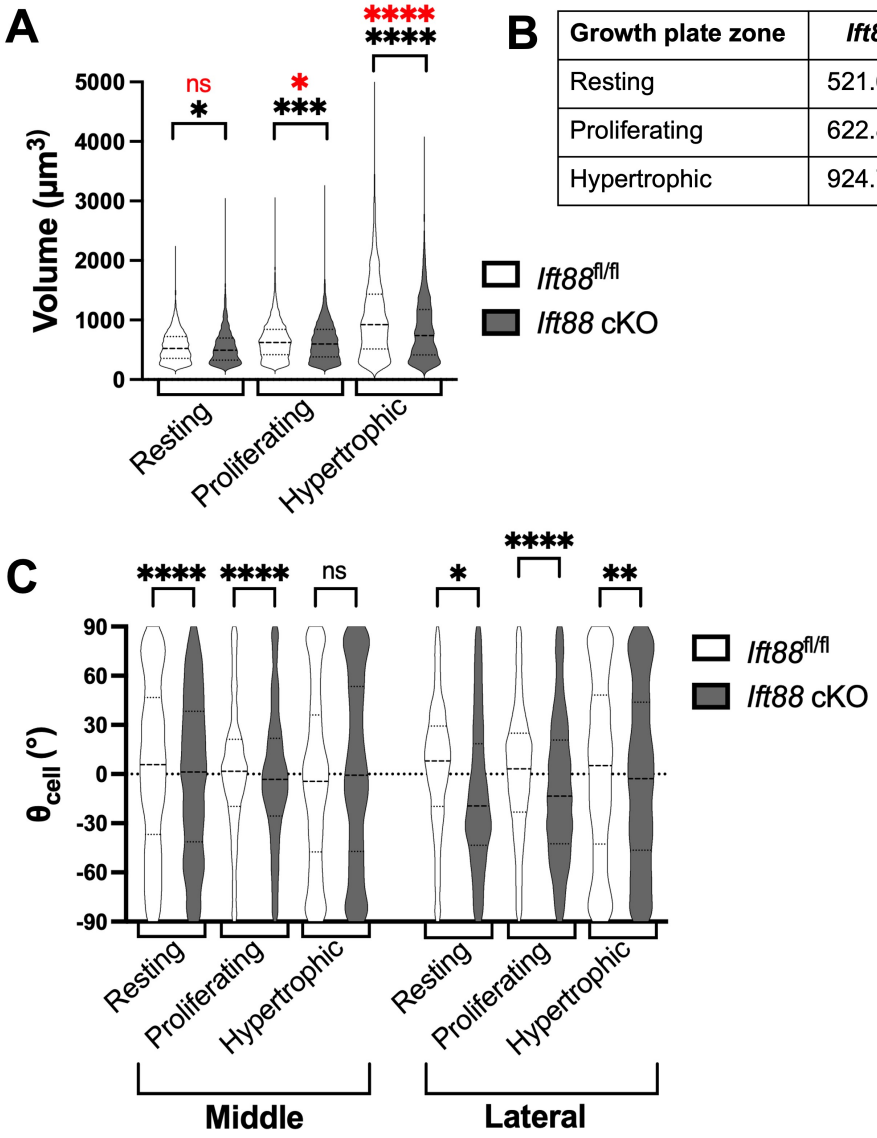


Figure 4.3: Safranin-O staining and primary cilia imaging of the *Ift88*$^{fl/fl}$ (A) and *Ift88* cKO (B) growth plates across ages. Primary cilia were imaged in the regions correspond to regions in yellow box on safranin-O stains.



Growth plate zone	*Ift88*$^{fl/fl}$	*Ift88* cKO
Resting	521.6 µm^3	492.6 µm^3
Proliferating	622.8 µm^3	598.0 µm^3
Hypertrophic	924.7 µm^3	741.5 µm^3

Figure 4.4: Differences in cell organisation between the *Ift88*$^{fl/fl}$ and *Ift88* cKO growth plates. **(A)** Cell volume in the resting, proliferating and hypertrophic zones of the *Ift88*$^{fl/fl}$ and *Ift88* cKO growth plates. Dashed lines represent median (longer dashes) and first and third quartiles (shorter dashes). Black asterisks - p* = 0.0161, p*** = 0.00013, p**** < 0.0001 (Kolmogorov–Smirnov test adjusted for multiple comparisons). Red asterisks - p* = 0.0487, p**** < 0.0001 (two-way ANOVA) n = 14-18 mice (585 to 3622 cells per zone/region). **(B)** Median cell volumes in the *Ift88*$^{fl/fl}$ and *Ift88* cKO growth plates. **(C)** Distribution of θ_{cell} in the resting, proliferating and hypertrophic zones of the middle and lateral regions of the *Ift88*$^{fl/fl}$ and *Ift88* cKO growth plates. Dashed lines represent median (longer dashes) and first and third quartiles (shorter dashes). p* = 0.042, p** = 0.0018, p**** < 0.0001. (Kolmogorov–Smirnov test adjusted for multiple comparisons). n = 14-18 mice (585 to 3622 cells per zone/region).

representative of decrease in volume in hypertrophic with cKO of *Ift88*, as the control line cell volume is measured in the same way.

Next, the cell orientation was measured via θ_{cell}. This is a measure of the inclination of the cell compared to the horizontal, medial/lateral axis (Fig. 3.6 C, D). When performing statistical tests on the distributions, sometimes the distributions were statistically different from each other but this does not change the physical orientation of the cell. For example, in the middle region, though the distributions of θ_{cell} for the resting chondrocytes between the *Ift88*$^{\text{fl/fl}}$ and *Ift88* cKO were statistically different from each other, these would translate into similar 3D random organisation of cells in all directions, as they both span all θ_{cell} angle values (Fig. 4.4 C). This also true for the proliferating chondrocytes which are generally centred around $\theta_{\text{cell}} = 0°$ in both *Ift88*$^{\text{fl/fl}}$ and *Ift88* cKO, which translates to a horizontal orientation. The distribution of θ_{cell} for the hypertrophic chondrocytes were similar between *Ift88*$^{\text{fl/fl}}$ and *Ift88* cKO. Conversely, statistical difference between distributions sometimes did highlight differences in cell organisation. In the lateral region, the resting chondrocytes had a statistically significant different in distribution, with a mode that was around $\theta_{\text{cell}} = -30°$ in the *Ift88* cKO compared with a mode around $\theta_{\text{cell}} = 10°$ for *Ift88*$^{\text{fl/fl}}$. This suggests that *Ift88* cKO resting chondrocytes in the lateral region are slightly inclined down as opposed to even slighter inclined upwards. The distributions of proliferating chondrocytes in the *Ift88* cKO was more spread out compared with the equivalent zone in the *Ift88*$^{\text{fl/fl}}$ growth plate. The hypertrophic chondrocytes in the lateral region had a statistically significant difference in distribution between *Ift88*$^{\text{fl/fl}}$ and *Ift88* cKO, however they are both spread across all values of θ_{cell}, suggesting cell random orientation.

Percentage ciliation in the *Ift88* cKO growth plate

As *Ift88* deletion should disrupt ciliation, I next mapped primary cilia structure across the growth plate. Across the entire growth plate, there was no difference in percentage ciliation between the *Ift88*$^{\text{fl/fl}}$ and *Ift88* cKO growth plates (Fig. 4.5

A). When comparing the *Ift88*$^{fl/fl}$ and *Ift88* cKO ciliation in the different zones across the width of the growth plate (averaged middle and lateral regions), there was no statistically significant difference between the cKO and control (Fig. 4.5 B). The overall resting zone percentage ciliation in the *Ift88* cKO is lower in the hypertrophic zone compared with the two others. When comparing the *Ift88*$^{fl/fl}$ and *Ift88* cKO ciliation in the different regions (averaged across the resting, proliferating and hypertrophic zones) there was a statistically significant difference in the lateral region, with a lower percentage in the *Ift88* cKO (Fig. 4.5 C). Percentage ciliation was measured in the different zones and regions of the *Ift88* cKO growth plate (Fig. 4.5 E). The pattern of ciliation was in the same range (40 to 60%) and followed the same trend in the cKO compared with the control (Fig. 4.5 D, E). In the lateral region, the hypertrophic zone had a statistically significant lower ciliation than the resting zone, a reduction that was also observed in the control but to a lesser extent. This reduction explains the difference measured in the lateral region between *Ift88*$^{fl/fl}$ and *Ift88* cKO (Fig. 4.5 C).

Primary cilia length in the *Ift88* cKO growth plate

Next, as with the *Ift88*$^{fl/fl}$ mouse, the length of primary cilia in the growth plate of the *Ift88* cKO was measured (Fig. 4.6). The lengths measured were in the same range in the *Ift88* cKO compared with the *Ift88*$^{fl/fl}$. Across the regions, the hypertrophic region had the longest cilia in the *Ift88*$^{fl/fl}$ and *Ift88* cKO (Fig. 4.6 A). There was no difference between the *Ift88*$^{fl/fl}$ and *Ift88* cKO. The primary cilia length in the *Ift88* cKO followed a similar pattern to the *Ift88*$^{fl/fl}$ (Fig. 4.6 B, C). In the *Ift88* cKO, the length was the longest in the hypertrophic zone of the middle region.

Primary cilia orientation in the *Ift88* cKO growth plate

Primary cilia 3D orientation in the *Ift88* cKO was mapped using the method described in Chapter 2. This organisation was compared with that of the control line *Ift88*$^{fl/fl}$ (Fig. 4.7). The distributions of ϕ_{cilium} in the *Ift88* cKO were different in the

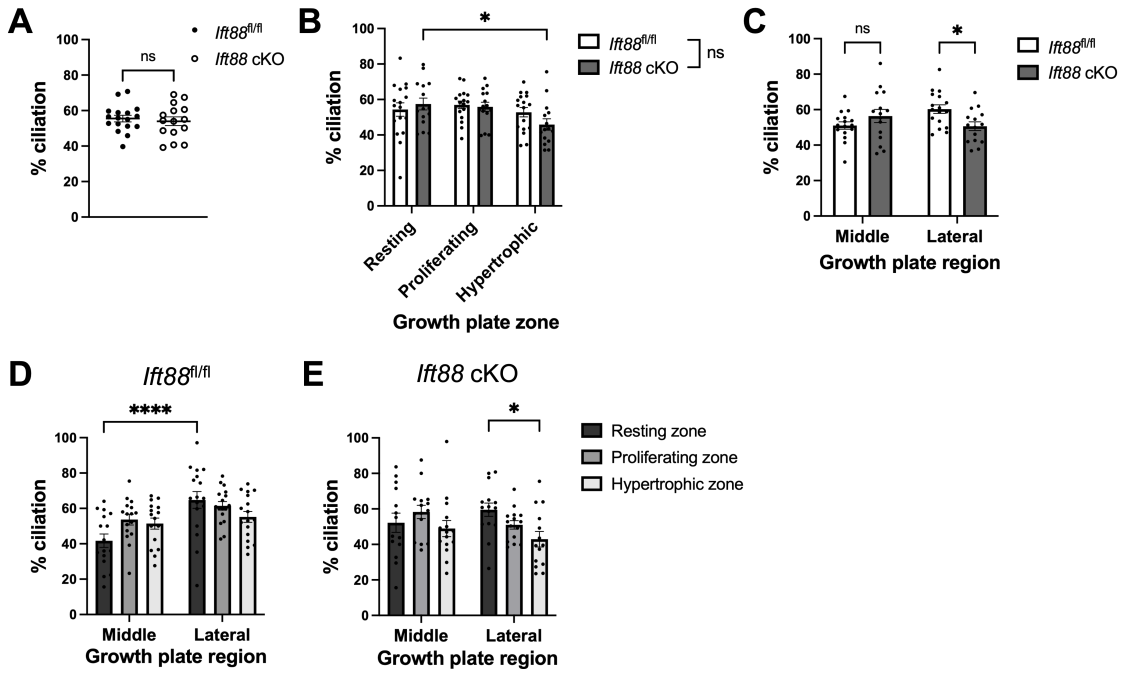


Figure 4.5: Differences in percentage ciliation between the *Ift88*$^{fl/fl}$ and *Ift88* cKO growth plates. **(A)** Overall percentage ciliation (unpaired t test). **(B)** Percentage ciliation by growth plate zone. p* = 0.0291. All other comparisons are not statistically significant (two-way ANOVA). **(C)** Percentage ciliation by growth plate region. p* = 0.0138 (two-way ANOVA). Percentage ciliation in the different zones and regions of the *Ift88*$^{fl/fl}$ **(D)** and *Ift88* cKO **(E)** growth plates. p* = 0.0159, p**** < 0.0001. All other comparisons are not statistically significant (two-way ANOVA). Mean ± SEM. n = 14-18 mice (585 to 3622 cells per zone/region).

proliferating zone in both the middle and lateral regions (Fig. 4.7 A). In the other zones, the distributions were unchanged compared with the *Ift88*$^{fl/fl}$. Within the *Ift88* cKO, there was no difference in distributions between the zones. ϕ_{cilium} was distributed between 60° and 120°, with fewer cilia at 90°. This corresponds to horizontal orientation, slightly inclined up and down, similar to the *Ift88*$^{fl/fl}$ cilia (Fig. 4.7 B, C).

The θ_{cilium} was unchanged between the *Ift88* cKO and *Ift88*$^{fl/fl}$ cilia (Fig. 4.7 D). θ_{cilium} was clustered around 180° and 0/360°. This corresponds to forward and back orientation (Fig. 4.7 E, F). This ϕ_{cilium} and θ_{cilium} distribution visually resembles that of the control ((Fig. 4.7G, 3.12 A).

The resultant, which measures how aligned primary cilia are, was measured in the *Ift88* cKO (Fig. 4.8). The values of resultant, between 0.5 and 1, were similar to the

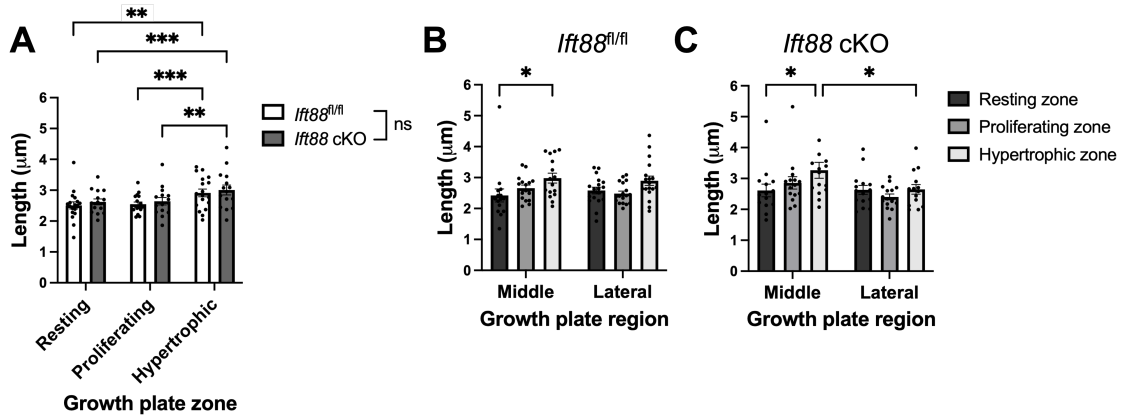


Figure 4.6: Differences in primary cilia length between the *Ift88*$^{fl/fl}$ and *Ift88* cKO growth plates. (A) Primary cilia length in the growth plate zones. p** = 0.0031 (resting vs hypertrophic *Ift88* cKO), p*** = 0.0006 (resting vs hypertrophic *Ift88*$^{fl/fl}$), p*** = 0.0003 (proliferating vs hypertrophic *Ift88*$^{fl/fl}$), p** = 0.0013 (proliferating vs hypertrophic *Ift88* cKO) All other comparisons are not statistically significant (two-way ANOVA). Primary cilia length in the different zones and regions of the *Ift88*$^{fl/fl}$ **(B)** and *Ift88* cKO **(C)** growth plates. (B) p* = 0.0198 (C) p* = 0.464 (resting vs hypertrophic middle region), p* = 0.0194 (hypertrophic middle vs lateral). All other comparisons are not statistically significant (two-way ANOVA). Mean ± SEM. n = 14-18 mice (301 to 1922 cilia per zone/region).

Ift88$^{fl/fl}$, with the highest also being in the resting zone of the middle region.

Centriole position in the *Ift88* cKO growth plate

The position of centrioles in the cell were next studied, to determine whether the base of the cilium was in a different position with *Ift88* cKO. As in *Ift88*$^{fl/fl}$, the Ift88 cKO centrioles were distributed almost uniformly around the cell (Fig. 4.9 A, B, C). $\phi_{\text{centriole}}$ was ranged mainly between 40° and 140°, with more values around 20° and 160° for the hypertrophic zones in both *Ift88*$^{fl/fl}$ and Ift88 cKO. The distributions of the resting zone in both middle and lateral regions were different from each other between the mouse lines. $\theta_{\text{centriole}}$ was spread across all values between 0° and 360° with narrowing between 135° and 225° (Fig. 4.9 D, E, F). Despite some statistical difference between some of the distributions, they correspond to similar positions of the centriole, all across the range of $\theta_{\text{centriole}}$. This combination of $\phi_{\text{centriole}}$ and $\theta_{\text{centriole}}$ angles covered the whole of the 3D coordinate system (Fig. 4.9 G, 3.12 B).

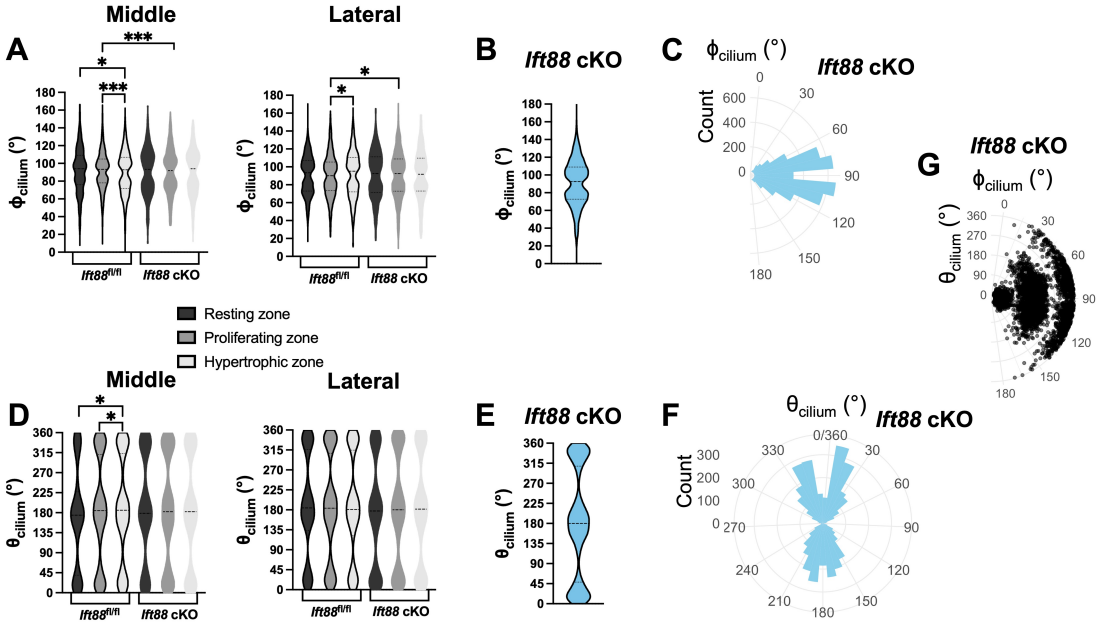


Figure 4.7: Differences in primary cilia orientation between the 6-week old *Ift88*$^{fl/fl}$ and *Ift88* cKO growth plates. **(A)** Distribution of primary cilia ϕ_{cilium} angles in the resting, proliferating and hypertrophic zones of the middle and lateral regions of the growth plates. Dashed lines represent median (longer dashes) and first and third quartiles (shorter dashes). p* = 0.027 (fl/fl resting middle vs hypertrophic middle), p* = 0.041 (fl/fl proliferating lateral vs hypertrophic lateral), p* = 0.012 (proliferating lateral fl/fl vs proliferating lateral cKO, p*** = 0.00083 (proliferating middle vs hypertrophic middle), p*** = 0.00084 (proliferating middle fl/fl vs proliferating middle cKO). All other comparisons within mouse line or across the same zone in different lines were not statistically significant (Kolmogorov–Smirnov test adjusted for multiple comparisons). n = 14-18 mice (301 to 1922 cilia per zone/region) **(B)** Distribution and **(C)** rose plots and circular scatter plot of ϕ_{cilium} angles across the whole *Ift88* cKO growth plate. n = 14 mice (4276 cilia). **(D)** Distribution of primary cilia θ_{cilium} angles in the resting, proliferating and hypertrophic zones of the middle and lateral regions of the growth plate. Dashed lines represent median (longer dashes) and first and third quartiles (shorter dashes). p* = 0.047 (fl/fl resting middle vs proliferating middle), p* = 0.047 (fl/fl resting middle vs hypertrophic middle). All other comparisons within mouse line or across the same zone in different lines were not statistically significant (Kolmogorov–Smirnov test adjusted for multiple comparisons). n = 14-18 mice (301 to 1922 cilia per zone/region). **(E)** Distribution and **(F)** rose plots and circular scatter plot of θ_{cilium} angles across the whole *Ift88* cKO growth plate. n = 14 mice (4276 cilia). **(G)** Circular scatter plot of ϕ_{cilium} and θ_{cilium} angles across the whole *Ift88* cKO growth plate. n = 14 mice (4276 cilia).

Cell proliferation in the *Ift88* cKO growth plate

Cells ciliate when they are not dividing. Therefore, when a cell isn't ciliated in the imaging presented above, it could be because it is dividing or in the case of the

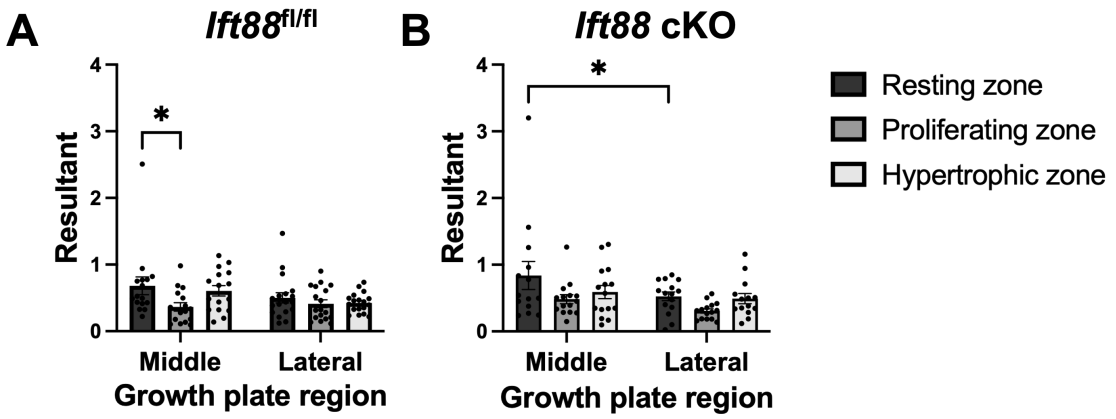


Figure 4.8: Average resultant per cilium in the resting, proliferating and hypertrophic zones of the middle and lateral regions of the *Ift88*$^{fl/fl}$ (A) and *Ift88* cKO (B) growth plates. Mean ± SEM.p* = 0.019 (A), p* = 0.0317 (B). All other comparisons are not statistically significant (two-way ANOVA) n = 14-18 mice.

Ift88 cKO because it does not have functional protein to do so. In order to measure differences in proliferation extent in the growth plates of *Ift88*$^{fl/fl}$ and *Ift88* cKO, Ki-67 IHC was performed on paraffin-embedded tibial sections. Ki-67 is a protein found in the cell nucleus that is present during all active phases of the cell cycle (G_1, S, G_2, and M phases) but not in the resting phase (G_0) [265].

Ki-67 staining was first performed in growth plates of different ages in order to assess the validity of the technique. Young growth plates (2-6 weeks) are very active and chondrocytes should proliferate more than in older growth plates (10 weeks). 2 week-old growth plates had 50.3% ± 4.4% Ki-67 positive cells, compared with 44.9% ± 5.6% and 30.7% ± 7.6% in the 4 week and 10-week old growth plates, respectively (Fig. 4.10). This decrease in Ki-67 positive cells with age suggests the staining can detect differences in number of proliferating cells in growth plates.

Subsequently, the growth plates of *Ift88*$^{fl/fl}$ and *Ift88* cKO mice were stained at 6 weeks. Ki-67 positive cells were mainly located in the proliferating zone (Fig. 4.11 A). Growth plates from both *Ift88*$^{fl/fl}$ and *Ift88* cKO mice had an average of ~33% Ki-67 positive cells, with no difference between the two (Fig. 4.11 B).

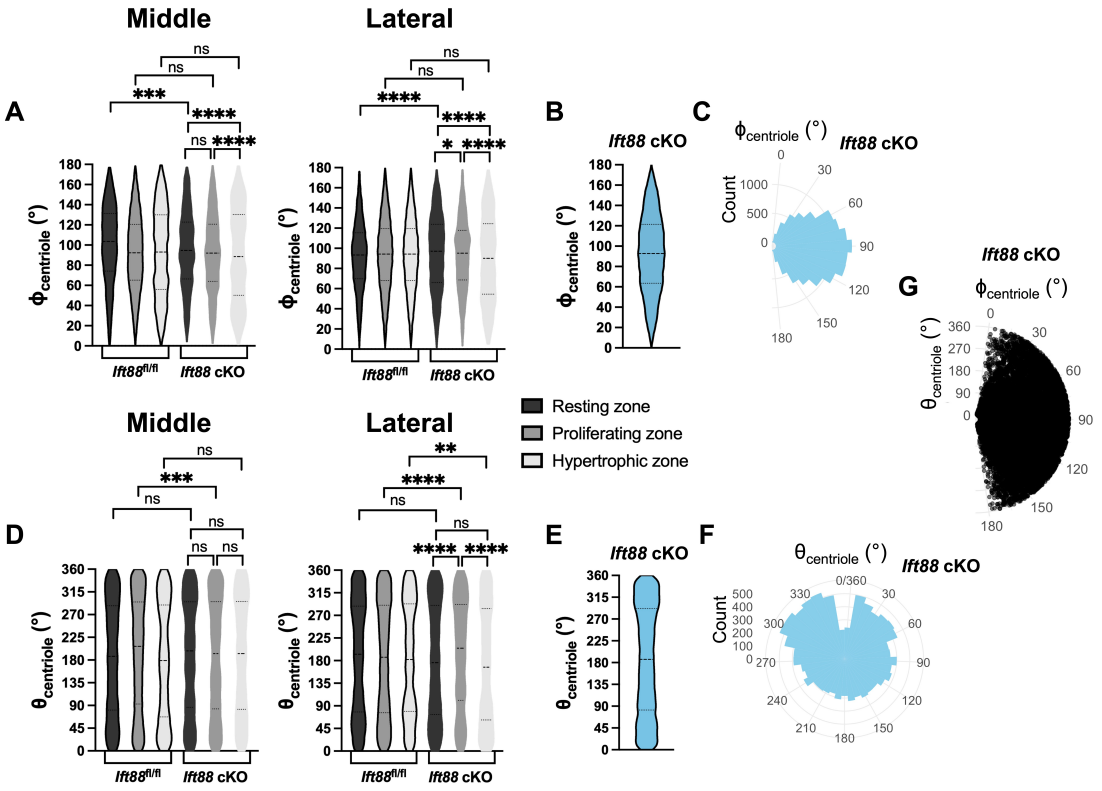


Figure 4.9: Differences in centriole position between the 6-week old *Ift88*$^{fl/fl}$ and *Ift88* cKO growth plates. **(A)** Distribution of centriole $\phi_{centriole}$ angles in the resting, proliferating and hypertrophic zones of the middle and lateral regions of the growth plates. Dashed lines represent median (longer dashes) and first and third quartiles (shorter dashes). p* = 0.014, p*** = 0.00047, p**** < 0.0001, comparisons within *Ift88*$^{fl/fl}$ are in Fig. 3.11 (Kolmogorov–Smirnov test adjusted for multiple comparisons). n = 14-18 mice (1105 to 8204 centrioles per zone/region) **(B)** Distribution and **(C)** rose plots and circular scatter plot of $\phi_{centriole}$ angles across the whole *Ift88* cKO growth plate. n = 14 mice (14,086 centrioles). **(D)** Distribution of centriole $\theta_{centriole}$ angles in the resting, proliferating and hypertrophic zones of the middle and lateral regions of the growth plate. Dashed lines represent median (longer dashes) and first and third quartiles (shorter dashes). p** = 0.0033, p*** = 0.00022, p**** < 0.0001, comparisons within *Ift88*$^{fl/fl}$ are in Fig. 3.11 (Kolmogorov–Smirnov test adjusted for multiple comparisons). n = 14-18 mice (1105 to 8204 centrioles per zone/region). **(E)** Distribution and **(F)** rose plots and circular scatter plot of $\theta_{centriole}$ angles across the whole *Ift88* cKO growth plate. n = 14 mice (14,086 centrioles). **(G)** Circular scatter plot of $\phi_{centriole}$ and $\theta_{centriole}$ angles across the whole *Ift88* cKO growth plate. n = 14 mice (14,086 centrioles).

4.3.2 Growth plate phenotype of the offloaded and contralateral *Ift88*$^{fl/fl}$ growth plates

Primary cilia are intrinsically linked to mechanotransduction in the cell, and previous disruptions of loading in the limb have resulted in growth plate phenotypes [47]. In

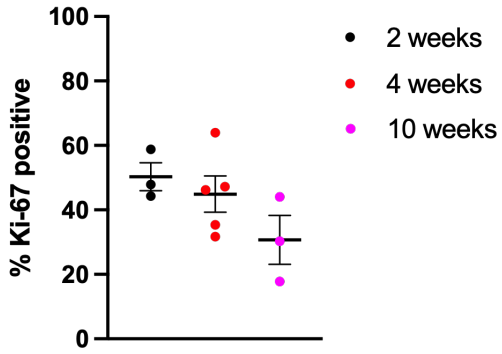


Figure 4.10: Change in percentage of Ki-67 positive cells in the growth plates of 2, 4 and 10 week old mice. Mean ± SEM. n = 3-5 mice.

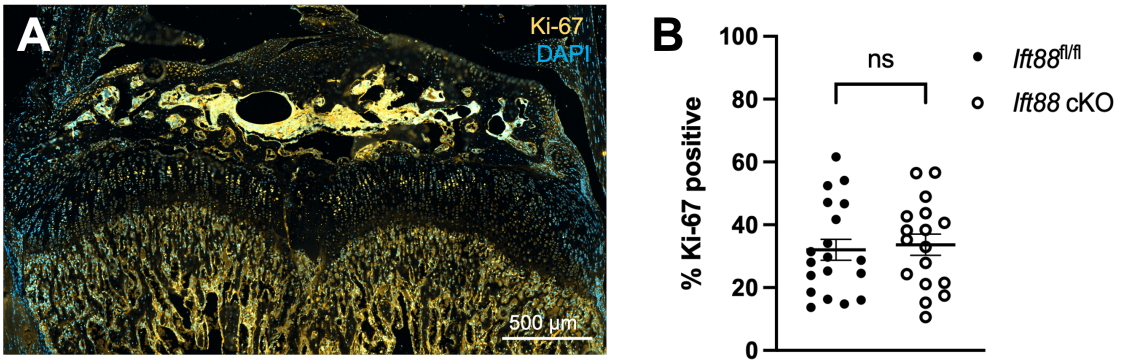


Figure 4.11: (A)Ki-67 staining in the growth plate of a 6 week-old *Ift88*$^{fl/fl}$ mouse. (B) Percentage of Ki-67 positive cells in the *Ift88*$^{fl/fl}$ and *Ift88* cKO growth plates. Mean ± SEM (unpaired t test) n = 17-19 mice.

Chapter 3, higher percentage ciliation observed in the periphery of the growth plate compared with the centre might be correlated with greater strains in the periphery, and thus reduction in loading might reduce ciliation. Therefore, I hypothesised that removing mechanical loading on the limb would disrupt cilia organisation in the growth plate. Double neurectomy surgeries were performed on the right limbs of mice to render them incapable of bearing load. The left limb, called the contralateral, became the predominant weight-bearing limb, experiencing more load than when two limbs are in use. Due to mouse availability and time constraints, the double neurectomy surgeries were only performed in 4 male mice.

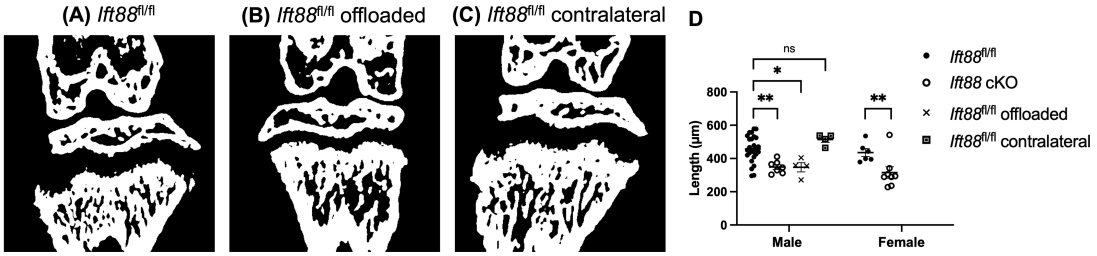


Figure 4.12: Differences in length measured from thresholded microCT images of the *Ift88*$^{fl/fl}$ (A), *Ift88*$^{fl/fl}$ offloaded (B) and *Ift88*$^{fl/fl}$ contralateral (C) growth plates. (D) Thresholded growth plate lengths of *Ift88*$^{fl/fl}$, *Ift88* cKO, *Ift88*$^{fl/fl}$ offloaded and *Ift88*$^{fl/fl}$ contralateral limbs. Mean ± SEM. p* = 0.0168, p** = 0.0023 (male) (one-way ANOVA) p = 0.005988 (female) (unpaired t test corrected for multiplicity).n = 4-18 mice.

Table 4.1: Ratio of the number of resting to proliferating to hypertrophic cells in the growth plate.

Mouse line / growth plate zone	Resting	Proliferating	Hypertrophic
Ift88$^{fl/fl}$	1	3.1	1.5
Ift88 cKO	1	3.1	1.5
Ift88$^{fl/fl}$ offloaded	1	2.7	1.3
Ift88$^{fl/fl}$ contralateral	1	5.3	2.4

Ift88$^{fl/fl}$ offloaded and contralateral growth plate lengths

The growth plates of offloaded limbs were imaged by microCT and compared to *Ift88*$^{fl/fl}$. The offloaded growth plates were shorter than control mice, approximately the same length as *Ift88* cKO growth plates (Fig. 4.12). The contralateral limbs did not experience shortening and were approximately the same length as control growth plates. They also resembled the *Ift88*$^{fl/fl}$ growth plates by microCT.

The ratios of number of resting, to proliferating to hypertrophic cells was different in the offloaded growth plates and in the contralateral growth plates compared with the *Ift88*$^{fl/fl}$ growth plates (Table 4.1). Offloaded growth plates had fewer proliferating cells, which may explain the growth plate shortening. Contralateral growth plates, on the other hand, had more proliferating and hypertrophic chondrocytes relative to resting chondrocytes compared with *Ift88*$^{fl/fl}$ growth plates.

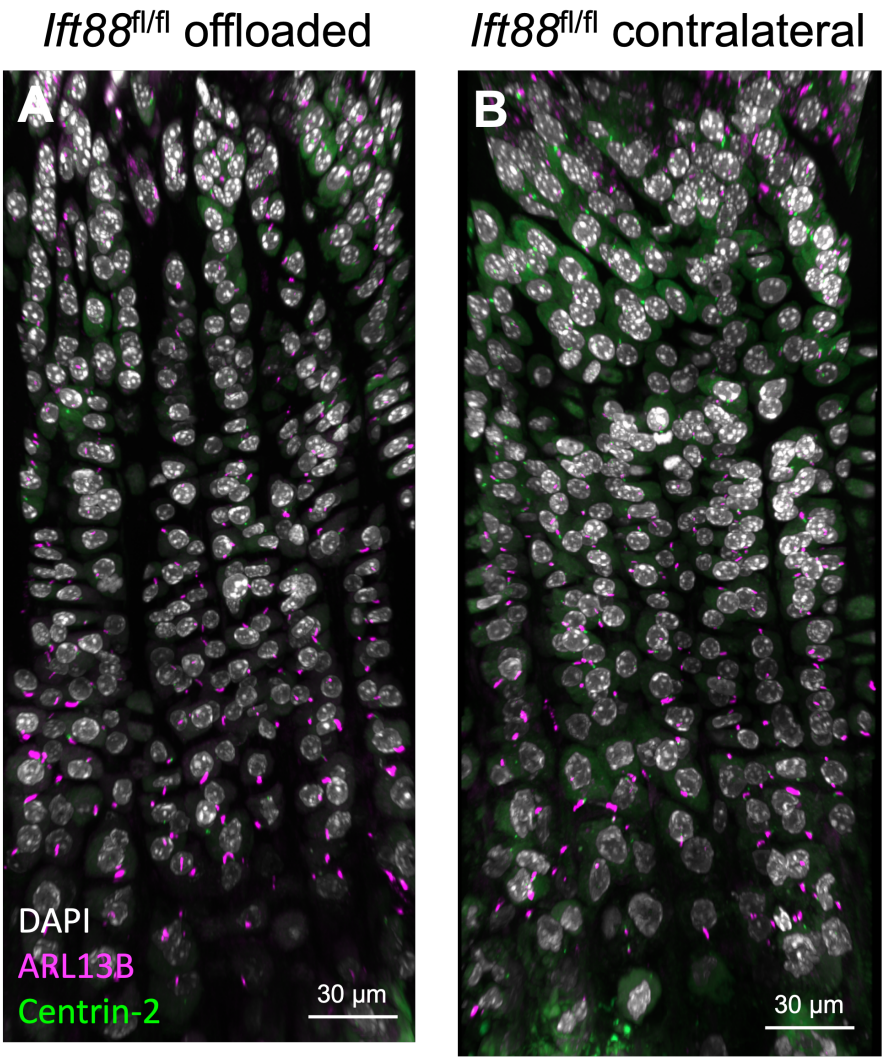
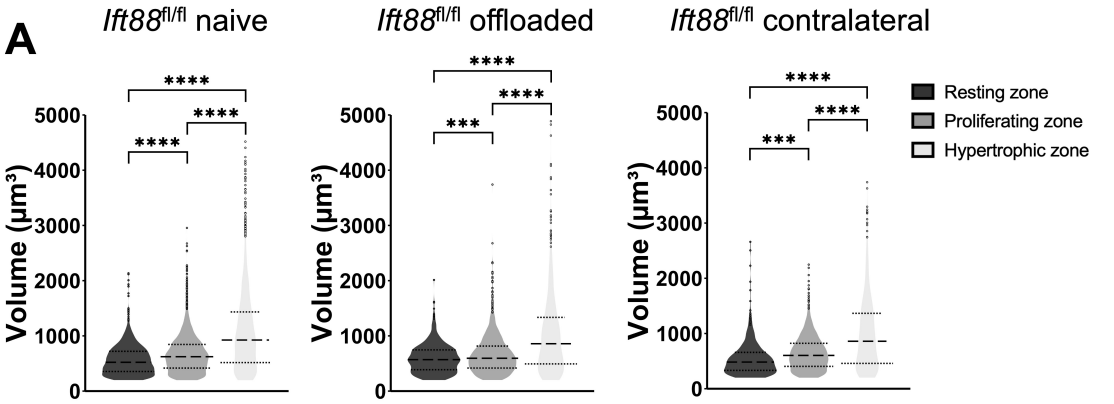


Figure 4.13: Primary cilia imaging in the middle of the growth plates of *Ift88*$^{fl/fl}$ offloaded (A) and contralateral (B) limbs.

Cell volume and organisation in the *Ift88*$^{fl/fl}$ offloaded and contralateral growth plates

Due to only 4 mice being analysed for these experiments, analysis was performed across the growth plate (medial and lateral regions averaged) and presented by zone. The growth plates of the offloaded and contralateral limbs appeared ciliated with cells arranged in columns (Fig. 4.13).

The cell volume distributions and means of the *Ift88*$^{fl/fl}$ offloaded and contralateral growth plates were similar to that of *Ift88*$^{fl/fl}$ (Fig. 4.14 A). Due to the different



B

Growth plate zone	*Ift88*$^{fl/fl}$	*Ift88* cKO	*Ift88*$^{fl/fl}$ offloaded	*Ift88*$^{fl/fl}$ contralateral
Resting	521.6 µm³	492.6 µm³	569.5 µm³	482.8 µm³
Proliferating	622.8 µm³	598.0 µm³	594.6 µm³	602.9 µm³
Hypertrophic	924.7 µm³	741.5 µm³	857.9 µm³	859.8 µm³

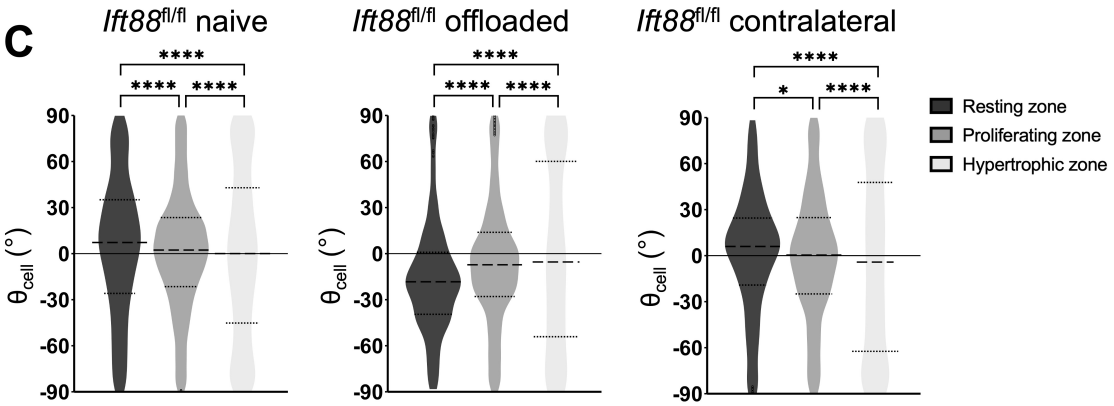


Figure 4.14: Cell organisation in *Ift88*$^{fl/fl}$, *Ift88*$^{fl/fl}$ offloaded and *Ift88*$^{fl/fl}$ contralateral growth plates. **(A)** Cell volume in the resting, proliferating and hypertrophic zones of the *Ift88*$^{fl/fl}$, *Ift88*$^{fl/fl}$ offloaded and *Ift88*$^{fl/fl}$ contralateral growth plates. Dashed lines represent median (longer dashes) and first and third quartiles (shorter dashes). p*** = 0.00024, p**** < 0.0001 (Kolmogorov–Smirnov test adjusted for multiple comparisons). n = 18 mice (2074 to 6349 cells per zone) (naive), n = 4 mice (332 to 1715 cells per zone) (offloaded, contralateral). **(B)** Median cell volumes in the *Ift88*$^{fl/fl}$, *Ift88* cKO, *Ift88*$^{fl/fl}$ offloaded and *Ift88*$^{fl/fl}$ contralateral growth plates. **(C)** Distribution of θ_{cell} in the resting, proliferating and hypertrophic zones of the *Ift88*$^{fl/fl}$, *Ift88*$^{fl/fl}$ offloaded and *Ift88*$^{fl/fl}$ contralateral growth plates. Dashed lines represent median (longer dashes) and first and third quartiles (shorter dashes). p* = 0.019, p**** < 0.0001. (Kolmogorov–Smirnov test adjusted for multiple comparisons). n = 18 mice (2074 to 6349 cells per zone) (naive), n = 4 mice (332 to 1715 cells per zone) (offloaded, contralateral).

number of mice used between the *Ift88*$^{fl/fl}$ growth plate and the *Ift88*$^{fl/fl}$ offloaded and contralateral growth plates, the distributions were not compared across mouse lines. However, the median cell volume values show that the *Ift88*$^{fl/fl}$ offloaded resting and proliferating chondrocytes were similar to that of *Ift88*$^{fl/fl}$ (Fig. 4.14 B). The *Ift88*$^{fl/fl}$ offloaded hypertrophic chondrocytes were smaller that those of the *Ift88*$^{fl/fl}$ growth plate. The *Ift88*$^{fl/fl}$ contralateral chondrocytes had slightly smaller resting and hypertrophic chondrocytes, and similar size proliferating chondrocytes, compared with the *Ift88*$^{fl/fl}$.

The θ_{cell} distribution appearances also looked similar between the mouse lines with a few differences (Fig. 4.14 C). The offloaded resting zone mode skewed towards -20° compared with 10° in the resting zone of the control and contralateral limbs. This suggests the cells are less horizontal. The proliferating chondrocytes distributions all centre around 0° suggesting horizontal orientation of cells, which can then stack into columns. The hypertrophic chondrocytes all had broad distributions across all θ_{cell} values.

Percentage ciliation in the *Ift88*$^{fl/fl}$ offloaded and contralateral growth plates

Percentage ciliation, primary cilia length and orientation were next measured in order to determine whether the absence of mechanical loading affected the axoneme of the primary cilium, where receptors responding to mechanical signals are presumed to be located.

The overall growth plate percentage ciliation in the *Ift88*$^{fl/fl}$ offloaded and contralateral were the same as *Ift88*$^{fl/fl}$ and *Ift88* cKO, around 53% (Fig. 4.15 A). The percentage ciliation was also measured in the different zones in order to assess any differences at this level (Fig. 4.15 B). The *Ift88*$^{fl/fl}$ offloaded growth plate had lower percentage ciliation in the hypertrophic zone compared with the resting

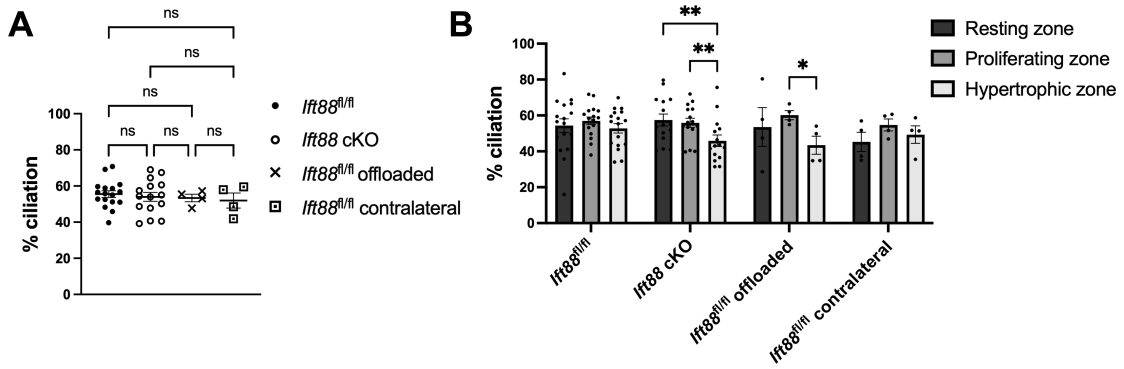


Figure 4.15: Percentage ciliation in the *Ift88*$^{fl/fl}$, *Ift88* cKO, *Ift88*$^{fl/fl}$ offloaded and contralateral growth plates. (A) Overall percentage ciliation (one-way ANOVA). **(B)** Percentage ciliation by growth plate zone. p* = 0.0164, p** = 0.0061 (resting vs hypertrophic *Ift88* cKO), p** = 0.0013 (proliferating vs hypertrophic *Ift88* cKO) All other comparisons were not statistically significant (two-way ANOVA). Mean ± SEM. n = 14-18 mice (1660 to 6349 cells per zone) (*Ift88*$^{fl/fl}$, *Ift88* cKO), n = 4 mice (332 to 1715 cells per zone) (offloaded, contralateral).

and proliferating zones. The zones of the *Ift88*$^{fl/fl}$ contralateral growth plate all had similar percentages of ciliation.

Primary cilia length in the *Ift88*$^{fl/fl}$ offloaded and contralateral growth plates

The primary cilia lengths in the *Ift88*$^{fl/fl}$ offloaded and contralateral growth plate followed a similar pattern to *Ift88*$^{fl/fl}$ and *Ift88* cKO. The primary cilia were longer in the hypertrophic zone with a mean around 3 µm compared to ~2.6 µm in the resting and proliferating zones (Fig. 4.16).

Primary cilia orientation in the *Ift88*$^{fl/fl}$ offloaded and contralateral growth plates

In order to determine whether absence of loading or increased loading changes the direction the axoneme of primary cilia point in chondrocytes the spherical coordinates of the *Ift88*$^{fl/fl}$ offloaded and contralateral growth plate cilia was measured. Loading in the limbs comes mainly from ambulatory load, therefore is in the proximal-distal

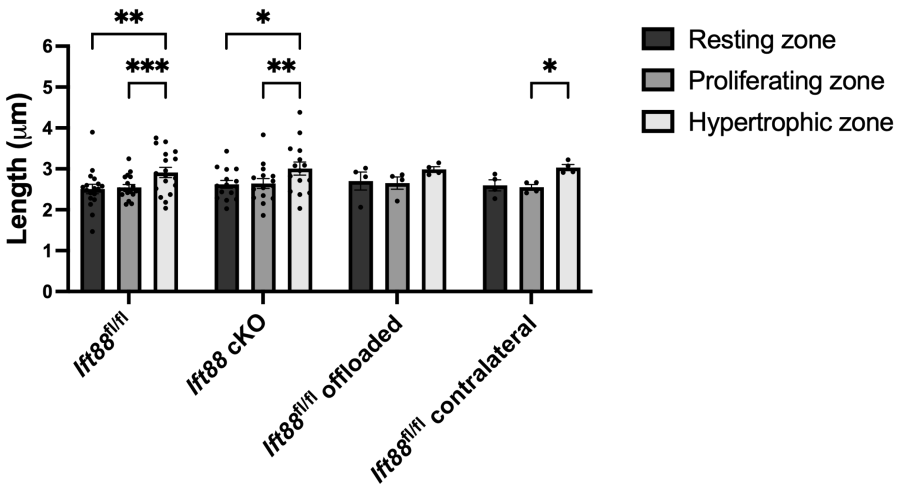


Figure 4.16: Differences in primary cilia length between the *Ift88*$^{fl/fl}$, Ift88 cKO, *Ift88*$^{fl/fl}$ offloaded and *Ift88*$^{fl/fl}$ contralateral growth plates. Mean ± SEM. p* = 0.0127 (resting vs hypertrophic *Ift88* cKO), p* = 0.0240 (proliferating vs hypertrophic *Ift88*$^{fl/fl}$ contralateral), p** = 0.0031 (resting vs hypertrophic *Ift88*$^{fl/fl}$), p** = 0.0046 (proliferating vs hypertrophic *Ift88* cKO), p*** = 0.0004. All other comparisons were not statistically significant (two-way ANOVA). n = 14-18 mice (778 to 3299 cilia per zone) (*Ift88*$^{fl/fl}$, Ift88 cKO), n = 4 mice (128 to 901 cilia per zone) (offloaded, contralateral).

direction. This directed load could be directing axoneme orientation.

The *Ift88*$^{fl/fl}$ offloaded and contralateral growth plates generally had primary cilia orientations that were similar to *Ift88*$^{fl/fl}$ and *Ift88* cKO in terms of ϕ_{cilium} and θ_{cilium} (Fig. 4.17). The ϕ_{cilium} in the *Ift88*$^{fl/fl}$ offloaded and contralateral growth plates had shorter tails (Fig. 4.17 A). This may be due to lower mouse numbers. No statistical tests were run due to the lower mouse numbers in the offloaded and contralateral conditions which would skew the tests. In addition, the *Ift88*$^{fl/fl}$ contralateral growth plate had more cilia at $\phi_{\text{cilium}} = 90°$ in the resting zone. The θ_{cilium} distribution was very similar across all conditions (Fig. 4.17 B).

Centriole position in the *Ift88*$^{fl/fl}$ offloaded and contralateral growth plates

As with the primary cilia, the spherical coordinates of the centrioles in the *Ift88*$^{fl/fl}$ offloaded and contralateral were compared to *Ift88*$^{fl/fl}$ and *Ift88* cKO. The position of the centrioles in the *Ift88*$^{fl/fl}$ offloaded and contralateral growth plates were similar as *Ift88*$^{fl/fl}$ offloaded and contralateral growth plates (Fig. 4.18). The ϕ_{cilium} values

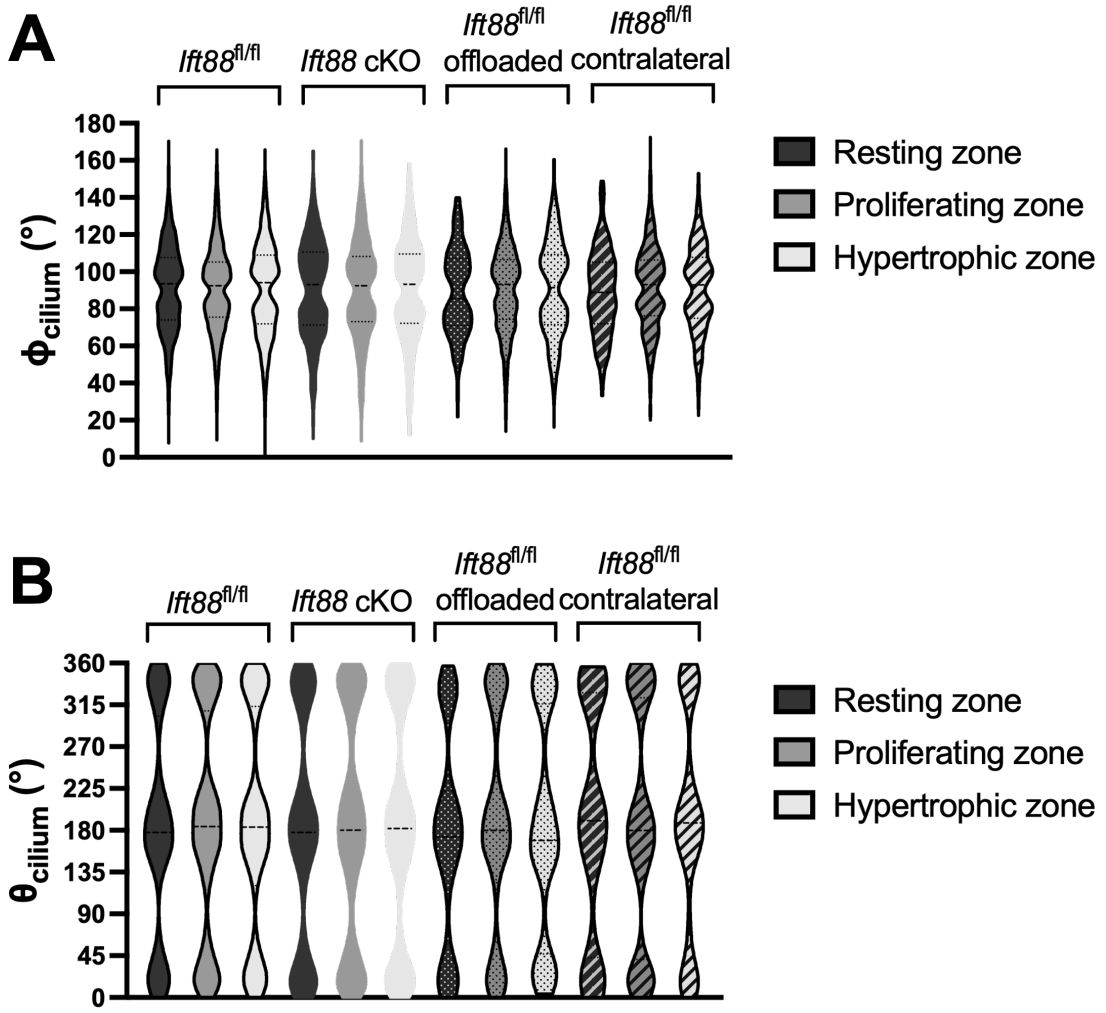


Figure 4.17: Differences in primary cilia orientation between the 6-week old *Ift88*$^{fl/fl}$, Ift88 cKO, *Ift88*$^{fl/fl}$ offloaded and *Ift88*$^{fl/fl}$ contralateral growth plates. **(A)** Distribution of primary cilia ϕ_{cilium} angles in the resting, proliferating and hypertrophic zones across the growth plates. Dashed lines represent median (longer dashes) and first and third quartiles (shorter dashes). n = 14-18 mice (778 to 3299 cilia per zone) (*Ift88*$^{fl/fl}$, Ift88 cKO), n = 4 mice (128 to 901 cilia per zone) (offloaded, contralateral). **(B)** Distribution of primary cilia θ_{cilium} angles in the resting, proliferating and hypertrophic zones across the growth plate. Dashed lines represent median (longer dashes) and first and third quartiles (shorter dashes) n = 14-18 mice (778 to 3299 cilia per zone) (*Ift88*$^{fl/fl}$, Ift88 cKO), n = 4 mice (128 to 901 cilia per zone) (offloaded, contralateral).

of the hypertrophic zones always had a broader distribution, not narrowing below 40° and above 140° (Fig. 4.18 A). The hypertrophic zone of the *Ift88*$^{fl/fl}$ offloaded growth plate had $\theta_{\text{centriole}}$ had fewer centrioles between 90° and 270° , with a lower median (Fig. 4.18 B). No narrowing was observed in the *Ift88*$^{fl/fl}$ contralateral, with a uniform distribution of values in all zones.

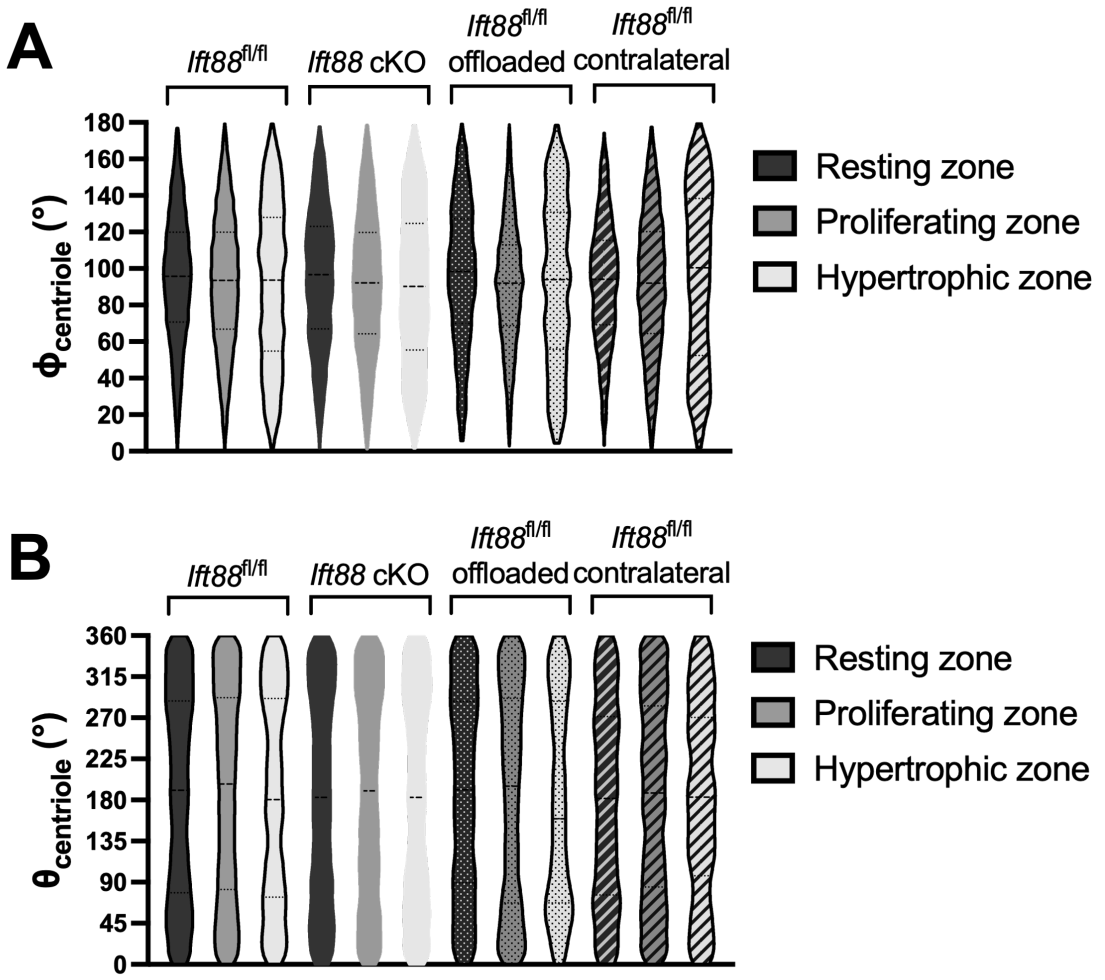


Figure 4.18: Differences in centriole position between the 6-week old *Ift88*$^{fl/fl}$, Ift88 cKO, *Ift88*$^{fl/fl}$ offloaded and *Ift88*$^{fl/fl}$ contralateral growth plates. (A) Distribution of centriole $\phi_{\text{centriole}}$ angles in the resting, proliferating and hypertrophic zones across the growth plates. Dashed lines represent median (longer dashes) and first and third quartiles (shorter dashes). n = 14-18 mice (2518 to 14,587 centrioles per zone) (*Ift88*$^{fl/fl}$, Ift88 cKO), n = 4 mice (950 to 4611 centrioles per zone) (offloaded, contralateral). **(B)** Distribution of centriole $\theta_{\text{centriole}}$ angles in the resting, proliferating and hypertrophic zones across the growth plate. Dashed lines represent median (longer dashes) and first and third quartiles (shorter dashes) n = 14-18 mice (2518 to 14,587 centrioles per zone) (*Ift88*$^{fl/fl}$, Ift88 cKO), n = 4 mice (950 to 4611 centrioles per zone) (offloaded, contralateral).

4.4 Discussion

In this chapter, I investigated how the organisation of cells and primary cilia within the growth plate described in Chapter 3 might be altered by conditional deletion of *Ift88*, a key component of the intraflagellar transport machinery, and in response to offloading. Building on the methods and observations established in the control growth plate (Chapter 3), I applied the same high-resolution imaging and quantitative analysis pipeline to examine differences in 3D orientation between *Ift88* cKO, offloaded and contralateral growth plates. This allowed me to assess the extent to which genetic disruption of cilia formation and reduction in mechanical load influence chondrocyte organisation and polarity. As the growth plate exhibits a well-defined columnar architecture and orientation gradients, it serves as an appropriate tissue model for evaluating how perturbations to ciliary function or mechanical stimuli affect structural alignment at the cellular and subcellular level. By comparing these experimental conditions, I aimed to disentangle the relative contributions of cilia-mediated signalling and biomechanical forces in maintaining growth plate organisation.

4.4.1 Effect of *Ift88* knockout on growth plate cell and primary cilia organisation

Ift88 cKO growth plate length

The aggrecan-cre driving *Ift88* deletion was activated with tamoxifen at 4 weeks of age. The tibias were then collected 2 weeks later, at 6 weeks. Whilst deletion efficacy was not directly measured here, Coveney et al. (2022) crossed the $AggrecanCreER^{T2}$ with a TdTomato reporter line to assess recombination levels and patterning in the growth plate. This revealed evenly spread $AggrecanCreER^{T2}$ activity across the growth plate [47].

By using *Ift88*$^{fl/fl}$ as the control, I controlled for any potential effects of tamoxifen. The tamoxifen dose used here was also below concentrations shown to affect bone structure [266]. Nevertheless, data I have collected and that of the wider group has revealed that tamoxifen, particularly in combination with changes in loading, influences growth plate length.

In this study, *Ift88* cKO led to shortening of the growth plate, in particular narrowing of the peripheral region (Fig. 4.2). This is in contrast with previous work in our group that witnessed a lengthening of the growth plate upon deletion of *Ift88* at 4 weeks [47]. This was in the *AggrecanCreER*^{T2}*;Ift88*$^{fl/fl}$ mouse line, therefore the same as ours before it was crossed with the *Centrin-2-GFP.ARL13b-mCherry* line. The *Centrin-2-GFP.ARL13b-mCherry* line is on a mixed BALB/c x C57BL/6 x FVB/N background (Jackson Laboratory, strain #027967). The *Ift88*$^{fl/fl}$ line is on a C57BL/6J background (Jackson Laboratory, strain #022409). This line was previously crossed with the *AggrecanCreER*^{T2} mouse line, originally generated at the Kennedy Institute of Rheumatology, to generate the *AggrecanCreER*^{T2}*;Ift88*$^{fl/fl}$ line [267]. The *AggrecanCreER*^{T2}*;Ift88*$^{fl/fl}$ and *Ift88*$^{fl/fl}$ lines were then crossed with the *Centrin-2-GFP.ARL13b-mCherry* line, to generate the *Ift88* cKO and *Ift88*$^{fl/fl}$ used in this project. The addition of the *Centrin-2-GFP.ARL13b-mCherry* line will therefore have changed the genetic strain background of the mice compared with those used in Coveney et al. (2022). The body weight information of the mice from these different strains does not differ significantly therefore, it can be assumed that the *Ift88* deletion occurred at similar physiological ages [268–270]. Nevertheless, it is likely that the difference in phenotypes can be explained by different mouse backgrounds through mechanisms which are yet unclear.

On the other hand, other studies have witnessed a similar shortening of the growth plate upon deletion of ciliary genes. Deletion of *Ift88* in osteochondro-progenitors of the periosteum and perichondrium at 1 week and 2.5 weeks of age resulted in stunted growth caused by limited differentiation, proliferation, columnar arrangement and abnormal hypertrophic differentiation in the growth plate [114]. Deletion of *Ift88*

in the early limb mesenchyme during embryonic development resulted in limb and growth plate shortening with accelerated hypertrophic differentiation and polydactyly [86]. When *Kif3a*, a subunit of the Kinesin II motor complex that is required for IFT and the formation of primary cilia, and *Ift88* were deleted in separate mouse lines via *Col2a*-Cre-mediated recombination, a premature loss of the growth plate and dwarfism was observed at P30. This was due to reduced proliferation and accelerated hypertrophic differentiation of chondrocytes [88]. These earlier deletions match the growth plate shortening phenotype in this project, suggesting the mice might have been physiologically younger than mice used in Coveney et al. (2022).

The ratio of number of cells in the different zones of the growth plate did not change with *Ift88* cKO, suggesting the relative zone sizes did not change. There may nevertheless be disruptions in transitions between cell zones. The transition from resting to proliferating to hypertrophic may be accelerated, which would lead to the growth plate narrowing faster. I also observed some cell disorganisation in the *Ift88* cKO growth plate compared with the $Ift88^{\mathrm{fl/fl}}$ growth plate, particularly in the proliferating zone of the lateral region, with θ_{cell} less skewed around 0° with corresponds to a horizontal orientation (Fig. 4.4 C). This is in line with the described observations of the growth plate disorganisation with ciliary disruption in previous studies. In addition, despite inverted phenotypes, Coveney et al. (2022) also observed the most disruptions in the peripheral regions of the growth plate compared with the middle, particularly with disruption in the cellular organisation in the hypertrophic zone [47].

The *Ift88* cKO had smaller hypertrophic chondrocytes than $Ift88^{\mathrm{fl/fl}}$ (Fig. 4.4 A, B). Smaller hypertrophic chondrocytes would shorten the length of the growth plate. A growth differentiation factor 5 knockout mouse also presents reduced hypertrophic volume, abnormal cell orientation and column formation in the growth plate, resulting in shorter limbs [241].

As Indian Hedgehog (Ihh) signalling is crucial for skeletal development and its key components are localised to the primary cilium, many ciliary deletion studies have measured Ihh signalling in phenotypes. Ihh is a pro-proliferation signal, therefore loss of cilia and subsequently of Ihh should lead to loss of proliferation and shortening in the growth plate. Conditional postnatal deletion of Ihh in chondrocytes leads to loss of columnar structure, premature vascular invasion, ectopic hypertrophic chondrocytes, destruction of the articular surface and premature fusion of the growth plate, ultimately resulting in dwarfism [271–274].

In this study, Ihh signalling was not measured, though it may be involved in the *Ift88* cKO phenotype observed as some of the changes in the growth plate are reminiscent of Ihh deletion studies. Changes in Ihh signalling has been observed in murine ciliary deletion phenotypes. Reduction in *Ptch1* expression was measured in pre-hypertrophic chondrocytes embryonically but not postnatally in *Kif3a* deficient mice [88]. Deletion of *Ift88* in the post-natal growth plate was associated with a small increases in *Gli1* expression, predominantly in the non-hypertrophic chondrocytes with no differences in observed between the peripheral to middle regions [47]. These differences between embryonic and post-natal observations suggest Ihh may have distinct role postnatally compared with during embryonic development.

There is recent evidence that Ihh promotes epiphyseal skeletal stem cells proliferation, providing a continuous cell source for the growth plate [275]. This points to a novel role for Ihh in a different region of the growth plate. It is yet to be determined how primary cilia are involved in this pathway, however this signalling may contribute to the phenotypes observed with ciliary gene deletions.

Percentage ciliation in the *Ift88* cKO

Despite deleting a key ciliary protein, *Ift88*, whose deletion should prevent ciliogenesis, only small changes in ciliation were observed in the growth plate (Fig. 4.5). The hypertrophic zone of the lateral region was the only area of notable change with a

small reduction in percentage ciliation. As mentioned previously, the hypertrophic zone of the peripheral region of the growth plate is also the region with the most disruption in the *Ift88* deletion in Coveney et al. (2022) [47].

The previous study deleting *Ift88* in the growth plate showed a reduction in percentage ciliation from ~40% to ~35% at 10 weeks. This was measured by acetylated α-tubulin staining [47]. Chondrocytes from the *Ift88* hypomorphic line (*orpk*) do not ciliate when cultured in 2D [231]. In *orpk* mice, growth plates are shorter and characterised by changes in cellular organisation. In particular, hypertrophic chondrocytes failed to differentiate. This was accompanied by a reduction in cilia numbers and lengths. This suggests that cilia structural disruption affects chondrocyte differentiation [81]. Deletion of *Ift88* in oligodendrocyte progenitor cells resulted in a ~90% reduction of ciliated cells compared with controls [263]. Similarly, deletion of *Ift88* in tendons resulted in a 64% decrease in percentage ciliation [264]. Deletion of kinesin subunit *Kif3a* reduced cilia numbers in the embryonic and newborn growth plates [88].

The method for measuring percentage ciliation used here covers thousands of cells, a larger scale than used in previous studies, and uses an endogenous ciliary signal as opposed to IHC. Therefore, I may have detected cilia that weren't detected in previous methods. In addition, the timing of the deletion and mouse line may explain the difference in data. In any case, in my model, *Ift88* deletion in the adolescent growth plate does not lead to a large reduction in overall percentage ciliation, only small changes in certain regions, particularly the hypertrophic zone of the lateral region (Fig. 4.5 E).

A limitation of this study concerns the confirmation of *Ift88* deletion at the molecular level in the *Ift88* cKO. While the growth plate phenotype suggests partial ciliary disruption, the absence of direct validation through mRNA transcript (qPCR) or protein (Western blot or immunostaining) measurements means that the extent of *Ift88* loss in the targeted tissue cannot be definitely established. Incomplete recombination following tamoxifen induction could have resulted in residual IFT88

expression, leading to a mixed population of ciliated and non-ciliated cells. This would attenuate observable differences in cilia orientation and prevalence between control and cKO groups. Future studies should therefore include quantitative assessment of *Ift88* expression at both mRNA and protein levels in the growth plate to verify recombination efficiency and strengthen the interpretation of ciliary phenotypes.

Primary cilia length in the *Ift88* cKO

As with the controls, the *Ift88* cKO growth plates had longer primary cilia in the hypertrophic zone of the growth plate (Fig. 4.6). This difference is particularly marked in the middle region. This absence of change in cilia length suggests that a dysfunctional IFT88 does not shorten the ciliary axonemal length. A study comparing the ciliary length between of *Smad1/5*cKO with wild-types found no difference between the two groups [210].

The longest cilia and lowest percentage ciliation are in the hypertrophic region. This is also the most disrupted zone in terms of cellular organisation in *Ift88* cKO in Coveney et al. (2022) [47]. Therefore, the cilia in this zone may be particularly affected sensitised to loss of IFT88 function.

The growth plate phenotype observed indicates that there is disruption in IFT88 function. The cilia may therefore be structurally unchanged but functionally defective. This phenomenon has been observed in previous studies. Cells isolated from an *Ift80* hypomorphic mouse line displayed no change in cilia presence and structure, despite the mouse presenting with growth retardation and polydactyly, and disrupted Hh signalling [118]. The authors propose a "threshold model of *Ift80* requirement", whereby "low to mid level expression as seen in hypomorphs of this line is sufficient for normal ciliation (...), but leads to disruption of the Hh signalling pathway and thus to perinatal lethality and skeletal malformations. Wild-type levels of Ift80 are required for efficient Hh signalling and therefore for development to proceed normally".

This suggestion that ciliation is less sensitive to reduction in *Ift80* levels than Hh signalling may apply to *Ift88* as well. *Ift88* null mutations are embryonically lethal, therefore total loss of gene expression is not viable. This suggests that the Cre mediated deletion used here causes only partial loss of gene function, which may be sufficient for primary cilia formation but with defective function. Hh signalling was not measured in this study but would be interesting to determine whether this signalling pathway plays a role in the phenotype observed.

This also brings forward the question of whether the amount of Ift88 directly regulates cilium length. IFT anterograde train size (associated IFT proteins and their motor proteins) have been linked to rate of axonemal assembly in alga flagellar [276]. Changes in IFT88 abundance have been positively correlated with variations in length of primary cilia. In particular, IFT88 silencing resulted in shortened cilia and cells that overexpressed IFT88 had longer primary cilia in renal cells and chondrocytes *in vitro* [277, 278]. In motile cilia, it has been suggested that IFT directs dynamic length changes and differences in length may reflect differences in signalling capabilities [279].

Therefore, there is evidence linking IFT abundance and cilia length. This needs to be investigated further in the growth plate and for IFT88 in particular. For example, IFT88 staining on the growth plate sections could identify whether the signal is continuous along the axoneme or if there are breaks which could suggest that the IFT machinery and ciliary trafficking is disrupted.

In addition, *Ift88* deletion may have non-ciliary effects that cause the growth plate phenotype. IFT88 has been shown to regulate actin assembly and dynamics, altering cell mechanical properties [81, 280]. These altered biomechanics may influence the response of chondrocytes in the growth plate to mechanical force, contributing to the phenotype.

IFT88 has also been shown to regulate the activity of Yes-Associated Protein (YAP), a key effector in the Hippo signalling pathway, and downstream BMP in zebrafish and mouse models, independently of primary cilia. Proper YAP modulation by IFT

proteins restricts excessive development of tissues during heart formation [281]. YAP distribution has been shown to be altered in immobilised embryonic joints, which could be accompanied by IFT88 disruption [282].

Primary cilia 3D orientation in *Ift88* cKO

I found no statistically significant difference between the organisation of primary cilia in *Ift88* cKO and *Ift88*$^{fl/fl}$ (Fig. 4.7). Primary cilia are therefore also pointing forwards and backs, slightly up and down, with an absence of cilia pointing in the lateral and medial directions (left and right) (Fig. 3.12 A).

The study that compared *Smad1/5* cKO with wild-types found differences in cilia organisation with wild-type ϕ_{cilium} values clustering around 10° and 80° and *Smad1/5* cKO ϕ_{cilium} only clustering around 80°. Since the *Smad1/5* cKO had disorganised growth plate, they suggest the clustering at 10° contains the information for columnar organisation of cells [210]. This effect was not observed in my study, suggesting that *Ift88* deletion may not disrupt the upstream signalling or structural cues required for cilia orientation in the same way as perturbations to *Smad1/5* signalling. Alternatively, the persistence of 3D cilia orientation could indicate compensatory mechanisms maintaining spatial cilia polarity despite the loss of IFT88 or a threshold level of residual IFT88 function in the cKO model. It is also possible that while IFT88 is required for cilia formation and function, it may not be essential for maintaining orientation once cilia are formed, particularly in postnatal tissues where orientation cues are already established. Differences in timing, extent of recombination or genetic background could also contribute to the discrepancy.

siRNA knockdown of *Ift88* in neuronal precursors resulted in a reduction in percentage ciliation and cilia length and disrupted orientation, with fewer pointing 'vertically' (into the mounting media), ultimately leading to fewer neurons differentiating [283]. Different organs have different ciliary functions, with therefore relative importance of orientation depending on tissue-specific signalling and spatial organisation. In the

nervous system, cilia orientation may be critical for sensing morphogen gradients along defined tissue axes during neurogenesis. In contrast, in the growth plate, the preservation of ciliary orientation despite loss of IFT88 may reflect a reduced dependence on directional ciliary signalling for differentiation or the presence of redundant mechanisms guiding spatial organisation.

Centriole position in the *Ift88* cKO

Similarly to primary cilia orientation, no change in position of centrioles in the cell was observed when comparing *Ift88*$^{fl/fl}$ and *Ift88* cKO growth plates (Fig. 4.9). This may indicate that centriole positioning is regulated independently of IFT88-mediated ciliary trafficking. Whilst the extent of column orientation was not quantified in this study, upon observation the *Ift88* cKO did not seem to have less of a columnar organisation compared with *Ift88*$^{fl/fl}$ (Fig. 4.3). Therefore, as centriolar positioning is key for establishing cell polarity, I do not expect a disruption of centriolar positioning in the absence of disruption in cell polarity in the *Ift88* cKO.

Nevertheless, there is some evidence of IFT88 being involved in establishing cell polarity. In both ciliated and non-ciliated proliferating cells, IFT88 remains closely associated with the centrosomes throughout the cell cycle. IFT88 localises to the spindle poles during mitosis formed by centrosomes during mitosis, when cells are not ciliated, and play a role in guiding spindle orientation and regulating cell cycle progression [84, 284]. IFT88 is also required for establishing epithelial planar cell polarity. In an *Ift88* cKO, the centrioles were mispositioned and the basal body misaligned during the establishment of cell polarity in the mouse cochlear [83]. The study suggests that *Ift88* essential for directing orientation of the basal body in this tissue. In addition, non-dividing cells showed improper positioning of their centrosomes with *Ift120* disruption in kidney cells [145].

Mutations directly targeting centrosomal genes do have an affect on growth plate chondrocyte organisation. Mutations affecting centriolar gene *Poc1a* disrupt mi-

crotubule organisation, leading to abnormal chondrocyte morphology, increased apoptosis and loss of the columnar structure in the growth plate, highlighting the importance of centrosome integrity for proper division plane orientation [285].

Kinesin-1 subunit mutation changed centrosome position from anterior to central and posterior, and disrupted stacking of chondrocytes in craniofacial cartilage [286]. The preserved centriole position in the *Ift88* cKO suggests that centrosome orientation in the growth plate may be more resilient to loss of ciliary trafficking than to disruption of kinesin-based transport. It is possible that centrosome positioning is already stabilised in postnatal growth plate chondrocytes via ECM constraints or cytoskeletal anchoring, and that IFT88 is not essential for maintaining this arrangement once established. Timing of *Ift88* deletion (postnatal) may allow for establishment of centriole position during early development, with maintenance being less reliant on the protein later on.

Cell proliferation

To determine whether the reduction in percentage ciliation observed in the hypertrophic zone of the *Ift88* cKO was due to impaired IFT88 function or reduced proliferation (dividing cells don't ciliate), Ki-67 staining was performed on the growth plate (Fig. 4.11). Ki-67 is a well-established marker of cell proliferation, expressed during all active phases of the cell cycle but absent in quiescent cells [265]. The percentage of Ki-67 positive cells was the same between controls and cKO - ~33%.

The percentage of Ki-67 positive cells in E14.5 and 3 week-old growth plates was 15 to 20% and 25%, respectively [48, 287]. These numbers are lower than the ones measured here in the 6 week-old growth plate. The discrepancy could be due to Ki-67 positive cells detection methods, which can produce variable depending on the threshold for positivity set. Here, the Ki-67 staining was used for comparing the *Ift88*$^{fl/fl}$ and *Ift88* cKO values. Since the same detection method was applied consistently to both groups, the comparative results can be considered reliable.

As there is no difference in number of Ki-67 positive cells between *Ift88*$^{fl/fl}$ and *Ift88* cKO, the reduction in percentage ciliation is not due to altered proliferative capacity of chondrocytes and that both control and cKO chondrocytes maintain similar cell cycle activity. This implies that IFT88 is directly required for either the formation or maintenance of primary cilia in growth plate chondrocytes, independent of their proliferative state. It also argues against cell cycle–dependent deciliation being the primary driver of the ciliation phenotype. The shortening in the growth plate is thus also not due to reduced proliferation, as has been in other ciliary knockouts [88].

4.4.2 Effect of mechanical loading on growth plate cell and primary cilia organisation

While *Ift88* deletion disrupts cilia structure genetically, mechanical offloading represents a physiological perturbation of the ciliary signalling environment. To understand whether these distinct forms of interference lead to similar or different phenotypes, I next turned to analysis of offloaded and contralateral growth plates.

Effect of changes in mechanical loading on growth plate length

Offloaded *Ift88*$^{fl/fl}$ growth plates were shorter than *Ift88*$^{fl/fl}$, approximately the same length as *Ift88* cKO growth plates (Fig. 4.12). In comparison, the contralateral limbs to the offloaded limbs, which can be assumed to be experiencing increased load, had the same length as *Ift88*$^{fl/fl}$. Therefore, the absence of load mimics the phenotype of *Ift88* cKO, and accelerates growth plate shortening.

When the same double neurectomy surgery was performed in 8 week-old mice, a small increase in growth plate length was observed 2 weeks later at 10 weeks. Contralateral growth plates were longer than offloaded, but also longer than controls [47].

In the *Ift80* hypomorphic mouse (*orpk)*, the embryonic growth plates have a disrupted organisation and at birth mice were the same size as wild-type [118]. A difference in

size appeared three weeks later, perhaps under the effect of ambulatory load as the mice started to move around, pointing to a mechanical sensitivity of the growth plate. Fibroblasts isolated from this mouse presented no structural defects however the cilia in the growth plate were not imaged. Similarly, although cilia are already reduced in the cartilage of *Col2a-Cre;Kif3a*$^{fl/fl}$ mice by E15.5, disruptions in growth plate organisation were not observed until 7 to 10 days after birth [88]. In both cases, the lag between cilia loss and growth plate disorganisation may, at least in part, reflect the onset of mechanical loading and the cells' inability to respond appropriately due to dysfunctional cilia during a critical developmental window.

The impact of altered mechanical loading during growth has been examined in previous studies - there is evidence both for growth plate narrowing and growth plate expansion. Two-day old chickens holding an extra 10% of their bodyweight for 4 days had narrower growth plates with decreased proliferation, abnormal differentiation and cell morphology, leading to shorter tibias. The growth plate also presented increased *Ift88* expression and cilia prevalence in the growth plate as measured by acetylated α-tubulin IHC [49, 288]. Growth plate narrowing due to mechanical loading is coupled with reduced collagens types II and X expression [289].

Medium and high impact loading on 4 week-old rats for 7-8 weeks also had shorter tibias, but with expanded growth plates [290, 291]. The longer growth plates might be explained by the catch-up growth phenomenon, whereby accelerated growth occurs after a period of temporary growth inhibition [292]. Thus, differences in loading regimens affect the growth plate and growth in different ways depending on development stage, time points of measurement and what is measured.

Effect of changes in mechanical loading on cell organisation in the growth plate

The ratios of number of resting, to proliferating to hypertrophic cells was different in offloaded growth plates - they had fewer proliferating chondrocytes compared to

Ift88$^{fl/fl}$ growth plates (Table 4.1). There was however no change in cell volume (Fig. 4.14 A, B). Contralateral growth plates, on the other hand, had relatively fewer resting chondrocytes more proliferating and hypertrophic chondrocytes relative compared to *Ift88*$^{fl/fl}$ growth plates. In addition, only small changes in cell orientation were observed in *Ift88*$^{fl/fl}$ offloaded growth plates compared with *Ift88*$^{fl/fl}$ growth plates (Fig. 4.14 C). The resting zone chondrocytes were inclined more downwards.

Increased mechanical load on 2 day-old chicken growth plates increased the number of cells but decreased the size of cells [288]. Intermittent tensile loading has been shown to significantly increase DNA synthesis (a marker of proliferation) in growth plate chondrocytes *in vitro* [293]. When limbs are paralysed to eliminate mechanical load at P8, growth plates up to 8 weeks later exhibit less proliferation, altered actin cytoskeleton organisation, disrupted column formation and ultimately reduced bone growth [48]. The authors hypothesised that reduced mechanical loading of the growth plate leads to changes in cellular tension, triggering reorganisation of the actin cytoskeleton. This reorganisation may disrupt the columnar arrangement of chondrocytes by altering their rotational behaviour, ultimately contributing to defects in the length and shape of long bones. Due to the observation of reduced number of proliferating cells in the offloaded growth plate in this study, a similar mechanism may be at play.

In *Ift88* cKO the shortening may be due to smaller hypertrophic chondrocytes, whereas in offloaded growth plates it may be due to a reduced number of proliferating cells. This suggests different disrupted mechanisms and signalling pathways.

Using computational modelling, one group identified the emergence of stress anisotropy - different stresses experienced in different direction - in the proliferative zone. This anisotropy results from the geometric organisation of chondrocytes into columns and is amplified by chondrocyte hypertrophy. This stress anisotropy is crucial for longitudinal bone growth, reinforcing organised column formation and efficient linear expansion [242]. This biomechanical feedback between cell arrangement, cell growth,

and tissue-level forces is crucial for proper bone morphogenesis. This mechanical stress triggers local signalling changes such as increased expression of Ihh, which is known to promote chondrocyte proliferation and proper column formation. In addition, Hh signalling is mechanosensitive and increases in response to mechanical loading *in vitro*. This increase is not observed in chondrocytes lacking cilia [65].

Effect of changes in mechanical loading on primary cilia in the growth plate

My results show no large difference in primary cilia proportion, length or orientation and centriole position in response to altered mechanical loading postnatally (Fig. 4.15,4.16, 4.17, 4.18). There is polarisation in primary cilia orientation offloaded growth plates, but this preferential orientation is similar to controls.

In contrast, muscle-less mutant (immobile) embryos (E14.5) have shorter cilia in humerus chondrocytes compared with wild-type with no significant difference in the proportion of ciliated cells [244]. The wild-type positional bias of cilia bases - away from the joint in the resting zone and medially in the proliferative zone - was preserved in mutants. However, in the hypertrophic zone, the medial bias positioning seen in wild-type was lost, with cilia shifting laterally or proximally. The wild-type bimodal proximal-distal orientation in the resting zone was also lost in mutants, while the random orientation seen in the proliferative zone remained unchanged.

This suggests that while embryonic cilia dynamics may be sensitive to early muscle-generated forces, primary cilia in the postnatal growth plate are more resistant to mechanical perturbation, potentially reflecting developmental stage-specific mechanosensitivity. Mechanical forces acting on the growth plate increase substantially after birth, due to weight-bearing and limb use. As a result, postnatal chondrocytes may experience a higher baseline level of mechanical input, making them less sensitive to relative changes in load. Alternatively, it is possible that cilia architecture becomes more stable or less plastic after embryonic development, reflecting a shift in how chondrocytes sense and respond to mechanical cues at different developmental stages.

Previous studies have shown that mechanical loading can influence primary cilia orientation and structure in other connective tissues. As discussed in Chapter 3, superficial articular cartilage chondrocytes point their primary cilia away from the articular surface in load-bearing conditions, a distinct orientation that is not seen in non-load bearing regions [81, 141]. Similarly, in tendons primary cilia align with the principal loading direction of the tissue, and increased loading reduces cilia number, while unloading increases it. [139, 264]. The lack of such change in cilia organisation in my findings may reflect a greater structural or functional resilience of growth plate chondrocyte cilia to mechanical changes at this developmental stage.

In vitro, mechanical compression of chondrocytes decreased cilia presence and length, suggesting that cilia shortening or resorption may serve as an adaptive mechanism to dampen mechanosensory input under sustained load. [65, 208]. *In vitro* condition are however very different to *in situ*. Exposure of renal duct cells to orbital shaking caused cilia to shorten [294]. The same study determined that the drag force experienced by the cilium is proportional to its length.

Chondrocytes and renal epithelial cells from the *Ift88* hypomorphic mice (*orpk*) had shorter or absent cilia and a blunted increase in intracellular Ca^{2+} concentration in response to mechanical stimulation [295, 296]. These studies link defective cilia-driven mechanotransduction to impaired intracellular calcium signalling, contributing to the ciliopathy-like organ abnormalities observed in this mouse. In growth plate chondrocytes, the results I present here suggest that shorter cilia are not observed in *Ift88* cKO mice, therefore the defective signalling is not translated into defects in structure.

In summary, there are a lot of discrepancies in studies - different phenotypes at different ages, some accompanied by cilia structural disruption, others accompanied by disrupted Hh signalling, others not.

While the *Ift88* cKO and mechanical offloading experiments provided valuable insight into the mechanobiology of primary cilia in the growth plate, several limitations

must be acknowledged. Firstly, the absence of a no-tamoxifen control group limits the ability to fully exclude off-target effects of tamoxifen administration on cartilage and bone homeostasis. Although tamoxifen dosing was consistent across experimental groups, its known influence on metabolism and tissue remodelling may have contributed to subtle phenotypic differences. Secondly, the number of animals in the *Ift88* cKO experiment was relatively high for animal studies (14-18 mice), however only 4 animals were subjected to limb offloading. This limited sample size reduces statistical power and may mask subtle inter-individual variation. In addition, while the offloading model effectively simulated reduced mechanical input, it did not fully capture the dynamic range of physiological loading or compensate for potential stress responses associated with immobilisation. Finally, given that *Ift88* deletion efficiency and recombination timing can vary between cells and anatomical regions, residual ciliated cells may have influenced the observed phenotypes, introducing biological variability. Together, these factors highlight the need for complementary approaches and larger cohorts to further validate and refine these findings.

Together, my findings highlight the complex and context-dependent role of primary cilia in regulating growth plate organisation. While *Ift88* deletion and mechanical offloading both led to subtle but detectable changes in cilia orientation and cell polarity, these phenotypes were not identical, suggesting that cilia contribute to growth plate architecture through both structural and signalling-mediated mechanisms. The broader literature reveals substantial variability across studies, with differing phenotypes reported depending on developmental stage, genetic model and readout. Some were associated with overt structural disruption of cilia, others primarily with impaired Hh signalling, and some showing minimal effects despite clear genetic and tissue perturbation. This variability underscores the importance of precisely contextualising experimental conditions and highlights the need for integrated, multiscale approaches to fully understand how primary cilia mediate the interplay between genetic programmes and mechanical cues during skeletal development.

5

In vitro osteochondral model generation using murine cells

Contents

5.1 Introduction 135

5.1.1 *In vitro* models 135

5.1.2 BMP-2 137

5.1.3 GelMA 138

5.1.4 Buoyancy-driven BMP-2 gradient 140

5.2 Materials & Methods 144

5.2.1 Murine cell isolations &characterisation 144

5.2.2 RNA extraction 146

5.2.3 qPCR 146
5.2.4 Immunophenotypic characterisation by fluorescence-activated cell sorting (FACS) 147
5.2.5 GelMA & HepMA synthesis & characterisation 148
5.2.6 Mechanical testing 149
5.2.7 Buoyancy-based gradient generation 150
5.2.8 Histology 152
5.2.9 Statistical analysis 152
5.3 Results 153
5.3.1 MSC characterisation 153
5.3.2 Costal chondrocyte characterisation 158
5.3.3 Material synthesis and mechanical characterisation . . . 158
5.3.4 3D cell cultures inside gels 159
5.3.5 Gradient generation 165
5.4 Discussion 167
5.4.1 Murine MSC and costal chondrocyte characterisation . . 167
5.4.2 Material synthesis and characterisation 170
5.4.3 3D cell cultures inside gels 171

5.1 Introduction

5.1.1 *In vitro* models

Mouse models are a powerful tool for studying biological processes and disease mechanisms. Their genetic tractability allows for precise disruption of individual genes, enabling investigation of their physiological roles *in vivo*. However, these models also present limitations. Longitudinal studies in mice are both time-consuming

and costly, and experimental control over environmental factors such as mechanical loading is limited. This is particularly relevant in the context of primary cilia research, as these organelles play a key role in mechanotransduction. While mechanical loading can be manipulated in mice - through methods such as treadmill exercise or external loading devices - these approaches offer limited control over the magnitude, direction and precise location of the applied forces.

In contrast, *in vitro* systems provide a more accessible and controllable platform for applying defined mechanical stimuli. *In vitro* models offer a valuable complement to *in vivo* mouse studies, particularly when precise control over experimental variables is required. Among these, three-dimensional (3D) culture systems more closely recapitulate native tissue physiology than traditional two-dimensional (2D) monolayer cultures. By better preserving key cell–cell and cell–extracellular matrix (ECM) interactions, 3D models provide a more relevant environment for studying complex biological processes. Importantly, they also allow for controlled, reproducible perturbations, such as defined mechanical or biochemical stimuli, making them a powerful platform for dissecting specific mechanisms, including those involving primary cilia.

In order to combine the advantages of mouse and *in vitro* models, previous studies have used mouse cell lines or primary cells in 3D models of various organs [152, 185, 188, 297]. In particular, the mouse lines in this project offered the possibility of deleting a key ciliary gene, *Ift88*, in a cartilage-specific manner. The *Ift88*$^{fl/fl}$ and *Ift88* cKO presented fluorescent signals for two ciliary proteins - ARL13B and Centrin-2. This makes imaging of primary cilia in tissues or cells more efficient and precise than IHC techniques commonly used. Primary mouse cells are directly isolated from mouse tissues and retain characteristics close to the original tissue, making them biologically relevant for modelling *in vivo* conditions.

As the growth plate represents an interface between two tissues - cartilage and bone - there are many differential signals, expressed as gradients across the growth plate, which orchestrate the tightly regulated process of endochondral ossification.

Therefore it seems particularly relevant to use gradients of growth factors inside models trying to emulate the growth plate. The growth plate's spatial organisation into zones is directed by gradients of morphogens such as indian hedgehog (Ihh), parathyroid hormone-related protein (PTHrP) and bone morphogenetic proteins (BMPs) [298–301]. These gradients establish spatial and temporal cues that govern chondrocyte proliferation, maturation and hypertrophy, ensuring orderly columnar architecture and progressive tissue mineralisation. Disruption of these morphogen gradients can lead to aberrant tissue patterning and skeletal dysplasias. In this way, soluble factor gradients act as instructive signals that shape cellular dynamics and ECM composition. It is the importance of these spatial patterns that make the growth plate particularly challenging to model *in vitro*.

Among the gradient-generation techniques described in the introduction - including 3D bioprinting, microfluidics, and electrospinning - many are associated with high costs and require specialised technical expertise. While numerous gradient fabrication platforms have been demonstrated, they are often limited to single materials with specific properties (for example exact gelation kinetics or magnetic responsivity), molecules or specific tissue types. To meet the needs of a broader research community, there is a growing interest in developing methods that are versatile, cost-effective and applicable across multiple biological systems. One such approach leverages the principle of buoyancy, the upward force exerted by a fluid that on a a less dense object that is immersed in it. By using materials of differing densities, buoyancy can be exploited to generate gradients of growth factors. This method offers a straightforward and accessible alternative for creating gradients without the need for complex or expensive equipment.

5.1.2 BMP-2

BMP-2 plays a critical role early in skeletal development, where it regulates chondrocyte proliferation and maturation. It is particularly important for promoting

longitudinal bone growth by stimulating both the proliferation and hypertrophic differentiation of growth plate chondrocytes. In addition, BMP-2 enhances the expression of osteogenic markers and supports mineralisation in both human and mouse mesenchymal stem cells (MSCs) [302–307]. Creating a gradient of BMP-2, with higher concentrations in specific regions, can be used to drive spatially patterned differentiation. Areas with high BMP-2 concentrations would promote chondrogenic and osteogenic differentiation, while areas with lower concentrations could help maintain cells in a less differentiated or more proliferative state. This makes BMP-2 particularly valuable in *in vitro* cartilage models, where it is widely used to promote ECM synthesis, sustain proliferation and induce robust osteogenic and chondrogenic phenotypes [308, 309].

Li et al. (2019) have developed a buoyancy-driven BMP-2 inside a gelatin methacryloyl (GelMA) seeded with human MSCs [174]. This setup promoted site-specific osteogenesis and mineralisation, mimicking the complex structure of the osteochondral interface.

5.1.3 GelMA

Gelatin methacryloyl (GelMA) has emerged as a promising biomaterial for osteochondral applications due to its combination of biological functionality and tunable mechanical properties. Derived from gelatin, a denatured form of collagen primarily obtained from collagen type I, GelMA is synthesised by functionalising gelatin's amine-containing side groups with methacrylate groups (Fig. 5.1 A). This chemical modification enables GelMA to undergo photoinitiated crosslinking, forming stable hydrogels upon exposure to ultraviolet (UV) in the presence of a suitable photoinitiator (Fig. 5.1 B) [310, 311]. The photoinitiator converts the light energy into chemical energy in the form of free radicals and reactive cations, which then initiates the polymerisation of GelMA.

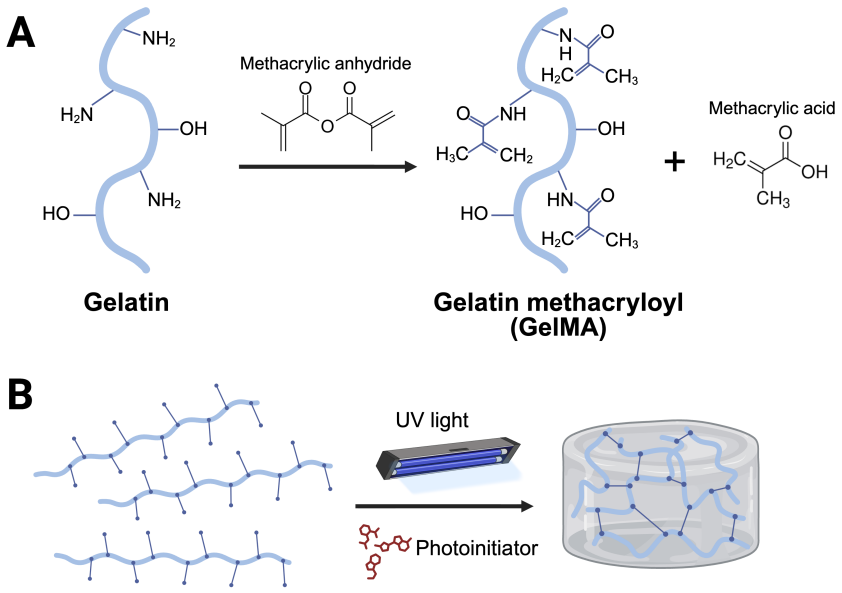


Figure 5.1: (A) GelMA synthesis with methacryloyl substitution. (B) GelMA photocrosslinking with UV light in the presence of a photoinitiator.

Although the methacrylation and hydrolysis processes partially disrupt the native structure of collagen, GelMA retains some properties of collagens and gelatin. These include cell-adhesive motifs and enzymatic degradability, which promote cell attachment, migration and matrix remodelling. As such, GelMA offers many of the biological advantages of natural ECM-based materials, while also allowing the precision and customisation characteristic of synthetic hydrogels [312].

One of GelMA's most attractive features is its versatility. It can be cast, moulded or 3D bioprinted into complex geometries. Its mechanical stiffness and degradation rate can be finely tuned by varying the degree of methacrylation, photoinitiator concentration or polymer concentration. It is cost-effective and readily derived from animal sources such as porcine or bovine skin. These properties make GelMA well suited for cartilage tissue engineering.

5.1.4 Buoyancy-driven BMP-2 gradient

In the model developed by Li et al. (2019), the top layer of the construct contains a GelMA-HepMA-BMP-2 complex (Fig. 5.2 A). Methacryloyl-modified heparin (HepMA) allows for covalent crosslinking with itself and the surrounding GelMA matrix, thereby stabilising the hydrogel structure. Importantly, HepMA also binds BMP-2 through electrostatic interactions, enabling controlled release of the growth factor over time and presentation of growth factor to cells in a manner more similar to that of nature (bound to matrix) [313]. The bottom layer consists of GelMA mixed with Ficoll, a density modifier that increases the density of the solution. Both layers contain embedded MSCs. Upon injection of the less dense, BMP-2-loaded top layer into the denser bottom layer, a gradient is formed, with a high concentration of BMP-2 at the top that progressively decreases towards the bottom (Fig. 5.2 B).

BMP-2 is locally and gradually released from the hydrogel over a 28-day period, maintaining a sustained concentration gradient throughout the *in vitro* culture. Embedding the growth factor directly within the scaffold mitigates the need for repeated replenishment and enables a more physiologically relevant, sustained release. Meanwhile, soluble transforming growth factor β (TGF-β) present in the culture medium induces general chondrogenesis across the construct, while the BMP-2 gradient drives a localised osteogenic response in MSCs.

Li et al. (2019) provided a proof-of-concept for this system, demonstrating its functionality using cell viability assays, histological staining, immunofluorescence for collagen type II and osteopontin, and mineral composition analysis via Raman spectroscopic imaging at one time point only (28 days) [174]. However, further characterisation is needed to fully assess its potential as an *in vitro* model of endochondral ossification, mimicking elements of the growth plate. Future work should examine gene expression profiles, cellular phenotypes, tissue architecture, and long-term stability to better evaluate its physiological relevance and applicability.

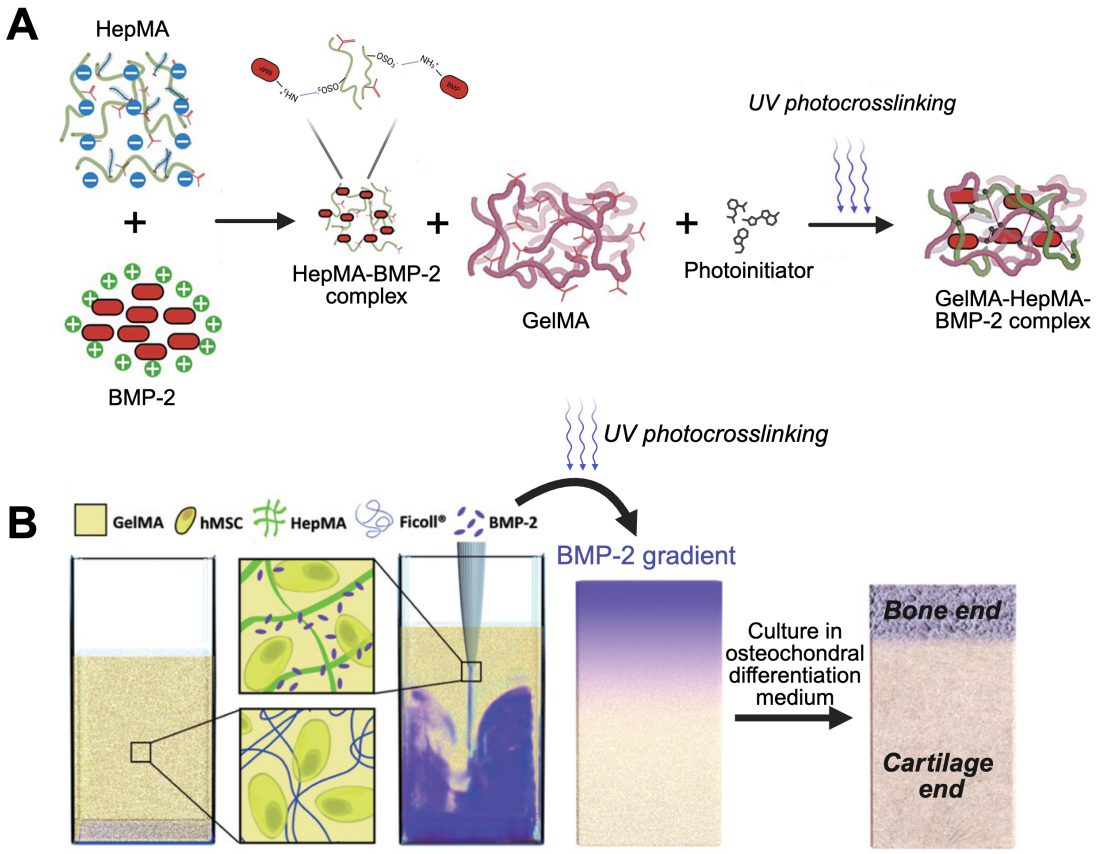


Figure 5.2: Schematic overview of the fabrication and application of a BMP-2 gradient hydrogel system for osteochondral tissue engineering. **(A)** HepMA is mixed with BMP-2 to form a complex, which is then combined with GelMA and photocrosslinked under UV light in the presence of a photoinitiator to generate a stable hydrogel complex. Modified from [195]. **(B)** Buoyancy-driven generation of a BMP-2 gradient. The GelMA-HepMA-BMP-2 complex mixed with MSCs is injected into a GelMA-MSC base containing the density modifier Ficoll layer, at a rate of 17 µL/s . Photocrosslinking preserves the gradient inside the hydrogel. The construct is cultured in osteochondral differentiation medium, producing a model with distinct bone- and cartilage-like regions aligned with the BMP-2 gradient. Modified from [174].

Thus, the aim of this part of the project was to build upon this buoyancy-driven BMP-2 gradient model to develop an osteochondral model of the growth plate. This *in vitro* system was designed with the purpose of investigating the role of primary cilia in coordinating cellular responses to mechanical loading during endochondral ossification. To enable genetic manipulation of cilia function, I used cells derived from the *Ift88*$^{fl/fl}$ and *Ift88* cKO mouse lines used in Chapters 2, 3, 4. These lines provide a robust tool for studying the contribution of the primary cilium to growth

plate biology via targeted gene disruption.

By adapting the BMP-2 gradient model for use with murine cells, I aimed to create a system that could complement *in vivo* findings and allow systematic exploration of how mechanical cues influence cilia organisation and function. To achieve this, I set out the following objectives:

- **Assess the feasibility of replacing human MSCs with murine MSCs in the BMP-2 gradient system.** The original BMP-2 gradient platform was optimised for human MSCs, which differ from murine cells in adhesion, proliferation rate and responsiveness to morphogens. Establishing whether murine cells can survive, proliferate and differentiate under similar hydrogel and gradient conditions was therefore essential. This step involved testing cell viability, morphology and early differentiation markers to determine whether the system could be directly translated or required modification of the GelMA concentration, photoinitiation conditions or BMP-2 dosing.

- **Identify the most suitable source or type of murine MSCs or progenitor cells for this application.** Several murine cell populations could potentially recapitulate the chondrogenic or osteogenic potential of human MSCs, including bone marrow and adipose-derived MSCs, and costal chondrocytes. Comparative analysis of these sources was designed to determine which most closely reproduces native cellular responses relevant to endochondral ossification. The chosen cell type needed to balance accessibility, stability in culture and yield.

- **Evaluate the behaviour of murine cells in a 3D GelMA hydrogel environment across culture time through quantitative polymerase chain reaction (qPCR) and histology stains.** To confirm the biological relevance of the adapted system, I aimed to monitor temporal changes in gene expression and matrix deposition during culture. qPCR assays targeted chondrogenic and osteogenic markers (e.g., *Col2a1*, *Sox9*, *Runx2*, *Col10a1*),

while histological stains such as safranin-O, alcian blue and alizarin red were used to visualise ECM composition and mineralisation. This would establish whether murine MSCs could maintain viability and lineage progression within a 3D microenvironment, providing a functional readout of how BMP-2 gradients shape differentiation outcomes.

- **Characterise the formation and stability of the BMP-2 gradient within the model.** Reliable generation and maintenance of a spatial BMP-2 concentration gradient are critical for linking biochemical patterning to ciliary and cellular responses. I therefore aimed to quantify the gradient profile using fluorescently labelled BMP-2.

5.2 Materials & Methods

Unless stated otherwise, all chemicals used were from Sigma Aldrich.

5.2.1 Murine cell isolations & characterisation

Unless otherwise stated, cells were cultured in complete growth medium (CGM) composed of MEMα GlutaMAX (ThermoFisher) supplemented with 10% FBS (ThermoFisher) and 1% penicillin-streptomycin (Penstrep), at 37°C, 5% CO_2. Cells were isolated from two mouse lines: *AggrecanCreER^{T2};Ift88$^{fl/fl}$;Centrin-2-GFP.ARL13b-mCherry* (*Ift88* conditional knockout (cKO)) and *Ift88$^{fl/fl}$;Centrin 2-GFP.ARL13b-mCherry* (*Ift88$^{fl/fl}$*) [47, 211].

Isolation of murine bone marrow-derived MSCs (BM MSCs)

Femurs and tibias were collected from 3 to 6 week-old mice. The epiphyses were removed and the bone marrow flushed out with CGM. Cells were purified using the Direct Lineage Cell Depletion Kit (Mulenyi Biotec) to deplete mature haematopoietic cells and their precursors. The cells were then seeded and cultured in CGM supplemented with 10 ng/mL FGF-2 (R&D Systems) [314].

Isolation of murine adipose-derived MSCs (AD MSCs)

The epididymal adipose tissue of 4 to 6 week old male mice was collected and digested in 4 mg/mL collagenase A in Hank's Balanced Salt Solution (ThermoFisher) for 45 minutes at 37°C. The cell suspension was passed through a 70 µm filter and plated.

Costal chondrocytes isolation

The ribs (without spine) from 3 to 4 week old mice were isolated, removing as much surrounding soft tissue as possible, and digested in 3 mg/mL collagenase type II (Worthington Product Corporation) in serum-free MEMα, GlutaMAX on a shaker at 37°C for 45 minutes followed by 6 hours in 0.5 mg/mL collagenase type II. The cell suspension was then passed through a 70 µm filter and plated.

Colony forming units (CFUs)

MSCs were plated at 50 cells/cm^2 and allowed to grow for 14 days before fixing with 4% paraformaldehyde (PFA) and staining with crystal violet.

Trilineage - Osteogenic and adipogenic differentiation

Once MSCs reached 80% confluence in CGM, the medium was changed to differentiation medium for 21 days. Control plates were cultured in CGM for 21 days.

For osteogenic differentiation, cells were cultured in osteogenic medium containing Dulbecco's modified eagle medium (DMEM) high glucose supplemented with 10% FBS, 1% penstrep, 50 µg/mL L-ascorbic acid, 10 mM β-glycerophosphate and 100 nM dexamethasone [315, 316]. Control wells were cultured in CGM.

For adipogenic differentiation, cells were cultured in adipogenic medium containing high glucose supplemented with DMEM 10% FBS, 1% penstrep, 1x sodium pyruvate, 1 µM dexamethasone, 500 µM IBMX (3-isobutyl-1-methylxanthine), 1 µg/mL insulin and 100 µM indomethacin [315, 316]. Control well were cultured in CGM.

After 21 days, the RNA was extracted from differentiated cultures for qPCR analysis or cells were fixed with 4% PFA for 15 minutes and stained for alizarin red (osteogenic cultures) and oil red O (adipogenic cultures).

Trilineage - Chondrogenic differentiation

To create MSC pellets, 500,000 cells were spun at 240 g for 5 minutes. Control pellets were cultured in CGM. Differentiated pellets were cultured in chondrogenic differentiation medium containing DMEM high glucose supplemented with 10% FBS, 1% penstrep, 1x sodium pyruvate, 50 µg/mL L-ascorbic acid, 100 nM dexamethasone, 40 µg/mL L-proline, 1x insulin–transferrin–selenium supplement (ITS+1) and 10 ng/mL TGF-β3 (Peprotech) [315, 316]. Cell pellets were with 4% PFA for 15 minutes, embedded in paraffin, sectioned at a thickness of 4 µm and baked at 65°C overnight. Sections were cleared in xylene, rehydrated in graded alcohols, and stained.

5.2.2 RNA extraction

After washing cells with phosphate buffered saline (PBS), the RNA was extracted from the cells using the RNAEasy Mini Kit (Qiagen). Tibial bone and costal cartilage tissue were snap frozen with liquid nitrogen, crushed and added to Trizol. After vortexing, samples were spun down and the supernatant mixed with 1-bromo-3-chloropropane. The samples were incubated for 5 minutes then spun down. The top phase was passed through the RNAEasy Mini Kit. RNA quantity and quality was measured using a NanoDrop Spectrophometer (ThermoFisher). RNA was converted to cDNA using the High-capacity cDNA Reverse Transcription Kit (ThermoFisher).

5.2.3 qPCR

In each well of 384-well plates, Taqman Fast Advanced Mastermix (ThermoFisher), Taqman probe (ThermoFisher), RNase-free water and cDNA were mixed in volumes described in Table 5.1. Technical duplicates were run for each sample. No template controls and blanks were run on the same plate. The plates were run on the

Table 5.1: qPCR reaction mix.

Component	Volume per reaction
Taqman Fast Advanced Mastermix	5 µL
Taqman probe	0.5 µL
RNase-free water	3.5 µL
cDNA	1 µL (= 1 µg)
Total	**10 µL**

QuantStudio 7 Pro Real-Time PCR system. The PCR reaction was held for 2 minutes at 90°C, then cycled 40 times through 35 seconds at 95°C and 20 seconds at 60°C.

To calculate relative expression levels of target genes, the $\Delta\Delta C_T$ method was used [317]:

$$\Delta\Delta C_T = (C_{T,\text{target}} - C_{T,\text{housekeeping}})_{\text{sample}} - \text{Mean}\,(C_{T,\text{target}} - C_{T,\text{housekeeping}})_{\text{control}}$$

$$\text{Fold-change} = 2^{-\Delta\Delta C_T} \tag{5.1}$$

The average CT value of Glyceraldehyde-3-phosphate dehydrogenase (*GAPDH*) and TATA-binding protein gene (*Tbp*) were used as the housekeeping gene CT value. Different housekeeping genes were tested in differentiating MSCs and *GAPDH* and *Tbp* were chosen as they had small variability and represented a gene with high and low expression, respectively (Appendix Fig. 3 A). TaqMan Gene Expression Assay IDs for the genes used can be found in Table 5.2.

5.2.4 Immunophenotypic characterisation by fluorescence-activated cell sorting (FACS)

To analyse the expression of specific cell surface proteins on AD MSCs, flow cytometric analysis was performed. Cells were labelled with the antibodies con-

Table 5.2: qPCR target genes and corresponding TaqMan Gene Expression Assay IDs (ThermoFisher).

Gene	TaqMan Gene Expression Assay ID
GAPDH	Mm99999915_g1
Tbp	Mm01277042_m1
Acan	Mm00545794_m1
Sox9	Mm00448840_m1
Prg4	Mm01284582_m1
Col2a1	Mm01309565_m1
Col10a1	Mm00487041_m1
Sp7	Mm04209856_m1
Runx2	Mm00501584_m1
Col1a2	Mm00483888_m1
Bglap	Mm03413826_m1
Spp1	Mm00436767_m1
Alpl	Mm00475834_m1
Ift88	Mm00493664_m1
Gli1	Mm00494654_m1
VegfA	Mm00437306_m1
Pparg	Mm00440940_m1
Fabp4	Mm00445878_m1

jugated to fluorochromes: APC-Sca-1, PerCP-Cy5.5-CD105, PB-CD45 and PE-CD34(Biolegend). The cells were analysed using the LSR II Flow Cytometer and analysis performed on FlowJo.

5.2.5 GelMA & HepMA synthesis & characterisation

GelMA was synthesised according to Loessner et al. (2016) [311]. Briefly, 5 mL of methacrylic anhydride (MAA) was reacted with 10% (w/v) of gelatin from porcine skin dissolved in deionised water (diH_20) at 55°C, 450 rpm stirring speed, for 3 hours while minimising air exposure to facilitate methacryloyl substitution. Unreacted MAA was removed by centrifugation and GelMA was dialysed against diH_20 for 7 days, freeze-dried and stored at -20°C.

HepMA synthesis was performed as per Benoit & Anseth (2005) [318]. Briefly, 5 g of MAA was added to a 2% (w/v) solution of heparin dissolved in diH_20 and stirred for

24 hours at 4°C, with pH repeatedly adjusted to 8.5 with NaOH. The solution was precipitated in 100% ethanol, dried under reduced pressure, rehydrated in and dyalised against diH_20 for 5 days. The purified HepMA was freeze-dried and stored at -20°C.

To quantify the methacryloyl substitution of unmodified gelatin, GelMA, unmodified heparin and HepMA, nuclear magnetic resonance (NMR) characterisation was performed. 10 mg of each of the freeze dried materials were dissolved in 800 µL deuterium oxide containing 0.05% 3-(trimethylsilyl) propionic-2,2,3,3-d4 acid as an internal standard and the spectra obtained using a 400 MHz, 1H-NMR spectrometer (Bruker).

The MestreNova software was used for NMR analysis. The degree of functionalisation (DoF) of GelMA was calculated according to this equation:

$$\text{DoF} = \frac{\int \text{Gelatin lysine proton peak} - \int \text{GelMA lysine proton peak}}{\int \text{Gelatin lysine proton peak}} \times 100\% \quad (5.2)$$

The DoF of HepMA was calculated according to this equation:

$$\text{DoF} = \frac{\text{Avg} \int \text{Disaccharide proton peaks} - \text{Avg} \int \text{Methacryloyl proton peaks}}{\text{Avg} \int \text{Disaccharide proton peaks}} \times 100\% \quad (5.3)$$

5.2.6 Mechanical testing

10% (w/v) GelMA was prepared by dissolving in 0.25% (w/v) IC2959 photoinitiator in PBS at 37°C for 20 minutes in the dark. Gels were cross-linked with UV lamp for 6 minutes at an irradiance of 6 mW/cm^2 at 365 nm.

Prior to mechanically testing the gels, they were incubated in PBS at 37°C for 24 hours to allow for swelling equilibration. The cross-sectional area of each gel was measured. Gels were mechanically tested using the ElectroForce 5500 (TA Instruments, 200 N load cell) under compression at a speed of 0.2 mm/second until fracture. A -0.01 N preload was applied to ensure contact between the hydrogel and the machine platen.

The Young's modulus is the slope of the elastic region of the stress-strain curve (approximately the first 10%). Stress and strain were calculated following the below equations.

$$\begin{aligned} \text{Stress (kPa)} &= \frac{\text{Load (N)}}{\text{Gel cross-sectional area (mm}^2\text{)}} \times 10^{-3} \\ \text{Strain (dimensionless)} &= \frac{\text{Displacement (mm)}}{\text{Gel height (mm)}} \end{aligned} \tag{5.4}$$

5.2.7 Buoyancy-based gradient generation

To demonstrate the ability to create different gradient patterns using different injection speeds, 1% (w/v) agarose supplemented with 5%(v/v) coomassie blue was injected into a base layer of 2.5% (w/v) agarose using different speeds on an electronic autopipette (Eppendorf). The base and injection layers were injected alone as controls.

To prepare the top layer of the GelMA-based gradient, BMP-2 (R&D Systems) was incubated with 10 µg/mL HepMA at 12.5 µg/mL for 4 hours at 37°C in the dark. The BMP-2-HepMA solution was mixed with 10% GelMA in 0.25% (w/v) IC2959 photoinitiator in PBS and cells at a density of 8 million cells/mL. For the bottom layer, cells were mixed with 10% GelMA in 0.25% (w/v) IC2959 photoinitiator, 50 mg/mL Ficoll in PBS and cells at a density of 8 million cells/mL. Silicone moulds of dimensions 8x4x3 mm were used (Fig. 5.3 A). 30 µL of top layer was injected into 60 µL of the bottom layer at a dispensing speed of 17 µL/s using the electronic autopipette with the 0.1 mL Combitip (eppendorf). The injection was performed

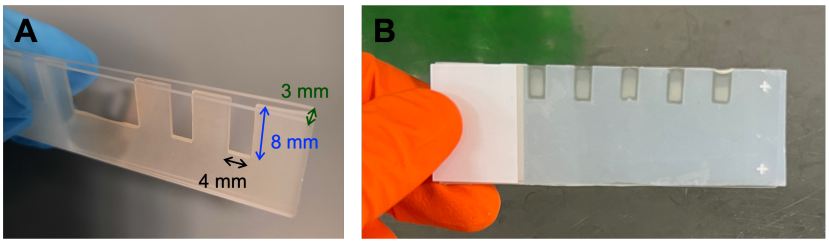


Figure 5.3: (A) Moulds used for the gradient gels - a 3 mm thick silicone sheet fit between two glass slides. (B) Polymerised GelMA gradient gels inside the moulds.

by inserting the tip vertically halfway into the bottom layer and maintaining this position throughout the injection. Gels were cross-linked with UV lamp for 6 minutes at an irradiance of 6 mW/cm^2 at 365 nm (Fig. 5.3 B). The final concentration of BMP-2 in the top layer was 1 µg/mL.

To visualise and quantify BMP-2 inside the gradients, the BMP-2 was replaced with a solution of fluorescein isothiocyanate (FITC)-conjugated BMP-2.

For the non-gradient gels, only the bottom layer without Ficoll or only the top layer containing BMP-2 were pipetted alone inside the moulds. For one condition of the non-gradient gels, 100 ng/mL BMP-2 was added to the culture medium on day 7.

The gels were cultured in osteochondral media containing DMEM high glucose supplemented with 1% penstrep, 50 µg/mL L-ascorbic acid, 2 mM β-glycerophosphate, 1x ITS+1, 100 nM dexamethasone, 50 µg/mL L-proline, and 10 ng/mL TGF-β3 (Peprotech).

Cell viability

Cell viability within the gels was assessed using a live/dead viability/cytotoxicity kit (Invitrogen). After washing with PBS, gels were stained with 2μM Calcein-AM (live) and 4μM ethidium homodimer-1 (dead) for 30 minutes at 37°C in the dark. Gels were imaged with the Olympus BX51 fluorescence microscope with the FITC and Cy3 channels, and analysed with ImageJ.

RNA extraction from 3D gel cultures

After washing with PBS, gels were snap frozen in Trizol at -80°C in tubes containing a TissueLyser bead. After thawing, gels were broken down by mixing at a rate of 15/s for 5 minutes in a TissueLyser (Qiagen). The RNA was subsequently extracted from cells with the same method as the bone and cartilage tissue described above. *GAPDH* was used a the housekeeping gene. Different housekeeping genes were tested in costal chondrocytes cultured in GelMA and *GAPDH* was chosen as it had small variability and high expression (Appendix Fig. 3 B). Compared with MSCs the expression of *Tbp* was too low to use as a housekeeping gene in 3D cultures.

RNA quantity and quality was measured using a NanoDrop Spectrophometer (ThermoFisher). To ensure the extraction of high quality RNA, RNA integrity was assessed by measuring the RNA integrity number (RIN) using the Agilent 2100 Bioanalyzer (Agilent Technologies).

5.2.8 Histology

Gels were fixed with 10% formalin for 30 minutes, embedded in paraffin, sectioned at a thickness of 7 µm and baked at 65°C overnight. Sections were cleared in xylene, rehydrated in graded alcohols, and stained.

5.2.9 Statistical analysis

No statistical analyses were performed in this chapter as the n numbers were often too low and the aim was to make qualitative assessments of whether lineage-specific gene expression could be activated, comparing them with tissue references.

5.3 Results

5.3.1 MSC characterisation

To determine what source of murine MSCs to use in the 3D osteochondral model, both AD and BM MSCs were characterised by assessing their morphology, proliferation capacity, trilineage differentiation potential and surface marker expression.

Both AD and BM MSCs display spindle-like morphology when cultured in 2D on plastic (Fig. 5.4 A, B). BM MSCs cultures contained some cells with a different morphology, suggesting a heterogeneous population.

To measure proliferation capacity of these MSCs, a CFU assay was performed, where AD and BM MSCs were seeded at low density and stained with crystal violet after 14 days (Fig. 5.4 C, D). AD MSCs formed large colonies visible by naked eye, whereas BM MSCs formed few dispersed colonies, indicating a higher proliferation potential for AD MSCs. In addition, AD MSCs had high yields, with cell cultures could easily be passaged and expanded. BM MSCs were slower to grow. AD MSCs yielded on average 270,000 cells per mouse at the first passage, compared with 100,000 cells per mouse for BM MSCs.

To assess differentiation potential, AD and BM MSCs were differentiated down three lineages: adipogenic, osteogenic and chondrogenic. These experiments were done in n of 2 or 3, with the aim of making qualitative assessments of whether lineage-specific gene expression could be activated, comparing them with tissue references. Therefore, no statistical analysis was performed.

In terms of adipogenic differentiation, both AD and BM MSC cultures stained for oil-red O at day 21 of differentiation in adipogenic medium (Fig. 5.5 A, B). Both MSC types also expressed high levels of adipogenesis genes fatty acid binding

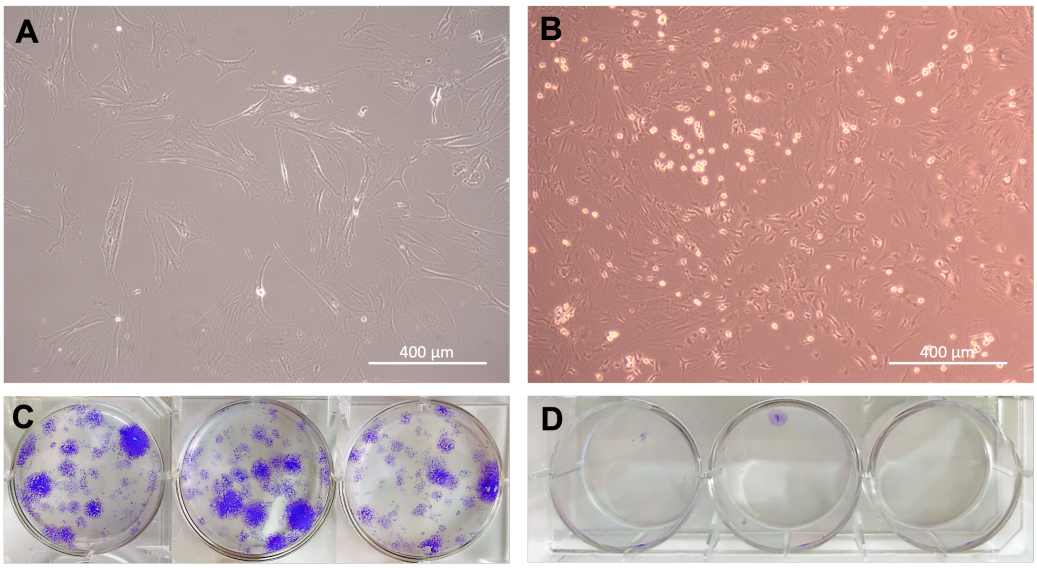


Figure 5.4: Morphology of AD (A) and BM (B) MSCs. Crystal violet staining of AD (C) and BM (D) MSC CFUs after 14 days of culture.

protein 4 (*Fabp4*) and peroxisome proliferator-activated receptor gamma (*Pparg*) when differentiated in adipogenic medium compared with CGM (Fig. 5.5 C).

In terms of osteogenic differentiation, both AD and BM MSC cultures displayed bone nodules that stained with alizarin red after 21 days of differentiation in osteogenic medium (Fig. 5.6 A, B). Gene expression if presented as fold-change from day 1. BM MSCs expressed high levels of osterix (*Sp7*), Runt-related transcription factor 2 (*Runx2*), collagen type I (*Col1a2*) and alkaline phosphatase (*Alpl*) when cultured in osteogenic medium. In BM MSC, *Sp7* and *Alpl* were also upregulated in CGM. AD MSCs expressed higher levels of osteocalcin (*Bglap*) when cultured in osteogenic medium compared with CGM. Both AD and BM MSCs expressed low levels of osteopontin (*Spp1*) in osteogenic media (Fig. 5.6 C). In bone, *Sp7*, *Col1a2* and *Bglap* at orders of magnitude higher than differentiated MSCs. However, in bone *Runx2* and *Alpl* were expressed in the same order of magnitude. *Spp1* was expressed at a lower level in bone compared with differentiated MSCs. This reflects their expression timelines in bone and role in osteogenic differentiation and tissue homeostasis.

For chondrogenic differentiation, MSCs were cultured in pellets as chondrogenesis is enhanced by 3D culture [150]. Yields of BM MSCs were not sufficient to make large

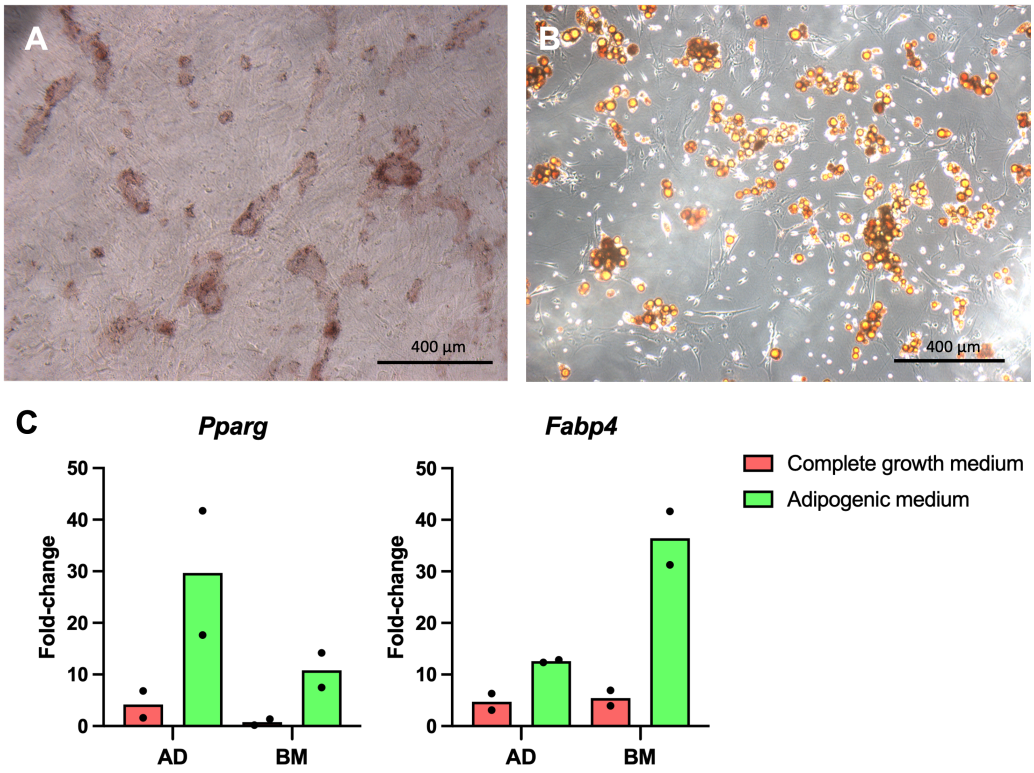


Figure 5.5: Adipogenic differentiation of MSCs. Oil-red O staining of AD **(A)** and BM **(B)** MSC cultures at day 21. **(C)** Expression of adipogenic-associated genes at day 21 of differentiation in CGM and adipogenic medium. Mean of replicates presented as fold-change from day 1. n = 2 (biological replicates).

enough pellets to complete all stainings and perform repeats for gene expression analysis. Staining and gene expression measurement was performed at day 21. AD and BM MSCs pellets stained positively for cartilage histological stains alcian blue, safranin-O and toluidine blue (Fig. 5.7 A). In addition, sirius red staining showed collagen fibres inside the AD MSCs pellets. No signal for aggrecan (*Acan*), collagen type 10 (*Col10a1*) and collagen type 2 (*Col2a1*) were detected in AD and BM MSC pellets cultured in both chondrogenic medium and CGM. AD MSCs expressed higher levels of lubricin (*Prg4*) but lower levels of sex determining region 9 (*Sox9*) in chondrogenic media compared with CGM. *Prg4* and *Sox9* are expressed in low levels in costal cartilage as well.

Murine MSCs were immunophenotyped using FACS analysis for the presence of the MSC markers Sca-1, and CD105 and the absence of haematopoietic markers CD34

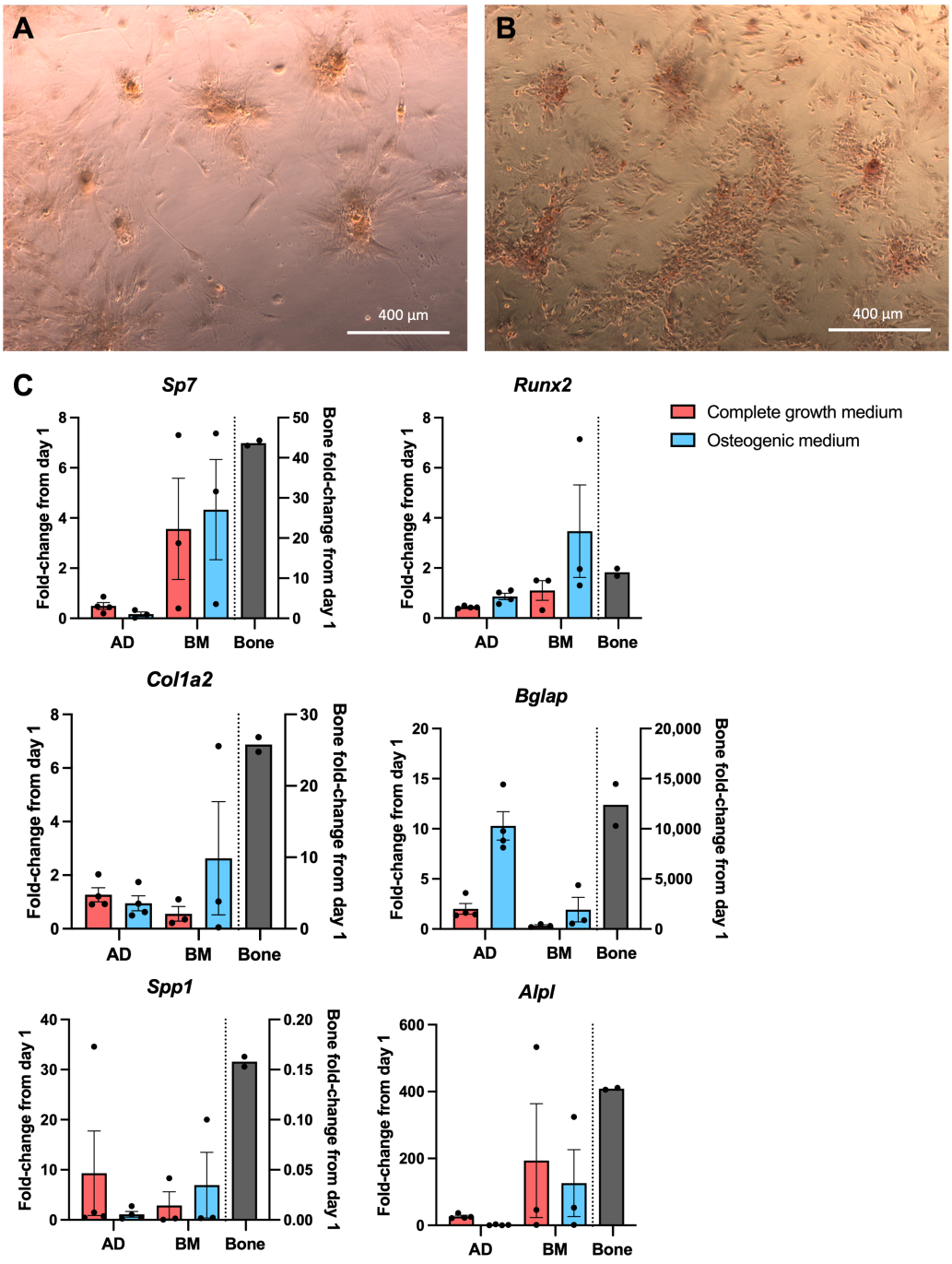


Figure 5.6: Osteogenic differentiation of MSCs. Alizarin red staining of AD **(A)** and BM **(B)** MSC cultures at day 21. **(C)** Expression of osteogenic-associated genes at day 21 of osteogenic differentiation. Whole mouse bones were used as reference for gene expression in bone. Mean ± SEM or mean of replicates when n = 2 presented as fold-change from day 1. n = 2-3 (biological replicates).

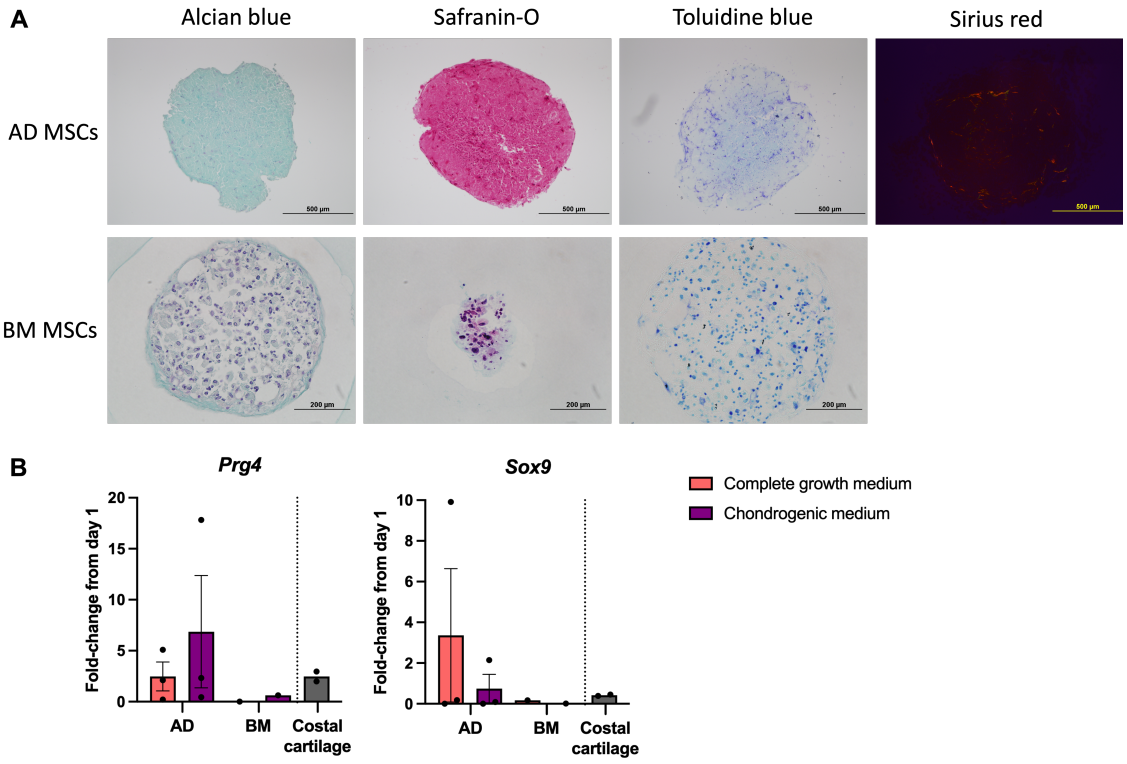


Figure 5.7: Chondrogenic differentiation of MSCs. (A) Staining of pellets after 21 days of chondrogenic differentiation cultures of AD MSCs and BM MSCs in pellets. **(B)** Expression of chondrogenic-associated genes at day 21 of chondrogenic differentiation. Costal cartilage from mice is used as reference for gene expression in cartilage. Mean ± SEM or mean of replicates when n = 1-2, presented as fold-change from day 1. n = 1-3 (biological replicates).

and CD45. 70.3% and 46.3% of AD MSCs stained positive for Sca-1 and CD105, respectively, and 53.9% double positive for Sca-1 and CD105. AD MSCs did not stain highly for haematopoietic stem cell markers: 2.46% for CD45 and 0.14% for CD34 (Fig. 5.8). Yields were not high enough to perform this analysis with BM MSCs.

Due principally to the relative yields of cells, but also bearing in mind their ability to differentiate to bone and cartilage as indicated by stains and typically expressed gene markers, AD MSCs were chosen as the MSC type to use in subsequent experiments in this project.

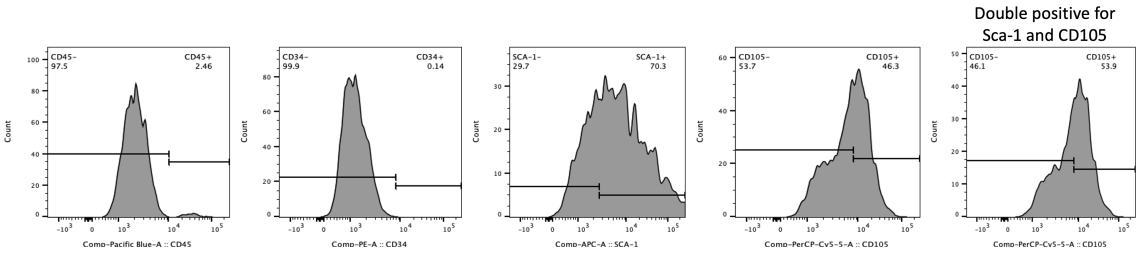


Figure 5.8: Percentage cells stained positive for MSC markers Sca-1 and CD105 and negative control hematopoietic stem cell markers CD45 and CD34. (Performed by Dr Swati Midha).

5.3.2 Costal chondrocyte characterisation

As an alternative to MSCs, costal chondrocytes were isolated from mice. These differentiate into the new bone of the rib cage, therefore go through endochondral ossification like the chondrocytes of the growth plate. When cultured in 2D, in isolated costal chondrocytes expressed *Acan* at the same level as costal cartilage, and *Sox9*, *Prg4* and *Col2a1* at higher levels. *Col10a1* was expressed at a lower level in costal chondrocytes than costal cartilage (Fig. 5.9).

5.3.3 Material synthesis and mechanical characterisation

The degree of functionalisation (DoF) of GelMA and HepMA was quantified by ^{1}H NMR spectroscopy. The GelMA spectrum presents two additional peaks at $\delta = 5.4$ ppm and 5.6 ppm (Fig. 5.10 A, red box), corresponding to methacryloyl linkage compared with the unmodified gelatin spectrum, as well as a decrease in the free lysine peak at $\delta = 2.9$ ppm (Fig. 5.10 A, green box). This confirms the successful methacrylation reaction. For this batch, the DoF of GelMA it was 59.5% and ranged between 45 and 68% across batches. Three batches of GelMA were used in this thesis.

Methacryloyl substitution of heparin was confirmed by the appearance of two peaks at $\delta = 5.7$ ppm and 6.2 ppm in the HepMA ^{1}H NMR spectrum (Fig. 5.10 B, red box) [319]. The DoF of the HepMA batch used was 89.5%.

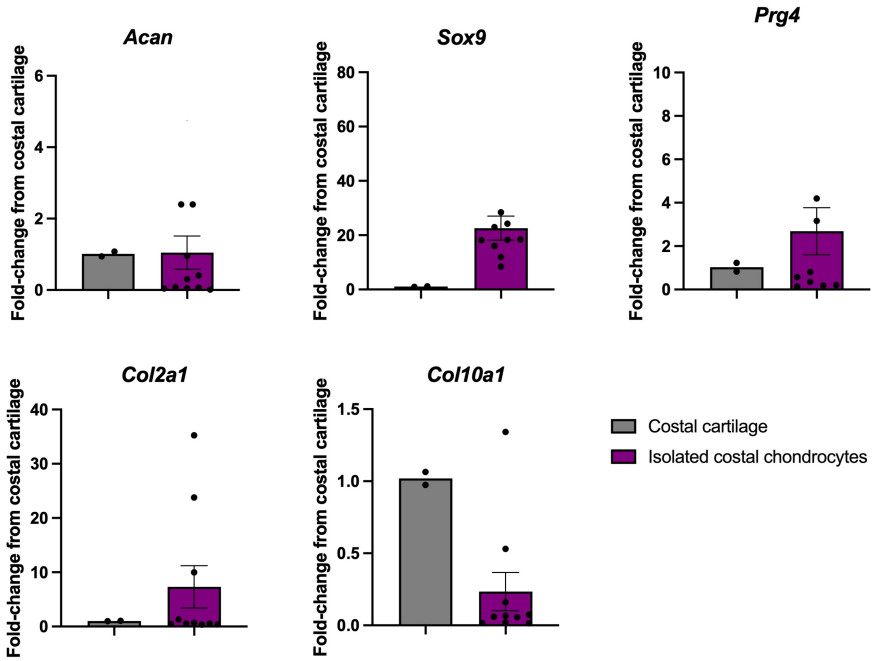


Figure 5.9: Comparative gene expression profiles of chondrogenic markers in costal chondrocytes cultured in flasks after isolation. Mean ± SEM or mean of replicates when n = 2, presented as fold-change from costal cartilage. n = 10 for isolated chondrocytes. n = 2 for costal cartilage (each is pooled tissue from 2 mice) (biological replicates).

A positive correlation was observed between UV gelation time and Young's modulus. The Young's modulus at the UV gelation time used of 6 minutes had a mean of 31.9 kPa (Fig. 5.10 C). A representative stress-strain curve of GelMA under compression is shown in Appendix Fig. 4.

5.3.4 3D cell cultures inside gels

Cell viability

To test cell viability when cultured inside GelMA, a live-dead assay was performed on both AD MSCs and costal chondrocytes cultured inside 10% GelMA in osteochondral medium for up to 42 days (Fig. 5.11). The majority of cells appear positive for the vital dye calcein AM (green) and negative for the cytotoxicity dye ethidium homodimer-1 (red) demonstrating the viability of the cells inside the GelMA con-

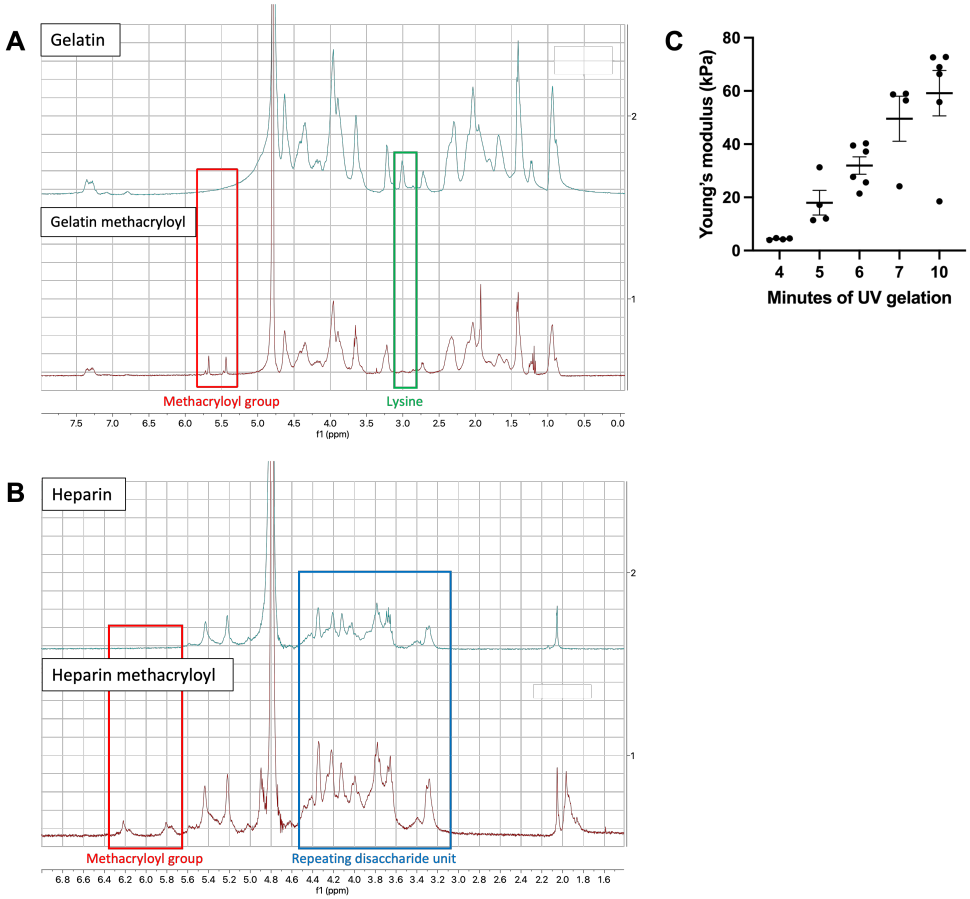


Figure 5.10: GelMA and HepMA synthesis. ^{1}H NMR spectra of unmodified gelatin and GelMA **(A)**, and unmodified heparin and HepMA **(B)**. **(C)** Young's modulus of 10% GelMA as a function of UV gelation time.

structs. Some cell death is present, which may be due to UV exposure, the physical confinement stress of the gel or limited nutrient diffusion. A positive control for cell death was performed by heating cells inside gels to 56°C for 45 minutes. After heating, no live green cells are observed.

Gene expression analysis in 3D

To assess the behaviour and differentiation potential of AD MSCs within 3D GelMA hydrogels as opposed to 2D cultures, cells were encapsulated in GelMA and cultured in three different culture conditions: (A) no BMP-2, (B) BMP-2 added to the medium on day 10, and (C) BMP-2 electrostatically bound to HepMA within a HepMA-GelMA composite gel (Fig. 5.12). These were performed to compared

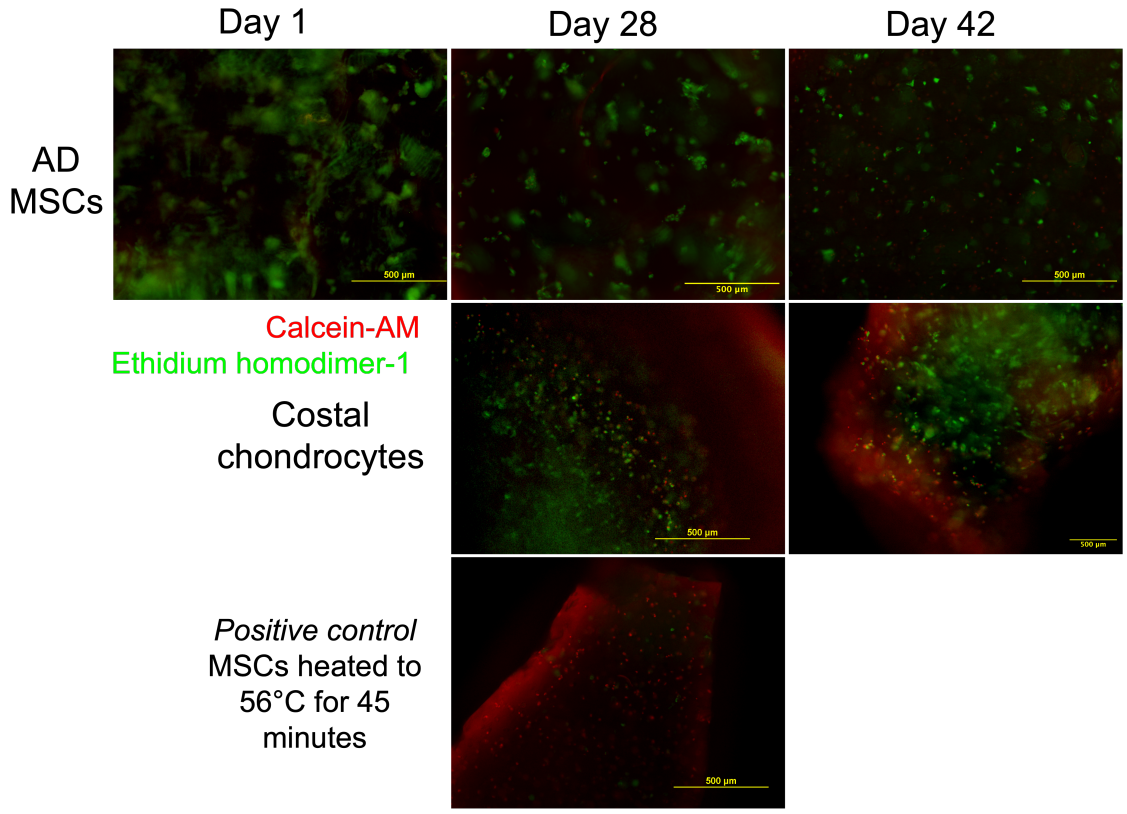


Figure 5.11: Live-dead assay of AD MSCs and costal chondrocytes cultured inside 10% GelMA. Green - live cells; red - dead cells

the effect and potency of BMP-2 in solution compared with matrix-bound. Gene expression of chondrogenic and osteogenic markers was quantified by qPCR every 7 days over a 42-day period, extending two weeks beyond the Li et al. (2019) culture period (Fig. 5.14) [174]. Gene expression profiles from mouse bone and costal cartilage were included as native tissue references.

In order to check the ability get reliable, high quality RNA from gels, the quality of the RNA extracted was measured using the Agilent Bioanalyzer. This system separates RNA fragments by size using microcapillary electrophoresis, generating an electropherogram that visualises the RNA sample as peaks. A RIN number is calculated, taking into account the size and height of the 28s and 18s rRNA peaks, as well as the presence of degradation products and anomalies in other regions of the electropherogram [320]. RIN values range from 1 to 10, with higher values indicating less degradation and better RNA quality. A RIN of 7 is often considered a threshold

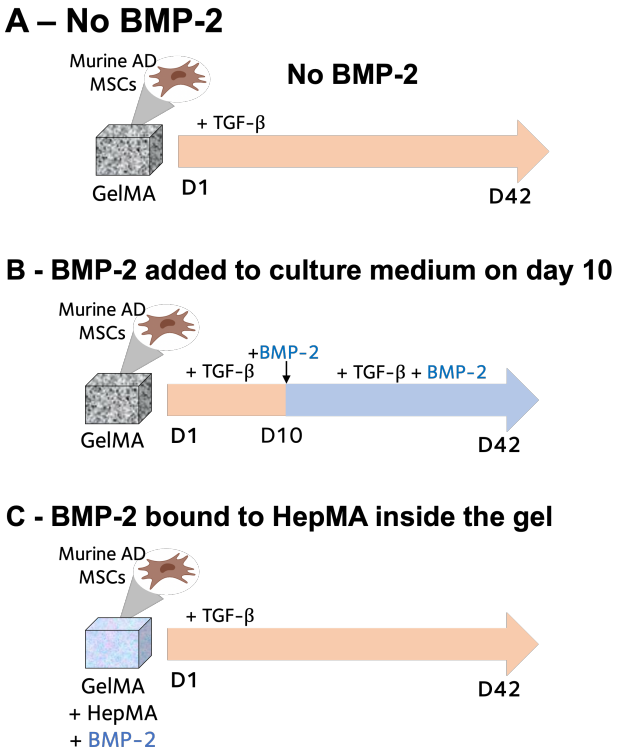


Figure 5.12: 3D GelMA culture conditions (no BMP-2 gradient). **(A)** No BMP-2, **(B)** BMP-2 added to the medium on day 10, **(C)** BMP-2 electrostatically bound to HepMA within a HepMA-GelMA composite gel.

for high-quality RNA suitable for many downstream applications, including RNA sequencing. On the electropherogram of RNA extracted from gels, the 18s and 28s peaks are visible (Fig. 5.13). The marker peak is used as a reference point and indicates the presence of smaller RNA fragments. There are few additional smaller peaks and smears, indicating good quality. The RIN number for this sample was 9, indicating it was of high quality. RIN numbers were always above 7 for all samples.

Generally, substantial variability in gene expression was observed between biological repeats across all culture conditions inside the gels. Moreover, the limited number of repeats performed restricts the ability to draw definitive conclusions regarding gene expression patterns. Nonetheless, certain trends can still be identified.

Firstly, some genes showed similar patterns of expression across all three culture conditions (Fig. 5.14). In 3D, as with 2D trilineage differentiation assays, no

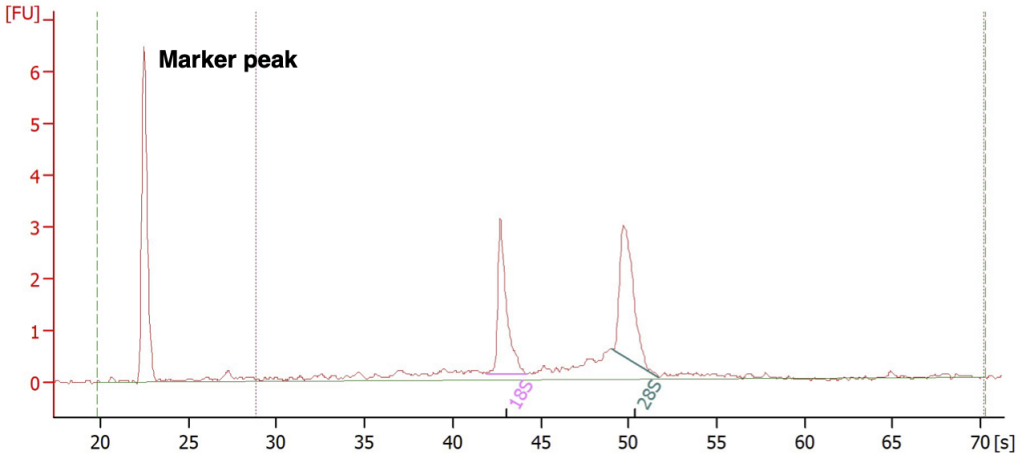


Figure 5.13: Electropherogram of the RNA extracted from AD MSCs cultured inside GelMA. 18S and 28S are ribosomal RNA peaks. FU = fluorescence unit.

expression of *Acan*, *Col2a1*, or *Col10a1* was detected in any gel condition. *Sox9* was consistently detected but remained at low levels across all samples, including bone and cartilage. There was a trend towards *Prg4* downregulation in gel cultures compared with day 1, mirroring its reduced expression in native tissues. Amongst osteogenic genes, *Runx2* showed weak upregulation compared with day 1 across all conditions, comparable to levels observed in bone. *Col1a2* expression increased up to day 21 before declining thereafter. *Spp1* expression remained minimal under all conditions.

Upon addition of BMP-2 in the culture medium, *Alpl* expression did not change scale, but shifted to earlier expression, although there were limited data points and high variability (Fig. 5.14 B). *Bglap* was more upregulated compared with day 1, when BMP-2 was added in solution.

When BMP-2 was bound to HepMA in the gel, *Alpl* expression was elevated by approximately 10- to 100-fold relative to the other two conditions, reaching levels similar to those in bone and cartilage (Fig. 5.14 C). *Bglap* also had higher fold-change from day 1 in this condition, though still at least 10-fold lower than in native tissues. Notably, *Sp7* was only detectable in the BMP-2–HepMA condition.

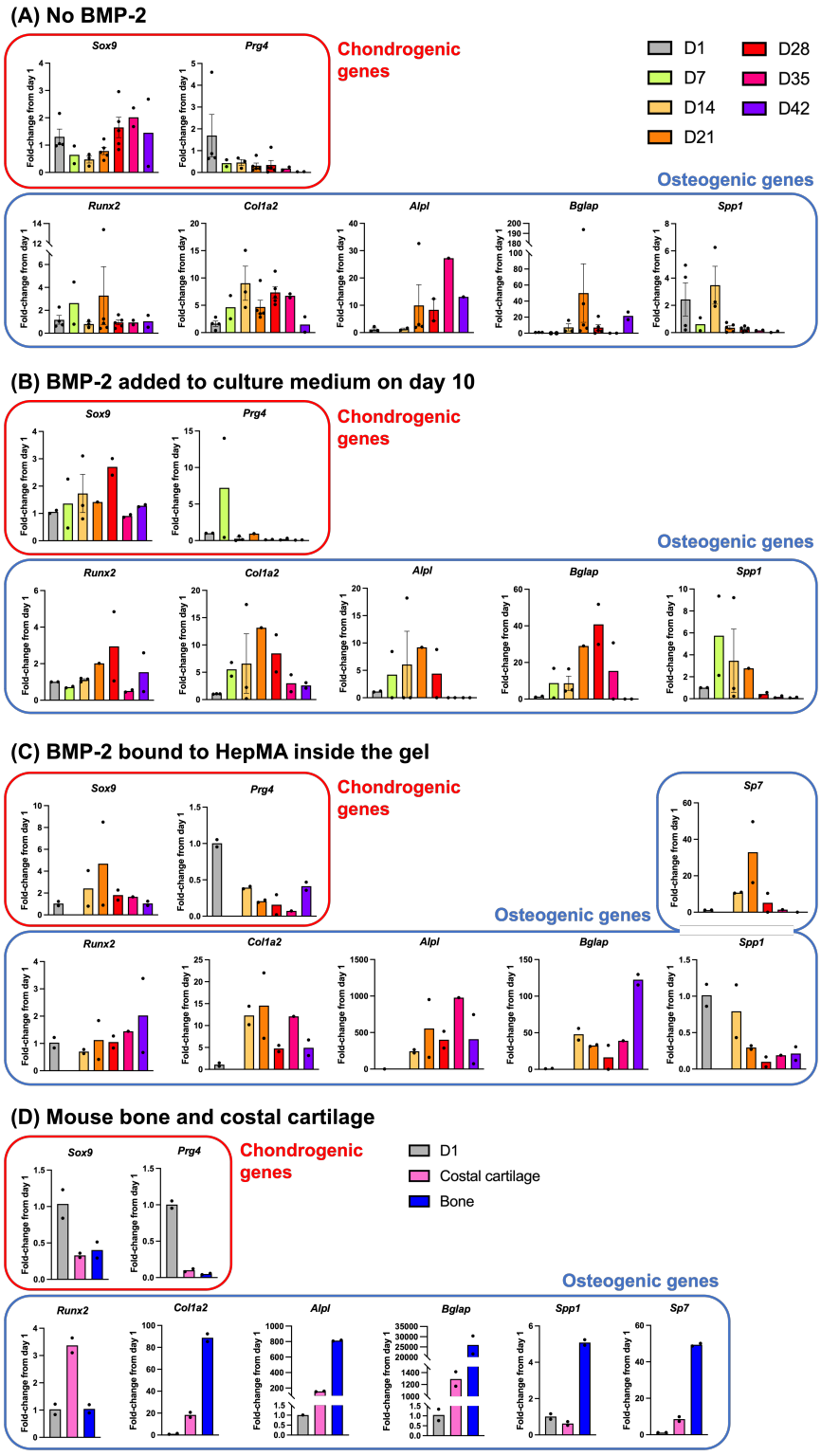


Figure 5.14: Gene expression profiles of AD MSCs cultured inside gels (no gradients) (A) without BMP-2, (B) with 100 ng/mL BMP-2 added to the culture medium on day 10, (C) with BMP-2 bound to HepMA inside the gel, and (D) gene expression profile of mouse tibial bone and costal cartilage for comparison. Mean ± SEM or mean of replicates when n = 2, presented as fold-change from day 1. n = 1-5 (biological replicates).

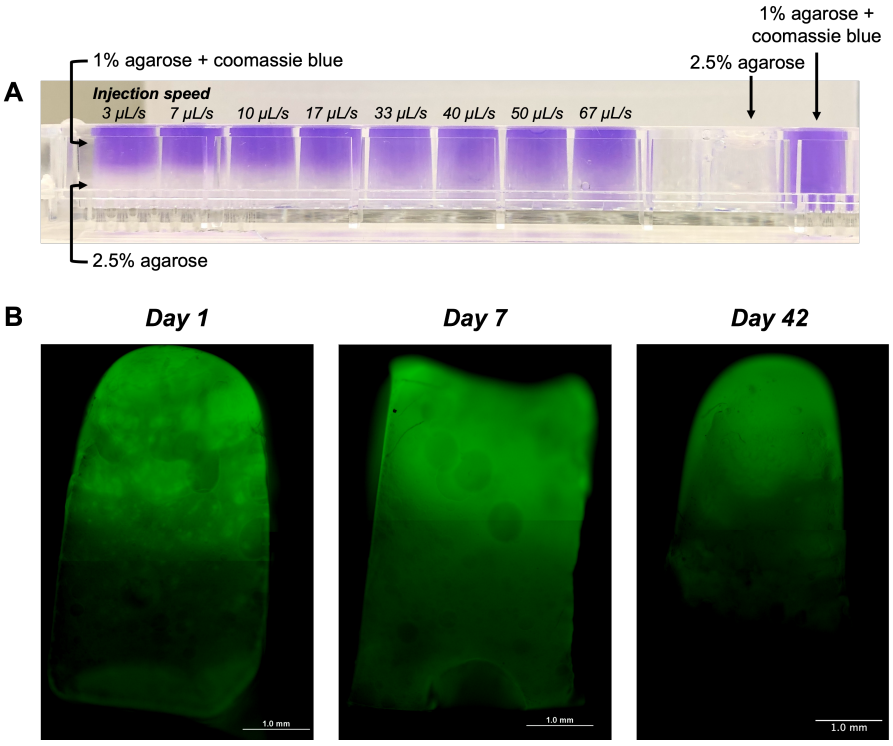


Figure 5.15: Buoyancy-driven gradient formation. **(A)** 1% (w/v) agarose supplemented with 5% (v/v) coomassie blue was injected into a base layer of 2.5% (w/v) agarose at different controlled rates. 2.5% (w/v) clear base and 1% (w/v) agarose with coomassie blue injected alone act as no-gradient controls. **(B)** FITC-BMP-2 distribution inside the gradients at different time points after their creation.

5.3.5 Gradient generation

To demonstrate that using the buoyancy-based method, gradient patterns can be tuned by changing the injection speed, dyed 1% coomassie- stained agarose was injected into a 2.5% clear agarose base. A slow injection speed results in a sharp gradient and a higher injection speed results in a smoother gradient (Fig. 5.15 A). The 17 μL/s speed was used in the generation of the gradient with cells.

Li et al. (2019) did not visualise the BMP-2 gradient inside the GelMA hydrogel nor characterise its stability [174]. To assess the presence and stability of BMP-2 inside the gradient, FITC-BMP-2, at the same concentration as in the cell-culture system, was used inside gradients without cells. There is a spatial gradient distribution of BMP-2 within the gel, with its highest concentration at one end and decrease

towards the other. BMP-2 can still be imaged and this gradient is maintained for up to 42 days of culture in PBS (Fig. 5.15 B).

5.4 Discussion

The gradient model developed by Li et al. (2019) [174] seeds human MSCs inside a GelMA construct with a gradient of BMP-2 concentration. Considering the genetic tools provided by mouse lines, in particular the *Ift88* cKO line, using MSCs derived from these would provide opportunities to delete *Ift88 in vitro* and observe the effects of ciliary disruption on cell differentiation in 3D. Therefore, different sources of murine cells were characterised in order to determine the most appropriate source (MSCs or costal chondrocytes) to be used in the osteochondral model. In addition, the aim was to adapt the Li et al. (2019) model with minimal alterations to the material properties, growth factor gradient and culture conditions. As a result, these parameters were retained as originally described and not further optimised in this study.

5.4.1 Murine MSC and costal chondrocyte characterisation

The Mesenchymal and Tissue Stem Cell Committee of the International Society for Cellular Therapy propose the minimal criteria to define MSCs to be that they must be plastic-adherent, express CD105, CD73 and CD90, not express CD45, CD34, CD14 or CD11b, CD79α or CD19 and HLA-DR surface molecules, and differentiate to osteoblasts, adipocytes and chondroblasts *in vitro* [321].

In this chapter, several features of MSCs were studied: their ability to proliferate in 2D cultures, to differentiate into different lineages and the presence of certain of the above MSC markers. A key consideration for the future development of the osteochondral model is the sheer number of MSCs. The 3D osteochondral models requires at least 10 million cells per batch, therefore it was essential for the cells used to have high proliferation potential in order to obtain a high number of MSCs to perform reliable experiments with repeats using these constructs. MSCs are limited

in the number of times they can be passaged before they lose their proliferative capacity and differentiation potential [322].

The sources of MSCs to characterise were chosen as those from the bone marrow and adipose tissue, as they have *in vitro* osteochondral differentiation potential and are relatively simple to access and isolate [155]. Isolation of periosteum-derived MSCs was also attempted, however these did not proliferate well *in vitro*. Ideally, the sources of MSCs in the growth plate itself would be used however these remain elusive and difficult to access [15, 151].

Both AD and BM MSC display spindle-like morphology (Fig. 5.4). However, despite purification to deplete haematopoietic cells, there remained non-spindle-like cells in BM MSCs cultures. AD MSCs were able to form colonies derived from single cells when seeded at low density, whereas BM MSC were not. This is in line with previous studies describing AD MSCs exhibiting superior proliferation rates compared with BM MSCs [323].

Both AD and BM MSCs were able to go through adipogenic differentiation as determined by the presence of lipid droplets and gene expression (Fig. 5.5). In terms of osteogenic differentiation, both sources of MSCs display bone nodules that stain with alizarin red, which detects calcium and accumulation and formation of chelates, however osteogenic gene expression was varied (Fig. 5.6). Overall, BM MSCs expressed a higher level of the osteogenic genes when cultured in osteogenic media compared with CGM. For AD MSCs, higher expression in osteogenic media compared with CGM was only observed for *Bglap*. The genes measured here are a general indication of osteogenic differentiation, however they are expressed at different time points during differentiation. For example, *Alpl* is expressed early in the first two weeks of differentiation of osteoblasts and later declines, whereas *Bglap* expression starts around day 14 [324]. *Runx2* is vital for the commitment of MSC to the osteoblast lineage in the first 7 days but is down-regulated for further bone maturation. *Spp1* and *Col1a2* are expressed early in osteogenic differentiation,

which could explain their low expression in AD MSCs. As gene expression was only measured at day 21, the transient peak expression of these genes may have been missed. As BM and AD MSCs may have different timelines of differentiation, this could explain the differences in gene expression.

Of the chondrogenic genes studied, only *Prg4* and *Sox9* were expressed in AD MSCs pellets in chondrogenic media (Fig. 5.7). In BM MSCs these were very low, at the same level as undifferentiated MSCs, though due to insufficient yield only one repeat could be performed. In AD MSCs, *Prg4* was more upregulated in chondrogenic media compared with CGM. Chondrogenic genes *Acan*, *Col2a1* and *Col10a1* were not expressed in any of the pellets. This is particularly important to note, in particular as the *Ift88* cKO mouse line is driven by an *Acan*-Cre, therefore requires *Acan* expression. Supplements that increase *Acan* expression or further promote chondrogenesis of AD MSCs, such as higher concentrations of TGF-β, BMP-6 or insulin-like growth factor-1, could be added to the culture medium to achieve this [325, 326]. Overall, the AD MSCs are more biased toward osteogenic differentiation over chondrogenic.

However, the AD MSCs pellets did stain positively for alcian blue, safranin-O and toluidine blue which stain components of cartilage ECM. Under polarised light, fibres of collagen could be visualised with sirius red staining (Fig. 5.7 A).

In terms of immunophenotyping, AD MSCs stained positively for MSC markers Sca-1 and CD105 and negatively for haematopoietic markers CD45 and CD34 (Fig. 5.8).

Practically, AD MSCs are simpler to harvest, yield more cells and have a higher proliferation rate compared with BM MSCs (270,000 vs 100,000 cells per mouse at the first passage). Culture of BM MSCs was very unpredictable and low yield. Therefore, considering all of these results and the number of cells required to make gel constructs, in the context of using a tissue-derived MSC, the project moved forward with AD MSCs.

In parallel, costal chondrocytes were isolated from mice as an alternative to MSCs, given even the AD MSCs had displayed poor chondrogenic differentiation potential. Chondrocytes dedifferentiate into a fibroblast-like cell when cultured in 2D, leading to intracellular and intranuclear changes that ultimately result in a loss of chondrocyte phenotype. However, chondrocytes can be redifferentiated by moving to 3D cultures [149, 150].

With the exception of *Col10a1*, isolated costal chondrocytes cultured in 2D expressed chondrogenic genes at the same or higher level than costal cartilage (Fig. 5.9). The expression of *Acan* potentially allows for the use of the *Acan*-cre in the *Ift88* cKO mouse line.

5.4.2 Material synthesis and characterisation

Synthesis of GelMA and HepMA was achieved with suitable DoF for use in cell cultures. The mechanical properties of GelMA-based gels can be tuned by varying the DoF, the GelMA and photo-initiator concentrations, and the UV photo-cross-linking time (Fig. 5.10).

To achieve successful osteogenic and chondrogenic differentiations, cells, both MSCs and costal chondrocytes, have been cultured in GelMA with a Young's moduli ranging from 15 to 30 kPa [310, 327–329]. This range provides a balance between mechanical support and a permissive environment for cell viability, spreading, and differentiation. 6 minutes of photo-cross-linking of the 10% GelMA concentration used in this study had a mean Young's modulus of 31.9 kPa. This is lower than native cartilage and bone tissue. The bulk Young's modulus of the growth plate ranges between 500 to 1000 kPa [239, 330]. The material in which the cells were cultured was therefore softer than the native growth plate, a necessary compromise to enable effective MSC differentiation. Moreover, optimisation of material stiffness and porosity fell outside the scope of this project.

5.4.3 3D cell cultures inside gels

AD MSCs were cultured within non-gradient GelMA-based hydrogels to investigate their differentiation behaviour and assess their potential suitability for use in gradient systems (Fig. 5.14). Biological variability was observed between experimental repeats, an issue common with use of primary cells. Even genetically identical mice can show variability due to differences in weight, metabolic status or subtle differences in cell and tissue micro-environment. In addition, AD MSCs can present some heterogeneity in cell types. This is reduced by passaging but would be improved by cell sorting based on MSC surface markers. Human MSCs also exhibit significant biological variability between donors. To reduce this source of variability and improve reproducibility, many studies employ a single MSC line or batch from one donor when developing *in vitro* models. However, this approach limits the generalisability of findings, as it does not capture donor-to-donor variability inherent in primary human MSC populations.

In addition, although the same GelMA batches and crosslinking times were used throughout, exposure to air or other environmental factors during gel preparation may have introduced variability between repeats. A larger number of biological replicates would be required to confirm the observed gene expression patterns with confidence. However, the primary aim of this experiment was to gain a general understanding of the behaviour of murine MSCs within the GelMA environment.

The absence of detectable expression of *Acan*, *Col2a1*, and *Col10a1* indicates minimal chondrogenic differentiation. This suggests that AD MSCs may be unable to initiate true chondrogenesis in GelMA alone, and that a more potent chondrogenic stimulus or the presence of a BMP-2 gradient may be necessary to promote lineage commitment. *Prg4* (lubricin), typically highly expressed in superficial zone chondrocytes of articular cartilage, showed consistently low expression across all gel conditions, consistent with its expression in native costal cartilage. Growth plate RNA sequencing data from our group reveals limited expression of *Prg4* in the 6-week old mouse

growth plate, substantially lower than the expression of *Acan*, *Col2a1* and *Col10a1* (Appendix Table 2).

The BMP-2–HepMA delivery system resulted in enhanced activation of osteogenic genes, particularly *Alpl*, *Bglap*, and *Sp7*. This suggests that localised, matrix-bound delivery of BMP-2 is more effective than soluble BMP-2 in culture medium in driving osteogenic commitment. This is in line with a previous study which showed that BMP-2 delivered inside GelMA enhanced osteogenic differentiation of human AD MSCs more effectively than exogenous BMP-2 in media [304]. The temporal pattern of *Col1a2*, peaking at day 21 followed by a decline, may reflect early matrix deposition prior to cellular transition. By contrast, the weak expression of *Spp1* across all conditions may indicate either insufficient maturation of osteoblasts or a lack of osteoclast-associated activity, potentially reflecting incomplete mineralisation.

Overall, the difference in gene expression levels between gel-cultured samples and native bone and cartilage highlights that differentiation of MSCs within GelMA hydrogels in this timescale (up to 42 days) - even under inductive conditions - does not fully replicate the transcriptional landscape of native tissues. With the exception of *Col1a2*, most genes showed neither strong temporal trends nor marked differential expression between the tested conditions.

In conclusion, AD MSCs were selected in this project as a more suitable murine MSC source compared to BM MSCs, primarily due to their higher yield and ease of isolation. While AD MSCs were able to survive and undergo differentiation within GelMA hydrogels, they exhibited limitations in chondrogenic potential under the current conditions. However, the incorporation of a BMP-2 gradient or the application of mechanical loading may enhance chondrogenesis in this system. Notably, BMP-2 bound to HepMA can be stably maintained in a gradient for up to 42 days, supporting its potential for sustained signalling in downstream applications (Fig. 5.15). The following Chapter explores the use of this *in vitro* model to investigate the role of primary cilia in growth plate organisation and function.

6

Application of the gradient osteochondral model to study the role of primary cilia organisation in osteochondral differentiation

Contents

6.1 Introduction **174**

6.2 Materials & Methods **177**

6.2.1 Gradient *in vitro* model 177

6.2.2 In vitro IFT88 deletion 178

6.2.3 Western blotting 179
6.3 Results 181
6.3.1 AD MSCs inside the BMP-2 gradient 181
6.3.2 Costal chondrocytes inside the BMP-2 gradient 182
6.3.3 In vitro *Ift88* deletion 186
6.3.4 *Ift88* and loading regulation of differentiation in vitro . . 190
6.4 Discussion 194
6.4.1 AD MSCs inside the BMP-2 gradient 194
6.4.2 Mechanical loading of AD MSCs inside the BMP-2 gradient 195
6.4.3 Costal chondrocytes inside the BMP-2 gradient 196
6.4.4 Mechanical loading of costal chondrocytes inside the BMP-2 gradient 198
6.4.5 *Ift88 in vitro* deletion 199

6.1 Introduction

Having a general understanding of the behaviour of murine cells within GelMA hydrogels, the next phase of the project focused on investigating primary cilium function in this 3D *in vitro* system. Several features make primary cilia particularly well suited for study in bioengineered models. Their micrometre-scale length necessitates high-resolution imaging, which poses significant challenges in native tissues due to optical scattering, structural complexity and the need for true 3D resolution. 3D imaging of primary cilia was succesfully performed in Chapters 2, 3, 4, however the large image file sizes and extensive processing times posed restricted the number of experiments that could be carried out efficiently. In contrast, bioengineered environments such as hydrogels offer greater optical clarity and accessibility for advanced microscopy, enabling detailed visualisation of cilia architecture and orientation.

Studying cilia in relation to mechanical loading is especially compelling, given their established role in mechanotransduction. However, *in vivo* approaches to apply controlled mechanical forces remain limited. Exercise-based protocols - such as giving mice access to running wheels - can increase mechanical load but are inherently variable and difficult to quantify, as the precise magnitude and frequency of loading cannot be directly measured or standardised across animals [47, 80]. Other studies have used more localised and targeted loading methods, including the implantation of micromotion devices, direct limb loading or customised apparatuses designed to apply defined mechanical stimuli [112, 113, 331, 332]. While these approaches offer greater control, they are technically complex, invasive and difficult to implement longitudinally or at scale.

Explant models, where isolated bone or cartilage tissues are subjected to controlled mechanical loading, have also been used to study mechanobiology in a more defined context [189, 191, 193]. However, these systems come with their own limitations, such as limited viability over time, difficulty in isolating effects of specific cell types, challenges in maintaining native mechanical properties or lack of genetic manipulability compared to cell-based systems.

Primary cilia have been studied in 3D *in vitro* systems using approaches such as agarose-embedded cultures or cell pellets. These models allow for the application of controlled mechanical loads and enable observation of ciliary responses under defined conditions [51, 231, 333]. More recently, advances in organoid technology have extended the study of primary cilia into complex, tissue-like 3D systems. For example, cerebral organoids derived from induced pluripotent stem cells (iPSCs) have been used to investigate the role of primary cilia in neocortical development [204]. In another study, Liu et al. (2024) generated condylar cartilage organoids using rat chondrocytes and successfully imaged primary cilia within these constructs, integrating their findings with RNA sequencing data to explore Hedgehog (Hh) signalling pathways [205]. These emerging models represent some of the first *in vitro*

systems that aim to replicate key aspects of tissue and organ complexity in 3D, while enabling detailed analysis of primary cilia function and organisation.

As discussed in the preceding Chapters, many questions remain regarding the role of primary cilia in the growth plate - particularly in relation to their involvement in cell differentiation, orientation and the integration of multiple signalling pathways. This Chapter aims to address some of these unresolved questions using a 3D *in vitro* osteochondral model. By employing cells derived from the *Ift88*$^{fl/fl}$ and *Ift88* cKO mouse lines, I have the possibility of conditionally deleting *Ift88 in vitro*, thereby disrupting primary cilium formation in a controlled environment. In addition, the fluorescent ciliary signals in these mouse cells allows imagine of primary cilia inside the *in vitro* model. Moreover, the *in vitro* system enables the application of defined mechanical forces, allowing us to test mechanosensitive hypotheses that are difficult to explore *in vivo*.

The specific objectives of this chapter were to:

- Characterise the behaviour of adipose-derived mesenchymal stem cell (AD MSCs) and costal chondrocytes inside the BMP-2 gradient, both with and without loading.
- Evaluate the potential of the BMP-2 gradient system as a physiologically relevant *in vitro* model of the growth plate.
- Induce the deletion *Ift88* within the BMP-2 gradient system and assess subsequent changes in cell differentiation.
- Map cilia orientation across the BMP-2 gradient system.

6.2 Materials & Methods

Unless stated otherwise, all chemicals used were from Sigma Aldrich.

6.2.1 Gradient *in vitro* model

BMP-2 gradient gels seeded with murine cells were generated and cultured as described in Chapter 5.5.2.

In vitro model loading

Dynamic compression was applied to the gradient gels (8 x 4 x 3 mm - same size as in Chapter 5) using the ElectroForce 5500 (TA Instruments, 200 N load cell) using the 24-Well Plate Compressive Loading Fixture. Gels were placed inside a 24-well plate and the pistons lowered until they came into contact with the surface of the gel (Fig. 6.1 A, B, C). The gels were loaded under sinusoidal displacement control for 1 hour per day, for 5 consecutive days at 1 Hz, at an amplitude of 10% strain (Fig. 6.1 A) [165, 334]. AD MSC gradients were loaded from day 14 to 18 and costal chondrocyte gradients from day 7 to 11 (Fig. 6.1 D). Gels were harvested for qPCR analysis immediately after their final loading cycle. RNA was extracted using the same method as described in Chapter 5.5.2. *GAPDH* was used as the housekeeping gene. Different housekeeping genes were tested in costal chondrocytes cultured in GelMA and *GAPDH* was chosen as it had small variability and high expression (Appendix Fig. 3 B). Compared with MSCs the expression of *Tbp* was too low to use as a housekeeping gene in 3D cultures.

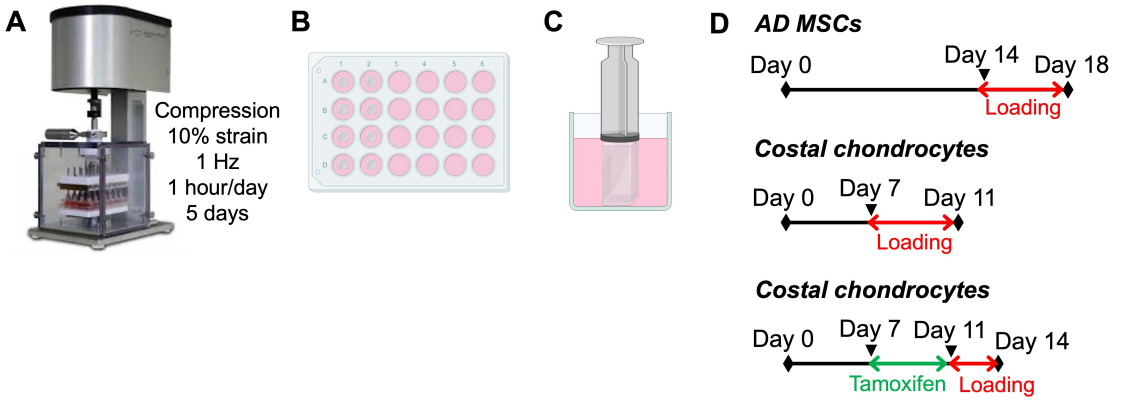


Figure 6.1: (A) Mechanical loading setup for GelMA gradients (8 x 4 x 3 mm) seeded with AD MSCs and costal chondrocytes using the ElectroForce 5500 system. (B) Gel setup in the 24-well plate. (C) Side view of a single gel in a well held in place by the piston at its top surface. (D) Gradient gel loading timeline.

6.2.2 In vitro IFT88 deletion

Ift88 mRNA stability study

To determine the *Ift88* mRNA stability, 80% confluent bone marrow-derived MSCs (BM MSCs) were exposed to 1 µg/mL actinomycin D dissolved in dimethyl sulfoxide (DMSO) for 24 hours to block transcription. Vehicle controls were treated with the same volume of DMSO. Expression of *Ift88* and other chondrogenic and osteogenic genes in treated cells compared to vehicles was measured by qPCR. RNA extraction and qPCR methods are described in Chapter 5.5.2. *18s rRNA* was used as a housekeeping gene as it is highly stable.

IFT88 protein stability study

To determine the IFT88 protein stability, 80% confluent AD and BM MSCs were exposed to 10 µg/mL cycloheximide dissolved in DMSO for 24 or 48 hours to block translation. Vehicle controls were treated with the same volume of DMSO. Protein content was measured by Western blotting.

Tamoxifen-driven IFT88 deletion in 2D cultures

80% confluent costal chondrocytes were treated with 2 μM of 4-hydroxytamoxifen (4-OH-T) (T176) dissolved in 100% ethanol for 72 hours. Vehicle controls were treated with the same volume of 100% ethanol. RNA extraction and qPCR methods are described in Chapter 5.5.2. The average CT value of *GAPDH* and *Tbp* were used as housekeeping gene CT value.

Tamoxifen-driven IFT88 deletion in 3D cultures

The BMP-2 gradients GelMA constructs seeded with costal chondrocytes were treated with 5 μM 4-OH-T dissolved in 100% ethanol for 96 hours from day 7. Vehicle controls were treated with the same volume of 100% ethanol. For loading experiments after 4-OH-T treatment, gels were loaded from day 11 to 14 (Fig. 6.1 D). Gels were harvested for qPCR analysis immediately after their final loading cycle. RNA was extracted using the same method as described in Chapter 5.5.2. *GAPDH* was used as the housekeeping gene.

6.2.3 Western blotting

Protein lysates were isolated by incubating cells with radioimmunoprecipitation assay lysis buffer for 5 minutes on ice, followed by lifting off with a cell lifter and incubating for a further 5 minutes. Cell lysates were centrifuged at 9,632 g for 10 minutes. The supernatant was collected and the total protein concentration measured using a bicinchoninic acid assay (ThermoFisher).

Lysates were diluted with milliQ water to standardise protein concentration across samples then denatured using 2.5% β-mercaptoethanol in Laemlli sample buffer (Bio-Rad). Samples were boiled for 5 minutes at 100°C and loaded onto 4-12% Bis-Tris NuPAGE gels (ThermoFisher). The Chameleon Duo Pre-Stained Protein ladder

(LI-COR) was also loaded. The gel electrophoresis was run for 1 hour and 15 minutes at 150 V in NuPAGE MOPS SDS running buffer (ThermoFisher) in a gel tank.

Separated proteins were transferred onto a polyvinylidene membrane (Bio-Rad) in transfer solution (196 mM glycine, 24 mM Tris base, 20% (v/v) methanol) in a transfer tank at 100 V for 1.5 hour at 4°C. After transfer, the membrane was incubated with 5% milk in Tris-buffered saline containing 0.1% Tween-20 (TBST) for 1 hour. The membrane was then incubated with primary antibodies in 5% milk in TBST overnight at 4°C. Subsequently, the membrane was incubated with secondary antibodies: IRDye 800CW donkey anti-rabbit and IRDye 680RD donkey anti-mouse (LI-COR) at a 1:5000 dilution, for 1 hour at room temperature. The membrane was imaged in the 700 and 800 nm channels of the LI-COR Odyssey CLX system, with imaging parameters set at at 160 μm resolution, medium quality and auto-exposure.

6.3 Results

6.3.1 AD MSCs inside the BMP-2 gradient

After choosing AD MSCs as the source of MSCs to use in the model, these were encapsulated in gradients of BMP-2 for up to 42 days. Samples were cut into three corresponding to regions of low, mid, and high BMP-2 concentration zones and assessed at multiple time points to evaluate spatial and temporal differentiation responses (Fig. 6.2). Gels with no BMP-2 gradient (from Chapter 5) were also plotted for comparison. In addition to osteogenic and chondrogenic genes, the expression ciliary-related genes *Ift88* and *Gli1* was also measured, as well as that of *VegfA*. *Gli1* is a downstream effector of the Hedgehog (Hh) pathway that localises to the primary cilium and thus serves as a readout of ciliary signalling activity. VegfA is a hypertrophy marker shown to be regulated by mechanical loading and IFT88 [47].

These experiments were performed with a minimum of three biological replicates (except day 42 in Fig. 6.2), with each data point in the graphs representing a separate batch of BMP-2 gradients generated using an independent murine cell isolation. Biological variability between replicates was observed. As a result, qualitative descriptions of trends are made and statistical testing was not performed, since higher sample numbers would be required to reliably detect significant differences.

No expression of *Acan*, *Col2a1*, or *Col10a1* was detected at any of the time points (Fig. 6.2). *Sox9* was expressed uniformly at low levels across the BMP-2 gradient, with no notable regional variation. *Prg4* showed consistently low expression across all zones and time points. *Runx2* and *Col1a2* exhibited the highest expression at day 14, followed by a decline at later time points. *Alpl* expression was higher in the high BMP-2 region at day 14. *Bglap* was upregulated compared to day 1 but did not show any clear spatial or temporal expression pattern. *Spp1* expression decreased across all zones compared to its level at day 1. *Ift88* expression remained stable

with no apparent zonal or temporal variation. *Gli1* was upregulated throughout the entire BMP-2 gradient. In contrast, *Vegfa* was consistently downregulated at all time points across all regions.

In terms of proteoglycan staining, the AD MSCs gradients stain uniformly across the length of the gel, suggesting it is the gel absorbing the staining rather than truly specific staining (Fig. 6.3 A, B).

Mechanical loading was applied to test whether it could raise chondrogenic markers and induce chondrogenic differentiation. Gene expression of ciliary genes could indicate whether this was through ciliary mechanotransduction [334, 335]. Gels were loaded for 1 hour at 10% strain, 1 Hz for 5 consecutive days. The load cell of the ElectroForce measures the load response of the gel to the displacement applied (Fig. 6.4 A). The load measurements initially increases before plateauing for the remainder of the cycle. As the loading is applied in displacement control the displacement remains consistent throughout the time course of the cycle (Fig. 6.4 B). The gradient gels measure 6 mm in height therefore 0.6 mm displacement was applied in compression (10% strain).

Mechanical loading did not lead to upregulation of any chondrogenic markers. Loading did not increase expression of osteogenic or cilia-related genes (Fig. 6.5). In many cases, expression levels were reduced compared to unloaded controls. In addition, across all gene categories, no evidence of spatial regulation was observed. Expression levels remained broadly similar across the BMP-2 gradient zones under loading conditions.

6.3.2 Costal chondrocytes inside the BMP-2 gradient

As I was not able to induce sufficient chondrogenic differentiation in AD MSCs, particularly *Acan* expression which was required to use the *Acan*-cre in the mouse cells, I did not continue with repeats of this experiment. Instead, they were replaced with

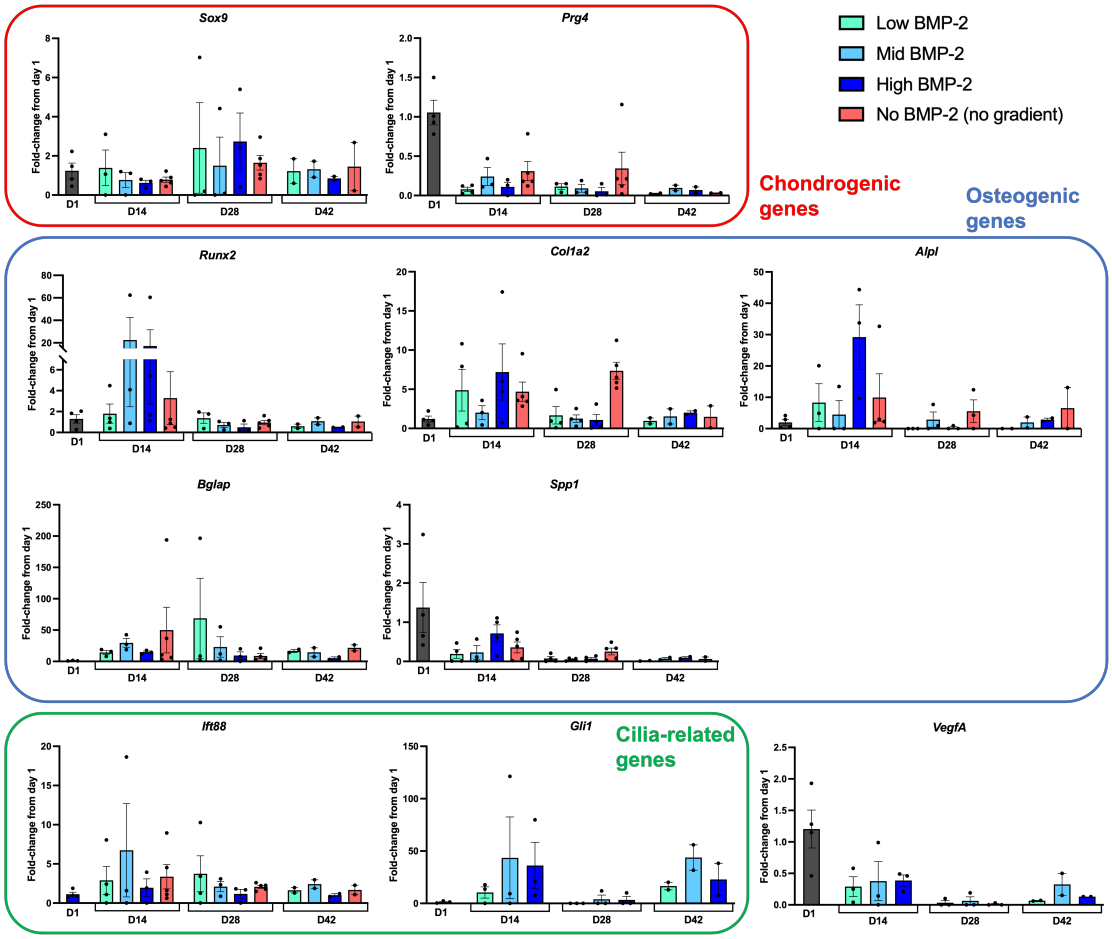


Figure 6.2: Gene expression profiles of AD MSCs cultured inside BMP-2 gradients across 42 days. Mean ± SEM presented as fold-change from day 1. n = 2-5 (biological replicates).

costal chondrocytes for the next steps of the project. These expressed chondrogenic genes in 2D (Fig. 5.9). Experiments were performed in triplicate with these cells to provide a indicative assessment of their response. Bearing in mind biological variability, statistical tests were not performed.

Costal chondrocytes were cultured in GelMA along a BMP-2 gradient and analysed for gene expression over 42 days (Fig. 6.6). Compared to AD MSCs, expression of *Acan*, *Col2a1* and *Col10a1* was detectable. *Sox9* showed a similar expression profile to that observed in MSCs, with a slight upregulation on day 28 compared to day 1. *Prg4* was downregulated across all conditions. *Col2a1* was upregulated to a limited extent, while *Col10a1* expression exhibited high biological variation

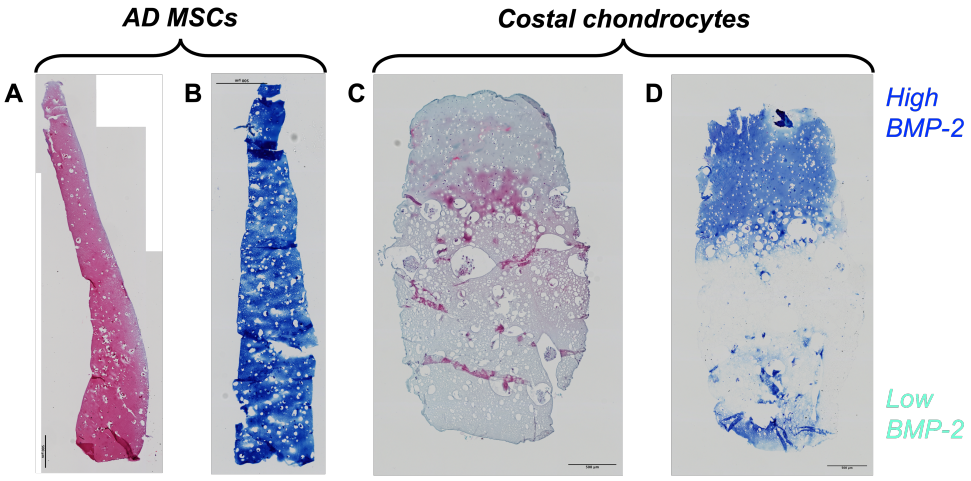


Figure 6.3: Safranin-O (A,C) and toluidine blue staining (B,D) of BMP-2 gradients gels seeded with AD MSCs and costal chondrocytes on day 28.

between repeats. *Acan* expression was upregulated, although no zonal BMP-2 concentration-dependent pattern was observed.

Runx2 showed more consistent upregulation compared to AD MSC cultures. *Col1a2* was also upregulated across the time course. *Alpl* displayed stronger upregulation than in AD MSCs, with higher expression in the mid and high BMP-2 regions, but expression declined by day 42. *Bglap* was upregulated at days 14 and 28 before being downregulated at day 42. *Spp1* showed no upregulation across any zone or time point. *Sp7* was also detectable compared to its absence in AD MSC cultures - it was upregulated across all time points.

Ift88 expression remained stable with no significant upregulation. *Gli1* showed strong upregulation at day 42, but only in one biological repeat. *Vegfa* expression remained unchanged across the 42 days.

The proteoglycan staining of the costal chondrocyte gradients was more heterogeneous than the AD MSC staining (Fig. 6.3 C, D). The top region of the gel, corresponding to the high BMP-2 zone, presented safranin-O and toluidine staining suggesting there was more proteoglycan deposition.

The same loading regimen (10% strain, 1 Hz, 1 hour/day for 5 days) was applied to

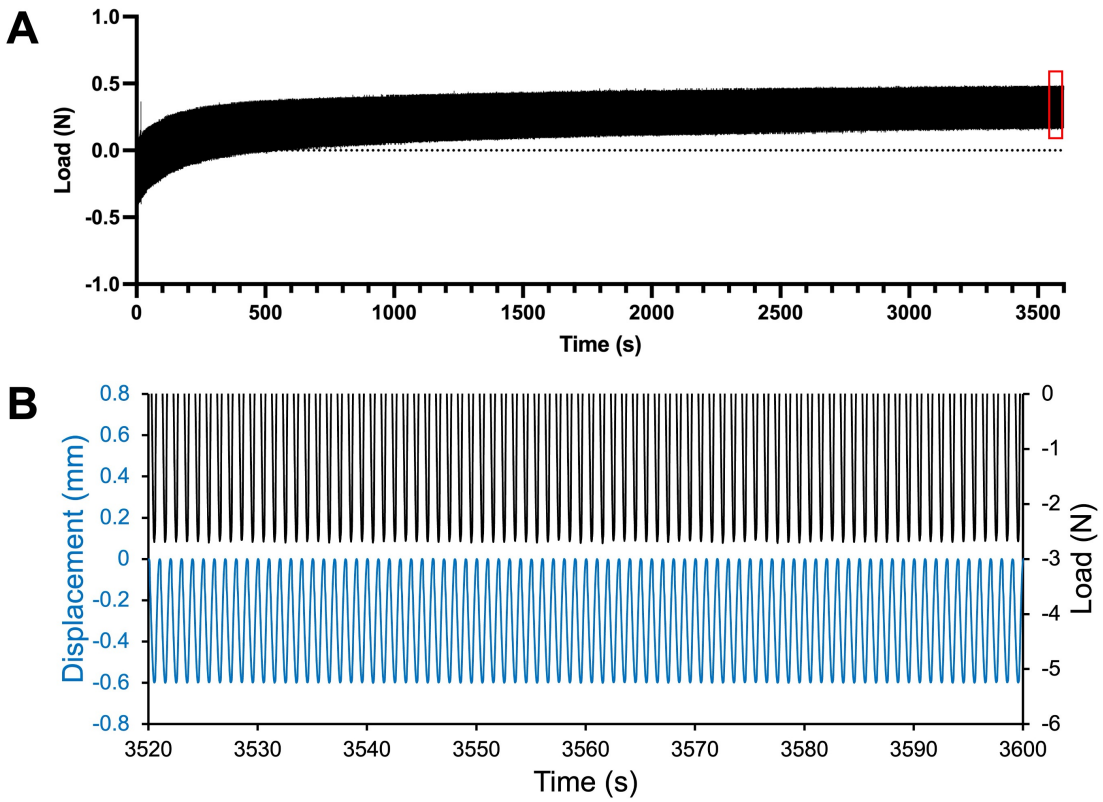


Figure 6.4: Gel loading under displacement control. (A) Load values over the time course of the loading cycle applied to the AD MSCs gradient gels on day 14. **(B)** Load and displacement values in the last 60 seconds of the loading cycle - corresponding to the red box in (A). Costal chondrocyte loading plots appeared similar.

costal chondrocyte gels as AD MSC gels (Fig. 6.7). However, the loading was applied 7 days earlier due to the more differentiated state of costal chondrocytes compared to MSCs. *Sox9* and *Prg4* expression levels remained stable in response to loading. Expression of *Col2a1*, *Col10a1*, and *Acan* decreased compared to unloaded conditions. *Runx2*, *Col1a2*, *Bglap*, *Spp1*, and *Sp7* showed no notable change in expression across BMP-2 region with loading. *Alpl* expression was reduced under loading conditions relative to unloaded controls in all BMP-2 regions. *Ift88*, *Gli1*, and *Vegfa* expression remained stable, showing no spatial changes in response to mechanical loading.

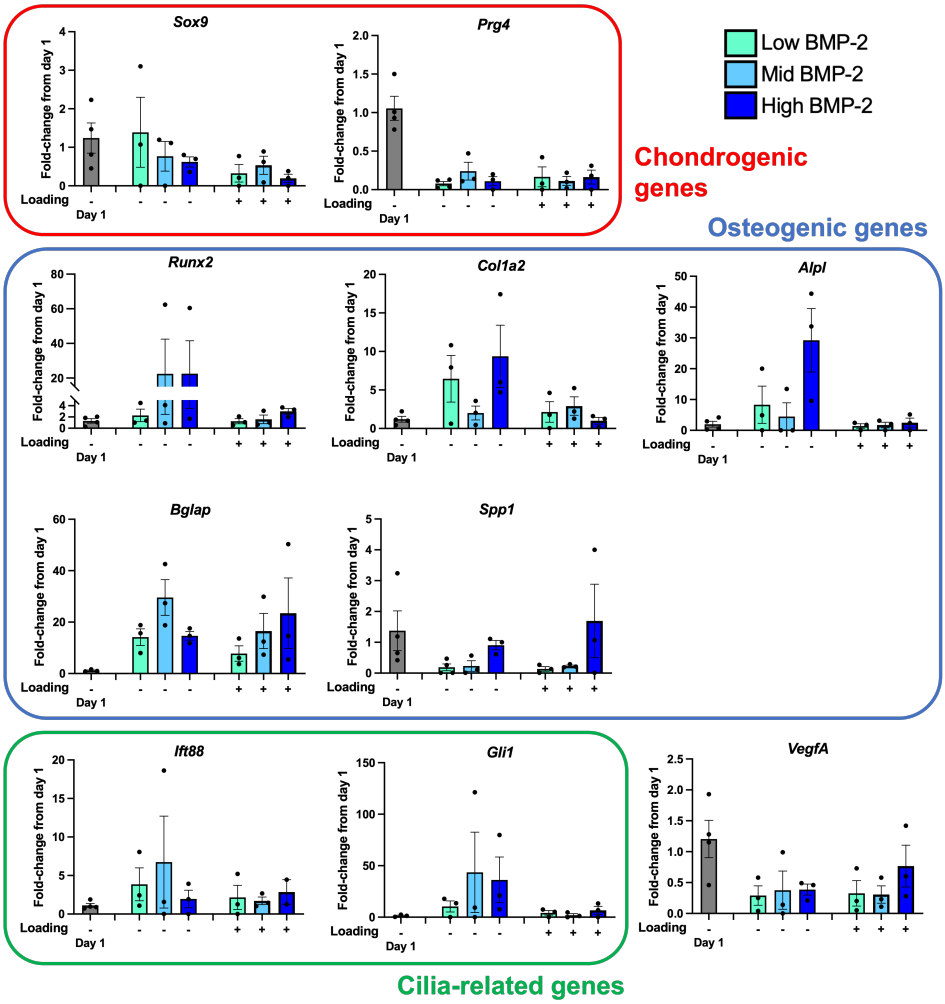


Figure 6.5: Gene expression profiles on day 18 of AD MSCs cultured inside BMP-2 gradients and loaded from day 14 to 18 at 10% strain for 1 hour at 1 Hz for 5 days compared to static culture. Mean ± SEM presented as fold-change from day 1. n = 3 (biological replicates).

6.3.3 In vitro *Ift88* deletion

As this project aimed to use this *in vitro* 3D model to study the role of primary cilia in endochondral ossification under mechanical loading - using AD MSCs from the *Ift88* cKO mouse - the ability to delete *Ift88 in vitro* was tested and its effects on differentiation within the model were examined. The *Ift88* cKO line is the $Aggrecan CreER^{T2}; Ift88^{fl/fl}; Centrin\text{-}2\text{-}GFP.ARL13b\text{-}mCherry$, which allows conditional deletion of Ift88 in aggrecan-expressing cells. The control line is $Ift88^{fl/fl}$

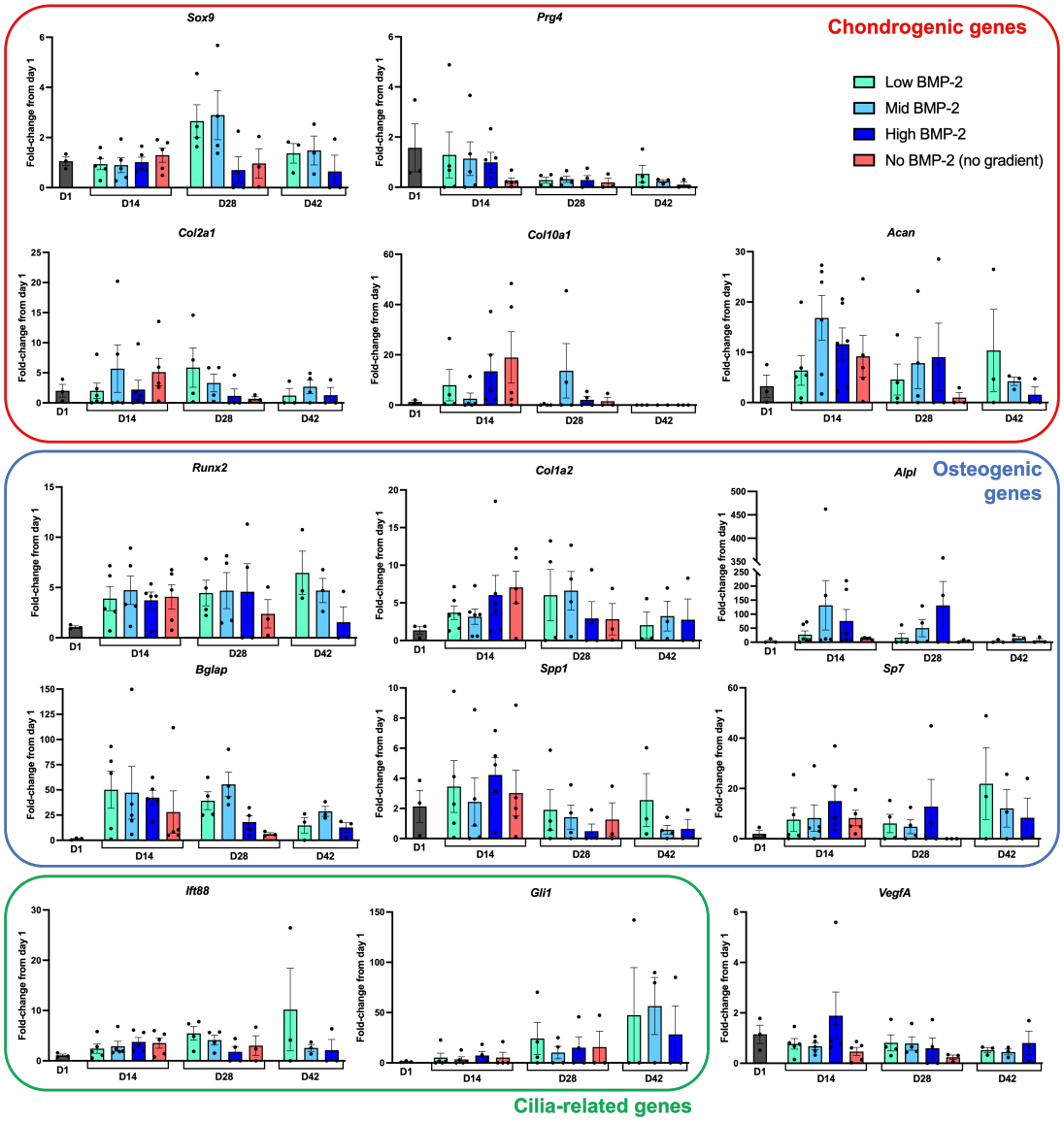


Figure 6.6: Gene expression profiles of costal chondrocytes cultured inside BMP-2 gradients across 42 days. Mean ± SEM presented as fold-change from day 1. n = 3-5 (biological replicates).

(*Ift88*$^{fl/fl}$*;Centrin 2-GFP.ARL13b-mCherry*), which is the same line as Ift88 cKO without the aggrecan-cre.

First, the stability the *Ift88* mRNA and IFT88 protein were studied in order to determine their stability to guide the design of tamoxifen-induced deletion experiments. BM MSCs were exposed to 1 µg/mL actinomycin D for 24 hours to block transcription. The *Ift88* mRNA was reduced by approximately 70% within

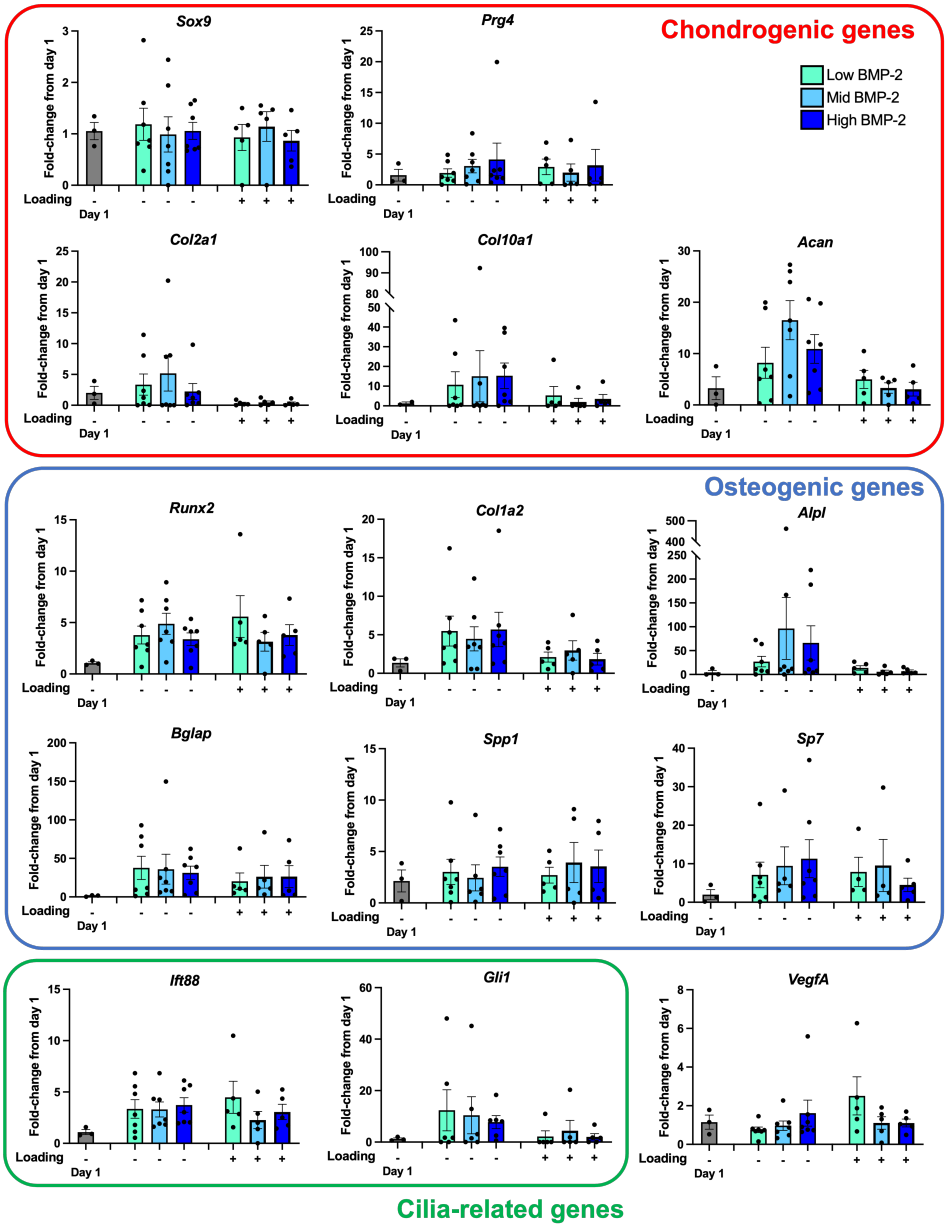


Figure 6.7: Gene expression profiles on day 11 of costal chondrocytes cultured inside BMP-2 gradients and loaded from day 7 to 11 at 10% strain for 1 hour at 1 Hz for 5 days compared to static culture. Mean ± SEM presented as fold-change from day 1. n = 5-7 (biological replicates).

this time (Fig. 6.8 A). The lifetime of *Ift88* mRNA was thus estimated to be approximately 30 hours. *18s rRNA* was used as a housekeeping gene as it is highly stable. Studies have shown that even after actinomycin D treatment, *18s rRNA* levels remained relatively stable over a 24-hour period [336].

Similarly, MSCs were exposed to cycloheximide to block translation. After 24 and

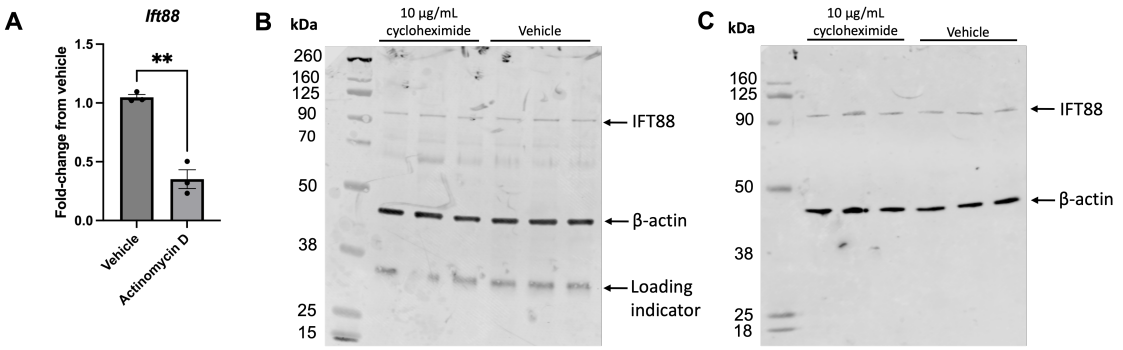


Figure 6.8: Ift88 stability study. (A) Comparative gene expression profile *Ift88* in BM MSCs treated with 1 µg/mL actinomycin D for 24 hours. CT values were normalised to *18s rRNA*. Mean ± SEM presented as fold-change from vehicle. n = 3 (biological repeats) p** = 0.0011 (paired student t test) **(B)** Western blot analysis of AD MSCs treated with 10 µg/mL cycloheximide for 24 hours. **(C)** Western blot analysis of AD MSCs treated with 10 µg/mL cycloheximide for 48 hours.

48 hours exposure to 10 µg/mL cycloheximide, bands for the IFT88 protein (93 kDa) are still visible in all lanes (Fig. 6.8 B,C). β-actin is an abundant and stable protein with an average protein half-life of about 20 hours and its levels generally do not decrease significantly during short-term cycloheximide treatment, justifying its use as a loading control [337, 338]. Nevertheless a loading indicator was also used to ensure consistent protein loading across gel lanes. Validation of the IFT88 antibody was performed by comparing wild-type and IFT88 hypomorphic lines (Appendix Fig. 5).

To test whether *Ift88* can be deleted *in vitro*, costal chondrocytes from the *Ift88* cKO mouse line were treated with 2 µM 4-OH-T for 72 hours, which is longer than the above estimated lifetime of the *Ift88* mRNA. Costal chondrocytes from the $Ift88^{fl/fl}$ (cre-negative) mouse lines were used as controls. A ~15% reduction in expression of *Ift88* is observed, though not statistically significant (Fig. 6.9 A). A statistically significant reduction in *Acan* and *Gli1* expression was observed. *Gli1* is a zinc finger transcription factor that acts downstream of the Hh signalling pathway which is localised to the primary cilium, thus relevant to *Ift88* deletion. The reduction in *Acan* and *Gli1* expressions are not observed in the control mouse line ($Ift88^{fl/fl}$) (Fig. 6.9 B).

Scaling this experiment to the gradient gels, a higher concentration and longer time frame of tamoxifen treatment were used to compensate for diffusion inside

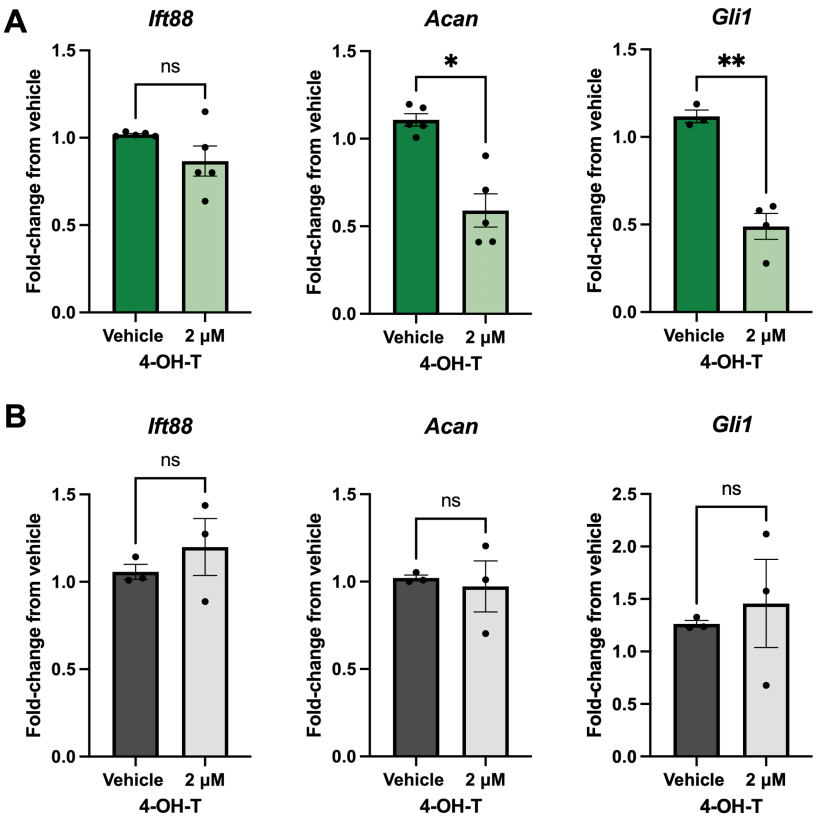


Figure 6.9: *In vitro Ift88* 2D deletion. Comparative gene expression profile *Ift88*, *Acan* and *Gli1* in costal chondrocytes from *Ift88* cKO **(A)** and *Ift88*$^{fl/fl}$ **(B)** mouse lines treated with 2 μM 4-OH-T for 72 hours. Mean ± SEM presented as fold-change from vehicle. n = 3-4 (biological repeats) p* = 0.0137, p** = 0.0039 (paired student t test).

the gel (Fig. 6.10). A ~30% reduction of *Ift88* was observed in the gels, again not statistically significant. *Gli1* was significantly downregulated, as in 2D. Of the other genes measured, only *Prg4* presented a statistically significant change in expression towards upregulation.

6.3.4 *Ift88* and loading regulation of differentiation in vitro

Throughout this chapter, I have evaluated the potential of the *in vitro* model to recapitulate aspects of endochondral ossification and to investigate biological mechanisms underlying *in vivo* phenomena, such as the growth plate shortening observed following *Ift88* deletion (Chapter 4). I hypothesise that the *Ift88*-mediated

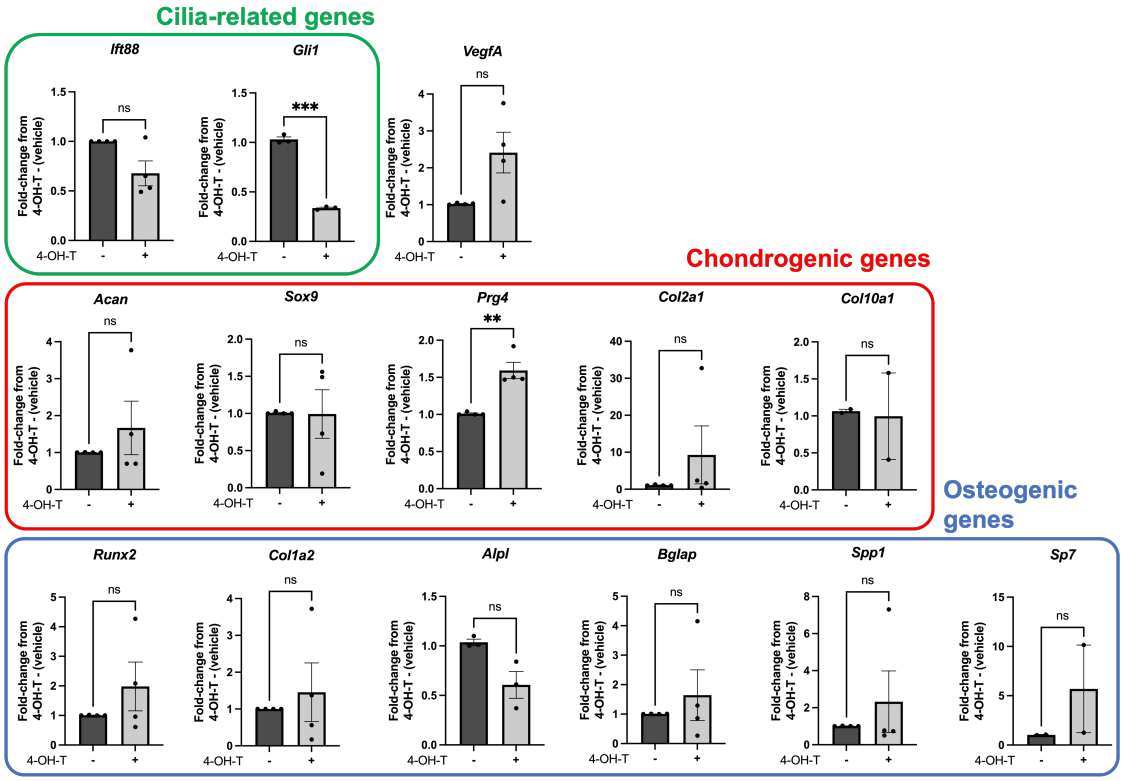


Figure 6.10: Gene expression profiles on day 11 of costal chondrocytes cultured inside BMP-2 gradients treated 5 µM 4-OH-T for 96 hours from day 7. Mean ± SEM presented as fold-change from vehicle. n = 4 (biological repeats) p** = 0.0099, p*** = 0.0007 (paired student t test)

regulation of genes associated with endochondral ossification is itself mechano-regulated, analogous to the mechano-dependent effects of *Ift88* deletion *in vivo* [47]. Accordingly, I propose that *Ift88* deletion *in vitro* would alter the differentiation trajectory of cells within the GelMA hydrogel and affect their responsiveness to mechanical loading. Since BMP-2 loading alone did not modulate the mechanical response of costal chondrocytes in the gels, I further explored whether *Ift88* deletion might trigger a distinct response.

To assess whether downregulation of *Ift88* and *Gli1* observed in Fig. 6.10 influences cell differentiation within the BMP-2 gradient model, gels were subjected to mechanical loading immediately following tamoxifen treatment. The loading protocol (10% strain, 1 Hz, 1 hour/day for 5 days) matched that used in previous experiments. Gene expression was measured after the final loading cycle (Fig. 6.11).

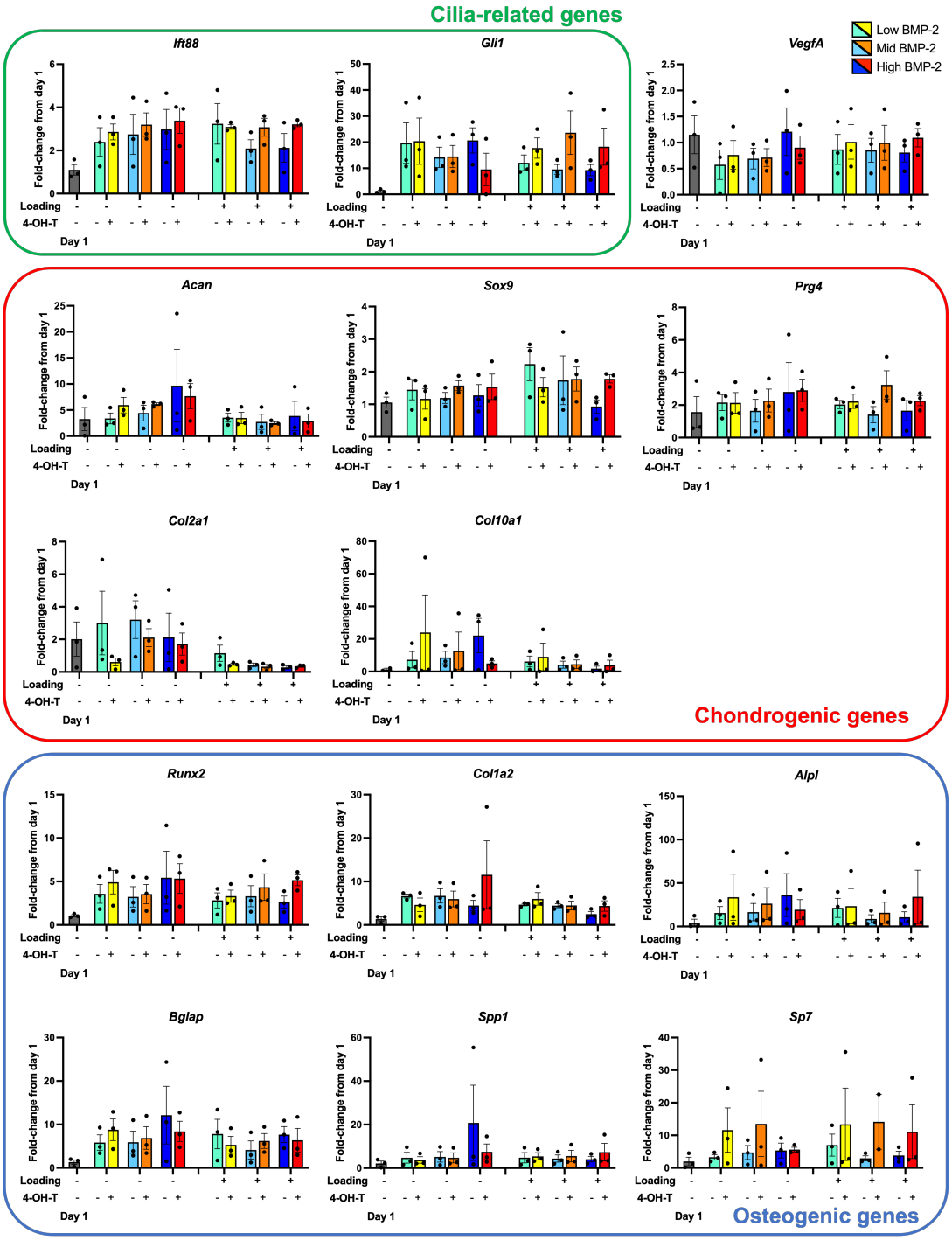


Figure 6.11: Gene expression profiles on day 14 of costal chondrocytes cultured inside BMP-2 gradients treated 5 µM 4-OH-T for 96 hours from day 7 to 11 and loaded from day 11 to 14 at 10% strain for 1 hour at 1 Hz compared to static culture. Mean ± SEM presented as fold-change from day 1. n = 3 (biological repeats).

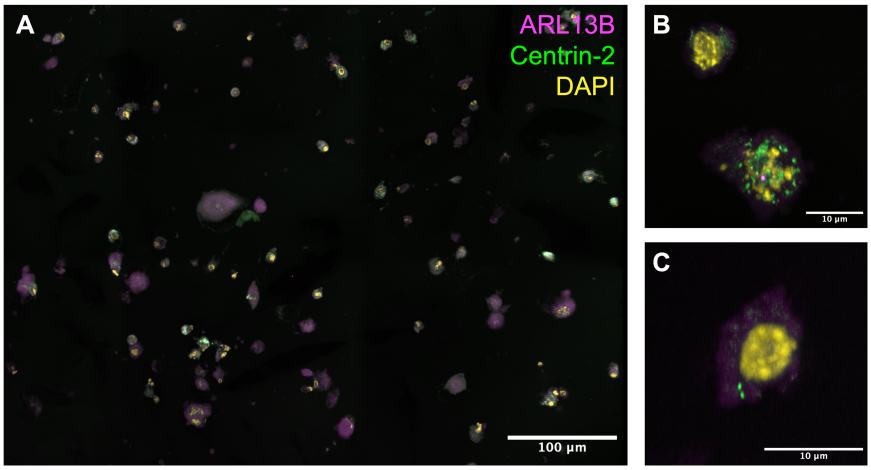


Figure 6.12: Costal chondrocytes inside the BMP-2 gradient on day 28. ARL13B and Centrin-2 are labelled with mCherry and GFP respectively and nuclei are stained with DAPI. **(B)** & **(C)** are higher magnification images of cells in **(A)**.

In the absence of loading, the tamoxifen-induced downregulation of *Ift88* and *Gli1* observed on day 11 was not maintained by day 14. However, under mechanical loading, tamoxifen instead led to increased expression of *Ift88* and *Gli1* in the mid and high BMP-2 regions, though this would need to be confirmed with more biological repeats.

Increased expression under tamoxifen and loading was also observed for *Prg4* and *Sp7*, particularly in the mid and high BMP-2 zones. Nevertheless, no consistent pattern of gene regulation emerged across conditions, suggesting that the effects of tamoxifen and mechanical loading on gene expression are context-dependent and potentially variable.

As the costal chondrocytes in the gradients are from the $Ift88^{fl/fl}$ or *Ift88* cKO mouse lines which present fluorescent signals for ciliary proteins ARL13B and Centrin-2, the gels were imaged using confocal microscopy. Cells are not ciliated inside the gradient gels (Fig. 6.12). Individual centrioles are visible with no ciliary axoneme (Fig. 6.12 B,C). Even without tamoxifen treatment, the cells are not ciliated therefore it was not possible to measure change in ciliation with tamoxifen treatment.

6.4 Discussion

Following their characterisation in Chapter 5, murine cells, both AD MSCs and costal chondrocytes, were cultured inside the BMP-2 gradient. Their potential use as a model of endochondral ossification to study ciliary function was subsequently assessed.

6.4.1 AD MSCs inside the BMP-2 gradient

The expression profiles of AD MSCs inside the BMP-2 gradient show limited spatial responsiveness of chondrogenic and osteogenic markers to the growth factor gradient within the GelMA hydrogel environment, with the caveat of limited repeats performed.

Sox9 expression peaked late (day 28) and lacked regional variation, indicating modest activation of early chondrogenic transcription without spatially guided differentiation (Fig. 6.2). Limited activation of a chondrogenic programme is reinforced by the absence of *Acan*, *Col2a1* and *Col10a1* expression. The consistently low *Prg4* levels indicate the lack of articular cartilage superficial chondrocyte phenotype development. This project being focused on growth plate cartilage, the low *Prg4* is in fact desired. Transcripts per million (TPM) values of gene expression in a 6-week old mouse growth plate from bulk RNA sequencing performed in our group can be found in Appendix Table 2.

Early osteogenic markers *Runx2* and *Col1a2* peaked at day 14 but declined thereafter, which is in line with their early expression in osteogenic differentiation of MSCs. *Alpl*'s more spatially restricted pattern may reflect localised progression towards osteoblastic differentiation. However, other osteogenic markers such as *Bglap* and *Spp1* did not follow clear trends, with *Spp1* (osteopontin) in particular showing consistent downregulation, potentially indicating incomplete matrix mineralisation as osteopontin is a major component of bone extracellular matrix (ECM) and is secreted by bone cells.

Osteogenic gene expression was overall not enhanced in the high BMP-2 region compared to the mid or low zones. This may suggest that BMP-2 alone is insufficient to induce robust spatial differentiation, and that additional signals such as matrix stiffness, hypoxia, or co-delivery of other growth factors might be required to activate a zonal response.

Cilia-associated signalling also appeared unaltered by the BMP-2 gradient. *Ift88* expression remained stable, while *Gli1* was broadly upregulated, suggesting Hh signalling but without zonal modulation. The consistent downregulation of *Vegfa* may reflect a general suppression of angiogenic pathways in this 3D culture system.

6.4.2 Mechanical loading of AD MSCs inside the BMP-2 gradient

Dynamic compressive loading of MSC-based constructs has been shown to upregulate chondrogenic genes, including *Acan*, especially when mechanical stimulation is applied after an initial period of chondrogenic pre-culture [334, 335]. Therefore, loading was applied to the gradient gels to enhance chondrogenesis and identify any mechanosensitive signalling pathways. The results indicate that mechanical loading applied in the context of murine AD MSCs encapsulated inside BMP-2 gradient in these conditions does not enhance gene expression of differentiation markers in AD MSCs (Fig. 6.5). Loading failed to upregulate chondrogenic genes (*Sox9*, *Prg4*), osteogenic markers (*Runx2*, *Col1a2*, *Alpl*, *Bglap*), or cilia-related genes (*Ift88*, *Gli1*). In several instances, gene expression under loading was even reduced compared to the unloaded state.

Timing of load application can affect whether load promotes chondrocyte homeostasis or hypertrophy. Duration of *in vitro* priming changes this response. Early loading preserves chondrocyte homeostasis, whilst later loading promotes cartilage maturation to hypertrophy [334].

Furthermore, no zonal differences were observed in gene expression across the BMP-2 gradient under loading, suggesting that the mechanical stimulus does not synergise with BMP-2 concentration to induce spatially resolved differentiation.

Overall, these findings using AD MSCs suggest that in in this *in vitro* model system, mechanical loading may blunt or suppress molecular responses to BMP-2 in 3D GelMA culture, potentially due to altered matrix-cell interactions, limited mechanosensitivity of AD MSCs or inadequate loading parameters.

6.4.3 Costal chondrocytes inside the BMP-2 gradient

Costal chondrocytes embedded in GelMA responded modestly to the BMP-2 gradient in terms of gene expression, showing some chondrogenic and osteogenic activation and minimal cilia-related signalling modulation (Fig. 6.6). Chondrogenic markers such as *Sox9* and *Acan* were upregulated, hence this chapter focusing on costal chondrocyte thereafter, although the response lacked spatial regulation along the BMP-2 gradient. The slight increase in *Col2a1* and variable *Col10a1* expression suggest partial activation of the chondrogenic programme, but the downregulation of *Prg4* indicates the absence of superficial zone articular cartilage-like phenotype. As this model was being developed to study growth plate cartilage, high *Prg4* expression was not desired. Notably, *Acan* was upregulated, suggesting a stronger inherent chondrogenic potential in primary chondrocytes, even in the absence of zonal BMP-2 effects.

Compared to AD MSCs, costal chondrocytes showed more robust and consistent osteogenic gene expression, with *Runx2*, *Col1a2*, *Alpl*, *Bglap*, and *Sp7* all being upregulated to varying degrees. However, this osteogenic response also lacked a clear spatial gradient, despite *Alpl* showing slightly higher expression in mid and high BMP-2 regions at earlier time points. *Alpl* and *Bglap* both declined by day 42, suggesting that osteogenic activation is potentially transient. *Spp1* remained unresponsive, consistent with incomplete osteogenic maturation.

Cilia-related gene expression remained largely unaffected by BMP-2 stimulation. *Ift88* showed no consistent change, and while *Gli1* was strongly upregulated at day 42, this effect appeared in only one replicate, making the result inconclusive. *Vegfa* expression remained unchanged, indicating no induction of angiogenic signalling in this context.

This absence of zonal differences in gene expression contrasts with the positive safranin-O and toluidine blue staining observed in the high BMP-2 region (Fig. 6.3). This discrepancy may reflect the temporal disconnect between mRNA expression and protein deposition, as the proteoglycan-rich matrix visualised by histological staining could have been synthesised at an earlier stage, not captured at the time of gene expression analysis.

Timing represents a key challenge in *in vitro* modelling, as differentiation dynamics often differ from those observed *in vivo*, despite the ability to sample more time points. In this project, weekly time points were assessed, with a primary focus on gene expression. However, additional insights into cellular differentiation could be gained through protein-level analyses, such as Western blotting or proteomics.

Together, these results show that while costal chondrocytes exhibit greater osteochondral differentiation than AD MSCs, they do not exhibit strong zonal patterning in response to the BMP-2 gradient. This suggests that BMP-2 alone is insufficient to induce spatially distinct gene expression in these 3D hydrogel cultures and that additional factors may be necessary to drive gradient-responsive behaviour.

By further characterising the BMP-2 gradient model developed by Li et al. (2019) using mouse cells, I identified several limitations [174]. While the simplicity of the system is advantageous for accessibility and reproducibility, it may be insufficient to fully replicate the complexity of endochondral ossification or the growth plate environment. To enhance its physiological relevance, additional refinements may be required, including optimisation of the culture medium, selection of appropriate growth factors, tuning of the gel's mechanical properties and choice of cell type.

6.4.4 Mechanical loading of costal chondrocytes inside the BMP-2 gradient

Costal chondrocytes cultured under mechanical loading within a BMP-2 gradient also showed minimal transcriptional response to the stimulus. There was no evidence of zonal regulation, and mechanical loading did not enhance chondrogenic or osteogenic gene expression (Fig. 6.7).

Chondrogenic markers (*Sox9*, *Prg4*) remained unchanged, while the matrix-related genes *Col2a1*, *Col10a1*, and *Acan* were downregulated. This suggests a possible suppression of the chondrogenic phenotype under mechanical load or a reduced capacity to maintain chondrocyte identity in the given hydrogel environment. Most osteogenic genes (*Runx2*, *Col1a2*, *Bglap*, *Spp1*, *Sp7*) also remained unaffected by loading. *Alpl*, a key marker of osteoblastic activity, presented reduced expression, further supporting the interpretation that loading did not synergise with BMP-2 to promote osteogenic differentiation in this system. Cilia-related signalling also appeared unresponsive, with *Ift88* and *Gli1* showing no change in expression, and *Vegfa* remaining at the same level as day 1. This contrasts with the hypothesised role of cilia in mediating mechanical signal transduction. This suggests that the model may not provide a supportive environment for investigating the role of primary cilia in mechanotransduction, particularly given that cilia could not be visualised within the hydrogel (Fig. 6.12).

Taken together, these findings suggest that mechanical loading does not enhance lineage-specific gene expression in costal chondrocytes cultured within a BMP-2 gradient in GelMA. Instead, loading may contribute to phenotypic suppression, particularly of cartilage matrix genes, and fails to enhance osteogenic or angiogenic programmes. The load values measured by the ElectroForce confirm that the gels were being loaded as a sinusoidal curve was observed (Fig. 6.4). However, the magnitude of these values cannot be reliably assessed or compared between gels as a

200 N load cell was used. Since the load values measured here were in the range of 1 N - below the optimal range for this load cell - the readings are unreliable. This load cell is better suited for testing stiffer, harder tissues.

These results support the conclusion that neither the BMP-2 gradient nor mechanical loading alone are sufficient to drive zonal tissue formation in this hydrogel system. In addition, all cell cultures encapsulated in GelMA exhibited substantial biological variability between replicates. Some genes had higher scale of fold-change (in the tens and hundreds). With more repeats, these might have potential of being truly differentially expressed genes. As discussed in Chapter 5, this variability may stem from the use of primary cells and subtle differences in the culture environment. High variability is also a recognised feature of *in vivo* studies, often necessitating large numbers of animals. Similarly, to strengthen the interpretation of my findings, a greater number of biological repeats would be required. Although one of the key advantages of *in vitro* systems is the reduction in animal use, this benefit diminishes if numerous mouse isolations are needed to achieve robust data. This highlights a broader argument in favour of using human cells, which may offer greater consistency and translational relevance.

6.4.5 *Ift88 in vitro* deletion

From the actinomycin D study, the *Ift88* mRNA lifetime is approximated to be 30 hours (Fig. 6.8). This suggests that with a tamoxifen treatment longer than 30 hours, transcription all new *Ift88* mRNA can be blocked. However the IFT88 protein seems to be very stable as blocking translation for 48 hours with cycloheximide does not remove the protein. Therefore, even if the mRNA is removed with tamoxifen treatment, functional IFT88 protein will still be present in the cell.

Tamoxifen treatment on costal chondrocytes cultured in 2D resulted in a ~15% decrease in *Ift88* expression (Fig. 6.9). IFT88 deletion using 10-week old Aggrecan-CreERT2;*Ift88*$^{fl/fl}$ mice resulted in a ~30% decrease in *Ift88*-positive cells in tibial

articular cartilage 2 weeks after tamoxifen treatment compared to *Ift88*$^{fl/fl}$ mice [80]. This suggests high IFT88 deletion efficiency is difficult to achieve in chondrocytes and a low deletion efficiency can still result in a phenotype *in vivo*. In addition, even with *Ift88* expression reduction, protein will remain in the cell due to its high stability. The magnitude of *Ift88* deletion could be increased with higher concentration and time frames of tamoxifen treatments. Previous studies have used siRNA or chloral hydrate treatment to successfully disrupt ciliogenesis [109, 110]. However, in my hands *Ift88* has also been difficult to inducibly delete, hence our group is now turning to CRISPR null *in vitro* systems, which presents other limitations.

Tamoxifen did significantly reduce *Acan* expression compared to controls. There is no existing evidence of a correlation or regulatory relationship between *Acan* and *Ift88* mRNA levels in cartilage. The results here, therefore, may point to a new mechanism *in vitro*. Give that the studies in Chapter 4 used an *Acan*-Cre driver to delete *Ift88*, these findings raise the possibility of a feedback mechanism *in vivo*, in which loss of *Ift88* may, in turn, suppress *Acan* expression.

Gli1, a marker of Hh pathway activity, expression was also significantly reduced. Therefore, the low *Ift88* expression reduction may be enough to disrupt primary cilium function. In AggrecanCreERT2;*Ift88*$^{fl/fl}$ mice, *Ift88* deletion resulted in an increase in *Gli1*-positive cells in articular cartilage [80]. Cells *in vivo* and *in vitro* may have different regulatory environment. *In vivo* adaptation may activate compensatory pathways that upregulate *Gli1* expression independent of ciliary function.

In the GelMA system, a ~30% reduction of in *Ift88* expression was observed, as well as a strong downregulation of *Gli1* (Fig. 6.10). Though other chondrogenic and osteogenic genes' expression were unchanged, this ciliary disruption could affect differentiation. This was assessed by loading the gels after tamoxifen treatment.

While day 7 results suggested that tamoxifen-induced deletion of *Ift88* reduces *Gli1* expression - consistent with disrupted Hh signalling downstream of cilia impairment - this effect was not sustained by day 14 in the absence of loading (Fig. 6.11).

Mechanical loading appeared to counteract this expected downregulation: both *Ift88* and *Gli1* were upregulated in the mid and high BMP-2 zones following tamoxifen treatment combined with mechanical stimulation.

This upregulation may reflect a compensatory response to cilia dysfunction or altered mechanosensory signalling in the context of ciliary disruption. Primary cilia mediate cell mechanotransduction and morphogen sensing, and their loss inside a gel culture system could sensitise cells to mechanical stimuli in ways that are not yet fully understood.

Gene expression of *Prg4* and *Sp7* - associated with superficial zone and osteogenic differentiation, respectively, were also elevated under combined tamoxifen and loading conditions in the mid and high BMP-2 regions. As these are the only genes that showed any differential expression, it is difficult to correlate this to any shift in differentiation trajectories following *Ift88* deletion. This suggests that the interaction between cilia disruption and mechanical load is complex and non-linear in this system. The observed effects may be dependent on BMP-2 concentration, spatial positioning within the gradient or timing post-*Ift88* deletion. Furthermore, the variability between biological replicates underscores the need for further studies to confirm these preliminary findings and dissect the mechanistic basis of the observed responses.

Taken together, these data suggest that mechanical loading may modulate the impact of *Ift88* deletion on gene expression in a spatially restricted manner, but does not uniformly amplify or disrupt differentiation.

Despite detectable *Ift88* expression, no primary cilia were observed in costal chondrocytes embedded in GelMA, as indicated by the absence of ciliary axonemes (Fig. 6.12). One possible explanation is that the cells were predominantly in a proliferative phase of the cell cycle, during which cilia are resorbed prior to mitosis. However, this is unlikely to fully account for the absence of ciliation, as no marked differences in cell number or total mRNA content were observed between time points.

Alternatively, the biophysical properties of the hydrogel micro-environment may impair ciliogenesis. Primary cilia assembly is sensitive to ECM stiffness, mechanical stress and cell shape constraints, all factors that are modulated in 3D hydrogels. Previous studies have shown that a soft or unstructured matrix, or limited substrate adhesion, can reduce cilia frequency or length. Mouse chondrocyte primary cilia shorten when cultured on softer substrates. Centrioles also position themselves differently depending on substrate stiffness [232]. The stiffness of the gels used here (~30 kPa) is within the range where primary cilia have been observed in cells cultured in gels.

Previous studies suggest primary cilia play a key role in chondrocyte mechanotransduction. One study applied the same loading regime (1 Hz, 10% strain) to mouse chondroprogenitor cells in 3D cultures promoted chondrogenesis, an effect that was abolished with the loss of primary cilia [110]. In another study, loading of mouse chondrocytes seeded inside agarose gels resulted in an increase in *Acan* expression, which was lost in the absence of primary cilia [296]. The absence of a primary cilium inside the gels may therefore explain the absence of response to mechanical load. Nevertheless, there are other mechanosensitive organelles and molecules, which the cells could use for mechanotransduction. The molecular mechanism of ciliary mechanosensing appear to differ between cell types and remains unknown for many [109, 110].

In conclusion, these results highlight the challenges of recapitulating spatially patterned differentiation *in vitro* using soluble gradients and suggest the need for more complex microenvironmental cues to guide cell fate with spatial precision. The choice of cell source, material type and stiffness, culture conditions all play a key role in guiding differentiation and needs to be precisely tuned for specific needs and applications.

Using mouse cells in this model has not been successful in creating a truly useful biological model. Mouse cells have previously been used successfully *in vitro* therefore

care must be taken as to what cell source to use and in what context [110]. The advantage of using mouse cells in *in vitro* models lies in being able to use the genetic tools these offer. If these cannot be exploited, then it remains more clinically relevant to use human cells and use tools such as siRNAs to manipulate genetic pathways. When human MSCs are used inside a gradient of BMP-2, osteogenic genes ALPL, SP7 and SPP1 were more highly expressed in the region of high BMP-2 concentration [195]. Although MSCs hold translational promise for tissue engineering, they may not accurately represent the biology of limb bud progenitor cells responsible for forming the cartilage anlage during development or the stem cells giving rise to resting chondrocytes in the growth plate.

In addition, growth factor choice is also very important in driving differentiation, and in view of these results, could be optimised in this context. Co-delivery of TGF-β3 and BMP-2 genes or proteins in hydrogels or explants enhances chondrogenesis and suppresses hypertrophy and calcification more effectively than either factor alone. This combination leads to higher levels of glycosaminoglycans and collagen type II, with reduced collagen type X (a marker of hypertrophy) [339, 340].

While BMP-2 remains a gold standard for bone and cartilage engineering in hydrogels, other BMPs can offer unique advantages in potency and specificity of differentiation. Combining or sequentially delivering BMP-2 with these factors can further enhance differentiation and tissue regeneration outcomes in stem cell and chondrocyte-based hydrogel systems. Sequential delivery of BMP-2 and BMP-7 from microcapsule-based scaffolds results in greater osteogenic differentiation and bone regeneration of osteoblast precursors than either factor alone [341]. This approach mimics the natural expression profile during bone healing and leads to higher alkaline phosphatase activity and bone mineral density.

Precisely directed stem cell differentiation enables the modelling of region-specific cartilage, including both articular and growth plate cartilage [153, 342, 343]. For example, activation of the TGF-β pathway in chondrogenic progenitors derived from

human pluripotent stem cells supports the generation of articular chondrocytes capable of forming stable cartilage both *in vitro* and *in vivo*. In contrast, BMP-4-driven chondrocytes exhibit hypertrophic features and produce cartilage that can initiate endochondral ossification *in vivo* [153]. These cell types are useful for repairing damaged articular cartilage and for creating models of cartilage degeneration and disease to support drug discovery. Therefore, many different signalling pathways can be activated to promote differentiation of stem cells or chondrocytes. Different cell sources may require tailored differentiation protocols and may be more suited to specific applications. This should be tuned according to application, but also behaviour of cells' in ones' hands.

7

Discussion

Contents

7.1 Overall discussion 205

7.2 Limitations 214

7.3 Future work 218

7.4 Conclusion 220

7.1 Overall discussion

This project has provided insights into the role of primary cilia and mechanical forces in growth plate endochondral ossification. By developing a high resolution

3D imaging method exploiting endogenous fluorescent ciliary signals within intact tissue, I was able to map 3D orientation of cells, primary cilia and centrioles in growth plates at a previously unprecedented scale, both in terms of cell and animal numbers. A key strength of this methodology lies in the combination of super-resolution microscopy and automated, highly specific signal detection, allowing us to capture large datasets with minimal user bias.

Conventional approaches to measuring cilia prevalence typically rely on 2D imaging and immunohistochemistry, which often underestimate true ciliation due to occlusion by the nucleus and non-specific background staining, particularly when using acetylated α-tubulin staining. My approach circumvents these limitations, enabling a more accurate spatial analysis of cilia orientation and distribution *in situ*.

In the tibial growth plate, the data describe a consistent pattern of primary cilia orientation, with axonemes pointing predominantly in the ventral-dorsal directions and more horizontally than vertically. This is in contrast with the evidence which existed up to this point, which described predominant proximal-distal orientations, parallel to the columnar organisation of the growth plate chondrocytes and compressive forces going through the growth plate during ambulatory movement. Only subtle differences were observed across zones and regions of the growth plate. While many studies have examined primary cilia length and prevalence *in vitro*, such analyses often miss the context-specific structural and functional cues that are only evident within tissue. My work highlights the importance of studying cilia within their native architecture.

This defined orientation of primary cilia may play a pivotal role in guiding how cells interpret spatial and directional cues within the highly anisotropic environment of the growth plate. Given their function as mechanosensory and chemosensory organelles, cilia aligned horizontally to the longitudinal bone axis may facilitate the directional capture of extracellular signals. Primary cilia are perhaps not pointing directly vertically up or down (proximal-distal direction) because this protects them from the direct impact of the mechanical load. Future work should investigate

whether changes in cilia orientation disrupt the spatial patterning of signalling pathways, thereby affecting cell columnar organisation and longitudinal bone growth. These are challenging experiments to conceive give how little we understand about how cilia orientation is regulated.

In Chapter 4, this thesis describes alterations to cellular orientations and primary cilia in the context of genetic targeting of cilia and with changes to limb loading. These experiments revealed subtle, often location-specific changes. For example, changes to primary cilia prevalence were often observed in the hypertrophic zone in the *Ift88* cKO and *Ift88*$^{fl/fl}$ offloaded growth plates. These effects were most pronounced in the peripheral region (outside of the limb), potentially reflecting altered mechanical environments. This is consistent with the known mechanical vulnerability of hypertrophic chondrocytes, which less stiff as proliferating chondrocytes and have larger cell volumes. Such mechanical vulnerability may be an intrinsic feature of the hypertrophic differentiation process, but may also make them more susceptible to disruptions in cilia function or mechanical loading [12, 249].

These observations raise broader questions about how primary cilia function as mechanosensory organelles: do they operate via binary switching mechanisms, triggering an all-or-nothing signal once a force threshold is reached, or do they transduce mechanical signals in a graded, rheostat-like manner, producing a proportional response that scales with the intensity of stimulation [344]? These questions are very challenging to address *in vivo.*

In certain contexts, such as kidney development, primary cilia act as molecular switches that toggle between canonical and non-canonical Wnt signalling in response to fluid flow [345]. Conversely, rheostat models suggest that changes in cilia length or composition modulate signalling intensity proportionally to the stimulus, akin to a dimmer switch. Computational modelling suggests the capture rate of signalling molecules increases with cilium length, supporting a graded, proportional response rather than a strict threshold effect [346]. In contrast, my findings suggest

that significant functional changes, evidenced by altered growth plate architecture, occur without measurable changes in cilium length, challenging both switch and rheostat models.

Other models exist as well. In the 'passive indicator' model, cilia length changes are incidental and do not influence signalling [234]. The 'local concentration' model posits that shorter cilia concentrate membrane proteins to facilitate signalling. It has been proposed that the longer primary cilia observed in senescent fibroblasts may impair their ability to respond to Hh signalling by diluting the concentration of receptors and downstream signalling components within the cilium [347]. In the altered composition model, changes in primary cilia length skew signalling towards a certain function, as length influences the composition and variety of receptors to alter the signalling capacity of the primary cilium.

Most of these models have been derived from studies in non-cartilaginous tissues. Given the diversity of ciliary functions across tissue types, their applicability to cartilage cannot be assumed. My data do not strongly support a switch or rheostat model in the growth plate, though changes in ciliary composition in *Ift88* mutants or unloaded conditions remain possible and warrant further investigation. The specific molecular mechanisms and how a cilium acts are still active areas of research. Many unanswered questions remain, particularly regarding which threshold, if any, dictates switching vs graded response in various tissues.

In addition to understanding signal output, important questions remain about how cilia are structurally organised. The molecular mechanisms governing axoneme formation, basal body positioning, and orientation in the cell are still poorly understood. Linking cilia structure to specific signalling pathways, ideally through molecular analysis combined with high-resolution imaging, is particularly needed. Although new techniques, such as live imaging, tissue clearing techniques and improved subcellular imaging, are advancing the field, current technologies still struggle to resolve the finer subcellular structural features of the cilium *in situ*.

The regulation of cilia length, its impact on bending dynamics and its relationship to signal transduction remain incompletely understood. In disease contexts such as osteoarthritis, cilia become longer and more prevalent in articular cartilage yet the functional consequences of these changes are still being elucidated [348]. Understanding the spatial organisation and function of primary cilia in the healthy postnatal growth plate has direct implications for developmental disorders such as chondrodysplasias, growth plate fusion syndromes and ciliopathies. Growth plate disorganisation has been observed in many of these conditions, therefore an understanding cilia organisation in these would further help understand the structure-function relationship of primary cilia. An ambition of this project was to use MSCs derived from ciliopathy mouse models inside the *in vitro* model in order to determine differences in cellular differentiation and ciliation. Moreover, these insights can inform tissue engineering approaches for skeletal repair. For instance, scaffolds or organoids that mimic physiological cilia organisation and mechanosensory dynamics may be better able to recapitulate *in vivo* growth plate behaviour.

Finite element modelling and other computational approaches are now being used to simulate mechanical strain experienced by cilia in tissues such as the growth plate [206]. These *in silico* tools, combined with experimental data, can refine our understanding of mechanotransduction and inform hypotheses about cilia behaviour under load. The high-resolution spatial data generated in this study, including orientation metrics, centriole positioning and ciliation percentages, represent a valuable resource for parameterising computational models of growth plate biomechanics and morphogen signalling. Finite element models, for instance, could incorporate local cilia orientation to simulate how mechanical strain is sensed and transduced at the cellular level. Similarly, models of morphogen diffusion and uptake could integrate cilia spatial data to predict how alterations in orientation or prevalence influence signal capture efficiency. By aligning empirical findings with theoretical frameworks, future work can bridge the gap between cellular architecture and tissue-scale behaviour.

Comparison of my results of ciliary deletion with other studies suggest that cilia function and organisation differ between embryonic and postnatal stages. Embryonic chondrocytes organise into columns via distinct mechanisms, and the cilium may have stage-specific roles in these processes [11]. During embryogenesis, cilia may exert more instructive functions, such as establishing morphogen gradients and planar cell polarity, whereas in the postnatal growth plate, their role may shift toward modulating proliferation, matrix production, and mechanical adaptation. This functional transition could reflect changes in both tissue architecture and signalling environment. For example, the embryonic growth plate may be exposed to different mechanical forces and more responsive to diffusible factors, whereas postnatal tissues must interpret a combination of biochemical and mechanical inputs. Understanding how cilia function evolves over time is essential for designing stage-specific interventions, particularly in paediatric growth disorders.

While this project focused on genetic and mechanical perturbation of ciliary function, future studies should aim to correlate these changes with molecular phenotypes. Immunohistochemical analysis of ECM components (collagen types II and X, aggrecan) and signalling pathways (Hh, Wnt) would help elucidate the downstream effects of altered ciliation. To further dissect the functional consequences of cilia organisation, integration with molecular profiling techniques such as spatial transcriptomics and proteomics could provide new insight. Spatial transcriptomics would enable the mapping of gene expression patterns in relation to cilia orientation, centriole position or cell architecture. Proteomic analyses could characterise the composition of the ciliary membrane and axoneme in different zones of the growth plate or under different loading conditions [349, 350]. These approaches would complement imaging-based analyses, allowing us to link structural organisation with signalling capacity and cellular state at high spatial resolution.

Although many ciliary gene deletion models in mice have now been characterised, they often yield redundant insights and have yet to drive translational advances. Nonetheless, they have clarified the central importance of cilia in tissue homeostasis.

Encouragingly, gene therapy approaches show promise. For example, adenoviral delivery of *Ift88* into olfactory neurons restored both cilia structure and sensory function in a ciliopathy model, demonstrating therapeutic potential [351].

Although not the primary focus of this study, factors such as genetic background and sex may influence primary cilia characteristics and growth plate behaviour. Mouse strains can exhibit differences in skeletal growth rates, cartilage composition and ciliary gene expression, all of which could affect experimental outcomes. Similarly, sex hormones are known to modulate chondrocyte proliferation and differentiation and may also influence cilia length or function, particularly during puberty [352]. While the primary cilia imaging was performed in both males and females, future studies could explore these variables more systematically to determine whether they contribute to variability in ciliary organisation.

However, *in vivo* models remain limited in their ability to investigate spatio-temporal changes within dynamically growing tissues. Here, *in vitro* systems offer an opportunity. Despite the challenges faced in this project with the *in vitro* model, these still offer a complementary platform with incredible potential to uncover underlying molecular biological mechanisms, especially when used in combination with more traditional *in vivo* models. By enabling controlled manipulation of specific variables, these systems can help dissect complex biological processes and bridge knowledge gaps left by whole-organism studies.

This potential is underscored by a recent study that applied single-cell RNA sequencing to embryonic human long bones across developmental stages, generating a high-resolution atlas of endochondral ossification [353]. By integrating this atlas with publicly available datasets of *in vitro* chondrogenesis, they uncovered substantial heterogeneity among *in vitro* methods, including variable and sometimes off-target cell states that did not always align with the natural developmental trajectory. Mapping these deviations highlighted inefficiencies and sources of error in current tissue engineering approaches. The work provides a framework for benchmarking and

refining *in vitro* protocols through developmental biology insights, while emphasising the inherent complexity of endochondral ossification and the challenges of faithfully modelling it outside the organism.

Creating an *in vitro* model of the growth plate will likely require a combination of methodologies and engineering tools. The buoyancy-driven BMP-2 model remains an interesting platform to develop an osteochondral model. Pursuing it further with human MSCs offers possibilities to study growth plate biology, as it currently being done in our group. In addition to the BMP-2, using techniques such as acoustic patterning to arrange cells into columns would model the tissue architecture of the growth plate even more. This has already successfully been done with MSCs and chondrocytes in GelMA [198]. Low-intensity ultrasounds can also be used to control the length and bending of primary cilia. 5.0 MHz ultrasounds increased the length and bending of primary cilia in bovine cartilage explants in a reversible manner [354].

Future refinements of this models could also include culture conditions. The right balance of exposure to TGF-β and BMP growth factors will direct MSCs into chondrocytic profiles matching the growth plate. Harnessing cells' self-organising capabilities may also allow spontaneous formation of columnar architecture in certain conditions [185].

Integration into microfluidic chips creates further opportunities. The BMP-2 gradient has successfully been formed onto a chip, offering opportunities of co-culture with different cell types, different forms of mechanical stimulation, integration of other readouts [195].

Though mechanical loading did not promote differentiation in the results presented here, there is evidence that it can drive chondrogenic and osteogenic differentiation in organoid and bioengineered models [334, 355, 356]. Mechanical modulation is also important to maintaining growth plate ECM composition [191]. Optimising displacement, frequency and duration parameters may be key to inducing robust responses. 'Healthy' loading regimes mimic walking and usual mechanical load

experienced by limbs. 'Pathological' loading regimes can also be applied to understand the impact of too much mechanical load on cartilage and bone health. In studies that have performed low, medium and high cyclic loading, they have increased the displacement range [291, 357]. Frequency and duration could also be increased.

In this context, loading should be an essential consideration when investigating primary cilia, particularly in tissues like the growth plate, where mechanotransduction is central to development.

Increasingly, *in vitro* models are being employed to study cartilage pathobiology and cilia-dependent signalling [205]. Novel *in vivo* and *in vitro* techniques will contribute to expanding the molecular, cellular and tissue-level understanding of growth plate dynamics and the role of primary cilia within it. For example, live-imaging techniques for the observation of the elongation of growth plate cartilage in murine long bone explants have been developed [358]. This would allow the live observation of the effects of disruptions in endochondral ossification on cellular behaviour.

Another study developed a computational pipeline capable of reconstructing temporal and spatial maps of gene activity during growth plate development from single cell RNA sequencing [359]. It refines our understanding of the cellular and molecular events that govern bone growth, provides a valuable resource of gene signatures for specific chondrocyte stages that could be used to design *in vitro* growth plate models.

Although this study used murine models, the pathways and structural features of primary cilia are highly conserved across mammals, suggesting that the findings have relevance for human growth plate biology. Importantly, the *in vitro* BMP-2 gradient model developed here could be adapted to human MSCs or patient-derived chondrocytes. Such a system would enable the study of human-specific growth plate responses to genetic or mechanical perturbations, providing a valuable translational avenue. Moreover, incorporating induced pluripotent stem cells (iPSCs) could allow disease modelling of patient-specific ciliopathies or skeletal dysplasias in a physiologically relevant context.

Together, the findings from this thesis advance our understanding of primary cilia as integrative structures that respond to spatial, mechanical and molecular cues in the growth plate. An evaluation of how the aims of this project were met is described in Table 7.1.

Ultimately, a combinatorial approach - combining *in vivo*, *in vitro*, and *in silico* models - will offer a multidimensional framework for studying how ciliary organisation contributes to skeletal development and how its disruption may lead to disease. Hybrid systems can harness the strengths of each to deliver a more holistic understanding of growth plate biology and the role of primary cilia in development and disease. The methodologies and concepts developed here not only clarify fundamental aspects of growth plate biology but also establish platforms for future research and therapeutic innovation.

7.2 Limitations

A key limitation of the imaging approach developed in this study and described in Chapter 2 lies in its computational intensity and technical demands. The image files generated can exceed 100 GB, requiring computers have to store and process them. This restricts accessibility to research groups without sufficient computational resources. Furthermore, the imaging strategy is contingent on the availability of a high-resolution, multiphoton or confocal microscope, as well as compatible image analysis software, arivis in this case. The use of a transgenic mouse line expressing endogenous fluorescent reporters for cilia and centrioles is critical to the success of this method. Together, these technical dependencies may limit reproducibility and scalability across laboratories, particularly those without access to advanced imaging platforms.

While the automated image analysis pipeline developed for this study enabled high-throughput quantification of primary cilia features across large tissue volumes, it

Table 7.1: Evaluation of the achievement of project aims set out in Chapter 1

Aim	Achievement
Characterise the spatial organisation and morphological features of primary cilia across distinct zones of the postnatal mouse growth plate, providing insights into their potential role in growth plate architecture and zonal function.	This objective was addressed through the development and application of a high-resolution 3D imaging and image analysis pipeline (Chapters 2, 3). The results demonstrated that primary cilia exhibit a distinct spatial organisation pattern across growth plate zones, with differences in prevalence and length.
Assess how this organisation is changed in an Ift88 conditional knockout model and in the absence of load.	This objective was achieved through comparative analysis of growth plates from *Ift88* cKO and control mice, as well as from mice subjected to mechanical offloading (Chapter 4). Although complete loss of *Ift88* function was not directly confirmed, morphological analysis indicated a small reduction in cilia prevalence in *Ift88* cKO growth plates. Offloaded limbs showed changes in growth plate morphology, with no significant changes cilia organisation.
Establish an in vitro model of osteochondral differentiation that recapitulates key aspects of growth plate development and organisation.	This objective was addressed through the design and fabrication of a GelMA-based hydrogel system incorporating a BMP-2 gradient (Chapter 5). Though some osteochondral differentiation was achieved, key aspects of the growth plate, such as columnar organisation, matrix deposition and gradients of gene expression patterns were not achieved and require further development.
Interrogate the role of primary cilia in orchestrating osteochondral differentiation under defined mechanical loading conditions using the in vitro model, to better understand how ciliary structure and function contribute to mechanotransduction during skeletal development.	This objective was addressed by combining the GelMA-based differentiation system with controlled compression to investigate how cilia disruption and mechanical loading interact to influence cell differentiation (Chapter 6). The results indicated that both mechanical loading and *Ift88* deletion did not modulate differentiation patterns to a great extent. These experiments nonetheless demonstrated the feasibility of integrating genetic and mechanical perturbations within a 3D *in vitro* framework.

also introduced certain limitations. The accuracy of cilia and centriole detection is dependent on signal intensity and contrast, which can vary across imaging depths and tissue regions due to light scattering or uneven expression of fluorescent reporters. Although thresholding parameters were optimised, some false positives or missed detections are inevitable, particularly in densely packed regions or near tissue edges. The analysis also assumes that cilia project linearly from the base, which may not be true for bent or curved axonemes.

While changes in cilia prevalence or orientation correlate with changes in growth plate architecture, causality cannot be definitively established. Other variables, such as effect of tamoxifen, systemic compensatory mechanisms to genetic disruptions, such as upregulating of other genes or signalling pathways with overlapping functions to compensate for the loss of function, could contribute to observed phenotypes, and cilia may be reactive rather than instructive in some contexts. In this same line of thought, *Ift88* deletion may have broader cellular effects beyond cilia disruption. Thus, phenotypes attributed to cilia loss may reflect broader disruptions.

The *in vitro* model developed in this study also has important limitations. Most notably, mouse-derived cells proved challenging to culture under the defined differentiation and loading conditions, leading to inconsistent results. Adipose-derived MSCs were used, which were isolated from the epididymal fat pads of male mice. This introduces a biological bias, as these cells are sex-specific and may not fully recapitulate the behaviour of growth plate progenitors. Additionally, AD-MSCs cultures are inherently heterogeneous, with considerable variability between isolation batches. This variability complicates reproducibility and may mask subtle effects caused by ciliary disruption or mechanical stimuli. In addition, the mechanical properties of GelMA were not characterised in detail, for example through rheological characterisation. The material properties of the scaffold could be more extensively optimised for a particular cell type to be pursued with this model.

A further limitation concerns the mechanical stimulation regime employed in the gradient gels. Although compression was applied using a controlled loading system, the forces transmitted to individual cells within the hydrogel were not directly quantified. Local variations in stiffness and crosslinking density may have led to non-uniform strain distribution, meaning that some regions experienced more or less mechanical deformation. Moreover, the applied loading parameters - frequency, amplitude, and duration - were based on those used in previous studies to mimic physiological loading *in vitro* but did not capture the full spectrum of physiological mechanical cues experienced *in vivo*, such as shear stress, interstitial fluid flow or multi-axial strain. Without precise mapping of the local mechanical environment, the relationship between ciliary response and mechanical stimulus remains partly inferential. Future refinements could include embedded microsensors or finite element modelling to better correlate cellular mechanotransduction with spatially resolved loading patterns.

The choice and presentation of growth factors in the morphogen gradient also introduce sources of variability and limitation. The current system used BMP-2 as a morphogen, representing one of several signalling pathways implicated in endochondral ossification. However, in the native growth plate, ciliary signalling integrates inputs from multiple gradients, including Ihh, PTHrP, and Wnt pathways, which were not incorporated here. As such, the single-factor gradient provides only a simplified representation of the complex biochemical landscape encountered by chondroprogenitor cells *in vivo*. Furthermore, the stability, diffusion kinetics and bioavailability of BMP-2 within the GelMA matrix were not directly measured, and may have varied over time or across regions of differing crosslinking density. Co-delivery of multiple factors or the use of microfluidic gradient systems allowing temporal modulation of morphogen exposure, could provide a more physiologically relevant and controllable environment.

While human MSCs may ultimately provide a more translationally relevant platform, their integration into the current gradient and loading systems poses other technical

challenges. Moreover, the *in vitro* system, although containing a morphogen gradients, lacks the complex vascular, hormonal and systemic interactions present *in vivo*, limiting its ability to fully recapitulate the dynamic environment of the growing growth plate.

7.3 Future work

The findings of this study open several avenues for future research into the mechanobiology of primary cilia and their role in growth plate regulation. A key priority would be to validate the extent and spatial distribution of *Ift88* deletion in the murine models. Quantification of recombination efficiency through qPCR, Western blotting, or immunofluorescence would confirm the degree of IFT88 depletion across growth plate zones and help clarify whether the partial or mosaic deletion observed may have contributed to the modest differences in cilia alignment and prevalence.

Future work should also aim to more precisely characterise the local mechanical environment experienced by chondrocytes in both *in vivo* and *in vitro* systems. Integration of modelling with high resolution imaging could provide 3D maps of strain distribution within the growth plate, linking microstructural organisation with mechanical load transmission.

In parallel, further optimisation of the GelMA-based gradient system could improve its physiological relevance and reproducibility. Systematic rheological characterisation across stiffness ranges and photopolymerisation conditions would help define consistent mechanical properties for cell culture experiments. The gradient system could also be extended to incorporate controlled co-gradients of multiple morphogens, including Ihh, PTHrP, and Wnt ligands, to better mimic the biochemical landscape of the native growth plate. Microfluidic or 3D bioprinting technologies could be applied to generate spatially and temporally dynamic morphogen distributions, allowing direct investigation of how cilia integrate competing mechanical and biochemical signals.

The imaging methodology developed in this thesis could also be extended to other biological structures. The segmentation and quantification pipeline for cilia and centrioles could be adapted to study other organelles, such as mitochondria or the Golgi apparatus, where spatial organisation underpins cell polarity and differentiation. Similarly, the volumetric imaging and analysis approach could be applied to other mechanically responsive tissues, including articular cartilage and the tendon, to explore how ciliary orientation correlates with directional load transmission and tissue anisotropy.

As mentioned previously, this imaging methodology did not measure primary cilium bending. Future studies could incorporate bending and deformation models of the cilium. Finite element or particle-based mechanical models of ciliary bending could be combined with empirical orientation data to infer local stress distributions and predict downstream signalling activation. Such models would bridge the gap between observed structural organisation and hypothesised mechanotransductive function, providing a quantitative framework to test how changes in ciliary length, stiffness or anchoring influence signal sensitivity and directionality.

At the cellular level, single-cell RNA sequencing or spatial transcriptomics applied to *Ift88* mutant and control growth plates, as is being done in the group, could reveal downstream transcriptional programs associated with ciliary dysfunction.

Finally, extending this work to human-derived MSCs and organoid models offers a translational bridge toward understanding how ciliary defects may contribute to skeletal dysplasias and growth disorders. Establishing humanised *in vitro* growth plate models with tunable mechanical and biochemical gradients would enable patient-specific modelling and therapeutic testing. Together, these future directions would not only strengthen the mechanistic understanding of ciliary function in endochondral ossification but also lay the foundation for regenerative or pharmacological strategies targeting ciliary pathways in skeletal tissue engineering and disease.

7.4 Conclusion

In conclusion, using an interdisciplinary approach that combined high-resolution imaging and conditional gene deletion mouse models, this thesis project has provided new insights into how primary cilia contribute to skeletal development. In addition, I have taken steps to develop a bioengineered gradient system of the growth plate.

I first characterised primary cilia orientation and prevalence across different zones and regions of the mouse adolescent growth plate, revealing a non-random spatial organisation that suggested functional significance in maintaining growth plate architecture. The use of an *Ift88* conditional knockout model allowed me to dissect the role of primary cilia *in vivo*, showing that deletion of *Ift88* disrupted growth plate and cell morphology. These structural changes occurred with subtle changes to primary cilia orientation and prevalence, with particular targeting of the hypertrophic zone. Offloading of the limb caused shortening of the growth plate and reduced the number of proliferating chondrocytes, which was also associated with subtle changes in cilia prevalence in the hypertrophic zone but without changes in ciliary orientation.

To further explore cilia function under controlled conditions, I developed an *in vitro* osteochondral differentiation model incorporating spatial gradients of BMP-2 and mechanical loading. This system allowed us to recapitulate aspects of the growth plate environment and test mechanobiological hypotheses. Mechanical characterisation confirmed stiffness in the physiologically relevant low-kPa range, supporting cell viability and differentiation. Adipose-derived MSCs and costal chondrocytes from *Ift88* cKO mice were subjected to cyclic mechanical stimulation within the gradient gels. Differentiation outcomes were evaluated by gene expression analyses of chondrogenic and osteogenic markers. Although the BMP-2 gradient did not generate directional cues, early cell differentiation was measured. However, cilia incidence and orientation could not be reliably quantified and reproducibility was limited by variability in primary cell cultures and loading responses.

Collectively, these findings underscore the importance of primary cilia as central integrators of mechanical and biochemical signals in the growth plate. By combining *in vivo* and *in vitro* methodologies, this thesis provides both a deeper mechanistic understanding and a versatile platform for further investigating skeletal development and its disorders. The tools and models developed here also lay the groundwork for future studies on ciliopathies and cartilage tissue engineering, with implications for therapeutic strategies targeting skeletal growth abnormalities.

Appendices

Figure 1: R code used for measuring the cell, primary cilia and centriole features from the Excel spreadsheet exported out of arivis for the analysis pipeline.

```
install.packages("readxl")
library(readxl)
install.packages("openxlsx")
library(openxlsx)
install.packages("ggplot2")
library(ggplot2)

violin_theme <- function() {
  theme_minimal() +
    theme(
      plot.background = element_rect(fill = "white"),
      panel.background = element_rect(fill = "white"),
      text = element_text(family = "Arial", size = 12),
      axis.title = element_text(size = 14, face = "bold"),
      axis.text = element_text(size = 12),
      plot.title = element_text(size = 16, face = "bold")
    )
}

# Function to convert degrees to radians
degrees_to_radians <- function(degrees) {
  return(degrees * pi / 180)
}

# Function to convert radians to degrees
radians_to_degrees <- function(radians) {
  return(radians * 180 / pi)
}

# Rotation matrix
rotation_matrix <- matrix(c(0, 0, -1, 1, 0, 0, 0, -1, 0), nrow = 3, byrow = TRUE)

# Function to perform a 3D rotation
rotate_point <- function(point, rotation_matrix) {
  rotated_point <- as.matrix(point) %*% t(rotation_matrix)
  return(t(rotated_point))
}

#Function to convert cartesian to spherical coordinates
cartesian_to_spherical <- function(x, y, z) {
  r <- sqrt(x^2 + y^2 + z^2)
  phi <- acos(z / r)
  theta <- atan2(y, x)
  return(c(r, phi, theta))
}

#Function to convert cartesian to stereonet coordinates/ trend and plunge
cartesian_to_stereonet <- function(x, y, z) {
  r <- sqrt(x^2 + y^2 + z^2)
  plunge <- asin(z / r)
  trend <- atan2(y, x)
  return(c(plunge, trend))
}

# Function to create and save the rose diagrams
create_rose_diagrams <- function(df_name, data) {
  # Create a rose diagram of theta
  theta_plot <- ggplot(data, aes(x = factor(round(`Cilia rotated theta positive` / 10)
```

```
* 10))) +
    geom_bar(aes(y = after_stat(count)), width = 1, fill = "skyblue") +
    theme_minimal() +
    coord_polar(start = 0) +  # Ensure 0/360 is at the top
    scale_x_discrete(breaks = c("0", "30", "60", "90", "120", "150", "180", "210",
"240", "270", "300", "330"),
                     labels = c("0/360", "30", "60", "90", "120", "150", "180", "210",
"240", "270", "300", "330"),
                     limits = as.character(seq(0, 360, by = 10))) +
    labs(x = "Theta (degrees)") +
    theme(plot.title = element_text(hjust = 0.5),
          axis.text.x = element_text(angle = 0, hjust = 0.5),  # Ensure labels are
centered
          legend.position = "none",
          panel.background = element_rect(fill = "white", colour = "white"),  # Set
background to white
          plot.background = element_rect(fill = "white", colour = "white"))  # Set plot
background to white

  ggsave(file.path(saving_directory, paste0(df_name, "_theta_rose_plot.png")), plot =
theta_plot, width = 6, height = 4)

  # Create a rose diagram of phi
  phi_plot <- ggplot(data, aes(x = factor(round(`Cilia rotated phi` / 10) * 10))) +
    geom_bar(aes(y = after_stat(count)), width = 1, fill = "skyblue") +
    theme_minimal() +
    coord_radial(start = 0, end = pi) +  # Use coord_radial for the phi plot
    scale_x_discrete(breaks = c("0", "30", "60", "90", "120", "150", "180"),
                     labels = c("0", "30", "60", "90", "120", "150", "180"),
                     limits = as.character(seq(0, 180, by = 10))) +
    labs(x = "Phi (degrees)") +
    theme(plot.title = element_text(hjust = 0.5),
          axis.text.x = element_text(angle = 0, hjust = 0.5),  # Ensure labels are
centered
          legend.position = "none",
          panel.background = element_rect(fill = "white", colour = "white"),  # Set
background to white
          plot.background = element_rect(fill = "white", colour = "white"))  # Set plot
background to white

  ggsave(file.path(saving_directory, paste0(df_name, "_phi_rose_plot.png")), plot =
phi_plot, width = 6, height = 4)
}

create_centriole_rose_diagrams <- function(df_name, data) {
  # Create a rose diagram of theta
  theta_plot <- ggplot(data, aes(x = factor(round(`Centriole rotated theta positive` /
10) * 10))) +
    geom_bar(aes(y = after_stat(count)), width = 1, fill = "skyblue") +
    theme_minimal() +
    coord_polar(start = 0) +  # Ensure 0/360 is at the top
    scale_x_discrete(breaks = c("0", "30", "60", "90", "120", "150", "180", "210",
"240", "270", "300", "330"),
                     labels = c("0/360", "30", "60", "90", "120", "150", "180", "210",
"240", "270", "300", "330"),
                     limits = as.character(seq(0, 360, by = 10))) +
    labs(x = "Theta (degrees)") +
    theme(plot.title = element_text(hjust = 0.5),
          axis.text.x = element_text(angle = 0, hjust = 0.5),  # Ensure labels are
centered
          legend.position = "none",
          panel.background = element_rect(fill = "white", colour = "white"),  # Set
background to white
          plot.background = element_rect(fill = "white", colour = "white"))  # Set plot
background to white

  ggsave(file.path(saving_directory, paste0(df_name, "_theta_rose_plot.png")), plot =
theta_plot, width = 6, height = 4)
```

```
  # Create a rose diagram of phi
  phi_plot <- ggplot(data, aes(x = factor(round(`Centriole rotated phi` / 10) * 10))) +
    geom_bar(aes(y = after_stat(count)), width = 1, fill = "skyblue") +
    theme_minimal() +
    coord_radial(start = 0, end = pi) +  # Use coord_radial for the phi plot
    scale_x_discrete(breaks = c("0", "30", "60", "90", "120", "150", "180"),
                     labels = c("0", "30", "60", "90", "120", "150", "180"),
                     limits = as.character(seq(0, 180, by = 10))) +
    labs(x = "Phi (degrees)") +
    theme(plot.title = element_text(hjust = 0.5),
          axis.text.x = element_text(angle = 0, hjust = 0.5),  # Ensure labels are
centered
          legend.position = "none",
          panel.background = element_rect(fill = "white", colour = "white"),  # Set
background to white
          plot.background = element_rect(fill = "white", colour = "white"))  # Set plot
background to white

  ggsave(file.path(saving_directory, paste0(df_name, "_phi_rose_plot.png")), plot =
phi_plot, width = 6, height = 4)
}


# Get file and directory
file_path <- file.choose()
saving_directory <- dirname(file_path)
data <- read_excel(file_path)
setwd(saving_directory)
data_original <- data

#Removes cilia (and their corresponding cell and centriole) that are cut off
max_value_planes <- max(data$`Last, Plane`)
names_to_remove_cplanes <- data[grepl("Cilia Threshold", data$Name) & data$`Last,
Plane` == max_value_planes, "Parent Names"]
names_to_remove_cplanes <- trimws(as.character(names_to_remove_cplanes$`Parent Names`))

#removes cells, cilia and centrioles that don't have a parent
data <- data[!(grepl("Cell Segmentation", data$Name, ignore.case = TRUE) &
is.na(data$`Parent Names`)), ]
data <- data[!(grepl("Cilia Threshold", data$Name, ignore.case = TRUE) &
is.na(data$`Parent Names`)), ]
data <- data[!(grepl("Centriole Threshold", data$Name, ignore.case = TRUE) &
is.na(data$`Parent Names`)), ]

#removes cilia and centriole below the sphericity threshold - they are not real
data <- data[!(grepl("Cilia Threshold", data$Name, ignore.case = TRUE) &
data$`Sphericity (Mesh), Sphericity` < 0.3), ]
data <- data[!(grepl("Centriole Threshold", data$Name, ignore.case = TRUE) &
data$`Sphericity (Mesh), Sphericity` < 0.5), ]


##### CILIA ANGLE CALCULATION
#Calculate coordinates of one end of the cilium based on xy and xz angles - these will
be coordinates lower than 1 - give direction
data$`X, cilia end` <- ifelse(grepl("Cilia Threshold", data$Name),
                              cos(degrees_to_radians(data$`Angle XZ, 3D Oriented
Bounds`)) * cos(degrees_to_radians(data$`Angle XY, 3D Oriented Bounds`)),NA)
data$`Y, cilia end` <- ifelse(grepl("Cilia Threshold", data$Name),
                              cos(degrees_to_radians(data$`Angle XZ, 3D Oriented
Bounds`)) * sin(degrees_to_radians(data$`Angle XY, 3D Oriented Bounds`)),NA)
data$`Z, cilia end` <- ifelse(grepl("Cilia Threshold", data$Name),
                              sin(degrees_to_radians(data$`Angle XZ, 3D Oriented
Bounds`)), NA)

#adjust for the fact that xz always positive
data$`X, cilia end adjusted` <-ifelse(grepl("Cilia Threshold", data$Name) & data$`Angle
YZ, 3D Oriented Bounds`<0,
                                      -data$`X, cilia end`,
                                      data$`X, cilia end`)
```

```
#Use direction to change coordinates of ends 1 and 2 so 1 isn't just all the lowest
values and 2 all the highest values
data$`X, cilia adjusted end 1` <- ifelse(data$`X, cilia end adjusted` < 0,
                                         data$`X2, Bounding Box (µm)`,
                                         data$`X1, Bounding Box (µm)`)
data$`X, cilia adjusted end 2` <- ifelse(data$`X, cilia end adjusted` < 0,
                                        data$`X1, Bounding Box (µm)`,
                                        data$`X2, Bounding Box (µm)`)
data$`Y, cilia adjusted end 1` = ifelse(data$`Y, cilia end` < 0,
                                        data$`Y2, Bounding Box (µm)`,
                                        data$`Y1, Bounding Box (µm)`)
data$`Y, cilia adjusted end 2` = ifelse(data$`Y, cilia end` < 0,
                                        data$`Y1, Bounding Box (µm)`,
                                        data$`Y2, Bounding Box (µm)`)
data$`Z, cilia adjusted end 1` = ifelse(data$`Z, cilia end` < 0,
                                        data$`Z2, Bounding Box (µm)`,
                                        data$`Z1, Bounding Box (µm)`)
data$`Z, cilia adjusted end 2` = ifelse(data$`Z, cilia end` < 0,
                                        data$`Z1, Bounding Box (µm)`,
                                        data$`Z2, Bounding Box (µm)`)

#Find distance of the two ends of the cilium to the centre of the cell (centre of
geometry)
#makes cilia vector with the 2 ends - shortest distance is the root, longest is the tip
library(dplyr)
data <- data %>%
  mutate(
    `Distance 1` = ifelse(
      grepl("Cilia Threshold", Name),
      sqrt((abs(data$`X, cilia adjusted end 1` - data$`X, Center of Geometry
(µm)`[match(`Parent Names`, data$Name)]))^2
           +(abs(data$`Y, cilia adjusted end 1` - data$`Y, Center of Geometry
(µm)`[match(`Parent Names`, data$Name)]))^2
           +(abs(data$`Z, cilia adjusted end 1` - data$`Z, Center of Geometry
(µm)`[match(`Parent Names`, data$Name)]))^2),
      NA
    ),
    `Distance 2` = ifelse(
      grepl("Cilia Threshold", Name),
      sqrt((abs(data$`X, cilia adjusted end 2` - data$`X, Center of Geometry
(µm)`[match(`Parent Names`, data$Name)]))^2
           +(abs(data$`Y, cilia adjusted end 2` - data$`Y, Center of Geometry
(µm)`[match(`Parent Names`, data$Name)]))^2
           +(abs(data$`Z, cilia adjusted end 2` - data$`Z, Center of Geometry
(µm)`[match(`Parent Names`, data$Name)]))^2),
      NA
    ),
    `Cilia vector x` = ifelse(`Distance 1` > `Distance 2`,
                              data$`X, cilia adjusted end 1` - data$`X, cilia
adjusted end 2`,
                              data$`X, cilia adjusted end 2` - data$`X, cilia
adjusted end 1`),
    `Cilia vector y` = ifelse(`Distance 1` > `Distance 2`,
                              data$`Y, cilia adjusted end 1` - data$`Y, cilia
adjusted end 2`,
                              data$`Y, cilia adjusted end 2` - data$`Y, cilia
adjusted end 1`),
    `Cilia vector z` = ifelse(`Distance 1` > `Distance 2`,
                              data$`Z, cilia adjusted end 1` - data$`Z, cilia
adjusted end 2`,
                              data$`Z, cilia adjusted end 2` - data$`Z, cilia
adjusted end 1`),
    #Assigns real coordinates of root to calculate distance to centriole later on
    `X, cilia root` = ifelse(`Distance 1` > `Distance 2`,
                             data$`X, cilia adjusted end 2`,
                             data$`X, cilia adjusted end 1`),
    `Y, cilia root` = ifelse(`Distance 1` > `Distance 2`,
```

```
                              data$`Y, cilia adjusted end 2`,
                              data$`Y, cilia adjusted end 1`),
    `Z, cilia root` = ifelse(`Distance 1` > `Distance 2`,
                              data$`Z, cilia adjusted end 2`,
                              data$`Z, cilia adjusted end 1`)
  )

detach("package:dplyr", unload = TRUE)

#substract for limit of resolution
data$`Cilia vector x` = ifelse(data$`Cilia vector x` > 0,
                               data$`Cilia vector x` - 0.6,
                               data$`Cilia vector x` + 0.6)
data$`Cilia vector y` = ifelse(data$`Cilia vector y` > 0,
                               data$`Cilia vector y` - 0.6,
                               data$`Cilia vector y` + 0.6)
data$`Cilia vector z` = ifelse(data$`Cilia vector z` > 0,
                               data$`Cilia vector z` - 1.1,
                               data$`Cilia vector z` + 1.1)

data$`X, cilia root` = ifelse(data$`X, cilia root` > 0,
                               data$`X, cilia root` - 0.6,
                               data$`X, cilia root` + 0.6)
data$`Y, cilia root` = ifelse(data$`Y, cilia root` > 0,
                               data$`Y, cilia root` - 0.6,
                               data$`Y, cilia root` + 0.6)
data$`Z, cilia root` = ifelse(data$`Z, cilia root` > 0,
                               data$`Z, cilia root` - 1.1,
                               data$`Z, cilia root` + 1.1)

#Rotate cilia coordinates
rotated_cilia_coordinates <- apply(data[, c("Cilia vector x", "Cilia vector y", "Cilia
vector z")], 1, function(row) {
  point <- matrix(row, nrow = 1)
  rotated_point <- as.matrix(point) %*% t(rotation_matrix)
  return(c(rotated_point[, 1], rotated_point[, 2], rotated_point[, 3]))
})

# Add new columns for rotated coordinates
data$`Cilia rotated X` <- rotated_cilia_coordinates[1,]
data$`Cilia rotated Y` <- rotated_cilia_coordinates[2,]
data$`Cilia rotated Z` <- rotated_cilia_coordinates[3,]

spherical_cilia_coords <- apply(data[, c("Cilia rotated X", "Cilia rotated Y", "Cilia
rotated Z")], 1, function(row) {
  cartesian_to_spherical(row[1], row[2], row[3])
})

cilia_radius_length <- spherical_cilia_coords[1,]
data$`Radius = length` <- cilia_radius_length
rotated_cilia_phi <- radians_to_degrees(spherical_cilia_coords[2,])
data$`Cilia rotated phi` <- rotated_cilia_phi
rotated_cilia_theta <- radians_to_degrees(spherical_cilia_coords[3,])
data$`Cilia rotated theta` <- rotated_cilia_theta

#makes theta range from 0 to 360 rather than -180 to 180
data$`Cilia rotated theta positive` <- ifelse(data$`Cilia rotated theta` < 0,
                                              data$`Cilia rotated theta` + 360,
                                              data$`Cilia rotated theta`)


#removes cilia that are too long therefore not actual cilia
data <- data[data$`Radius = length` <= 15 | is.na(data$`Radius = length`), ]

#Remove extra cilia attached to cells - keeps the longest cilium
cell_rows <- data[grepl("Cell", data$Name), ]
cell_names <- unique(cell_rows$Name)
for (cell_name in cell_names) {
  matching_rows <- data[data$`Parent Names` == cell_name & grepl("Cilia Threshold",
```

```
data$Name), ]
  if (nrow(matching_rows) > 1) {
    rows_to_remove <- matching_rows[matching_rows$`Radius = length` !=
max(matching_rows$`Radius = length`), ]
    data <- data[!data$Name %in% rows_to_remove$Name, ]
  }
}

#calculate whole GP percentage ciliation
cell_count <- sum(grepl("Cell", data$Name, ignore.case = TRUE))
cilium_count <- sum(grepl("Cilia", data$Name, ignore.case = TRUE))
whole_gp_ciliation <- (cilium_count / cell_count) * 100

####DISTANCE CILIA-CENTRE OF CELL
# Find the indices of rows with "Centriole Threshold" in the Name column
cilia_threshold_rows <- which(grepl("Cilia Threshold", data$Name))
data$`Centre of cell-cilium distance` <- NA #initialise column
# Loop through each index and find the corresponding cell parent row
for (idx in cilia_threshold_rows) {
  # Find the index of the row with "Cell Segmentation" and the same Name
  matching_row <- which(grepl("Cell Segmentation", data$Name) & data$`Name` ==
data$`Parent Names`[idx])[1]
  # If a matching row is found, calculate the distance
  if (!is.na(matching_row)) {
    data$`Centre of cell-cilium distance`[idx] <- sqrt((abs(data$`X, cilia root`[idx] -
data$`X, Center of Geometry (µm)`[matching_row]))^2
                                                       +(abs(data$`Y, cilia root`[idx] -
data$`Y, Center of Geometry (µm)`[matching_row]))^2
                                                       +(abs(data$`Z, cilia root`[idx] -
data$`Z, Center of Geometry (µm)`[matching_row]))^2)
  } else {
    NA
  }
}

#Convert cilia coordinates to stereonet coordinates
stereonet_cilia_coords <- apply(data[, c("Cilia rotated X", "Cilia rotated Y", "Cilia
rotated Z")], 1, function(row) {
  cartesian_to_stereonet(row[1], row[2], row[3])
})

stereonet_cilia_plunge <- radians_to_degrees(stereonet_cilia_coords[1,])
data$`Cilia plunge` <-stereonet_cilia_plunge
stereonet_cilia_trend <- radians_to_degrees(stereonet_cilia_coords[2,])
data$`Cilia trend` <- stereonet_cilia_trend


###### CENTRIOLE ANGLE CALCULATION
#Subtract centre of cell to centriole centre to calculate angle from centre of cell
data$`X centriole, original` <- ifelse(grepl("Centriole Threshold", data$Name),
                                       data$`X, Center of Geometry (µm)` - data$`X, Center
of Geometry (µm)`[match(data$`Parent Names`, data$Name)], NA)
data$`Y centriole, original` <- ifelse(grepl("Centriole Threshold", data$Name),
                                       data$`Y, Center of Geometry (µm)` - data$`Y, Center
of Geometry (µm)`[match(data$`Parent Names`, data$Name)], NA)
data$`Z centriole, original` <- ifelse(grepl("Centriole Threshold", data$Name),
                                       data$`Z, Center of Geometry (µm)` - data$`Z, Center
of Geometry (µm)`[match(data$`Parent Names`, data$Name)], NA)

#Rotate centriole coordinates
rotated_coordinates <- apply(data[, c("X centriole, original", "Y centriole, original",
"Z centriole, original")], 1, function(row) {
  point <- matrix(row, nrow = 1)
  rotated_point <- as.matrix(point) %*% t(rotation_matrix)
  return(c(rotated_point[, 1], rotated_point[, 2], rotated_point[, 3]))
})

# Add new columns for rotated coordinates
data$`X centriole, rotated` <- rotated_coordinates[1,]
```

```
data$`Y centriole, rotated` <- rotated_coordinates[2,]
data$`Z centriole, rotated` <- rotated_coordinates[3,]

spherical_coords <- apply(data[, c("X centriole, rotated", "Y centriole, rotated", "Z
centriole, rotated")], 1, function(row) {
  cartesian_to_spherical(row[1], row[2], row[3])
})

cell_centriole_distance  <- spherical_coords[1,] #distance from centre of cell to
centriole
data$`Cell centre-centriole distance` <- cell_centriole_distance
rotated_phi <- radians_to_degrees(spherical_coords[2,])
data$`Centriole rotated phi` <- rotated_phi
rotated_theta <- radians_to_degrees(spherical_coords[3,])
data$`Centriole rotated theta` <- rotated_theta

#makes theta range from 0 to 360 rather than -180 to 180
data$`Centriole rotated theta positive` <- ifelse(data$`Centriole rotated theta` < 0,
                                                  data$`Centriole rotated theta` + 360,
                                                  data$`Centriole rotated theta`)

#Convert centriole coordinates to stereonet coordinates
stereonet_centriole_coords <- apply(data[, c("X centriole, rotated", "Y centriole,
rotated", "Z centriole, rotated")], 1, function(row) {
  cartesian_to_stereonet(row[1], row[2], row[3])
})

stereonet_centriole_plunge <- radians_to_degrees(stereonet_centriole_coords[1,])
data$`Centriole plunge` <-stereonet_centriole_plunge
stereonet_centriole_trend <- radians_to_degrees(stereonet_centriole_coords[2,])
data$`Centriole trend` <- stereonet_centriole_trend

####DISTANCE CILIA-CENTRIOLE
# Find the indices of rows with "Centriole Threshold" in the Name column
centriole_threshold_rows <- which(grepl("Centriole Threshold", data$Name))
data$`Cilium-centriole distance` <- NA #initialise column
# Loop through each index and find the corresponding row with "Cilia Threshold" and
same Parent Name
for (idx in centriole_threshold_rows) {
  # Find the index of the row with "Cilia Threshold" and the same Parent Name
  matching_row <- which(grepl("Cilia Threshold", data$Name) & data$`Parent Names` ==
data$`Parent Names`[idx])[1]
  # If a matching row is found, calculate the distance
  if (!is.na(matching_row)) {
    data$`Cilium-centriole distance`[idx] <- sqrt((abs(data$`X, Center of Geometry
(µm)`[idx] - data$`X, cilia root`[matching_row]))^2
                                                  +(abs(data$`Y, Center of Geometry
(µm)`[idx] - data$`Y, cilia root`[matching_row]))^2
                                                  +(abs(data$`Z, Center of Geometry
(µm)`[idx] - data$`Z, cilia root`[matching_row]))^2)
  } else {
    NA
  }
}

#Removes cilia and centrioles with no phi angle
data <- data[!(grepl("Cilia Threshold", data$Name, ignore.case = TRUE) &
is.na(data$`Cilia rotated phi`)), ]
data <- data[!(grepl("Centrioles Threshold", data$Name, ignore.case = TRUE) &
is.na(data$`Centriole rotated phi`)), ]

#Rotate centre of cell coordinates
# Initialize rotated_cell_coordinates as an empty matrix
rotated_cell_coordinates <- matrix(NA, nrow = nrow(data), ncol = 3)

# Identify rows where "Name" contains "Cell Segmentation" and update
rotated_cell_coordinates
cell_seg_rows <- grepl("Cell Segmentation", data$Name)
rotated_cell_coordinates[cell_seg_rows, ] <- t(apply(data[cell_seg_rows,
```

```
                                                        c("X, Center of Geometry
(µm)",
                                                          "Y, Center of Geometry
(µm)",
                                                          "Z, Center of Geometry
(µm)")],
                                                    1, function(row) {
                                                      point <- matrix(row, nrow = 1)
                                                      rotated_point <-
as.matrix(point) %*% t(rotation_matrix)
                                                      return(c(rotated_point[, 1],
rotated_point[, 2], rotated_point[, 3]))
                                                    }))

# Add new columns for rotated coordinates
data$`X cell centre, rotated` <- rotated_cell_coordinates[, 1]
data$`Y cell centre, rotated` <- rotated_cell_coordinates[, 2]
data$`Z cell centre, rotated` <- rotated_cell_coordinates[, 3]


##########
# Filter rows containing 'Resting' in the 'Parent Names' column and their associated
cilium & centriole
resting_cell_names <- data[grep("Resting", data$'Parent Names'), 'Name']
resting_cell_names <- trimws(as.character(resting_cell_names$Name))
data$`Name` <- trimws(as.character(data$`Name`))
resting_cilia <- subset(data, grepl("Cilia Threshold", Name) & `Parent Names` %in%
resting_cell_names)
resting_centrioles <- subset(data, grepl("Centriole Threshold", Name) & `Parent Names`
%in% resting_cell_names)
cells_resting <- data[grep("Resting", data$'Parent Names', ignore.case = TRUE), ]

# Filter rows containing 'Proliferating' in the 'Parent Names' column and their
associated cilium
proliferating_cell_names <- data[grep("Proliferating", data$'Parent Names'), 'Name']
proliferating_cell_names <- trimws(as.character(proliferating_cell_names$Name))
proliferating_cilia <- subset(data, grepl("Cilia Threshold", Name) & `Parent Names`
%in% proliferating_cell_names)
proliferating_centrioles <- subset(data, grepl("Centriole Threshold", Name) & `Parent
Names` %in% proliferating_cell_names)
cells_proliferating <- data[grep("Proliferating", data$'Parent Names', ignore.case =
TRUE), ]

# Filter rows containing 'Hypertrophic' in the 'Parent Names' column and their
associated cilium
hyper_cell_names <- data[grep("Hypertrophic", data$'Parent Names'), 'Name']
hyper_cell_names <- trimws(as.character(hyper_cell_names$Name))
hyper_cilia <- subset(data, grepl("Cilia Threshold", Name) & `Parent Names` %in%
hyper_cell_names)
hyper_centrioles <- subset(data, grepl("Centriole Threshold", Name) & `Parent Names`
%in% hyper_cell_names)
cells_hypertrophic<- data[grep("Hypertrophic", data$'Parent Names', ignore.case =
TRUE), ]

# Create an empty data frame to store the summary results
df_summary <- data.frame(DataFrame = character(0),
                         "Percent ciliated cells" = numeric(0),
                         "Cell length (um)" = numeric(0),
                         "Cell volume (um3)" = numeric(0),
                         "Cell theta angle with medio-lateral direction" = numeric(0),
                         "Cilia length (um)" = numeric(0),
                         "Cilia volume (um3)"= numeric(0),
                         "Cilia phi angle" = numeric(0),
                         "Cilia theta angle" = numeric(0),
                         "Centriole phi angle" = numeric(0),
                         "Centriole theta angle" = numeric(0),
                         "Cilium-centriole distance" = numeric(0),
                         "Cilium-centriole distance median" = numeric(0),
                         "Cell centre-cilium distance" = numeric(0),
```

```
                          "Cell centre-centriole distance" = numeric(0),
                          "Resultant" = numeric(0),
                          "Average resultant per cilium" = numeric(0),
                          "Spherical variance" = numeric (0)
                          )


# List of data frame names starting with 'data_'
cell_frame_names <- ls(pattern = "^cells_")


centriole_threshold_rows <- which(grepl("Centriole Threshold", data$Name))
data$`Cilium-centriole distance` <- NA #initialise column
# Loop through each index and find the corresponding row with "Cilia Threshold" and
same Parent Name
for (idx in centriole_threshold_rows) {
  # Find the index of the row with "Cilia Threshold" and the same Parent Name
  matching_row <- which(grepl("Cilia Threshold", data$Name) & data$`Parent Names` ==
data$`Parent Names`[idx])[1]
  # If a matching row is found, calculate the distance
  if (!is.na(matching_row)) {
    data$`Cilium-centriole distance`[idx] <- sqrt((abs(data$`X, Center of Geometry
(µm)`[idx] - data$`X, cilia root`[matching_row]))^2
                                                  +(abs(data$`Y, Center of Geometry
(µm)`[idx] - data$`Y, cilia root`[matching_row]))^2
                                                  +(abs(data$`Z, Center of Geometry
(µm)`[idx] - data$`Z, cilia root`[matching_row]))^2)
  } else {
    NA
  }
}


# Loop through each cell data frame and make calculations
for (df_name in cell_frame_names) {
  ciliated_cells <- 0
  current_data <- get(df_name)
  if (nrow(current_data) > 0) {
  # Check if "Cilia Threshold" is present in the Name column of the data dataframe
  cilia_rows <- grepl("Cilia Threshold", data$Name)

  # Calculate percentage ciliation
  for (i in 1:nrow(current_data)) {
    if (current_data$`Name`[i] %in% data$`Parent Names`[cilia_rows]) {
      ciliated_cells <- ciliated_cells + 1
    }
  }
    ciliated_cells_percent <- (ciliated_cells / nrow(current_data)) * 100

  #Cell length
  cell_length <- as.numeric(current_data$`Long Side, 3D Oriented Bounds (µm)`)
  average_cell_length <- mean(cell_length, na.rm = TRUE)

  #Cell volume
  cell_volume <- as.numeric(current_data$`Volume (Mesh), Sphericity (µm³)`)
  cell_volume <- na.omit(cell_volume)
  average_cell_volume <- mean(cell_volume, na.rm = TRUE)

  #Cell theta
  cell_theta <- as.numeric(current_data$`Angle XY, 3D Oriented Bounds`)
  cell_theta <- na.omit(cell_theta)
  average_cell_theta <- mean(cell_theta, na.rm = TRUE)

  summary_data <- data.frame(DataFrame = df_name,
                             "Percent ciliated cells" = ciliated_cells_percent,
                             "Cell length (um)" = average_cell_length,
                             "Cell volume (um3)" = average_cell_volume,
                             "Cell theta angle with medio-lateral direction" =
```

```
average_cell_theta,
                              "Cilia length (um)" = NA,
                              "Cilia volume (um3)"= NA,
                              "Cilia phi angle" = NA,
                              "Cilia theta angle" = NA,
                              "Centriole phi angle" = NA,
                              "Centriole theta angle" = NA,
                              "Cilium-centriole distance" = NA,
                              "Cilium-centriole distance median" = NA,
                              "Cell centre-cilium distance" = NA,
                              "Cell centre-centriole distance" = NA,
                              "Resultant" = NA,
                              "Average resultant per cilium" = NA,
                              "Spherical variance" = NA
                              )
  df_summary <- rbind(df_summary, summary_data)
  }
}

# List of data frame names ending with 'cilia'
cilia_frame_names <- ls(pattern = "^[[:alnum:]]+_cilia$")

# Removes cilia that are cut off
for (df_name in cilia_frame_names) {
  assign(df_name, get(df_name)[!(get(df_name)$`Parent Names` %in%
names_to_remove_cplanes |
                                   get(df_name)$Name %in% names_to_remove_cplanes), ])
}

# Loop through each cilia data frame
for (df_name in cilia_frame_names) {
  current_data <- get(df_name)

  if (is.data.frame(current_data) && nrow(current_data) == 0) {
    # Skip empty data frames
    next
  }

  # Cilia length
  cilia_length <- as.numeric(current_data$`Radius = length`)
  average_cilia_length <- mean(cilia_length, na.rm = TRUE)

  # Cilia volume
  cilia_volume <- as.numeric(current_data$`Volume (Mesh), Sphericity (µm³)`)
  average_cilia_volume <- mean(cilia_volume, na.rm = TRUE)

  cilia_phi <- as.numeric(current_data$`Cilia rotated phi`)
  average_rotated_phi <- mean(cilia_phi, na.rm = TRUE)

  cilia_theta <- as.numeric(current_data$`Cilia rotated theta`)
  average_rotated_theta <- mean(cilia_theta, na.rm = TRUE)

  cell_cilia_distance <- as.numeric(current_data$`Centre of cell-cilium distance`)
  average_cell_cilia_distance <- mean(cell_cilia_distance, na.rm = TRUE)

  #Resultant and spherical variance
  N <- nrow(current_data)
  sum_x <- sum(current_data$`Cilia rotated X`)
  sum_y <- sum(current_data$`Cilia rotated Y`)
  sum_z <- sum(current_data$`Cilia rotated Z`)
  cilia_resultant <- sqrt(sum_x^2 + sum_y^2 + sum_z^2)
  average_resultant <- cilia_resultant/N
  cilia_spherical_variance <- (N - cilia_resultant) / N

  # Update the original data frame
  assign(df_name, current_data)

  summary_data <- data.frame(DataFrame = df_name,
                              "Percent ciliated cells" = NA,
```

```
                              "Cell length (um)" = NA,
                              "Cell volume (um3)" = NA,
                              "Cell theta angle with medio-lateral direction" = NA,
                              "Cilia length (um)" = average_cilia_length,
                              "Cilia volume (um3)"= average_cilia_volume,
                              "Cilia phi angle" = average_rotated_phi,
                              "Cilia theta angle" = average_rotated_theta,
                              "Centriole phi angle" = NA,
                              "Centriole theta angle" = NA,
                              "Cilium-centriole distance" = NA,
                              "Cilium-centriole distance median" = NA,
                              "Cell centre-cilium distance" =
average_cell_cilia_distance,
                              "Cell centre-centriole distance" = NA,
                              "Resultant" = cilia_resultant,
                              "Average resultant per cilium" = average_resultant,
                              "Spherical variance" = cilia_spherical_variance
                                )
  df_summary <- rbind(df_summary, summary_data)
}

# List of data frame names ending with 'centriole'
centriole_frame_names <- ls(pattern = "^[[:alnum:]]+_centrioles$")

# Loop through each centrioles data frame
for (df_name in centriole_frame_names) {
  current_data <- get(df_name)

  if (is.data.frame(current_data) && nrow(current_data) == 0) {
    # Skip empty data frames
    next
  }

  centriole_phi <- as.numeric(current_data$`Centriole rotated phi`)
  average_rotated_cent_phi <- mean(centriole_phi, na.rm = TRUE)

  centriole_theta <- as.numeric(current_data$`Centriole rotated theta`)
  average_rotated_cent_theta <- mean(centriole_theta, na.rm = TRUE)

  cell_centriole_distance <- as.numeric(current_data$`Cell centre-centriole distance`)
  average_cell_centriole_distance <- mean(cell_centriole_distance, na.rm = TRUE)

  cilia_centriole_distance <- as.numeric(current_data$`Cilium-centriole distance`)
  average_cilia_centriole_distance <- mean(cilia_centriole_distance, na.rm = TRUE)
  median_cilia_centriole_distance <- median(cilia_centriole_distance, na.rm = TRUE)

  # Update the original data frame
  assign(df_name, current_data)

  summary_data <- data.frame(DataFrame = df_name,
                              "Percent ciliated cells" = NA,
                              "Cell length (um)" = NA,
                              "Cell volume (um3)" = NA,
                              "Cell theta angle with medio-lateral direction" = NA,
                              "Cilia length (um)" = NA,
                              "Cilia volume (um3)"= NA,
                              "Cilia phi angle" = NA,
                              "Cilia theta angle" = NA,
                              "Centriole phi angle" = average_rotated_cent_phi,
                              "Centriole theta angle" = average_rotated_cent_theta,
                              "Cilium-centriole distance" =
average_cilia_centriole_distance,
                              "Cilium-centriole distance median" =
median_cilia_centriole_distance,
                              "Cell centre-cilium distance" = NA,
                              "Cell centre-centriole distance" =
average_cell_centriole_distance,
                              "Resultant" = NA,
                              "Average resultant per cilium" = NA,
```

```
                            "Spherical variance" = NA
  )
  df_summary <- rbind(df_summary, summary_data)
}

# Reset row names for the summary data frame
row.names(df_summary) <- NULL

# Loop through each cilia data frame to create violin plot
for (df_name in cilia_frame_names) {
  current_data <- get(df_name)

  if (is.data.frame(current_data) && nrow(current_data) == 0) {
    next
  }

  data_frame <- list(
    length = as.numeric(current_data$`Radius = length`),
    volume = as.numeric(current_data$`Volume (Mesh), Sphericity (µm³)`),
    rotated_phi = as.numeric(current_data$`Cilia rotated phi`),
    rotated_theta = as.numeric(current_data$`Cilia rotated theta`),
    cell_cilia_distance = as.numeric(current_data$`Centre of cell-cilium distance`)
  )

  iqr_values <- list(
    length = quantile(data_frame$length, c(0.25, 0.75), na.rm = TRUE),
    volume = quantile(data_frame$volume, c(0.25, 0.75), na.rm = TRUE),
    rotated_phi = quantile(data_frame$rotated_phi, c(0.25, 0.75), na.rm = TRUE),
    rotated_theta = quantile(data_frame$rotated_theta, c(0.25, 0.75), na.rm = TRUE),
    cell_cilia_distance = quantile(data_frame$cell_cilia_distance, c(0.25, 0.75), na.rm
= TRUE)
  )

  y_labels <- list(
    length = "Length (µm)",
    volume = "Volume (µm³)",
    rotated_phi = "Rotated phi (°)",
    rotated_theta = "Rotated theta (°)",
    cell_cilia_distance = "Cell centre-cilium distance (µm)"
  )

  ylim_rotated_phi <- c(0, 180)
  ylim_rotated_theta <- c(-180, 180)
  ylim_cilia_length <- c(0,15)
  ylim_cilia_volume <-c(0,8)

  for (var_name in names(data_frame)) {
    current_data <- data_frame[[var_name]]
    current_iqr <- iqr_values[[var_name]]
    y_label <- y_labels[[var_name]]

    y_data_frame <- data.frame(current_data)

    p <- ggplot(data = y_data_frame, aes(x = "", y = current_data)) +
      geom_violin(fill = "grey", color = "black", na.rm = TRUE) +
      geom_boxplot(width = 0.1, fill = "grey", outlier.shape = NA, na.rm = TRUE) +
      #stat_summary(fun = "median", geom = "point", shape = 18, size = 3, color =
"red", na.rm = TRUE) +
      geom_errorbar(aes(ymin = current_iqr[1], ymax = current_iqr[2]), width = 0.1,
color = "black", na.rm = TRUE) +
      geom_point(position = position_jitter(width = 0.2), size = 1, na.rm = TRUE) +
      violin_theme() +
      labs(
        x = NULL,
        y = y_label
      )

    # Set y-axis limits only for the rotated_phi and rotated_theta plot
    if (var_name == "rotated_phi") {
```

```
      p <- p + coord_cartesian(ylim = ylim_rotated_phi)
    }
    if (var_name == "rotated_theta") {
      p <- p + coord_cartesian(ylim = ylim_rotated_theta)
    }
    if (var_name == "length") {
      p <- p + coord_cartesian(ylim = ylim_cilia_length)
    }
    if (var_name == "volume") {
      p <- p + coord_cartesian(ylim = ylim_cilia_volume)
    }

    ggsave(file.path(saving_directory, paste0(df_name,"_",var_name, ".png")), plot = p,
width = 6, height = 4)
  }
}

# Loop through each cilia data frame to create half plot
for (df_name in cilia_frame_names) {
  current_data <- get(df_name)

  if (is.data.frame(current_data) && nrow(current_data) == 0) {
    next
  }

  rotated_phi <- as.numeric(current_data$`Cilia rotated phi`)
  rotated_theta <- as.numeric(current_data$`Cilia rotated theta positive`)

  current_data <- data.frame(rotated_phi, rotated_theta)

  # half circle plot
  p <- ggplot(data = current_data, aes(x = rotated_phi, y = rotated_theta)) +
    geom_point() +
    xlab(expression(phi)) +    # Add x title
    ylab(expression(theta)) +    # Add y title with Greek letter theta
    scale_x_continuous(limits = c(0, 180), breaks = seq(0, 180, by = 30)) +
    scale_y_continuous(limits = c(0, 360), breaks = seq(0, 360, by = 90))

  half <- p + coord_radial(
    start = 0,
    end = pi
  ) +
    ggtitle(df_name)

  ggsave(file.path(saving_directory, paste0(df_name, "_half_plot", ".png")), plot =
half, width = 6, height = 4)
}

# Loop through each cilia data frame to create rose diagrams
for (df_name in cilia_frame_names) {
  current_data <- get(df_name)

  if (is.data.frame(current_data) && nrow(current_data) == 0) {
    next
  }

  # Check if the necessary columns are present
  if (!all(c("Cilia rotated phi", "Cilia rotated theta positive") %in%
names(current_data))) {
    warning(paste("Data frame", df_name, "does not contain the required columns.
Skipping."))
    next
  }

  # Create and save the rose diagrams
  create_rose_diagrams(df_name, current_data)
}
```

```
# Loop through each centriole data frame to create violin plot
for (df_name in centriole_frame_names) {
  current_data <- get(df_name)

  if (is.data.frame(current_data) && nrow(current_data) == 0) {
    next
  }

  data_frame <- list(
    rotated_cent_phi = as.numeric(current_data$`Centriole rotated phi`),
    rotated_cent_theta = as.numeric(current_data$`Centriole rotated theta`),
    cell_centriole_distance = as.numeric(current_data$`Cell centre-centriole
distance`),
    cilia_centriole_distance = as.numeric(current_data$`Cilium-centriole distance`)
  )

  iqr_values <- list(
    rotated_cent_phi = quantile(data_frame$rotated_cent_phi, c(0.25, 0.75), na.rm =
TRUE),
    rotated_cent_theta = quantile(data_frame$rotated_cent_theta, c(0.25, 0.75), na.rm =
TRUE),
    cell_centriole_distance = quantile(data_frame$cell_centriole_distance, c(0.25,
0.75), na.rm = TRUE),
    cilia_centriole_distance = quantile(data_frame$cilia_centriole_distance, c(0.25,
0.75), na.rm = TRUE)
  )

  y_labels <- list(
    rotated_cent_phi = "Rotated phi (°)",
    rotated_cent_theta = "Rotated theta (°)",
    cell_centriole_distance = "Cell centre-centriole distance (µm)",
    cilia_centriole_distance = "Cilium base-centriole distance (µm)"
  )

  ylim_rotated_phi <- c(0, 180)
  ylim_rotated_theta <- c(-180, 180)
  ylim_cell_centriole <- c(0,20)
  ylim_cilia_centriole <- c(0,20)

  for (var_name in names(data_frame)) {
    current_data <- data_frame[[var_name]]
    current_iqr <- iqr_values[[var_name]]
    y_label <- y_labels[[var_name]]

    y_data_frame <- data.frame(current_data)

    p <- ggplot(data = y_data_frame, aes(x = "", y = current_data)) +
      geom_violin(fill = "grey", color = "black", na.rm = TRUE) +
      geom_boxplot(width = 0.1, fill = "grey", outlier.shape = NA, na.rm = TRUE) +
      #stat_summary(fun = "median", geom = "point", shape = 18, size = 3, color =
"red", na.rm = TRUE) +
      geom_errorbar(aes(ymin = current_iqr[1], ymax = current_iqr[2]), width = 0.1,
color = "black", na.rm = TRUE) +
      geom_point(position = position_jitter(width = 0.2), size = 1, na.rm = TRUE) +
      violin_theme() +
      labs(
        x = NULL,
        y = y_label
      )

    # Set y-axis limits
    if (var_name == "rotated_cent_phi") {
      p <- p + coord_cartesian(ylim = ylim_rotated_phi)
    }
    if (var_name == "rotated_cent_theta") {
      p <- p + coord_cartesian(ylim = ylim_rotated_theta)
    }
    if (var_name == "cell_centriole_distance") {
      p <- p + coord_cartesian(ylim = ylim_cell_centriole)
```

```
    }
    if (var_name == "cilia_centriole_distance") {
      p <- p + coord_cartesian(ylim = ylim_cilia_centriole)
    }


    ggsave(file.path(saving_directory, paste0(df_name,"_",var_name, ".png")), plot = p,
width = 6, height = 4)
  }
}

# Loop through each centriole data frame to create half plot
for (df_name in centriole_frame_names) {
  current_data <- get(df_name)

  if (is.data.frame(current_data) && nrow(current_data) == 0) {
    next
  }

  rotated_phi <- as.numeric(current_data$`Centriole rotated phi`)
  rotated_theta <- as.numeric(current_data$`Centriole rotated theta positive`)

  current_data <- data.frame(rotated_phi, rotated_theta)

  # half circle plot
  p <- ggplot(data = current_data, aes(x = rotated_phi, y = rotated_theta)) +
    geom_point() +
    xlab(expression(phi)) +    # Add x title
    ylab(expression(theta)) +    # Add y title with Greek letter theta
    scale_x_continuous(limits = c(0, 180), breaks = seq(0, 180, by = 30)) +
    scale_y_continuous(limits = c(0, 360), breaks = seq(0, 360, by = 90))

  half <- p + coord_radial(
    start = 0,
    end = pi
  ) +
    ggtitle(df_name)

  ggsave(file.path(saving_directory, paste0(df_name, "_half_plot", ".png")), plot =
half, width = 6, height = 4)
}

# Loop through each centriole data frame to create rose diagrams
for (df_name in centriole_frame_names) {
  current_data <- get(df_name)

  if (is.data.frame(current_data) && nrow(current_data) == 0) {
    next
  }

  # Check if the necessary columns are present
  if (!all(c("Centriole rotated phi", "Centriole rotated theta positive") %in%
names(current_data))) {
    warning(paste("Data frame", df_name, "does not contain the required columns.
Skipping."))
    next
  }

  # Create and save the rose diagrams
  create_centriole_rose_diagrams(df_name, current_data)
}


# Loop through each cell data frame to create violin plot
for (df_name in cell_frame_names) {
  current_data <- get(df_name)

  if (is.data.frame(current_data) && nrow(current_data) == 0) {
    next
```

```
  }

  data_frame <- list(
    length = as.numeric(current_data$`Long Side, 3D Oriented Bounds (µm)`),
    volume = as.numeric(current_data$`Volume (Mesh), Sphericity (µm³)`),
    theta = as.numeric(current_data$`Angle XY, 3D Oriented Bounds`)
  )

  iqr_values <- list(
    length = quantile(data_frame$length, c(0.25, 0.75), na.rm = TRUE),
    volume = quantile(data_frame$volume, c(0.25, 0.75), na.rm = TRUE),
    theta = quantile(data_frame$theta, c(0.25, 0.75), na.rm = TRUE)
  )

  y_labels <- list(
    length = "Length (µm)",
    volume = "Volume (µm³)",
    theta = "Cell theta with medio-lateral direction (°)"
  )

  ylim_length <- c(0, 50)
  ylim_volume <- c(0, 3000)
  ylim_theta <- c(-90, 90)

  for (var_name in names(data_frame)) {
    current_data <- data_frame[[var_name]]
    current_iqr <- iqr_values[[var_name]]
    y_label <- y_labels[[var_name]]

    y_data_frame <- data.frame(current_data)

    p <- ggplot(data = y_data_frame, aes(x = "", y = current_data)) +
      geom_violin(fill = "grey", color = "black", na.rm = TRUE) +
      geom_boxplot(width = 0.1, fill = "grey", outlier.shape = NA, na.rm = TRUE) +
      #stat_summary(fun = "median", geom = "point", shape = 18, size = 3, color =
"red", na.rm = TRUE) +
      geom_errorbar(aes(ymin = current_iqr[1], ymax = current_iqr[2]), width = 0.1,
color = "black", na.rm = TRUE) +
      geom_point(position = position_jitter(width = 0.2), size = 1, na.rm = TRUE) +
      violin_theme() +
      labs(
        x = NULL,
        y = y_label
      )

    # Set y-axis limits only for volume and length
    if (var_name == "length") {
      p <- p + coord_cartesian(ylim = ylim_length)
    }
    if (var_name == "volume") {
      p <- p + coord_cartesian(ylim = ylim_volume)
    }
    if (var_name == "theta") {
      p <- p + coord_cartesian(ylim = ylim_theta)
    }

    ggsave(file.path(saving_directory, paste0(df_name,"_",var_name, ".png")), plot = p,
width = 6, height = 4)
  }
}

# Create a new Excel workbook
wb <- createWorkbook()

addWorksheet(wb, sheetName = "Resting cells")
writeData(wb, sheet = "Resting cells", cells_resting)
addWorksheet(wb, sheetName = "Resting cilia")
writeData(wb, sheet = "Resting cilia", resting_cilia)
```

```
addWorksheet(wb, sheetName = "Resting centrioles")
writeData(wb, sheet = "Resting centrioles", resting_centrioles)
```



```
addWorksheet(wb, sheetName = "Proliferating cells")
writeData(wb, sheet = "Proliferating cells", cells_proliferating)
addWorksheet(wb, sheetName = "Proliferating cilia")
writeData(wb, sheet = "Proliferating cilia", proliferating_cilia)
addWorksheet(wb, sheetName = "Proliferating centrioles")
writeData(wb, sheet = "Proliferating centrioles", proliferating_centrioles)

addWorksheet(wb, sheetName = "Hypertrophic cells")
writeData(wb, sheet = "Hypertrophic cells", cells_hypertrophic)
addWorksheet(wb, sheetName = "Hypertrophic cilia")
writeData(wb, sheet = "Hypertrophic cilia", hyper_cilia)
addWorksheet(wb, sheetName = "Hypertrophic centrioles")
writeData(wb, sheet = "Hypertrophic centrioles", hyper_centrioles)

addWorksheet(wb, sheetName = "Summary")

# Write the updated 'df_summary' data frame to the 'Summary' sheet
df_summary$Whole_GP_percentage_ciliation <- whole_gp_ciliation
writeDataTable(wb, sheet = "Summary", x = df_summary)

# Measure the maximum width of column names
title_widths <- sapply(names(df_summary), nchar)
max_title_width <- max(title_widths)

# Set the column widths based on the maximum title width
for (col_index in 1:ncol(df_summary)) {
  setColWidths(wb, sheet = "Summary", cols = col_index, widths = max_title_width)
}

output_file <- file.path(saving_directory, "Sorted_cilia_data-.xlsx")

# Save the workbook with the specified path
saveWorkbook(wb, file = output_file)
save.image("workspace.rData")
```

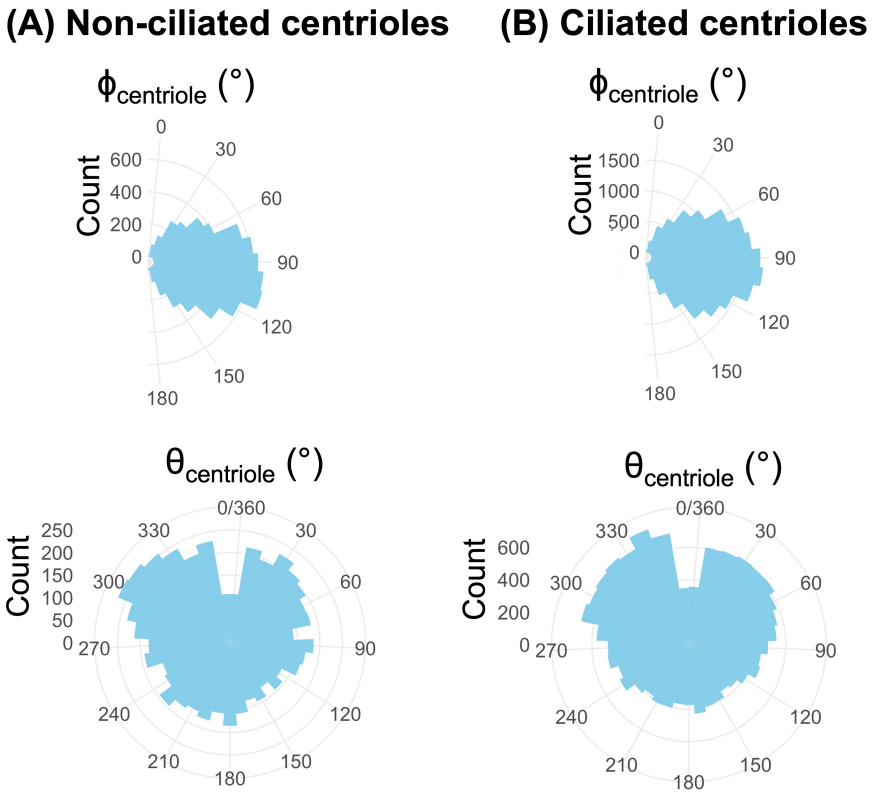


Figure 2: Spherical coordinates of the position of centrioles in (A) non-ciliated and (B) ciliated cells.

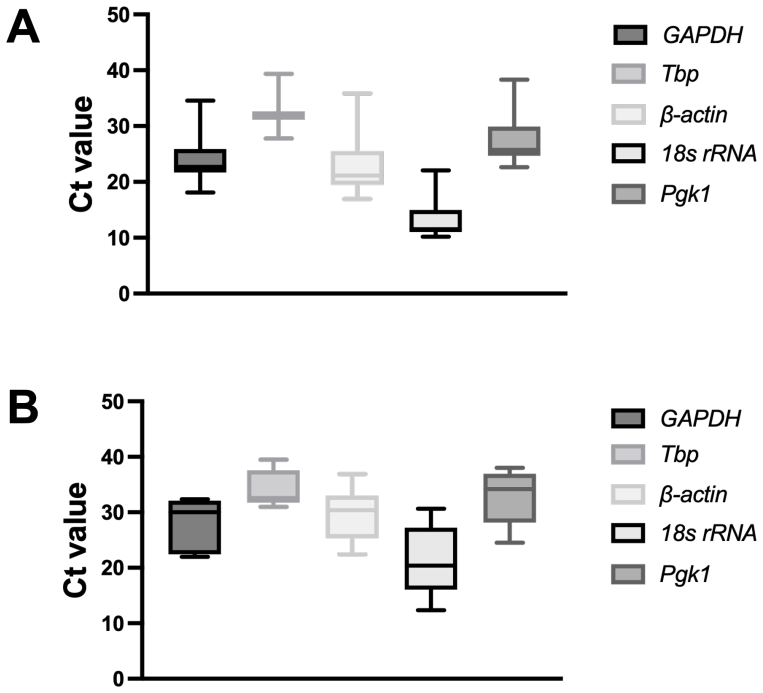


Figure 3: Ct values of housekeeping genes tested in MSCs differentiated in 2D (A) and costal chondrocytes cultured in GelMA (B).

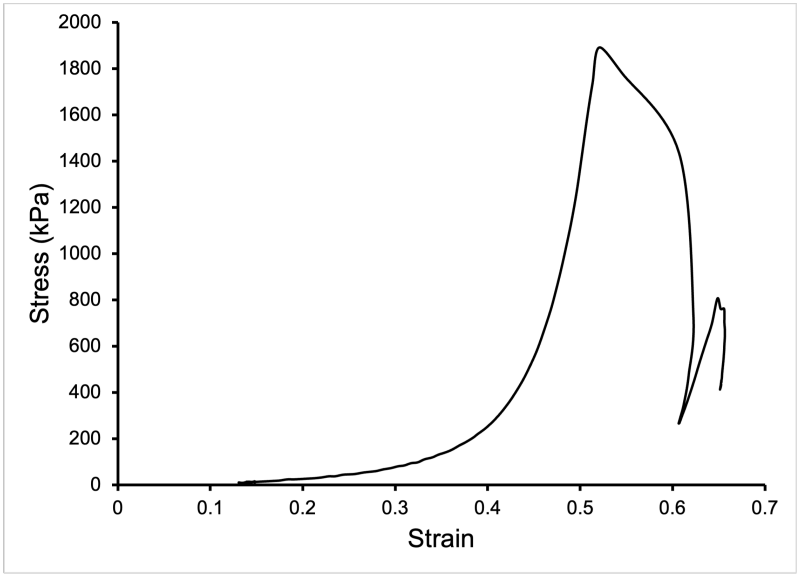


Figure 4: Stress–strain curve of a GelMA hydrogel. Stress–strain curve of a GelMA hydrogel using the ElectroForce 5500 (TA Instruments, 200 N load cell) under compression at a speed of 0.2 mm second^{-1}.

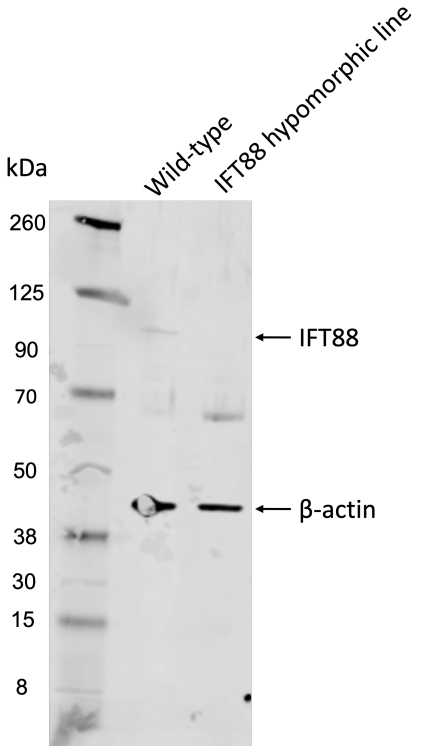


Figure 5: Western blot testing the IFT88 antibody. The IFT88 band disappears in the IFT88 hypomorphic cell line.

Table 2: Transcripts per million (TPM) from bulk RNA sequencing of the growth plate of a 6 week-old C57BL/6 wild-type mouse.

Gene	Transcripts per million (TPM)
Ift88	5.8
Gli1	21.1
Acan	2,395.9
Sox9	82.4
Col2a1	41,440.1
Col10a1	6,081.6
Prg4	17.7
Runx2	47.8
Alpl	856.7
Bglap	2,459.8
Spp1	2,883.3
Sp7	144.0
Col1a1	2,933.3
VegfA	50.5

Bibliography

1. Karsenty, G. The genetic transformation of bone biology. *Genes & Development* **13,** 3037–3051 (1999).

2. Olsen, B. R., Reginato, A. M. & Wang, W. Bone development. *Annual Review of Cell Developmental Biology* **16,** 191–220 (2000).

3. Long, F. & Ornitz, D. M. Development of the Endochondral Skeleton. *Cold Spring Harbor Perspectives in Biology* **5,** a008334 (2013).

4. Hall, B. K. & Miyake, T. The membranous skeleton: the role of cell condensations in vertebrate skeletogenesis. *Anatomy and Embryology* **186,** 107–124 (1992).

5. Hall, B. K. & Miyake, T. All for one and one for all: condensations and the initiation of skeletal development. *BioEssays* **22,** 138–147 (2000).

6. Kronenberg, H. M. Developmental regulation of the growth plate. *Nature* **423,** 332–336 (2003).

7. Lefebvre, V. & Smits, P. Transcriptional control of chondrocyte fate and differentiation. *Birth Defects Research Part C - Embryo Today: Reviews* **75,** 200–212 (2005).

8. Crombrugghe, B. d., Lefebvre, V. & Nakashima, K. Regulatory mechanisms in the pathways of cartilage and bone formation. *Current Opinion in Cell Biology* **13,** 721–728 (2001).

9. Pogue, R. & Lyons, K. BMP Signaling in the Cartilage Growth Plate. *Current Topics in Developmental Biology* **76,** 1–48 (2006).

10. Wang, Y. *et al.* IGF-1R Signaling in Chondrocytes Modulates Growth Plate Development by Interacting With the PTHrP/Ihh Pathway. *J Bone Miner Res* **26,** 1437–1446 (2011).

11. Rubin, S. *et al.* Limited column formation in the embryonic growth plate implies divergent growth mechanisms during pre- and postnatal bone development. *eLife* **13,** e95289 (2024).

12. Xie, M. *et al.* Secondary ossification center induces and protects growth plate structure. *eLife* **9,** 1–32 (Oct. 2020).

13. Abad, V. The Role of the Resting Zone in Growth Plate Chondrogenesis. *Endocrinology* **143,** 1851–1857 (2002).

14. Mizuhashi, K. *et al.* Resting zone of the growth plate houses a unique class of skeletal stem cells. *Nature* **563,** 254–258 (Nov. 2018).

15. Newton, P. T. *et al.* A radical switch in clonality reveals a stem cell niche in the epiphyseal growth plate. *Nature* **567,** 234–238 (Mar. 2019).

16. Kobayashi, T. *et al.* PTHrP and Indian hedgehog control differentiation of growth plate chondrocytes at multiple steps. *Development* **129,** 2977–2986 (2002).

17. Vortkamp, A. *et al.* Regulation of Rate of Cartilage Differentiation by Indian Hedgehog and PTH-Related Protein. *Science* **273,** 613–622 (1996).

18. Pacifici, M. *et al.* Hypertrophic Chondrocytes. *Annals New York Academy of Sciences* **599,** 45–57 (1990).

19. Dodds, G. Row formation and other types of arrangement of cartilage cells in endochondral ossification. *The Anatomical Record* (Sept. 1930).

20. Li, Y., Li, A., Junge, J. & Bronner, M. Planar cell polarity signaling coordinates oriented cell division and cell rearrangement in clonally expanding growth plate cartilage. *eLife* **6,** e23279 (2017).

21. Li, Y. & Dudley, A. T. Noncanonical frizzled signaling regulates cell polarity of growth plate chondrocytes. *Development* **136,** 1083–1092 (2009).

22. Aszodi, A., Hunziker, E. B., Brakebusch, C. & Fässler, R. β1 integrins regulate chondrocyte rotation, G1 progression, and cytokinesis. *Genes & Development* **17,** 2465–2479 (2003).

23. Yuan, J., Guo, L., Wang, J., Zhou, Z. & Wu, C. α-parvin controls chondrocyte column formation and regulates long bone development. *Bone Research* **11,** 46 (2023).

24. Buckwalter, J. A., Mower, D., Ungar, R., Schaeffer, J. & Ginsberg, B. Morphometric analysis of chondrocyte hypertrophy. *The Journal of bone and joint surgery. American volume* **68,** 243–55 (1986).

25. Arnold, M. A. *et al.* MEF2C Transcription Factor Controls Chondrocyte Hypertrophy and Bone Development. *Developmental Cell* **12,** 377–389 (2007).

26. Gerber, H.-P. *et al.* VEGF couples hypertrophic cartilage remodeling, ossification and angiogenesis during endochondral bone formation. *Nature Medicine* **5,** 623–628 (1999).

27. Xiong, J. *et al.* Matrix-embedded cells control osteoclast formation. *Nature Medicine* **17,** 1235–1241 (2011).

28. Luca, A. D., Blitterswijk, C. V. & Moroni, L. The osteochondral interface as a gradient tissue: From development to the fabrication of gradient scaffolds for regenerative medicine. *Birth Defects Research Part C: Embryo Today: Reviews* **105,** 34–52 (2015).

29. Vu, T. H. *et al.* MMP-9/Gelatinase B Is a Key Regulator of Growth Plate Angiogenesis and Apoptosis of Hypertrophic Chondrocytes. *Cell* **93,** 411–422 (1998).

30. Park, J. *et al.* Dual pathways to endochondral osteoblasts: A novel chondrocytederived osteoprogenitor cell identified in hypertrophic cartilage. *Biology Open* **4,** 608–621 (2015).

31. Tsang, K. Y., Chan, D. & Cheah, K. S. Fate of growth plate hypertrophic chondrocytes: Death or lineage extension? *Development Growth and Differentiation* **57,** 179–192 (Feb. 2015).

32. Haseeb, A. *et al.* SOX9 keeps growth plates and articular cartilage healthy by inhibiting chondrocyte dedifferentiation/osteoblastic redifferentiation. *Proceedings of the National Academy of Sciences* **118,** e2019152118 (2021).

33. Roach, H. I., Aigner, T. & Kouri, J. B. Chondroptosis: A variant of apoptotic cell death in chondrocytes? *Apoptosis* **9,** 265–277 (2004).

34. Pazzaglia, U. E. *et al.* New morphological evidence of the 'fate' of growth plate hypertrophic chondrocytes in the general context of endochondral ossification. *Journal of Anatomy* **236,** 305–316 (Feb. 2020).

35. Chang, C.-F. & Serra, R. Ift88 regulates Hedgehog signaling, Sfrp5 expression, and β-catenin activity in post-natal growth plate. *Journal of Orthopaedic Research* **31,** 350–356 (2013).

36. Racine, H. L. & Serrat, M. A. The Actions of IGF-1 in the Growth Plate and Its Role in Postnatal Bone Elongation. *Current Osteoporosis Reports* **18,** 210–227 (June 2020).

37. Chau, M. *et al.* Organization of the Indian hedgehog – parathyroid hormone-related protein system in the postnatal growth plate. *Journal of Molecular Endocrinology* **47,** 99–107 (2011).

38. Zhao, Q., Eberspaecher, H., Lefebvre, V. & Crombrugghe, B. d. Parallel expression of Sox9 and Col2a1 in cells undergoing chondrogenesis. *Developmental Dynamics* **209,** 377–386 (1997).

39. Drissi, M. H. *et al.* Runx2/Cbfa1 Stimulation by Retinoic Acid Is Potentiated by BMP2 Signaling Through Interaction with Smad1 on the Collagen X Promoter in Chondrocytes. *Journal of Cellular Biochemistry* **90,** 1287–1298 (Dec. 2003).

40. Zheng, Q. *et al.* Type X collagen gene regulation by Runx2 contributes directly to its hypertrophic chondrocyte-specific expression in vivo. *Journal of Cell Biology* **162,** 833–842 (Sept. 2003).

41. Zelzer, E. *et al.* VEGFA is necessary for chondrocyte survival during bone development. *Development* **131,** 2161–2171 (2004).

42. Dy, P. *et al.* Sox9 Directs Hypertrophic Maturation and Blocks Osteoblast Differentiation of Growth Plate Chondrocytes. *Developmental Cell* **22,** 597–609 (Mar. 2012).

43. Qin, X. *et al.* Runx2 is essential for the transdifferentiation of chondrocytes into osteoblasts. *PLoS Genetics* **16** (Nov. 2020).

44. Stokes, I. A., Aronsson, D. D., Dimock, A. N., Cortright, V. & Beck, S. Endochondral growth in growth plates of three species at two anatomical locations modulated by mechanical compression and tension. *Journal of Orthopaedic Research* **24,** 1327–1334 (2006).

45. Stokes, I. A., Clark, K. C., Farnum, C. E. & Aronsson, D. D. Alterations in the growth plate associated with growth modulation by sustained compression or distraction. *Bone* **41,** 197–205 (2007).

46. Villemure, I. & Stokes, I. A. Growth plate mechanics and mechanobiology. A survey of present understanding. *Journal of Biomechanics* **42,** 1793–1803 (Aug. 2009).

47. Coveney, C. R. *et al.* Ciliary IFT88 Protects Coordinated Adolescent Growth Plate Ossification From Disruptive Physiological Mechanical Forces. *Journal of Bone and Mineral Research* **37,** 1081–1086 (2022).

48. Killion, C. H., Mitchell, E. H., Duke, C. G. & Serra, R. Mechanical loading regulates organization of the actin cytoskeleton and column formation in postnatal growth plate. *Molecular Biology of the Cell* **28,** 1862–1870 (2017).

49. Reich, A. *et al.* Weight loading young chicks inhibits bone elongation and promotes growth plate ossification and vascularization. *Journal of Applied Physiology* **98,** 2381–2389 (2005).

50. Reich, A. *et al.* The effect of weight loading and subsequent release from loading on the postnatal skeleton (2008).

51. Shao, Y. Y., Wang, L., Welter, J. F. & Ballock, R. T. Primary cilia modulate Ihh signal transduction in response to hydrostatic loading of growth plate chondrocytes. *Bone* **50,** 79–84 (2012).

52. Wheatley, D. N., Wang, A. M. & Strugnell, G. E. Expression of primary cilia in mammalian cells. *Cell Biology International* **20,** 73–81 (1996).

53. Park, T. J., Haigo, S. L. & Wallingford, J. B. Ciliogenesis defects in embryos lacking inturned or fuzzy function are associated with failure of planar cell polarity and Hedgehog signaling. *Nature Genetics* **38,** 303–311 (2006).

54. Tummala, P., Arnsdorf, E. J. & Jacobs, C. R. The Role of Primary Cilia in Mesenchymal Stem Cell Differentiation: A Pivotal Switch in Guiding Lineage Commitment. *Cellular and Molecular Bioengineering* **3,** 207–212 (2010).

55. Pedersen, L. B., Veland, I. R., Schrøder, J. M. & Christensen, S. T. Assembly of primary cilia. *Developmental Dynamics* **237,** 1993–2006 (2008).

56. Satir, P. & Christensen, S. T. Overview of structure and function of mammalian cilia. *Annual Review of Physiology* **69,** 377–400 (2007).

57. Jensen, C. G. *et al.* Ultrastructural, tomographic and confocal imaging of the chondrocyte primary cilium in situ. *Cell Biology International* **28,** 101–110 (2004).

58. Benmerah, A. The ciliary pocket. *Current Opinion in Cell Biology* **25,** 78–84 (2013).

59. Molla-Herman, A. *et al.* The ciliary pocket: an endocytic membrane domain at the base of primary and motile cilia. *Journal of Cell Science* **123,** 1785–1795 (2010).

60. Poole, C. A. *et al.* Confocal analysis of primary cilia structure and colocalization with the Golgi apparatus in chondrocytes and aortic smooth muscle cells. *Cell Biology International* **21,** 483–494 (1997).

61. Ghossoub, R., Molla-Herman, A., Bastin, P. & Benmerah, A. The ciliary pocket: a once-forgotten membrane domain at the base of cilia. *Biology of the Cell* **103,** 131–144 (2011).

62. Mitchell, D. R. Eukaryotic Membranes and Cytoskeleton, Origins and Evolution. *Advances in Experimental Medicine and Biology* **607,** 130–140 (2007).

63. Hansen, J. N. *et al.* Intrinsic Diversity In Primary Cilia Revealed Through Spatial Proteomics. *bioRxiv,* 2024.10.20.619273 (2024).

64. Insinna, C. & Besharse, J. C. Intraflagellar transport and the sensory outer segment of vertebrate photoreceptors. *Developmental Dynamics* **237,** 1982–1992 (2008).

65. Thompson, C. L., Chapple, J. P. & Knight, M. M. Primary cilia disassembly down-regulates mechanosensitive hedgehog signalling: a feedback mechanism controlling ADAMTS-5 expression in chondrocytes. *Osteoarthritis and Cartilage* **22,** 490 (2014).

66. Anvarian, Z., Mykytyn, K., Mukhopadhyay, S., Pedersen, L. B. & Christensen, S. T. Cellular signalling by primary cilia in development, organ function and disease. *Nature Reviews Nephrology 2019 15:4* **15,** 199–219 (Feb. 2019).

67. Yuan, X. & Yang, S. Cilia/Ift protein and motor-related bone diseases and mouse models. *Frontiers in Bioscience* **20,** 515–555 (2015).

68. Pedersen, L. B., Schrøder, J. M., Satir, P. & Christensen, S. T. The ciliary cytoskeleton. *Comprehensive Physiology* **2,** 779–803 (2012).

69. Sorokin, S. Centrioles and the formation of rudimentary cilia by fibroblasts and smooth muscle cells. *The Journal of Cell Biology* **15,** 363–377 (1962).

70. Kozminski, K. G., Johnson, K. A., Forscher, P. & Rosenbaum, J. L. A motility in the eukaryotic flagellum unrelated to flagellar beating. *Proceedings of the National Academy of Sciences* **90,** 5519–5523 (1993).

71. Rosenbaum, J. L. & Witman, G. B. Intraflagellar transport. *Nature Reviews Molecular Cell Biology* **3,** 813–825 (2002).

72. Giluli, N. B. & Satir, P. The ciliary necklace: A Ciliary Membrane Specialization. *The Journal of Cell Biology* **53,** 494–509 (1972).

73. Ledbetter, M. C. & Porter, K. R. Morphology of microtubules of plant cells. *Science* **144,** 872–874 (1964).

74. Cole, D. G. *et al.* Chlamydomonas Kinesin-II–dependent Intraflagellar Transport (IFT): IFT Particles Contain Proteins Required for Ciliary Assembly in Caenorhabditis elegans Sensory Neurons. *The Journal of Cell Biology* **141,** 993–1008 (1998).

75. Pazour, G. J., Wilkerson, C. G. & Witman, G. B. A Dynein Light Chain Is Essential for the Retrograde Particle Movement of Intraflagellar Transport (IFT). *The Journal of Cell Biology* **141,** 979–992 (1998).

76. Orozco, J. T. *et al.* Movement of motor and cargo along cilia. *Nature* **398,** 674–674 (1999).

77. Mizuno, N., Taschner, M., Engel, B. D. & Lorentzen, E. Structural studies of ciliary components. *Journal of Molecular Biology* **422,** 163–180 (Sept. 2012).

78. Shi, P. *et al.* Increasing Ciliary ARL13B Expression Drives Active and Inhibitor-Resistant Smoothened and GLI into Glioma Primary Cilia. *Cells* **12,** 2354 (2023).

79. Lucker, B. F. *et al.* Characterization of the Intraflagellar Transport Complex B Core. *Journal of Biological Chemistry* **280,** 27688–27696 (2005).

80. Coveney, C. R. *et al.* The ciliary protein IFT88 controls post-natal cartilage thickness and influences development of osteoarthritis. *Arthritis & Rheumatology* **74,** 49–59 (2021).

81. McGlashan, S. R., Haycraft, C. J., Jensen, C. G., Yoder, B. K. & Poole, C. A. Articular cartilage and growth plate defects are associated with chondrocyte cytoskeletal abnormalities in Tg737 orpk mice lacking the primary cilia protein polaris. *Matrix Biology* **26,** 234–246 (2007).

82. Pazour, G. J. *et al.* Chlamydomonas IFT88 and Its Mouse Homologue, Polycystic Kidney Disease Gene Tg737, Are Required for Assembly of Cilia and Flagella. *The Journal of Cell Biology* **151,** 709–718 (2000).

83. Jones, C. *et al.* Ciliary proteins link basal body polarization to planar cell polarity regulation. *Nature Genetics* **40,** 69–77 (2008).

84. Robert, A. *et al.* The intraflagellar transport component IFT88/polaris is a centrosomal protein regulating G1-S transition in non-ciliated cells. *Journal of Cell Science* **120,** 628–637 (2007).

85. Boehlke, C. *et al.* A Cilia Independent Role of Ift88/Polaris during Cell Migration. *PLoS ONE* **10,** e0140378 (2015).

86. Haycraft, C. J. *et al.* Intraflagellar transport is essential for endochondral bone formation. *Development* **134,** 307–316 (2007).

87. McGlashan, S. R., Jensen, C. G. & Poole, C. A. Localization of extracellular matrix receptors on the chondrocyte primary cilium. *Journal of Histochemistry and Cytochemistry* **54,** 1005–1014 (Sept. 2006).

88. Song, B., Haycraft, C. J., Seo, H. s., Yoder, B. K. & Serra, R. Development of the post-natal growth plate requires intraflagellar transport proteins. *Developmental Biology* **305,** 202–216 (May 2007).

89. Yuan, X. & Yang, S. Deletion of IFT80 impairs epiphyseal and articular cartilage formation due to disruption of chondrocyte differentiation. *PLoS ONE* **10** (June 2015).

90. Poole, C. A., Zhang, Z.-J. & Ross, J. M. The differential distribution of acetylated and detyrosinated alpha-tubulin in the microtubular cytoskeleton and primary cilia of hyaline cartilage chondrocytes. *Journal of Anatomy* **199,** 393–405 (2001).

91. Praetorius, H. & Spring, K. Bending the MDCK Cell Primary Cilium Increases Intracellular Calcium. *The Journal of Membrane Biology* **184,** 71–79 (2001).

92. Nauli, S. M. *et al.* Polycystins 1 and 2 mediate mechanosensation in the primary cilium of kidney cells. *Nature Genetics* **33,** 129–137 (Feb. 2003).

93. Delling, M. *et al.* Primary cilia are not calcium-responsive mechanosensors. *Nature 2016 531:7596* **531,** 656–660 (2016).

94. Delling, M., Decaen, P. G., Doerner, J. F., Febvay, S. & Clapham, D. E. Primary cilia are specialized calcium signalling organelles. *Nature* **504,** 311–314 (2013).

95. Praetorius, H. A. & Spring, K. R. Removal of the MDCK cell primary cilium abolishes flow sensing. *Journal of Membrane Biology* **191,** 69–76 (2003).

96. Katoh, T. A. *et al.* Immotile cilia mechanically sense the direction of fluid flow for left-right determination. *Science* **379,** 66–71 (2023).

97. Yoshiba, S. *et al.* Cilia at the Node of Mouse Embryos Sense Fluid Flow for Left-Right Determination via Pkd2. *Science* **338,** 226–231 (2012).

98. Djenoune, L. *et al.* Cilia function as calcium-mediated mechanosensors that instruct left-right asymmetry. *Science* **379,** 71–78 (2023).

99. Resnick, A. & Hopfer, U. Mechanical stimulation of primary cilia. *Frontiers in Bioscience* **13,** 1665 (2008).

100. Graff, R. D., Lazarowski, E. R., Banes, A. J. & Lee, G. M. ATP release by mechanically loaded porcine chondrons in pellet culture. *Arthritis & Rheumatism* **43,** 1571–1579 (2000).

101. He, Z. *et al.* Strain-induced mechanotransduction through primary cilia, extracellular ATP, purinergic calcium signaling, and ERK1/2 transactivates CITED2 and downregulates MMP-1 and MMP-13 gene expression in chondrocytes. *Osteoarthritis and Cartilage* **24,** 892–901 (2016).

102. Knight, M. M., Mcglashan, S. R., Garcia, M., Jensen, C. G. & Poole, C. A. Articular chondrocytes express connexin 43 hemichannels and P2 receptors – a putative mechanoreceptor complex involving the primary cilium? *Journal of Anatomy* **214,** 275–283 (2009).

103. Yuan, X. *et al.* Ciliary IFT80 balances canonical versus non-canonical hedgehog signalling for osteoblast differentiation. *Nature Communications 2016 7:1* **7,** 1–13 (Mar. 2016).

104. Goetz, S. C., Ocbina, P. J. & Anderson, K. V. The primary cilium as a Hedgehog signal transduction machine. *Methods in cell biology* **94,** 199–222 (2009).

105. Corbit, K. C. *et al.* Vertebrate Smoothened functions at the primary cilium. *Nature* **437,** 1018–1021 (2005).

106. Rohatgi, R., Milenkovic, L. & Scott, M. P. Patched1 Regulates Hedgehog Signaling at the Primary Cilium. *Science* **317,** 372–376 (2007).

107. Haycraft, C. J. *et al.* Gli2 and Gli3 localize to cilia and require the intraflagellar transport protein polaris for processing and function. *PLoS Genetics* **1,** 0480–0488 (2005).

108. Huangfu, D. *et al.* Hedgehog signalling in the mouse requires intraflagellar transport proteins. *Nature* **426,** 83–87 (2003).

109. Hoey, D. A., Tormey, S., Ramcharan, S., O'Brien, F. J. & Jacobs, C. R. Primary Cilia-Mediated Mechanotransduction in Human Mesenchymal Stem Cells. *STEM CELLS* **30,** 2561–2570 (2012).

110. Deren, M. E., Yang, X., Guan, Y. & Chen, Q. Biological and Chemical Removal of Primary Cilia Affects Mechanical Activation of Chondrogenesis Markers in Chondroprogenitors and Hypertrophic Chondrocytes. *International Journal of Molecular Sciences* **17,** 188 (2016).

111. Tao, D. *et al.* Primary cilia support cartilage regeneration after injury. *International Journal of Oral Science* **15,** 22 (2023).

112. Leucht, P. *et al.* Primary cilia act as mechanosensors during bone healing around an implant. *Medical Engineering & Physics* **35,** 392–402 (2013).

113. Temiyasathit, S. *et al.* Mechanosensing by the Primary Cilium: Deletion of Kif3A Reduces Bone Formation Due to Loading. *PLOS ONE* **7,** e33368 (Mar. 2012).

114. Moore, E. R., Yang, Y. & Jacobs, C. R. Primary cilia are necessary for Prx1-expressing cells to contribute to postnatal skeletogenesis. *Journal of Cell Science* **131** (2018).

115. Koyama, E. *et al.* Conditional Kif3a ablation causes abnormal hedgehog signaling topography, growth plate dysfunction, and excessive bone and cartilage formation during mouse skeletogenesis. *Development* **134,** 2159–2169 (2007).

116. Bosakova, M. *et al.* Mutations in GRK2 cause Jeune syndrome by impairing Hedgehog and canonical Wnt signaling. *EMBO Molecular Medicine* **12,** e11739 (Nov. 2020).

117. Hruba, E. *et al.* Loss of Sprouty Produces a Ciliopathic Skeletal Phenotype in Mice Through Upregulation of Hedgehog Signaling. *Journal of Bone and Mineral Research* **36,** 2258–2274 (2021).

118. Rix, S., Calmont, A., Scambler, P. J. & Beales, P. L. An Ift80 mouse model of short rib polydactyly syndromes shows defects in hedgehog signalling without loss or malformation of cilia. *Human Molecular Genetics* **20,** 1306–1314 (2011).

119. Terpstra, L. *et al.* Reduced chondrocyte proliferation and chondrodysplasia in mice lacking the integrin-linked kinase in chondrocytes. *The Journal of Cell Biology* **162,** 139–148 (2003).

120. Wang, G. *et al.* Genetic ablation of Rac1 in cartilage results in chondrodysplasia. *Developmental Biology* **306,** 612–623 (2007).

121. Reiter, J. F. & Leroux, M. R. Genes and molecular pathways underpinning ciliopathies. *Nature Reviews Molecular Cell Biology* **18,** 533–547 (2017).

122. Huber, C. & Cormier-Daire, V. Ciliary disorder of the skeleton. *American Journal of Medical Genetics, Part C: Seminars in Medical Genetics* **160 C,** 165–174 (2012).

123. Li, S., Zhang, H. & Sun, Y. Primary cilia in hard tissue development and diseases. *Frontiers of Medicine* **15,** 657–678 (2021).

124. Schmidts, M. & Mitchison, H. M. Severe skeletal abnormalities caused by defects in retrograde intraflagellar transport dyneins. *Dyneins,* 357–401 (2018).

125. Tobin, J. L. & Beales, P. L. The nonmotile ciliopathies. *Genetics in Medicine* **11,** 386–402 (2009).

126. Mokrzan, E. M., Lewis, J. S. & Mykytyn, K. Differences in Renal Tubule Primary Cilia Length in a Mouse Model of Bardet-Biedl Syndrome. *Nephron Experimental Nephrology* **106,** 88–96 (2007).

127. Besschetnova, T. Y. *et al.* Identification of Signaling Pathways Regulating Primary Cilium Length and Flow-Mediated Adaptation. *Current Biology* **20,** 182–187 (2010).

128. Massinen, S. *et al.* Increased Expression of the Dyslexia Candidate Gene DCDC2 Affects Length and Signaling of Primary Cilia in Neurons. *PLoS ONE* **6,** 20580 (2011).

129. Chekuri, A. *et al.* IFT88 mutations identified in individuals with non-syndromic recessive retinal degeneration result in abnormal ciliogenesis. *Human Genetics* **137,** 447–458 (2018).

130. Murcia, N. S. *et al.* The Oak Ridge Polycystic Kidney (orpk) disease gene is required for left-right axis determination. *Development* **127,** 2347–2355 (2000).

131. Moyer, J. H. *et al.* Candidate Gene Associated with a Mutation Causing Recessive Polycystic Kidney Disease in Mice. *Science* **264,** 1329–1333 (1994).

132. Lehman, J. M. *et al.* The Oak Ridge Polycystic Kidney mouse: Modeling ciliopathies of mice and men. *Developmental Dynamics* **237,** 1960–1971 (2008).

133. Hammarsjö, A. *et al.* Novel KIAA0753 mutations extend the phenotype of skeletal ciliopathies. *Scientific Reports* **7** (2017).

134. Duran, I. *et al.* Mutations in IFT-A satellite core component genes IFT43 and IFT121 produce short rib polydactyly syndrome with distinctive campomelia. *Cilia* **6** (2017).

135. Iomini, C., Tejada, K., Mo, W., Vaananen, H. & Piperno, G. Primary cilia of human endothelial cells disassemble under laminar shear stress. *The Journal of Cell Biology* **164,** 811–817 (2004).

136. Heiden, K. V. d. *et al.* Endothelial primary cilia in areas of disturbed flow are at the base of atherosclerosis. *Atherosclerosis* **196,** 542–550 (2008).

137. Lu, C. *et al.* Non-Random Distribution and Sensory Functions of Primary Cilia in Vascular Smooth Muscle Cells. *Kidney and Blood Pressure Research* **31,** 171–184 (2008).

138. Monfared, R. V. *et al.* Cilia in the brain display region-dependent oscillations of length and orientation. *PLOS Biology* **23,** e3003197 (2025).

139. Donnelly, E., Ascenzi, M. G. & Farnum, C. Primary cilia are highly oriented with respect to collagen direction and long axis of extensor tendon. *Journal of orthopaedic research : official publication of the Orthopaedic Research Society* **28,** 77 (2010).

140. Farnum, C. E., Williams, R. M. & Donnelly, E. Analyzing Primary Cilia by Multiphoton Microscopy. *Methods in Cell Biology* **94,** 117–135 (2009).

141. Farnum, C. E. & Wilsman, N. J. Orientation of Primary Cilia of Articular Chondrocytes in Three-Dimensional Space. *The Anatomical Record: Advances in Integrative Anatomy and Evolutionary Biology* **294,** 533–549 (2011).

142. Jenkins, P. M., McEwen, D. P. & Martens, J. R. Olfactory Cilia: Linking Sensory Cilia Function and Human Disease. *Chemical Senses* **34,** 451–464 (2009).

143. Genovese, F., Reisert, J. & Kefalov, V. J. Sensory Transduction in Photoreceptors and Olfactory Sensory Neurons: Common Features and Distinct Characteristics. *Frontiers in Cellular Neuroscience* **15,** 761416 (2021).

144. Jones, C. & Chen, P. Chapter Eight Primary Cilia in Planar Cell Polarity Regulation of the Inner Ear. *Current Topics in Developmental Biology* **85,** 197–224 (2008).

145. Jonassen, J. A., Agustin, J. S., Follit, J. A. & Pazour, G. J. Deletion of IFT20 in the mouse kidney causes misorientation of the mitotic spindle and cystic kidney disease. *The Journal of Cell Biology* **183,** 377–384 (2008).

146. Heydeck, W., Zeng, H. & Liu, A. Planar cell polarity effector gene Fuzzy regulates cilia formation and Hedgehog signal transduction in mouse. *Developmental Dynamics* **238,** 3035–3042 (2009).

147. Haycraft, C. J. & Serra, R. Cilia Involvement in Patterning and Maintenance of the Skeleton. *Current Topics in Developmental Biology* **85,** 303–332 (2008).

148. Rape, A. D., Zibinsky, M., Murthy, N. & Kumar, S. A synthetic hydrogel for the high-throughput study of cell-ECM interactions. *Nature Communications* **6** (2015).

149. Benya, P. D. & Shaffer, J. D. Dedifferentiated chondrocytes reexpress the differentiated collagen phenotype when cultured in agarose gels. *Cell* **30,** 215–224 (1982).

150. Caron, M. *et al.* Redifferentiation of dedifferentiated human articular chondrocytes: comparison of 2D and 3D cultures. *Osteoarthritis and Cartilage* **20,** 1170–1178 (2012).

151. Chan, C. K. *et al.* Identification of the Human Skeletal Stem Cell. *Cell* **175,** 43–56.e21 (Sept. 2018).

152. Craft, A. M. *et al.* Specification of chondrocytes and cartilage tissues from embryonic stem cells. *Development* **140,** 2597–2610 (2013).

153. Craft, A. M. *et al.* Generation of articular chondrocytes from human pluripotent stem cells. *Nature Biotechnology 2015 33:6* **33,** 638–645 (2015).

154. Li, C. *et al.* Directed differentiation of human pluripotent stem cells into articular cartilage reveals effects caused by absence of WISP3, the gene responsible for Progressive Pseudorheumatoid Arthropathy of Childhood. *bioRxiv* (2023).

155. Huang, C.-P., Hsu, K.-C., Wu, C.-P. & Wu, H.-T. Osteogenic Differentiation from Mouse Adipose-Derived Stem Cells and Bone Marrow Stem Cells. *Chinese Journal of Physiology* **65,** 21–29 (2022).

156. Sakaguchi, Y., Sekiya, I., Yagishita, K. & Muneta, T. Comparison of human stem cells derived from various mesenchymal tissues: Superiority of synovium as a cell source. *Arthritis & Rheumatism* **52,** 2521–2529 (2005).

157. Wu, L. *et al.* Trophic Effects of Mesenchymal Stem Cells Increase Chondrocyte Proliferation and Matrix Formation. *Tissue Engineering Part A* **17,** 1425–1436 (2011).

158. Deszcz, I. & Bar, J. Co-Culture Approaches in Cartilage and Bone Tissue Regeneration. *International Journal of Molecular Sciences* **26,** 5711 (2025).

159. Aydin, H. M. A Three-Layered Osteochondral Plug: Structural, Mechanical, and in vitro Biocompatibility Analysis. *Advanced Engineering Materials* **13,** B511–B517 (2011).

160. Armiento, A. R., Stoddart, M. J., Alini, M. & Eglin, D. Biomaterials for articular cartilage tissue engineering: Learning from biology. *Acta Biomaterialia* **65,** 1–20 (2018).

161. Zhao, W., Jin, X., Cong, Y., Liu, Y. & Fu, J. Degradable natural polymer hydrogels for articular cartilage tissue engineering. *Journal of Chemical Technology & Biotechnology* **88,** 327–339 (2013).

162. Jiang, J. *et al.* Bioactive Stratified Polymer Ceramic-Hydrogel Scaffold for Integrative Osteochondral Repair. *Annals of Biomedical Engineering* **38,** 2183–2196 (2010).

163. Maherani, M., Eslami, H., Poursamar, S. A. & Ansari, M. A modular approach to 3D-printed bilayer composite scaffolds for osteochondral tissue engineering. *Journal of Materials Science: Materials in Medicine* **35,** 62 (2024).

164. Chang, R. A. S. H., Shanley, J. F., Kersh, M. E. & Harley, B. A. Tough and tunable scaffold-hydrogel composite biomaterial for soft-to-hard musculoskeletal tissue interfaces. *Science Advances* **6,** eabb6763 (2020).

165. Horner, C. B., Maldonado, M., Tai, Y., Rony, R. M. K. & Nam, J. Spatially Regulated Multiphenotypic Differentiation of Stem Cells in 3D via Engineered Mechanical Gradient. *ACS Applied Materials and Interfaces* **11,** 45479–45488 (2019).

166. Levingstone, T. J., Matsiko, A., Dickson, G. R., O'Brien, F. J. & Gleeson, J. P. A biomimetic multi-layered collagen-based scaffold for osteochondral repair. *Acta Biomaterialia* **10,** 1996–2004 (2014).

167. Kim, T. H. *et al.* Creating stiffness gradient polyvinyl alcohol hydrogel using a simple gradual freezing–thawing method to investigate stem cell differentiation behaviors. *Biomaterials* **40,** 51–60 (2015).

168. Major, L. G. *et al.* Volume Adaptation Controls Stem Cell Mechanotransduction. *ACS Applied Materials & Interfaces* **11,** 45520–45530 (2019).

169. Tong, X., Jiang, J., Zhu, D. & Yang, F. Hydrogels with Dual Gradients of Mechanical and Biochemical Cues for Deciphering Cell-Niche Interactions. *ACS Biomaterials Science & Engineering* **2,** 845–852 (2016).

170. Luca, A. D. *et al.* Influencing chondrogenic differentiation of human mesenchymal stromal cells in scaffolds displaying a structural gradient in pore size. *Acta Biomaterialia* **36,** 210–219 (2016).

171. Xu, G. *et al.* Electric field-driven building blocks for introducing multiple gradients to hydrogels. *Protein & Cell* **11,** 267–285 (2020).

172. Canadas, R. F. *et al.* Biochemical Gradients to Generate 3D Heterotypic-Like Tissues with Isotropic and Anisotropic Architectures. *Advanced Functional Materials* **28,** 1804148 (2018).

173. Nowicki, M. A., Castro, N. J., Plesniak, M. W. & Zhang, L. G. 3D printing of novel osteochondral scaffolds with graded microstructure. *Nanotechnology* **27,** 414001 (2016).

174. Li, C. *et al.* Buoyancy-Driven Gradients for Biomaterial Fabrication and Tissue Engineering. *Advanced Materials* **31** (2019).

175. Gunnewiek, M. K. *et al.* Creeping Proteins in Microporous Structures: Polymer Brush-Assisted Fabrication of 3D Gradients for Tissue Engineering. *Advanced Healthcare Materials* **4,** 1169–1174 (2015).

176. Li, C. *et al.* Glycosylated superparamagnetic nanoparticle gradients for osteochondral tissue engineering. *Biomaterials* **176,** 24–33 (2018).

177. Mahadik, B. P., Wheeler, T. D., Skertich, L. J., Kenis, P. J. & Harley, B. A. Microfluidic Generation of Gradient Hydrogels to Modulate Hematopoietic Stem Cell Culture Environment. *Advanced Healthcare Materials* **3,** 449–458 (2014).

178. Oh, S. H., Kim, T. H. & Lee, J. H. Creating growth factor gradients in three dimensional porous matrix by centrifugation and surface immobilization. *Biomaterials* **32,** 8254–8260 (2011).

179. Ko, H. *et al.* A simple layer-stacking technique to generate biomolecular and mechanical gradients in photocrosslinkable hydrogels. *Biofabrication* **11,** 025014 (2019).

180. Dormer, N. H., Singh, M., Wang, L., Berkland, C. J. & Detamore, M. S. Osteochondral Interface Tissue Engineering Using Macroscopic Gradients of Bioactive Signals. *Annals of Biomedical Engineering* **38,** 2167–2182 (2010).

181. Spinella-Jaegle, S. *et al.* Opposite effects of bone morphogenetic protein-2 and transforming growth factor-β1 on osteoblast differentiation. *Bone* **29,** 323–330 (2001).

182. Phillips, J. E., Burns, K. L., Doux, J. M. L., Guldberg, R. E. & García, A. J. Engineering graded tissue interfaces. *Proceedings of the National Academy of Sciences* **105,** 12170–12175 (2008).

183. Gool, S. A. v. *et al.* Fetal Mesenchymal Stromal Cells Differentiating towards Chondrocytes Acquire a Gene Expression Profile Resembling Human Growth Plate Cartilage. *PLoS ONE* **7,** e44561 (2012).

184. Randall, R. M., Shao, Y. Y., Wang, L. & Ballock, R. T. Activation of Wnt Planar cell polarity (PCP) signaling promotes growth plate column formation in vitro. *Journal of Orthopaedic Research* **30,** 1906–1914 (2012).

185. Alsberg, E., Anderson, K. W., Albeiruti, A., Rowley, J. A. & Mooney, D. J. Engineering growing tissues. *Proceedings of the National Academy of Sciences of the United States of America* **99,** 12025–12030 (2002).

186. Loh, K. M. *et al.* Mapping the Pairwise Choices Leading from Pluripotency to Human Bone, Heart, and Other Mesoderm Cell Types. *Cell* **166,** 451–467 (2016).

187. Matsuda, M. *et al.* Recapitulating the human segmentation clock with pluripotent stem cells. *Nature* **580,** 124–129 (2020).

188. Erickson, A. G. *et al.* A Tunable, Three-Dimensional In Vitro Culture Model of Growth Plate Cartilage Using Alginate Hydrogel Scaffolds. *Tissue Engineering. Part A* **24,** 94 (Jan. 2018).

189. Amini, S., Veilleux, D. & Villemure, I. Tissue and cellular morphological changes in growth plate explants under compression. *Journal of Biomechanics* **43,** 2582–2588 (2010).

190. Kaviani, R., Londono, I., Parent, S., Moldovan, F. & Villemure, I. Growth plate cartilage shows different strain patterns in response to static versus dynamic mechanical modulation. *Biomechanics and Modeling in Mechanobiology* **15,** 933–946 (2016).

191. Kaviani, R., Londono, I., Parent, S., Moldovan, F. & Villemure, I. Changes in growth plate extracellular matrix composition and biomechanics following in vitro static versus dynamic mechanical modulation. *Journal of musculoskeletal & neuronal interactions* **18,** 81–91 (2018).

192. Sergerie, K., Lacoursière, M.-O., Lévesque, M. & Villemure, I. Mechanical properties of the porcine growth plate and its three zones from unconfined compression tests. *Journal of Biomechanics* **42,** 510–516 (2009).

193. Sergerie, K. *et al.* Growth plate explants respond differently to in vitro static and dynamic loadings. *Journal of Orthopaedic Research* **29,** 473–480 (2011).

194. Othman, H., Thonar, E. J. & Mao, J. J. Modulation of neonatal growth plate development by ex vivo intermittent mechanical stress. *Journal of Biomechanics* **40,** 2686–2693 (2007).

195. Hopkins, T. *et al.* Engineering growth factor gradients to drive spatiotemporal tissue patterning in organ-on-a-chip systems. *Journal of Tissue Engineering* **16** (2025).

196. González-Guede, I., Garriguez-Perez, D. & Fernandez-Gutierrez, B. Osteochondral Tissue-On-a-Chip: A Novel Model for Osteoarthritis Research. *International Journal of Molecular Sciences* **25,** 9834 (2024).

197. Armstrong, J. P. K. *et al.* Engineering Anisotropic Muscle Tissue using Acoustic Cell Patterning. *Advanced Materials* **30,** 1802649 (2018).

198. Armstrong, J. P. *et al.* Tissue Engineering Cartilage with Deep Zone Cytoarchitecture by High-Resolution Acoustic Cell Patterning. *Advanced Healthcare Materials* (2022).

199. Grigoryan, B. *et al.* Multivascular networks and functional intravascular topologies within biocompatible hydrogels. *Science* **364,** 458–464 (2019).

200. Kolesky, D. B., Homan, K. A., Skylar-Scott, M. A. & Lewis, J. A. Three-dimensional bioprinting of thick vascularized tissues. *Proceedings of the National Academy of Sciences* **113,** 3179–3184 (2016).

201. Wu, W., DeConinck, A. & Lewis, J. A. Omnidirectional Printing of 3D Microvascular Networks. *Advanced Materials* **23,** H178–H183 (2011).

202. Voelkl, I. *et al.* In vitro approaches to study centriole and cilium function in early mouse embryogenesis. *bioRxiv* (2025).

203. Pretemer, Y. *et al.* Differentiation of Hypertrophic Chondrocytes from Human iPSCs for the In Vitro Modeling of Chondrodysplasias. *Stem Cell Reports* **16,** 610–625 (2021).

204. Boutaud, L. *et al.* 2D and 3D Human Induced Pluripotent Stem Cell-Based Models to Dissect Primary Cilium Involvement during Neocortical Development. *JoVE (Journal of Visualized Experiments),* e62667 (2022).

205. Liu, Z. *et al.* Constructing condylar cartilage organoid to explore primary cilia functions. *Heliyon* **10,** e35972 (2024).

206. Carrion, P. M. J. & Williams, J. L. Primary Chondrocyte Cilium Strains Increase with Depth Within the Growth Plate Reserve Zone and Reflect Loading Direction Across the Growth Plate. *Mechanobiology Journal* **3,** 1–10 (2022).

207. Johnson, T., Midha, S. & Wann, A. Volumetric Imaging and Analysis of Primary Cilia in Musculoskeletal Tissue using the ARL13B-CENTRIN-2 Mouse Model. *Journal of Visualized Experiments* (2025).

208. McGlashan, S. R. *et al.* Mechanical loading modulates chondrocyte primary cilia incidence and length. *Cell Biology International* **34,** 441–446 (2010).

209. Andrea, C. E. D. *et al.* Primary cilia organization reflects polarity in the growth plate and implies loss of polarity and mosaicism in osteochondroma. *Laboratory Investigation 2010 90:7* **90,** 1091–1101 (2010).

210. Ascenzi, M.-G. *et al.* Effect of localization, length and orientation of chondrocytic primary cilium on murine growth plate organization. *Journal of Theoretical Biology* **285,** 147–155 (2011).

211. Bangs, F. K., Schrode, N., Hadjantonakis, A. K. & Anderson, K. V. Lineage specificity of primary cilia in the mouse embryo. *Nature Cell Biology* **17,** 113–122 (2015).

212. Larkins, C. E., Aviles, G. D. G., East, M. P., Kahn, R. A. & Caspary, T. Arl13b regulates ciliogenesis and the dynamic localization of Shh signaling proteins. *Molecular Biology of the Cell* **22,** 4694–4703 (2011).

213. Higginbotham, H., Bielas, S., Tanaka, T. & Gleeson, J. G. Transgenic Mouse Line with Green-fluorescent Protein-labeled Centrin 2 allows Visualization of the Centrosome in Living Cells. *Transgenic Research* **13,** 155–164 (2004).

214. arivis. *Application Note #47 - Applying Cellpose models in arivis Vision4D* tech. rep. (2021), 1–20.

215. Cooper, K. L. *et al.* Multiple phases of chondrocyte enlargement underlie differences in skeletal proportions. *Nature* **495,** 375–378 (2013).

216. Ascenzi, M.-G., Lenox, M. & Farnum, C. Analysis of the orientation of primary cilia in growth plate cartilage: A mathematical method based on multiphoton microscopical images. *Journal of Structural Biology* **158,** 293–306 (2007).

217. Huff, J., Bergter, A. & Luebbers, B. Application Note: Multiplex mode for the LSM 9 series with Airyscan 2: fast and gentle confocal super-resolution in large volumes. *Nature Methods* (2019).

218. Ning, K. *et al.* Cilia-associated wound repair mediated by IFT88 in retinal pigment epithelium. *Scientific Reports* **13,** 8205 (2023).

219. Palla, A. R. *et al.* Primary cilia on muscle stem cells are critical to maintain regenerative capacity and are lost during aging. *Nature Communications* **13,** 1439 (2022).

220. Brewer, K. K. *et al.* Postnatal Dynamic Ciliary ARL13B and ADCY3 Localization in the Mouse Brain. *Cells* **13,** 259 (2024).

221. Kubalová, I., Němečková, A., Weisshart, K., Hřibová, E. & Schubert, V. Comparing Super-Resolution Microscopy Techniques to Analyze Chromosomes. *International Journal of Molecular Sciences* **22,** 1903 (2021).

222. Katoh, Y., Chiba, S. & Nakayama, K. Practical method for superresolution imaging of primary cilia and centrioles by expansion microscopy using an amplibody for fluorescence signal amplification. *Molecular Biology of the Cell* **31,** 2195–2206 (2020).

223. Moore, A. S. *et al.* Actin cables and comet tails organize mitochondrial networks in mitosis. *Nature* **591,** 659–664 (2021).

224. Lauring, M. C. *et al.* New software for automated cilia detection in cells (ACDC). *Cilia* **8,** 1 (2019).

225. Hansen, J. N., Rassmann, S., Stüven, B., Jurisch-Yaksi, N. & Wachten, D. CiliaQ: a simple, open-source software for automated quantification of ciliary morphology and fluorescence in 2D, 3D, and 4D images. *The European Physical Journal E* **44,** 18 (2021).

226. Hua, K. & Ferland, R. J. Fixation methods can differentially affect ciliary protein immunolabeling. *Cilia* **6,** 5 (2017).

227. Dummer, A., Poelma, C., DeRuiter, M. C., Goumans, M.-J. T. H. & Hierck, B. P. Measuring the primary cilium length: improved method for unbiased high-throughput analysis. *Cilia* **5,** 7 (2016).

228. Goldstein, B., Takeshita, H., Mizumoto, K. & Sawa, H. Wnt Signals Can Function as Positional Cues in Establishing Cell Polarity. *Developmental Cell* **10,** 391–396 (2006).

229. Whitaker, A. T., Berthet, E., Cantu, A., Laird, D. J. & Alliston, T. Smad4 regulates growth plate matrix production and chondrocyte polarity. *Biology Open* **6,** 358–364 (2017).

230. Anderson, C. T. *et al.* Primary Cilia: Cellular Sensors for the Skeleton. *The Anatomical Record: Advances in Integrative Anatomy and Evolutionary Biology* **291,** 1074–1078 (2008).

231. Wann, A. K. T. & Knight, M. M. Primary cilia elongation in response to interleukin-1 mediates the inflammatory response. *Cellular and Molecular Life Sciences* **69,** 2967–2977 (2012).

232. Willantarra, I., Leung, S., Choi, Y. S., Chhana, A. & McGlashan, S. R. Chondrocyte-specific response to stiffness-mediated primary cilia formation and centriole positioning. *American Journal of Physiology-Cell Physiology* (2022).

233. Miyoshi, K. *et al.* Lack of Dopaminergic Inputs Elongates the Primary Cilia of Striatal Neurons. *PLoS ONE* **9,** e97918 (2014).

234. Abdul-Majeed, S., Moloney, B. C. & Nauli, S. M. Mechanisms regulating cilia growth and cilia function in endothelial cells. *Cellular and Molecular Life Sciences* **69,** 165–173 (2012).

235. Kim, J. *et al.* Functional genomic screen for modulators of ciliogenesis and cilium length. *Nature* **464,** 1048–1051 (2010).

236. Miyoshi, K., Kasahara, K., Miyazaki, I. & Asanuma, M. Factors That Influence Primary Cilium Length. *Acta Medica Okayama* **65,** 279–285 (2011).

237. Chavali, P. L., Pütz, M. & Gergely, F. Small organelle, big responsibility: the role of centrosomes in development and disease. *Philosophical Transactions of the Royal Society B: Biological Sciences* **369,** 20130468 (2014).

238. Staines, K. A., Madi, K., Javaheri, B., Lee, P. D. & Pitsillides, A. A. A computed microtomography method for understanding epiphyseal growth plate fusion. *Frontiers in Materials* **4** (2018).

239. Gao, J., Roan, E. & Williams, J. L. Regional Variations in Growth Plate Chondrocyte Deformation as Predicted By Three-Dimensional Multi-Scale Simulations. *PLoS ONE* **10,** e0124862 (2015).

240. Poole, C. A., Flint, M. H. & Beaumont, B. W. Analysis of the morphology and function of primary cilia in connective tissues:A cellular cybernetic probe? *Cell Motility* **5,** 175–193 (1985).

241. Rubin, S. *et al.* Application of 3D MAPs pipeline identifies the morphological sequence chondrocytes undergo and the regulatory role of GDF5 in this process. *Nature Communications* **12,** 5363 (2021).

242. Yokoyama, Y., Kameo, Y., Sunaga, J., Maki, K. & Adachi, T. Chondrocyte hypertrophy in the growth plate promotes stress anisotropy affecting long bone development through chondrocyte column formation. *Bone,* 117055 (2024).

243. Prein, C. *et al.* Structural and mechanical properties of the proliferative zone of the developing murine growth plate cartilage assessed by atomic force microscopy. *Matrix Biology* **50,** 1–15 (2016).

244. Shea, C. A. & Murphy, P. The Primary Cilium on Cells of Developing Skeletal Rudiments; Distribution, Characteristics and Response to Mechanical Stimulation. *Frontiers in Cell and Developmental Biology* **9,** 725018 (2021).

245. Stam, L. B. & Clark, A. L. Chondrocyte primary cilia lengthening and shortening in response to mediators of osteoarthritis; a role for integrin α1β1 and focal adhesions. *Osteoarthritis and Cartilage Open* **5,** 100357 (2023).

246. Kanamaru, T., Neuner, A., Kurtulmus, B. & Pereira, G. Balancing the length of the distal tip by septins is key for stability and signalling function of primary cilia. *The EMBO Journal* **41,** 2021108843 (2022).

247. Srivastava, S. *et al.* A human patient-derived cellular model of Joubert syndrome reveals ciliary defects which can be rescued with targeted therapies. *Human Molecular Genetics* **26,** 4657–4667 (2017).

248. Lim, Y. C., McGlashan, S. R., Cooling, M. T. & Long, D. S. Culture and detection of primary cilia in endothelial cell models. *Cilia* **4,** 11 (2015).

249. Fischenich, K. M., Schneider, S. E., Neu, C. P., Payne, K. A. & Ferguson, V. L. Material properties and strain distribution patterns of bovine growth plate cartilage vary with anatomic location and depth. *Journal of Biomechanics* **134,** 111013 (2022).

250. Upadhyai, P., Guleria, V. S. & Udupa, P. Characterization of primary cilia features reveal cell-type specific variability in in vitro models of osteogenic and chondrogenic differentiation. *PeerJ* **8,** e9799 (2020).

251. Spasic, M. & Jacobs, C. R. Lengthening primary cilia enhances cellular mechanosensitivity. *European cells & materials* **33,** 158 (Feb. 2017).

252. Gopalakrishnan, J. *et al.* Emerging principles of primary cilia dynamics in controlling tissue organization and function. *The EMBO Journal* **42,** e113891 (2023).

253. Kukic, I., Rivera-Molina, F. & Toomre, D. The IN/OUT assay: a new tool to study ciliogenesis. *Cilia* **5,** 23 (2016).

254. Rohatgi, R. & Snell, W. J. The ciliary membrane. *Current Opinion in Cell Biology* **22,** 541–546 (2010).

255. Sun, S., Fisher, R. L., Bowser, S. S., Pentecost, B. T. & Sui, H. Three-dimensional architecture of epithelial primary cilia. *Proceedings of the National Academy of Sciences* **116,** 9370–9379 (2019).

256. Urban, J. P. G. The chondrocyte: A cell under pressure. *British Journal of Rheumatology* **33,** 901–908 (1994).

257. Guilak, F. *et al.* Mechanically induced calcium waves in articular chondrocytes are inhibited by gadolinium and amiloride. *Journal of Orthopaedic Research* **17,** 421–429 (1999).

258. Roberts, S. R., Knight, M. M., Lee, D. A. & Bader, D. L. Mechanical compression influences intracellular Ca2+ signaling in chondrocytes seeded in agarose constructs. *Journal of Applied Physiology* **90,** 1385–1391 (2001).

259. Qin, Y. *et al.* A Stretchable Scaffold with Electrochemical Sensing for 3D Culture, Mechanical Loading, and Real-Time Monitoring of Cells. *Advanced Science* **8,** 2003738 (2021).

260. Bell, A. The pipe and the pinwheel: Is pressure an effective stimulus for the 9 + 0 primary cilium? *Cell Biology International* **32,** 462–468 (2008).

261. Hale, C. M. *et al.* SMRT analysis of MTOC and nuclear positioning reveals the role of EB1 and LIC1 in single-cell polarization. *Journal of Cell Science* **124,** 4267–4285 (2011).

262. Théry, M. *et al.* Anisotropy of cell adhesive microenvironment governs cell internal organization and orientation of polarity. *Proceedings of the National Academy of Sciences* **103,** 19771–19776 (2006).

263. Hoi, K. K. *et al.* Primary cilia control oligodendrocyte precursor cell proliferation in white matter injury via Hedgehog-independent CREB signaling. *Cell Reports* **42,** 113272 (2023).

264. Fang, F., Schwartz, A. G., Moore, E. R., Sup, M. E. & Thomopoulos, S. Primary cilia as the nexus of biophysical and hedgehog signaling at the tendon enthesis. *Science Advances* **6,** eabc1799 (2020).

265. Scholzen, T. & Gerdes, J. The Ki-67 protein: From the known and the unknown. *Journal of Cellular Physiology* **182,** 311–322 (2000).

266. Xie, Z. *et al.* Low-Dose Tamoxifen Induces Significant Bone Formation in Mice. *JBMR Plus* **5** (2021).

267. Cascio, L. L. *et al.* Generation of a mouse line harboring a bi-transgene expressing luciferase and tamoxifen-activatable creERT2 recombinase in cartilage. *genesis* **52,** 110–119 (2014).

268. Laboratory, T. J. *Body Weight Information for BALBc*

269. Laboratory, T. J. *Body Weight Information for B6J (000664)*

270. Laboratory, T. J. *Body Weight Information for FVB (001800)*

271. Amano, K., Densmore, M. J. & Lanske, B. Conditional Deletion of Indian Hedgehog in Limb Mesenchyme Results in Complete Loss of Growth Plate Formation but Allows Mature Osteoblast Differentiation. *Journal of Bone and Mineral Research* **30,** 2262–2272 (2015).

272. Maeda, Y. *et al.* Indian Hedgehog produced by postnatal chondrocytes is essential for maintaining a growth plate and trabecular bone. *Proceedings of the National Academy of Sciences* **104,** 6382–6387 (2007).

273. Lanske, B. *et al.* Ablation of the PTHrP gene or the PTH/PTHrP receptor gene leads to distinct abnormalities in bone development. *Journal of Clinical Investigation* **104,** 399–407 (1999).

274. St-Jacques, B., Hammerschmidt, M. & McMahon, A. P. Indian hedgehog signaling regulates proliferation and differentiation of chondrocytes and is essential for bone formation. *Genes & Development* **13,** 2072–2086 (1999).

275. Trompet, D. *et al.* Stimulation of skeletal stem cells in the growth plate promotes linear bone growth. *JCI Insight* **9,** e165226 (2024).

276. Engel, B. D., Ludington, W. B. & Marshall, W. F. Intraflagellar transport particle size scales inversely with flagellar length: revisiting the balance-point length control model. *Journal of Cell Biology* **187,** 81–89 (2009).

277. Komarynets, O. *et al.* Aldosterone controls primary cilium length and cell size in renal collecting duct principal cells. *The FASEB Journal* **34,** 2625–2640 (2020).

278. Wang, Z. *et al.* Intraflagellar transport protein 88 interacts with polycystin 2 to regulate mechanosensitive hedgehog signaling in mandibular condylar chondrocytes. *Archives of Oral Biology* **143,** 105548 (2022).

279. Marshall, W. F. Size control in dynamic organelles. *Trends in Cell Biology* **12,** 414–419 (2002).

280. Wang, Z. *et al.* IFT88 influences chondrocyte actin organization and biomechanics. *Osteoarthritis and Cartilage* **24,** 544–554 (2016).

281. Peralta, M. *et al.* Intraflagellar Transport Complex B Proteins Regulate the Hippo Effector Yap1 during Cardiogenesis. *Cell Reports* **32** (2020).

282. Shea, C. A., Rolfe, R. A., McNeill, H. & Murphy, P. Localization of YAP activity in developing skeletal rudiments is responsive to mechanical stimulation. *Developmental Dynamics* **249,** 523–542 (2020).

283. Coschiera, A. *et al.* Primary cilia promote the differentiation of human neurons through the WNT signaling pathway. *BMC Biology* **22,** 48 (2024).

284. Delaval, B., Bright, A., Lawson, N. D. & Doxsey, S. The cilia protein IFT88 is required for spindle orientation in mitosis. *Nature Cell Biology* **13,** 461–468 (2011).

285. Geister, K. A. *et al.* LINE-1 Mediated Insertion into Poc1a (Protein of Centriole 1 A) Causes Growth Insufficiency and Male Infertility in Mice. *PLoS Genetics* **11,** e1005569 (2015).

286. Santos-Ledo, A., Garcia-Macia, M., Campbell, P. D., Gronska, M. & Marlow, F. L. Kinesin-1 promotes chondrocyte maintenance during skeletal morphogenesis. *PLoS Genetics* **13,** e1006918 (2017).

287. Almubarak, A. & Berry, F. B. Cell-Cycle Synchronization, Methods and Protocols. *Methods in Molecular Biology* **2579,** 227–233 (2022).

288. Rais, Y. *et al.* The growth plate's response to load is partially mediated by mechano-sensing via the chondrocytic primary cilium. *Cellular and Molecular Life Sciences* **72,** 597–615 (2015).

289. Cancel, M., Grimard, G., Thuillard-Crisinel, D., Moldovan, F. & Villemure, I. Effects of in vivo static compressive loading on aggrecan and type II and X collagens in the rat growth plate extracellular matrix. *Bone* **44,** 306–315 (2009).

290. Mustafy, T., Londono, I., Moldovan, F. & Villemure, I. High Impact Exercise Improves Bone Microstructure and Strength in Growing Rats. *Scientific Reports* **9,** 13128 (2019).

291. Ning, B., Mustafy, T., Londono, I., Laporte, C. & Villemure, I. Impact loading intensifies cortical bone (re)modeling and alters longitudinal bone growth of pubertal rats. *Biomechanics and Modeling in Mechanobiology,* 1–18 (2023).

292. Finkielstain, G., Lui, J. & Baron, J. Catch-Up Growth: Cellular and Molecular Mechanisms. *World Review of Nutrition and Dietetics* **106,** 100–104 (2013).

293. Ueki, M. *et al.* The Effect of Mechanical Loading on the Metabolism of Growth Plate Chondrocytes. *Annals of Biomedical Engineering* **36,** 793–800 (2008).

294. Resnick, A. & Hopfer, U. Force-Response Considerations in Ciliary Mechanosensation. *Biophysical Journal* **93,** 1380–1390 (2007).

295. Liu, W. *et al.* Mechanoregulation of intracellular Ca2+ concentration is attenuated in collecting duct of monocilium-impaired orpk mice. *American Journal of Physiology-Renal Physiology* **289,** F978–F988 (2005).

296. Wann, A. K. T. *et al.* Primary cilia mediate mechanotransduction through control of ATP-induced Ca 2+ signaling in compressed chondrocytes. *The FASEB Journal* **26,** 1663–1671 (2012).

297. Baydoun, M. *et al.* Three-dimensional (3D) culture of adult murine colon as an in vitro model of cryptosporidiosis: Proof of concept. *Scientific Reports* **7,** 17288 (2017).

298. Grimsrud, C. D. *et al.* BMP signaling stimulates chondrocyte maturation and the expression of Indian hedgehog. *Journal of Orthopaedic Research* **19,** 18–25 (2001).

299. Minina, E. *et al.* BMP and Ihh/PTHrP signaling interact to coordinate chondrocyte proliferation and differentiation. *Development* **128,** 4523–4534 (2001).

300. Minina, E., Kreschel, C., Naski, M. C., Ornitz, D. M. & Vortkamp, A. Interaction of FGF, Ihh/Pthlh, and BMP Signaling Integrates Chondrocyte Proliferation and Hypertrophic Differentiation. *Developmental Cell* **3,** 439–449 (2002).

301. Gao, B. *et al.* Wnt Signaling Gradients Establish Planar Cell Polarity by Inducing Vangl2 Phosphorylation through Ror2. *Developmental Cell* **20,** 163–176 (2011).

302. Xu, H. *et al.* BMP-2 releasing mineral-coated microparticle-integrated hydrogel system for enhanced bone regeneration. *Frontiers in Bioengineering and Biotechnology* **11,** 1217335 (2023).

303. Zhang, Q., Liu, Y., Li, J., Wang, J. & Liu, C. Recapitulation of growth factor-enriched microenvironment via BMP receptor activating hydrogel. *Bioactive Materials* **20,** 638–650 (2023).

304. Samorezov, J. E., Headley, E. B., Everett, C. R. & Alsberg, E. Sustained presentation of BMP-2 enhances osteogenic differentiation of human adipose-derived stem cells in gelatin hydrogels. *Journal of Biomedical Materials Research Part A* **104,** 1387–1397 (2016).

305. Luca, F. D. *et al.* Regulation of Growth Plate Chondrogenesis by Bone Morphogenetic Protein-2. *Endocrinology* **142,** 430–436 (2001).

306. Shu, B. *et al.* BMP2, but not BMP4, is crucial for chondrocyte proliferation and maturation during endochondral bone development. *Journal of Cell Science* **124,** 3428–3440 (2011).

307. Bandyopadhyay, A. *et al.* Genetic Analysis of the Roles of BMP2, BMP4, and BMP7 in Limb Patterning and Skeletogenesis. *PLoS Genetics* **2,** e216 (2006).

308. Gründer, T. *et al.* Bone morphogenetic protein (BMP)-2 enhances the expression of type II collagen and aggrecan in chondrocytes embedded in alginate beads. *Osteoarthritis and Cartilage* **12,** 559–567 (2004).

309. Whitty, C. *et al.* Sustained delivery of the bone morphogenetic proteins BMP-2 and BMP-7 for cartilage repair and regeneration in osteoarthritis. *Osteoarthritis and Cartilage Open* **4,** 100240 (2022).

310. Levett, P. A. *et al.* A biomimetic extracellular matrix for cartilage tissue engineering centered on photocurable gelatin, hyaluronic acid and chondroitin sulfate. *Acta Biomaterialia* **10,** 214–223 (2014).

311. Loessner, D. *et al.* Functionalization, preparation and use of cell-laden gelatin methacryloyl-based hydrogels as modular tissue culture platforms. *Nature Protocols* **11,** 727–746 (2016).

312. Schuurman, W. *et al.* Gelatin-Methacrylamide Hydrogels as Potential Biomaterials for Fabrication of Tissue-Engineered Cartilage Constructs. *Macromolecular Bioscience* **13,** 551–561 (2013).

313. Ruppert, R., Hoffmann, E. & Sebald, W. Human Bone Morphogenetic Protein 2 Contains a Heparin-Binding Site which Modifies Its Biological Activity. *European Journal of Biochemistry* **237,** 295–302 (1996).

314. Caroti, C. M. *et al.* A novel technique for accelerated culture of murine mesenchymal stem cells that allows for sustained multipotency. *Scientific Reports* **7** (2017).

315. Xu, L. *et al.* Tissue source determines the differentiation potentials of mesenchymal stem cells: A comparative study of human mesenchymal stem cells from bone marrow and adipose tissue. *Stem Cell Research and Therapy* **8** (2017).

316. Lageneste, O. D. D. *et al.* Periosteum contains skeletal stem cells with high bone regenerative potential controlled by Periostin. *Nature Communications* **9** (2018).

317. Livak, K. J. & Schmittgen, T. D. Analysis of relative gene expression data using real-time quantitative PCR and the 2-ΔΔCT method. *Methods* **25,** 402–408 (2001).

318. Benoit, D. S. & Anseth, K. S. Heparin functionalized PEG gels that modulate protein adsorption for hMSC adhesion and differentiation. *Acta Biomaterialia* **1,** 461–470 (2005).

319. Jeon, O., Powell, C., Solorio, L. D., Krebs, M. D. & Alsberg, E. Affinity-based growth factor delivery using biodegradable, photocrosslinked heparin-alginate hydrogels. *Journal of Controlled Release* **154,** 258–266 (2011).

320. Schroeder, A. *et al.* The RIN: an RNA integrity number for assigning integrity values to RNA measurements. *BMC Molecular Biology* **7,** 3 (2006).

321. Dominici, M. *et al.* Minimal criteria for defining multipotent mesenchymal stromal cells. The International Society for Cellular Therapy position statement. *Cytotherapy* **8,** 315–317 (2006).

322. Wagner, W. *et al.* Replicative Senescence of Mesenchymal Stem Cells: A Continuous and Organized Process. *PLoS ONE* **3,** e2213 (2008).

323. Strioga, M., Viswanathan, S., Darinskas, A., Slaby, O. & Michalek, J. Same or not the same? comparison of adipose tissue-derived versus bone marrow-derived mesenchymal stem and stromal cells. *Stem Cells and Development* **21,** 2724–2752 (2012).

324. Huang, Z., Nelson, E. R., Smith, R. L. & Goodman, S. B. The sequential expression profiles of growth factors from osteroprogenitors to osteoblasts in vitro. *Tissue Engineering* **13,** 2311–2320 (2007).

325. Kim, H. J. & Im, G. I. Chondrogenic differentiation of adipose tissue-derived mesenchymal stem cells: Greater doses of growth factor are necessary. *Journal of Orthopaedic Research* **27,** 612–619 (2009).

326. Estes, B. T., Wu, A. W. & Guilak, F. Potent induction of chondrocytic differentiation of human adipose-derived adult stem cells by bone morphogenetic protein 6. *Arthritis and Rheumatism* **54,** 1222–1232 (2006).

327. Walejewska, E. *et al.* Tuning Physical Properties of GelMA Hydrogels through Microarchitecture for Engineering Osteoid Tissue. *Biomacromolecules* **25,** 188–199 (2024).

328. Guo, A., Zhang, S., Yang, R. & Sui, C. Enhancing the mechanical strength of 3D printed GelMA for soft tissue engineering applications. *Materials Today Bio* **24,** 100939 (2024).

329. Ghosh, R. N. *et al.* An insight into synthesis, properties and applications of gelatin methacryloyl hydrogel for 3D bioprinting. *Materials Advances* **4,** 5496–5529 (2023).

330. Gao, J., John, L. W. & Esra, R. On the State of Stress in the Growth Plate under Physiologic Compressive Loading. *Open Journal of Biophysics* **04,** 13–21 (2014).

331. Souza, R. L. D. *et al.* Non-invasive axial loading of mouse tibiae increases cortical bone formation and modifies trabecular organization: A new model to study cortical and cancellous compartments in a single loaded element. *Bone* **37,** 810–818 (2005).

332. Poulet, B., Hamilton, R. W., Shefelbine, S. & Pitsillides, A. A. Characterizing a novel and adjustable noninvasive murine joint loading model. *Arthritis & Rheumatism* **63,** 137–147 (2011).

333. Rowson, D. T., Shelton, J. C., Screen, H. R. & Knight, M. M. Mechanical loading induces primary cilia disassembly in tendon cells via TGFβ and HDAC6. *Scientific Reports 2018 8:1* **8,** 1–12 (2018).

334. McDermott, A. M., Eastburn, E. A., Kelly, D. J. & Boerckel, J. D. Effects of chondrogenic priming duration on mechanoregulation of engineered cartilage. *Journal of Biomechanics* **125,** 110580 (2021).

335. Huang, A., Farrell, M., Kim, M. & Mauck, R. Long-term dynamic loading improves the mechanical properties of chondrogenic mesenchymal stem cell-laden hydrogel. *European Cells and Materials* **19,** 72–85 (2010).

336. Barta, N. *et al.* Identifying Suitable Reference Gene Candidates for Quantification of DNA Damage-Induced Cellular Responses in Human U2OS Cell Culture System. *Biomolecules* **13,** 1523 (2023).

337. Eliseeva, I., Vasilieva, M. & Ovchinnikov, L. P. Translation of Human β-Actin mRNA is Regulated by mTOR Pathway. *Genes* **10,** 96 (2019).

338. Li, K. *et al.* Acetylation of WRN Protein Regulates Its Stability by Inhibiting Ubiquitination. *PLoS ONE* **5,** e10341 (2010).

339. Shintani, N., Siebenrock, K. A. & Hunziker, E. B. TGF-ß1 Enhances the BMP-2-Induced Chondrogenesis of Bovine Synovial Explants and Arrests Downstream Differentiation at an Early Stage of Hypertrophy. *PLoS ONE* **8,** e53086 (2013).

340. Gonzalez-Fernandez, T., Tierney, E. G., Cunniffe, G. M., O'Brien, F. J. & Kelly, D. J. Gene Delivery of TGF-β3 and BMP2 in an MSC-Laden Alginate Hydrogel for Articular Cartilage and Endochondral Bone Tissue Engineering. *Tissue Engineering Part A* **22,** 776–787 (2016).

341. Li, X., Yi, W., Jin, A., Duan, Y. & Min, S. Effects of sequentially released BMP-2 and BMP-7 from PELA microcapsule-based scaffolds on the bone regeneration - PMC. *American Journal of Translational Research.* **8** (2015).

342. Takao, T. *et al.* Modeling human limb skeletal development using human pluripotent stem cell-derived skeletal assembloids. *bioRxiv,* 2025.01.09.631479 (2025).

343. Lamandé, S. R. *et al.* Modeling human skeletal development using human pluripotent stem cells. *Proceedings of the National Academy of Sciences* **120,** e2211510120 (2023).

344. Macarelli, V., Leventea, E. & Merkle, F. T. Regulation of the length of neuronal primary cilia and its potential effects on signalling. *Trends in Cell Biology* **33,** 979–990 (2023).

345. Simons, M. *et al.* Inversin, the gene product mutated in nephronophthisis type II, functions as a molecular switch between Wnt signaling pathways. *Nature Genetics* **37,** 537–543 (2005).

346. Hickey, D., Vilfan, A. & Golestanian, R. Ciliary chemosensitivity is enhanced by cilium geometry and motility. *eLife* **10,** e66322 (2021).

347. Breslin, L., Prosser, S. L., Cuffe, S. & Morrison, C. G. Ciliary abnormalities in senescent human fibroblasts impair proliferative capacity. *Cell Cycle* **13,** 2773–2779 (2014).

348. McGlashan, S. R., Cluett, E. C., Jensen, C. G. & Poole, C. A. Primary Cilia in osteoarthritic chondrocytes: From chondrons to clusters. *Developmental Dynamics* **237,** 2013–2020 (2008).

349. Mick, D. U. *et al.* Proteomics of Primary Cilia by Proximity Labeling. *Developmental Cell* **35,** 497–512 (2015).

350. Ishikawa, H., Thompson, J., Yates, J. R. & Marshall, W. F. Proteomic Analysis of Mammalian Primary Cilia. *Current Biology* **22,** 414–419 (2012).

351. McIntyre, J. C. *et al.* Gene therapy rescues cilia defects and restores olfactory function in a mammalian ciliopathy model. *Nature Medicine* **18,** 1423–1428 (2012).

352. Talwar, R. M., Wong, B. S., Svoboda, K. & Harper, R. P. Effects of Estrogen on Chondrocyte Proliferation and Collagen Synthesis in Skeletally Mature Articular Cartilage. *Journal of Oral and Maxillofacial Surgery* **64,** 600–609 (2006).

353. Lawrence, J. E. *et al.* Single-cell transcriptomics identifies chondrocyte differentiation dynamics in vivo and in vitro. *Developmental Cell* (2025).

354. Subramanian, A., Budhiraja, G. & Sahu, N. Chondrocyte primary cilium is mechanosensitive and responds to low-intensity-ultrasound by altering its length and orientation. *The International Journal of Biochemistry & Cell Biology* **91,** 60–64 (Oct. 2017).

355. Zhang, J. *et al.* Long-term mechanical loading is required for the formation of 3D bioprinted functional osteocyte bone organoids. *Biofabrication* **14** (July 2022).

356. McDermott, A. M. *et al.* Recapitulating bone development through engineered mesenchymal condensations and mechanical cues for tissue regeneration. *Science Translational Medicine* **11,** 7756 (2019).

357. Mustafy, T., Londono, I. & Villemure, I. Experimental and finite element analyses of bone strains in the growing rat tibia induced by in vivo axial compression. *Journal of the Mechanical Behavior of Biomedical Materials* **94,** 176–185 (2019).

358. Hirota, K. *et al.* Live imaging analysis of the growth plate in a murine long bone explanted culture system. *Scientific Reports 2018 8:1* **8,** 1–10 (2018).

359. Li, J. *et al.* Systematic Reconstruction of Molecular Cascades Regulating GP Development Using Single-Cell RNA-Seq. *Cell Reports* **15,** 1467–1480 (2016).